

Gel Polymer Electrolytes and Battery Designs for Rechargeable Zinc-Air Batteries

by

Thuy Nguyen Thanh Tran

A thesis submitted in partial fulfillment of the requirements for the degree of

Doctor of Philosophy

in

Chemical Engineering

Department of Chemical and Materials Engineering

University of Alberta

© Thuy Nguyen Thanh Tran, 2020

## Abstract

To accelerate the world's transition to renewable sources, rechargeable Zn-air batteries (ZABs) have regained interest in recent years for distributed energy storage. ZAB technology has several advantages including operational safety, high theoretical energy density and low cost. This is mainly due to Zn being environmentally benign and abundant in the Earth's crust, while the other electroactive species (oxygen) can be withdrawn directly from the air. Although primary ZABs have been commercially available for almost a century, there are still numerous issues to be addressed for their rechargeable counterparts. For example, problems arise during recharging of ZABs due to instability of the air electrode. Additionally, batteries using aqueous electrolytes suffer from carbonation, leakage and evaporation of the electrolyte, and dendrite formation on the Zn electrode, all of which can be mitigated by using gel polymer electrolytes (GPEs). The thesis focuses on (1) preparation techniques, characterization and compositional optimization of GPEs, and (2) configurations for solid-state ZABs to improve energy efficiency and cycle life.

The first study involved the synthesis and characterization of different hydrogel networks, i.e., poly(vinyl alcohol) (PVA), poly(acrylic acid) (PAA) and poly(4-vinylbenzenesulfonate-co-[3-(methacryloylamino)propyl]trimethylammonium chloride) (PAM). Their chemical stability, electrochemical windows and mechanical properties are evaluated. The relationship between ionic conductivity, water uptake and temperature are also discussed. This study demonstrated that PAA-based GPEs show considerable promise for use as electrolytes in ZABs.

The second study investigated cyclability of solid-state ZAB using tri-electrode designs such as sandwich and planar cells. Various additives for the PAA-based GPEs, such as crosslinker and zinc oxide (ZnO), were also evaluated. Crosslinking density affects the physical state of GPEs, which in turn affects the oxygen evolution reaction, since oxygen bubbles may be trapped in the

GPE-air electrode interface. Meanwhile, the effects of ZnO on discharge and charge were studied separately. The addition of ZnO to the oxygen reduction reaction side of the sandwich cell enhanced the cycling performance of ZABs; i.e., the battery can withstand at least 100 cycles at 5 mA cm<sup>-2</sup> with an efficiency of 62% during the first cycle.

The third study compared cyclability of ZABs using aqueous electrolytes and GPEs with a bi-electrode design. In general, ZABs with GPEs exhibit better initial performance than those with aqueous 6 M KOH. Although the efficiency of the ZAB using the aqueous electrolyte gradually improved during cycling, there is visible evidence of flooding and degradation of the air electrode. Gels with lower crosslinking concentrations are weaker, but they have higher conductivity and better water retention, whereas gels with higher crosslinking concentrations can reduce dendrite growth, but they can facilitate passivation of the Zn electrode, resulting in early failure of the battery.

The fourth study optimized PAA as a promising host to support alkaline electrolytes and other additives, including ZnO and zinc acetate in ZABs. Most importantly, stiffness and adhesion of the PAA matrix to the air electrode influence battery performance. Alternative ideas for battery designs besides bi- and tri- electrode configurations are also discussed. With a vertical double air electrode configuration, ZABs using PAA-based GPEs show unprecedented performance including high specific energy (1036 Wh kg<sub>Zn</sub><sup>-1</sup>), excellent cycling stability (190 cycles at 2×10 mA cm<sup>-2</sup>) and high power density output (2×135 mW cm<sup>-2</sup>). The study represents a viable option to replace aqueous electrolytes for high performing ZABs.

## Preface

This thesis focusses on the synthesis and characterization of GPEs, battery design and electrochemical testing of rechargeable solid-state ZABs. The research presented in Chapters 3, 4, 5, 6, along with their supporting information and the Appendix, are my original work.

Chapters 3, 4, 5 and 6 summarize work done in collaboration with Ming Xiong (PhD), Michael Clark (PhD), Drew Aasen (MSc), Dinara Zhalmuratova (MSc) and Matthew Labbe (MSc). Ming, Michael and Matthew contributed discussions regarding electrochemical testing. Michael performed SEM analysis on catalysts (Chapter 4 and 5). Drew prepared (Co,Fe)<sub>3</sub>O<sub>4</sub>/nitrogen-doped carbon nanotube bifunctional catalysts (Chapter 6). Dinara performed tensile and peeling tests (Chapter 6). Other characterization analysis, optimization of synthesis parameters of GPEs, battery setups, electrochemical testing and interpretation of the results were conducted by myself. Manuscript preparation was accomplished with the help of Dr. Douglas G. Ivey and Dr. Hyun-Joong Chung.

Versions of Chapter 3 and Chapter 5 of this thesis have been published as:

Chapter 3: Tran, T.N.T., Chung, H.-J. and Ivey, D.G., *A Study of Alkaline Gel Polymer Electrolytes for Rechargeable Zinc-Air Batteries*. *Electrochimica Acta*, 2019. **327**: p. 135021.

Chapter 5: Tran, T.N.T., Clark, M.P., Chung, H.-J. and Ivey, D.G., *Effects of Crosslinker Concentration in Poly(Acrylic Acid)–KOH Gel Electrolyte on Performance of Zinc-Air Batteries*. *Batteries and Supercaps*, 2020. **3**(5): p. 409–416.

A version of Chapter 6 of this thesis has been accepted as:

Chapter 6: Tran, T.N.T., Aasen, D., Zhalmuratova, D., Labbe, M., Chung, H.-J. and Ivey, D.G., *Compositional Effects of Gel Polymer Electrolyte and Battery Design for Zinc-Air Batteries*. Batteries and Supercaps, 2020. doi:10.1002/batt.202000054.

A version of Chapter 4 of this thesis has been submitted as:

Chapter 4: Tran, T.N.T., Xiong, M., Clark, M.P., Chung, H.-J. and Ivey, D.G., *A Tri-Electrode Configuration for Zinc-Air Batteries Using Gel Polymer Electrolytes*, *Electrochimica Acta*, submitted January, 2020.

The Appendix represents my previous work regarding electrochemical sensors which was done in collaboration with Shide Qiu (MSc). Shide performed SEM analysis. I was responsible for synthesis of the sensors, electrochemical analysis, and interpretation of the results. Manuscript preparation was accomplished with the help of Dr. Hyun-Joong Chung. A version of the Appendix of this thesis has been published as:

Appendix: Tran, T.N.T., Qiu, S. and Chung, H.-J., *Potassium Ion-selective Electrode Using Polyaniline and Matrix-Supported Ion-Selective PVC Membrane*. *IEEE Sensors Journal*, 2018. **18**(22): p. 9081–9087.

In addition to the above publications, I also contributed to two of my group members' publications (not included in this thesis):

(1) Li, X., Charaya, H., Tran, T.N.T., Lee, B., Cho, J.-Y. and Chung, H.-J., *Direct Visualization of Nano and Microscale Polymer Morphologies in As-Prepared and Dialyzed Polyampholyte Hydrogels by Electron Microscopy Techniques*. *MRS Communications*, 2018. **8**(3): p. 1079–1084.

(2) Zheng, L., Tran, T.N.T., Zhalmuratova, D., Ivey, D.G. and Chung, H.-J., *Colorimetric Voltmeter Using Colloidal Fe<sub>3</sub>O<sub>4</sub>@SiO<sub>2</sub> Nanoparticles as an Overpotential Alarm System for Zinc-air Batteries*. ACS Applied Nano Materials, 2019. **2**(11): p. 6982–6988.

For publication (1), my contribution included synthesizing polyampholyte using a thermoinitiator and performing Fourier transform infrared (FTIR) spectroscopy for comparison purposes. For publication (2), I contributed ideas and helped with battery fabrication.

## **Acknowledgements**

First of all, I would like to thank my supervisors, Dr. Hyun-Joong Chung and Dr. Douglas G. Ivey for giving me the opportunity to pursue doctoral studies at University of Alberta. Their insightful guidance helped me overcome countless difficulties in my research, and their wisdom and tolerance inspired me to continuously grow as a better person. Without their support, this work would have been much more difficult to complete.

I would like to thank Dr. Anastasia Elias and Dr. Xiaoli Tan for access to their laboratories. I would also like to thank Dr. Marco da Silva, Hemant Charaya, Minshan Meng and nanoFAB staff for their experimental support.

Financial support from the Natural Sciences and Engineering Research Council of Canada (NSERC), the Graduate Student's Association (GSA), the Faculty of Graduate Studies and Research (FGSR), and Future Energy Systems (FES, T06 P03) are gratefully acknowledged.

I am grateful to our group members and the friends I have made over the duration of my study in Edmonton. Thank you for encouraging me and bringing so much joy to the journey. Shide Qiu, Chungyeon Cho, Fanghui Liu, Ming Xiong, Michael Clark, Lelin Zheng, Dinara Zhalmuratova, Arjun Dhiman, Drew Aasen, Rosmi Abraham and Matthew Labbe, I am blessed to have worked with such talented and kind-hearted people like you.

My partner, you are my rock. Thank you for patiently listening, giving me helpful advice and pep talks, and tolerating me when I was not all pleasant to be around.

I am deeply thankful to my parents. My moms, thank you for being self-sacrificing and uncomplaining about all the hardships you had to endure to give me this carefree life. My sister, thank you for the endless support and memorable trips around the world.

## Table of Contents

<b>Abstract.....</b>	<b>ii</b>
<b>Preface.....</b>	<b>iv</b>
<b>Acknowledgements .....</b>	<b>vii</b>
<b>Table of Contents .....</b>	<b>viii</b>
<b>List of Tables .....</b>	<b>xii</b>
<b>List of Figures.....</b>	<b>xiii</b>
<b>Chapter 1. Introduction.....</b>	<b>1</b>
<b>Chapter 2. Literature Review .....</b>	<b>5</b>
2.1. ZINC-AIR BATTERIES .....	5
2.1.1. Chemical reactions in ZABs.....	5
2.1.2. Battery components .....	8
2.1.3. Potential application of ZABs .....	10
2.1.3. Challenges for ZABs .....	11
2.2. ELECTROLYTES FOR ZABs.....	12
2.2.1. Aqueous electrolytes.....	12
2.2.2. Room temperature ionic liquids .....	14
2.2.3. Polymer electrolytes .....	15
2.2.4. Electrolyte additives .....	19
2.3. BATTERY CONFIGURATIONS .....	21
2.3.1. Cell design .....	21
2.3.2. Stack design.....	27
2.4. KEY CHARACTERIZATION TECHNIQUES .....	32
2.4.1. Electrochemical testing.....	32
2.4.2. Scanning electron microscopy and energy dispersive X-ray spectroscopy.....	36
2.4.3. Fourier transform infrared spectroscopy .....	38
2.4.4. Rheology.....	39
2.5. SUMMARY .....	41

<b>Chapter 3. A Study of Alkaline Gel Polymer Electrolytes for Rechargeable Zinc-air Batteries</b>	<b>42</b>
3.1. INTRODUCTION.....	42
3.2. EXPERIMENTAL PROCEDURE .....	45
3.2.1. Synthesis of gel electrolytes .....	45
3.2.2. Materials characterization.....	46
3.2.3. Electrochemical measurements .....	47
3.2.4. Water uptake study .....	47
3.2.5. Cell testing.....	48
3.3. RESULTS AND DISCUSSION .....	49
3.3.1. Mechanical strength, electrochemical window and alkaline stability .....	49
3.3.2. Ionic conductivity in relation to water uptake and temperature .....	55
3.3.3. Performance of Zn-air battery .....	59
3.4. CONCLUSIONS .....	63
3.5. SUPPORTING INFORMATION.....	64
<b>Chapter 4. A Tri-Electrode Configuration for Zinc-air Batteries Using Gel Polymer Electrolytes</b>	<b>67</b>
4.1. INTRODUCTION.....	67
4.2. EXPERIMENTAL PROCEDURE .....	71
4.2.1 Synthesis of catalysts.....	71
4.2.2. Synthesis of gel polymer electrolytes (GPEs).....	72
4.2.3. Cell fabrication .....	72
4.2.4. Material characterization .....	73
4.2.5. Battery testing.....	74
4.3. RESULTS AND DISCUSSION .....	75
4.3.1. Battery configuration.....	75
4.3.2. Effect of crosslinking density .....	77
4.3.3. Effect of ZnO additive.....	81
4.3.4. Cycling performance of batteries using GPEs.....	86
4.4. CONCLUSIONS .....	91
4.5. SUPPORTING INFORMATION.....	91

<b>Chapter 5. Effects of Crosslinker Concentration in Poly(Acrylic Acid)–KOH Gel Electrolyte on Performance of Zinc-air Batteries.....</b>	<b>96</b>
5.1. INTRODUCTION.....	96
5.2. EXPERIMENTAL PROCEDURE .....	99
5.2.1 Synthesis of catalysts.....	99
5.2.2. Synthesis of hydrogel electrolyte .....	100
5.2.3. Cell fabrication .....	100
5.2.4. Material characterization .....	101
5.2.5. Battery testing.....	103
5.3. RESULTS AND DISCUSSION .....	104
5.3.1. Properties of PAA–KOH gel electrolytes.....	104
5.3.2. Performance of Zn-air batteries .....	108
5.3.3. Post testing analysis of Zn electrode .....	113
5.4. CONCLUSIONS .....	115
5.5. SUPPORTING INFORMATION.....	117
<b>Chapter 6. Compositional Effects of Gel Polymer Electrolyte and Battery Design for Zinc-air Batteries .....</b>	<b>123</b>
6.1. INTRODUCTION.....	123
6.2. EXPERIMENTAL PROCEDURE .....	126
6.2.1 Synthesis of catalysts.....	126
6.2.2. Synthesis of hydrogel electrolyte .....	127
6.2.3. Cell fabrication .....	128
6.2.4. Materials characterization.....	129
6.2.5. Battery testing.....	131
6.3. RESULTS AND DISCUSSION .....	132
6.3.1. Evaluation of PAA–KOH gel electrolytes.....	132
6.3.2. Effects of PAA matrix on cycling performance of ZABs .....	139
6.3.3. Effect of battery design on ZAB performance .....	143
6.4. CONCLUSIONS .....	147
6.5. SUPPORTING INFORMATION.....	148
<b>Chapter 7. Conclusions and Future Work.....</b>	<b>153</b>

7.1 CONCLUSIONS .....	153
7.1.1. Influence of different hydrogel networks on characteristics of GPEs.....	153
7.1.2. Optimization of poly(acrylic acid) (PAA)-based GPEs .....	153
7.1.3. Battery configurations .....	154
7.2. FUTURE WORK.....	155
7.2.1. Further investigation on polymer matrix.....	155
7.2.2. Further investigation on electrolyte additives .....	156
7.2.3. Device optimization.....	156
<b>References .....</b>	<b>157</b>
<b>Appendix. Potassium Ion-selective Electrode Using Polyaniline and Matrix-Supported Ion-Selective PVC Membrane.....</b>	<b>175</b>
A.1. INTRODUCTION.....	175
A.2. MATERIALS AND METHODS .....	179
A.2.1. Materials and instruments.....	179
A.2.2. PANI polymerization.....	180
A.2.3. Preparation of K <sup>+</sup> ion-selective electrode .....	180
A.2.4. Electromotive force (EMF) measurements.....	181
A.2.5. Electrochemical impedance spectroscopy (EIS) .....	181
A.2.6. Potential stability measurements .....	182
A.3. RESULTS AND DISCUSSION .....	182
A.3.1. Characterization of polyaniline.....	182
A.3.2. Selectivity test.....	185
A.3.3. Sensitivity test.....	186
A.3.4. EIS .....	187
A.3.5. Artificial serum test .....	188
A.3.6. Potential stability .....	189
A.4. CONCLUSIONS .....	190

## List of Tables

Table 2.1. Possible reactions in ZABs .....	7
Table 2.2. Comparison of different battery types [37-42] .....	11
Table 2.3. Reactions for ZABs in aqueous electrolyte at different pH values [46] .....	13
Table 2.4. Composition and properties of alkaline GPEs for ZABs.....	16
Table 2.5. Comparisons of typical electrolyte systems for ZABs .....	20
Table 3.1. Compressive modulus (kPa) of hydrogels after immersion in DIW and in 6 M KOH	51
Table 3.2. Fitting of EIS results before and after cycling tests.....	62
Table 4.1. Comparison of recent rechargeable ZABs.....	69
Table 4.2. Comparison of rechargeable tri-electrode ZABs in chronological order .....	90
Table 5.1. EDX analysis of Zn surface after cycling test at $5 \text{ mA cm}^{-2}$ .....	115
Table 6.1. Compositions of PAA–KOH samples .....	128
Table 6.2. Mechanical property parameters for PAA–KOH .....	139
Table 6.3. Comparison of ZAB cycling performance and maximum power density for this work and the recent literature.....	146
Table A.1. Summary of recent studies of solid-state potassium ion-selective electrodes .....	179

## List of Figures

Figure 1.1. (a) Theoretical and practical specific energy of various types of rechargeable batteries [11]. (b) Theoretical specific energy, volumetric energy density and nominal cell voltage for various metal-air batteries [12].	3
Figure 2.1: Schematic polarization curves of Zn and air electrodes in ZABs. The black line represents the theoretical equilibrium potential of 1.65 V. The red and blue lines represent the actual working voltages during discharge and charge, respectively.	7
Figure 2.2: Schematic illustration of ZABs, including different forms of Zn anodes and different electrocatalysts for the air cathode.	8
Figure 2.3. Pourbaix diagram of Zn and water at 25 °C.	14
Figure 2.4. Cross section through a ZAB button cell.	22
Figure 2.5. Schematic of two cell designs for bi-electrode ZABs in (a) vertical and (b) horizontal placements. 1) Acrylic sheets, 2) Zn, 3) GDL, 4) current collector Ni and 5) refilling hole.	24
Figure 2.6. Schematic of two typical flexible ZABs: (a) planar-shaped and (b) cable-shaped batteries.	25
Figure 2.7. Schematic of structures for tri-electrode (a) horizontal cell and (b) vertical cell.	26
Figure 2.8. Illustration of various configurations in stretchable solid-state ZABs: (a) 4 cells in parallel, (b) 2 modules in series with each module having 2 cells in parallel and (c) 4 cells in series. (d) Photographs of a solid-state ZAB stretched under 0%, 50%, 75%, 100% and 125% strain.	27
Figure 2.9. Schematic of a multi-cell ZAB pack with (a) monopolar arrangement and (b) bipolar arrangement.	29
Figure 2.10. (a) Schematic of a tri-electrode flow stack and (b) photograph of a pilot plant (1 kW/4 kWh) [13]. (c) Design of Zn-O <sub>2</sub> stack and (d) photograph of the system (500 W/500 Wh) [112].	31
Figure 2.11. Two representative Nyquist plots for EIS data: (a) Ionic conductivity of electrolytes and (b) full cell testing.	33
Figure 2.12. An example of CV curve where current is plotted against the voltage applied.	34
Figure 2.13. Examples of galvanodynamic techniques: (a) discharge-charge polarization profiles and (b) rate test.	35
Figure 2.14. Examples of galvanostatic techniques: (a and b) depth of discharge curve and specific capacity of the battery, and (c) cycling test in a short interval (10 min per cycle)	36
Figure 2.15. Schematic diagram of the core components of an SEM.	37
Figure 2.16: Sample FTIR spectrum corresponding to cellulose molecular structure. Common types of bonds absorbed in the approximate regions are also shown.	39

Figure 2.17. Different geometries of rheometers.....	40
Figure 2.18. Presets for oscillatory tests: (a) amplitude sweep and (b) frequency sweep. ....	40
Figure 2.19. Sinusoidal function of shear strain $\gamma$ and shear stress $\tau$ versus time for a viscoelastic sample. The two curves are offset by phase shift $\delta$ . ....	41
Figure 3.1. (a) Chemical structure of PVA, PAA and PAM. PAM is a random copolymer of two monomers. (b) Schematic illustration of the polymer states in deionized water (DIW) and 6 M KOH solution. ....	45
Figure 3.2. Coin cell configurations for (a) CV and EIS measurements and (b) full cell testing using GPEs.....	49
Figure 3.3. (a) Images of PVA, PAA and PAM after storage for 3 months. The PVA and PAM images shown are for the as-prepared condition and after immersion in DIW and 3, 6, and 9 M KOH solutions. (b) Compression test results for PVA, PAA and PAM in DIW and 6 M KOH. ....	51
Figure 3.4. FESEM secondary electron (SE) cross section images of PVA, PAA and PAM after immersion in DIW and 6 M KOH. ....	51
Figure 3.5. FTIR spectra for (a) PVA, (b) PAA and (c) PAM. Dashed lines represent the hydrogels in DIW. Blue solid lines represent the hydrogels in 6 M KOH after rinsing with DIW. The red line in (b) represents PAA6M rinsed with HCl and then with DIW. ....	54
Figure 3.6. CV curves of PVA6M, PAA6M and PAM6M in (a) hydrated states and (b) freeze-dried states. ....	55
Figure 3.7. (a) Ionic conductivities of aqueous solutions, hydrogels and a commercial separator (Cellgard) at different KOH concentrations. (b) Water content in KOH solutions and GPEs. (c) Conductivities of GPEs in 6 M KOH at different temperatures. Each data point represents an average of 5 measurements and the error bars correspond to one standard deviation.....	58
Figure 3.8. (a) Discharge curves for ZABs at various current densities with different electrolytes. (b) Discharge-charge cycling tests at $0.5 \text{ mA cm}^{-2}$ . EIS plots at 1.2 V vs. Zn/Zn <sup>2+</sup> before (c) and after (d) cycling tests. Symbols represent the measured data and solid lines represent the best fit using the equivalent circuit shown in Figure S3.1b. (e) Discharge-charge efficiency vs. current density (1 <sup>st</sup> cycle) for ZABs using GPEs. ....	60
Figure 4.1. Tri-electrode cell assembly: (a) planar and (b) sandwich configurations. 1) Acrylic sheets, 2) current collector, 3) GDL, 4) Ni foam, 5) polypropylene film, 6) GPE, 7) Zn, 8) bolts, 9) nuts.....	73
Figure 4.2. Electrochemical evaluation of Zn-air batteries with different configurations, i.e., planar and sandwich. (a) Rate discharge-charge curves and (b) cycling performance at $5 \text{ mA cm}^{-2}$ . Comparison of the effects of cell configuration on the Zn electrode after cycling tests for the (c) planar cell and (d) sandwich cell. ....	77
Figure 4.3. (a) Rheology measurements of GPEs with different crosslinking density. (b–d) Electrochemical evaluation of GPEs with different crosslinking density: b) Rate discharge-charge curves; (c,d) electrical resistance of ZABs before and after rate testing for (c) discharge at	

1.2 V and (d) charge at 1.9 V. (e) Schematic illustration that describes the degree of penetration of GPEs into Ni foam and its effect on oxygen bubble trapping as a function of crosslinking density of the GPEs..... 80

Figure 4.4. Electrochemical evaluation of ZABs using PAA with 0.5 mol% MBAA and 7.5 M KOH, with and without ZnO: (a) Discharge-charge rate curves, (b) charge rate curves and (c) cycling performance at 5 mA cm<sup>-2</sup>. ..... 85

Figure 4.5. Schematic illustration of the effect of ZnO on discharge and charge of a ZAB: (a) Without ZnO, (b) ZnO in OER and (c) ZnO in ORR. .... 86

Figure 4.6. (a) Cycling performance of ZABs at 5 mA cm<sup>-2</sup> with different OER catalysts. (b) Discharge-charge efficiency calculated from (a). (c) Cycling performance at 5 mA cm<sup>-2</sup> with different positions: (i) horizontal position (OER at the bottom), (ii) vertical position and (iii) horizontal position (ORR at the bottom). (d) Discharge-charge efficiency calculated from (c). . 88

Figure 5.1. Homemade cell assembly for bi-electrode ZABs using (a) a PAA–KOH electrolyte and (b) an aqueous electrolyte. 1) Acrylic sheets, 2) current collector Ni, 3) GDL, 4) polypropylene film, 5) GPE, 6) Zn, 7) refilling hole. .... 101

Figure 5.2. Rheological properties of PAA–KOH with varying crosslinking concentrations. (a) Photograph showing flow behavior of various GPEs 2 min after the containers have been inverted. (b) LVER region for the GPEs determined by amplitude sweeps from 0.1 to 100% strain at 1 Hz. (c) G' and G'' moduli as a function of frequency. (d) Complex viscosity determined by a frequency sweep. In (b) and (c), the solid lines represent the G' modulus and the dashed lines represent the G'' modulus. .... 105

Figure 5.3. (a) Ratio between the weight of as-prepared PAA–KOH and dry PAA. (b) Gel fraction, (c) ionic conductivity and (d) water loss for PAA–KOH as a function of crosslinker concentration. In (d), each colour bar represents an hourly measurement. .... 108

Figure 5.4. (a) FESEM SE image of MnOx/CoFe on GDL. Evaluation of ZABs using PAA–KOH with various MBAA concentrations: (b) rate discharge-charge curves and (c) cycling performance at 5 mA cm<sup>-2</sup>. (d) Schematic illustration of the effects of crosslinking density on discharge and charge of a ZAB. White regions in the schematic represent cracks in the catalyst layer or gaps at the catalyst/electrolyte interface. .... 112

Figure 5.5. Morphology of Zn electrode from ZABs after cycling tests at 5 mA cm<sup>-2</sup> using (a) aqueous electrolyte (6 M KOH), (b – e) PAA–KOH with 0.3, 0.5 0.7, and 0.9 mol% MBAA, respectively. .... 114

Figure 6.1. Homemade cell assembly for bi-electrode ZABs. (a) Single air electrode (SAE) and (b) double air electrode (DAE) designs. 1) Acrylic sheets, 2) Ni current collector, 3) GDL impregnated with (Co,Fe)<sub>3</sub>O<sub>4</sub> decorated N–CNTs, 4) polypropylene film, 5) PAA–KOH, 6) Zn, 7) bolts and nuts. .... 129

Figure 6.2. Evaluation of PAA–KOH. (a) Conductivity of aqueous electrolytes, with different amounts of AA monomer, as a function of KOH concentration. (b) Conductivity of PAA–KOH,

with and without ZnO, as a function of PAA concentration. (c) Mass ratio of 6 M KOH and volume ratio of AA contained within the PAA–KOH gels. .... 134

Figure 6.3. Electrochemical evaluation of PAA–KOH gels with various concentrations of ZnO. (a) Rate test with the sequence discharge-charge-charge for ZABs using P–K2, with and without 0.25 M ZnO, at different current densities. Dashed lines represent the second charging cycle. (b) Discharge-charge curves for ZABs using different concentrations of ZnO in P–K2 gels at a current density of 20 mA cm<sup>-2</sup>. .... 137

Figure 6.4. Mechanical properties of PAA–KOH gels. (a) Tensile stress–strain curves at a rate of 10 mm min<sup>-1</sup> and (b) peeling strengths of PAA–KOH on GDL at a rate of 50 mm min<sup>-1</sup>. ..... 138

Figure 6.5. Evaluation of ZABs using PAA–KOH with various PAA concentrations. (a) Discharge-charge rate curves. (b) Full discharge and overcharge performance at 20 mA cm<sup>-2</sup>. Arrows indicate the moment PAA–KOH protruded through and fractured the GDL. (c) Photographs showing the appearance of ZAB cells after charging. P–K2 squeezed between the acrylic plates and P–K5 penetrated through the GDL. (d) Electrical resistance for ZABs at 1.2 V before and after cycling at 20 mA cm<sup>-2</sup>. .... 142

Figure 6.6. (a) Cycling performance at 20 mA cm<sup>-2</sup> for ZAB with vertical and horizontal orientations. (b–d) Comparison of ZABs using P–K2–ZnO electrolyte with two battery designs: (b) full discharge curves at 5 and 20 mA; (c) polarization and power curves, and (d) cycling performance of ZABs at 10 and 20 mA cm<sup>-2</sup> using the SAE design and at 2×10 mA cm<sup>-2</sup> using the DAE design. .... 145

Figure A.1. Schematics that describe: (a) the water layer that forms between the ion-selective membrane and electronically conducting substrate and (b) how an electrochemically transducing intermediate layer, such as polyaniline (PANI), mitigates the adverse effect by the water layer. .... 178

Figure A.2. Modified electrode configuration of solid contact K<sup>+</sup> ISE (ion-selective electrode). .... 181

Figure A.3. SEM SE images showing morphology of (a) SPE (bare carbon WE) and (b) SPE/PANI (PANI deposited on carbon WE by 30 CV cycles). .... 182

Figure A.4. Cyclic voltammetry (CV) spectra obtained (a) during deposition of PANI in 0.5 M HCl (30 cycles overlapped; red line shows the first scan) and (b) after the 30-cycle deposition of PANI in 0.1 M KCl for quality evaluation (third scan). The spectrum from pure SPE is overlain for comparison. .... 183

Figure A.5. (a) EIS results at high frequency for the WE before and after aniline polymerization in 0.1 M KCl. The dot results were obtained from experiments, while the lines represent fitting of data using ZSimpWin. (b) Two equivalent circuits to fit SPE (top) and SPE/PANI (bottom). .... 184

Figure A.6. Response of K<sup>+</sup> ISE for different cations at the same activity (0.1 M). (a) Potential values from potentiometry measurement and (b) selectivity coefficient  $K_{ij}^{pot}$  calculated from (a). .... 186

Figure A.7. (a) Electromotive force (EMF) measurements recorded for decreasing concentration of  $K^+$  in DIW. (b) Average calibration curve ( $N = 3$ )..... 187

Figure A.8. (a) Impedance measurements for SPE/V, SPE/PANI/V (with as-received RE) and SPE/PANI/V with PVB modified RE. (b) Equivalent circuit used for simulations to fit the measured EIS spectra. .... 188

Figure A.9. (a) EMF measurements recorded for decreasing concentration of  $K^+$  in artificial serum. (b) Average calibration curve (■) showing linear range from  $10^{-3}$  to 1 M with  $54.8 \pm 1.2$  mV/decade. Grey marks (×) represent data for three sensors with similar sensitivity. .... 189

Figure A.10. EMF measurements in 0.1 M KCl of  $K^+$  ISE with and without PVB/NaCl layer on the RE..... 190

## Chapter 1. Introduction

To sustain energy supply, reliable solutions for large-scale energy storage are required to bridge the gap along the energy supply chain and make consumers active participants in the grid. First, energy generation from power plants can be stored during off-peak hours for later use. As such, energy storage devices help secure source reliability during peak hours, decrease strain on the power plants and eventually reduce cost [1]. Second, energy storage helps overcome the intermittent, unpredictable or geographically dependant limitations from renewable energy, such as solar, wind, geothermal and biomass energy [2]. Clean and abundant sources of energy are desired everywhere in the world to lower the adverse effects, such as greenhouse gas generation from fossil fuels. The British Petroleum statistical review of world energy in June 2019 estimates that the remaining time to exploit coal is 130 years and that for gas and oil it is only about 50 years, based on known existing reservoirs and assuming production were to continue at the same rate [3].

Energy storage technologies, such as pumped hydro, hydrogen, electromechanical (flywheel, compressed air), electrochemical and thermal energy storage systems, have been the subject of many investigations [4]. While pumped hydro storage is the most mature and widely used large scale technology, which accounts for 96 – 99% of the total installed capacity in the world, it requires specific geographical standards, water availability and may cause ecological problems [5]. On the other hand, rechargeable batteries (electrochemical systems) offer versatility, low maintenance and stable delivery due to their high energy density [6]. Among various battery types, metal-air batteries (MABs) show high energy density, as depicted in Figure 1.1a, since one of the electroactive components (oxygen) is stored outside of the battery until discharge. Figure 1.1b represents several choices for the metal electrode that can be used in MABs. Based on the electrolytes utilized, MABs can be essentially divided into the following two classes: (1)

nonaqueous electrolyte-based devices (Li-O<sub>2</sub>, K-O<sub>2</sub> and Na-O<sub>2</sub>) and (2) aqueous electrolyte-based devices (Mg-air, Al-air, Zn-air and Fe-air). Although a Li-O<sub>2</sub> battery offers high theoretical specific and volumetric energy densities, metallic Li is water-sensitive and unstable in humid environments because Li reacts violently with water to form alkaline hydroxide and hydrogen gas. K-O<sub>2</sub> and Na-O<sub>2</sub> have similar problems to Li-O<sub>2</sub> batteries. An open system always requires additional components, such as air-dehydration membranes and nonaqueous electrolytes, which increase cost and can be harmful to the environment [7, 8]. One of the key drawbacks associated with Mg-air and Al-air batteries is that they are difficult to recharge electrically after the discharge process because of their low reduction potentials; consequently, they can only be charged by physically replacing the metal anodes [9, 10]. Compared with other metals, it is easier to control dissolution and deposition of Zn in aqueous electrolytes. Zn is the 24th most abundant element in the earth and it is also inexpensive, environmentally benign and recyclable. Therefore, Zn-air batteries (ZABs) are the most promising candidate for future industrial applications among all the various kinds of MABs.

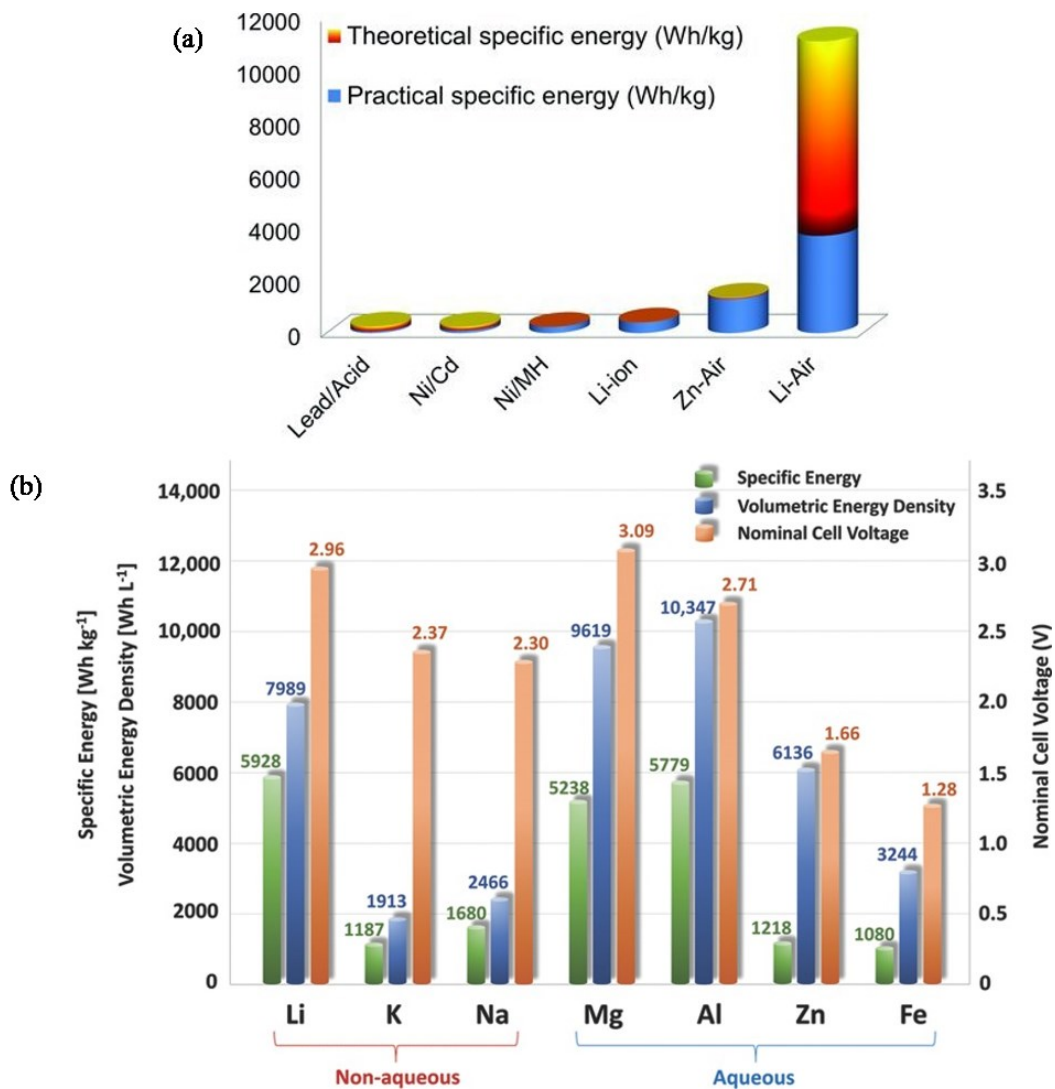


Figure 1.1. (a) Theoretical and practical specific energy of various types of rechargeable batteries [11]. (b) Theoretical specific energy, volumetric energy density and nominal cell voltage for various metal-air batteries [12].

(Reproduced with permission from references [11, 12].)

Although Zn is stable with water and water vapor, leakage and flooding of the aqueous electrolyte in ZABs are two of the main challenges for scaling up the batteries [13]. On the other hand, practical application of rechargeable ZABs using gel polymer electrolytes (GPEs) is limited because of the following reasons:

1. The reliability of the polymeric material in highly concentrated alkaline solutions, including chemical, electrochemical and mechanical performance, needs to be established for the duration of the desired battery lifetime.
2. Ionic conductivity in the gel state is compromised when compared with that in the liquid state, so optimization of gel synthesis parameters is required.
3. The roles of interfacial contact between GPEs and electrodes in battery performance have not been investigated thoroughly.

The goals of this study are as follows: (1) To correlate battery performance with the physicochemical properties of the GPEs, such as chemical and electrochemical stability, physical strength, ionic conductivity, water retention and adhesion; (2) to optimize GPE composition to achieve better utilization of the Zn electrode and to improve battery rechargeability; and (3) to elucidate the impact of battery architecture on energy efficiency and cycle life.

In Chapter 1, the Introduction and content of the thesis are provided. Chapter 2 provides a literature review and establishes the basis for Chapters 3 through 6. Chapter 3 investigates different polymer materials for GPEs. Chapter 4 explores an alternative tri-electrode design, which enables the effects of additives on charge/discharge to be independently studied. Chapter 5 discusses the effects of crosslinking concentration on battery cycling performance and failure mechanisms of ZABs using GPEs. Chapter 6 optimizes GPEs components, as well as evaluates the components in different battery designs. Conclusions and recommendations for future work are given in Chapter 7.

## Chapter 2. Literature Review

### 2.1. Zinc-air batteries

Zn-air batteries (ZABs) contain no toxic compounds and are neither highly reactive nor flammable. They generate electrical power from chemical reactions with one of their main reactants is oxygen from the air. Thus, ZABs have several advantages, such as high specific energy (1218 Wh kg<sup>-1</sup>) and energy density (6136 Wh L<sup>-1</sup>), operational safety and environmental compatibility. They also benefit from extensive global reserves of Zn, which lead to low cost [12, 14]. It is well-known that primary ZABs have long shelf life if sealed and can be safely disposed or recycled without any special handling [15, 16].

#### 2.1.1. Chemical reactions in ZABs

Table 2.1 shows the many reactions that can occur in ZABs [7, 17]. The most representative reactions in a rechargeable ZAB with an alkaline electrolyte are *Reaction 2.1*, *Reaction 2.2* and *Reaction 2.3*. During discharge, Zn reacts with hydroxide ions (OH<sup>-</sup>) to form zincate ions (Zn(OH)<sub>4</sub><sup>2-</sup>) while the oxygen reduction reaction (ORR) consumes oxygen (O<sub>2</sub>) and water to produce OH<sup>-</sup> [17]. The standard electrode potential for *Reaction 2.1* is -1.25 V vs. SHE (standard hydrogen electrode), while the standard electrode potential for *Reaction 2.2* is 0.4 V vs. SHE. Therefore, the standard equilibrium potential of ZABs is 0.4 - (-1.25) = 1.65 V. However, upon discharge and charge, the majority of activation polarization losses occur at the air electrode (Figure 2.1). Thus, the practical discharging voltage obtained is ~1.2 V or even lower, while the charging voltage is significantly higher at 2.0–2.4 V [18]. As a result, electrically rechargeable ZABs usually have a low round-trip energy efficiency of <60%. At the beginning of discharge, oxygen diffusion and the activity of electrocatalysts affect rate limiting processes of fresh ZABs.

As discharge continues, the remaining active area of the Zn electrode decreases and becomes the rate limiting process [15].

It should be noted that there are many other side reactions that can happen in the battery. As the electrolyte becomes saturated with zincate ions ( $\text{Zn}(\text{OH})_4^{2-}$ ), zinc oxide will precipitate (*Reaction 2.4*), changing the overall reaction to *Reaction 2.5*. ZnO is an insulator and will increase the internal resistance of the battery. Thus, the discharging and charging currents will gradually decrease and increase, respectively. This is one of the main reasons for the difficulty in making a successful electrically rechargeable ZABs [15]. On the other hand, the mechanism for the oxygen reduction reaction (ORR) depends on the nature of the electrode and electrolyte and can follow the direct 4-electron pathway (*Reaction 2.2*) or a 2-step, 2-electron peroxide pathway (*Reaction 2.6*, *Reaction 2.7* and *Reaction 2.8*) [19]. In the later pathway, oxygen reduction first forms a peroxide-free radical ( $\text{O}_2\text{H}$ ) (*Reaction 2.6*), followed by a subsequent reduction or decomposition of the peroxide (*Reaction 2.7* and *Reaction 2.8*, respectively). This effectively restricts performance of the cell in practice [15]. Thus, catalysts that favor the 4-electron pathway for ORR are in demand for energy conversion devices, such as fuel cells and batteries [20].

The first parasitic reaction in ZABs is the hydrogen evolution reaction (HER), as shown in *Reaction 2.9*. When the HER is combined with Zn dissolution (*Reaction 2.1*), self-discharge or corrosion of Zn metal occurs (*Reaction 2.10*). The process is spontaneous and unavoidable. In the reverse reaction, water still consumes some of the electrons provided to the Zn electrode to generate  $\text{H}_2$  on the Zn surface; thus ZABs cannot be charged with 100% Coulombic efficiency [21]. Another detrimental reaction in the Zn-air battery is the production of  $\text{K}_2\text{CO}_3$ , which accumulates in the pores of the air electrode (*Reaction 2.11*). This reaction reduces oxygen diffusion and electrolyte conductivity, thus limiting battery lifetime [16].

Table 2.1. Possible reactions in ZABs

$\text{Zn} + 4\text{OH}^- \rightarrow \text{Zn}(\text{OH})_4^{2-} + 2\text{e}^-$	$E^\circ = -1.25 \text{ V vs. SHE}$	<i>Reaction 2.1</i>
$\text{O}_2 + 2\text{H}_2\text{O} + 4\text{e}^- \rightarrow 4\text{OH}^-$	$E^\circ = +0.4 \text{ V vs. SHE}$	<i>Reaction 2.2</i>
$\text{Zn} + \frac{1}{2}\text{O}_2 + \text{H}_2\text{O} + 2\text{OH}^- \rightarrow \text{Zn}(\text{OH})_4^{2-}$	$E_{\text{eq}} = 1.65 \text{ V}$	<i>Reaction 2.3</i>
$\text{Zn}(\text{OH})_4^{2-} \rightarrow \text{ZnO} + \text{H}_2\text{O} + 2\text{OH}^-$	Precipitation of ZnO	<i>Reaction 2.4</i>
$\text{Zn} + \frac{1}{2}\text{O}_2 \rightarrow \text{ZnO}$		<i>Reaction 2.5</i>
$\text{O}_2 + \text{H}_2\text{O} + 2\text{e}^- \rightarrow \text{OH}^- + \text{O}_2\text{H}^-$	2-electron pathway	<i>Reaction 2.6</i>
$\text{O}_2\text{H}^- + \text{H}_2\text{O} + 2\text{e}^- \rightarrow 3\text{OH}^-$		<i>Reaction 2.7</i>
$\text{O}_2\text{H}^- \rightarrow \text{OH}^- + \frac{1}{2}\text{O}_2$		<i>Reaction 2.8</i>
$2\text{H}_2\text{O} + 2\text{e}^- \rightarrow 2\text{OH}^- + \text{H}_2$	HER, $E^\circ = -0.829 \text{ V vs. SHE}$	<i>Reaction 2.9</i>
$\text{Zn} + \text{H}_2\text{O} \rightarrow \text{ZnO} + \text{H}_2$	Zn corrosion	<i>Reaction 2.10</i>
$2\text{KOH} + \text{CO}_2 \rightarrow \text{K}_2\text{CO}_3 + \text{H}_2\text{O}$	Carbonate formation	<i>Reaction 2.11</i>

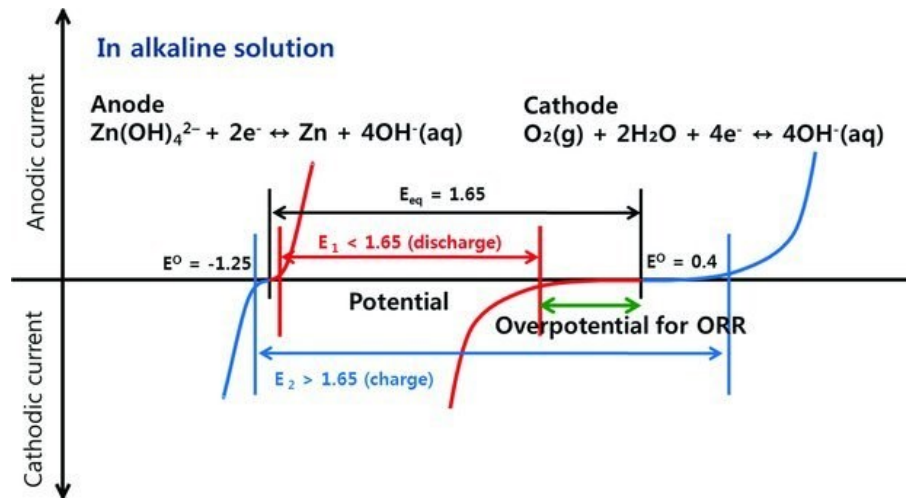


Figure 2.1: Schematic polarization curves of Zn and air electrodes in ZABs. The black line represents the theoretical equilibrium potential of 1.65 V. The red and blue lines represent the actual working voltages during discharge and charge, respectively.

(Reproduced with permission from reference [11].)

### 2.1.2. Battery components

A typical ZAB is composed of three main components: (1) a Zn electrode, (2) an electrolyte-soaked separator and (3) an air electrode comprising a catalyst-coated gas diffusion layer (GDL) [22]. The most common electrolyte in a rechargeable ZABs is an aqueous alkaline solution, while the separator acts as a physical barrier to prevent short circuit resulting from direct contact of the anode and cathode. Since both Zn and air electrodes determine the final performance of ZABs, many strategies have been developed to improve their performance as demonstrated in Figure 2.2 [23].

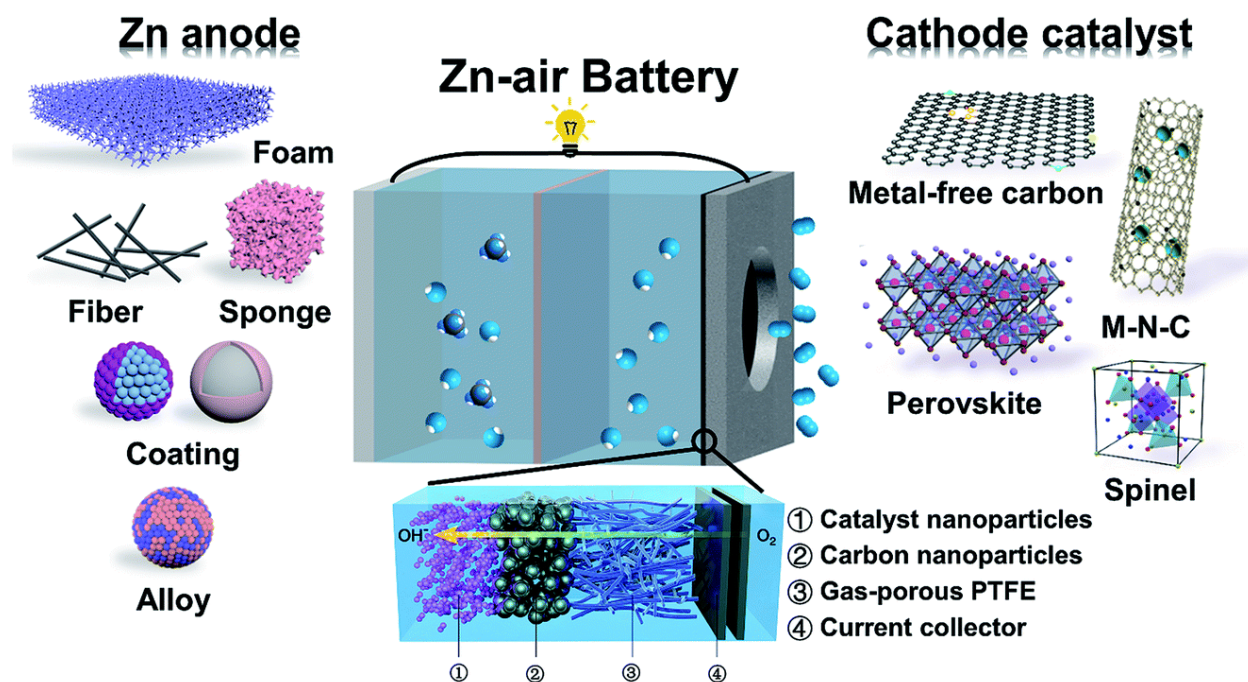


Figure 2.2: Schematic illustration of ZABs, including different forms of Zn anodes and different electrocatalysts for the air cathode.

(Reproduced from reference [23] - Published by The Royal Society of Chemistry.)

Firstly, the Zn electrode suffers from dendrite formation, shape change, passivation and HER. To tackle these problems, the Zn electrode components are optimized through electrode structure modification, corrosion inhibitors, polymer additives and surface protective layers [21,

24, 25]. High surface area Zn in the form of foams, fibers or sponges can be used to enhance discharge performance, although they also promote corrosion [21, 26]. Thus, the Zn electrode is often alloyed with other metals (e.g., Pb, Cd, Bi, Ca, Ni, Cu and Al) to suppress HER and corrosion to some extent [21, 23, 24, 26]. The Zn electrode can be incorporated with other additives (e.g., carbon, and polymer binders) to suppress dendrite formation although this may affect its electronic conductivity [27]. Alternatively, efforts have been made to coat the Zn electrode with thin graphene oxide layers, metal oxides/hydroxides (TiO<sub>2</sub>) or conducting polymers (e.g., polypyrrole) to better capture zincate discharge products, yet still allow hydroxide ions to pass freely [28-31]. This is beneficial in suppressing Zn dendrite growth and enhancing electrode reversibility.

Secondly, the air electrode experiences sluggish oxygen reaction kinetics, which remains as the bottleneck for developing robust rechargeable ZABs [32]. There are two parts in an air electrode: (1) the gas diffusion layer (GDL) and (2) the catalysts. Generally, an effective GDL should possess chemical and electrochemical stability in concentrated alkaline conditions, have high porosity and tortuosity, and allow fast oxygen diffusion and migration of OH<sup>-</sup>, while preventing water flooding [10]. The catalysts should have high electrochemical activity for both oxygen reduction and oxygen evolution reactions (ORR and OER). Noble metals, such as Pt-based catalysts, have been the standard for ORR performance, while the most active OER catalysts are Ir-based or Ru-based catalysts [33]. Recent research has focused on investigation of low cost, abundant and, most importantly, efficient and durable ORR and OER bifunctional catalysts, such as carbon-based catalysts, metal-based catalysts or a hybrid of both. With good electrical conductivity, large surface area and versatility for surface modification, nanostructured carbon materials, such as carbon nanotubes (CNTs), graphene and others, employing different doping techniques using N, S, P, and B, have been extensively studied. Although some carbon-based

catalysts have achieved good ORR and OER performance, they still have limitations when compared with the best noble metal catalysts since most carbon nanomaterials undergo a two-electron pathway while Pt-based catalysts undergo a four-electron pathway [33, 34]. Alternatively, many new species of perovskite and spinel oxides have been developed and are considered as promising bifunctional catalysts. However, the electrocatalytic activities of these metal oxides have been limited by their insufficient electronic conductivities. Therefore, the integration of metal oxide/hydroxide with a conductive carbon frame may facilitate fast electron transport, thus leading to improved electrochemical and battery performance [7].

### **2.1.3. Potential application of ZABs**

Currently, commercial ZABs are either non-rechargeable or using flowing electrolytes for the purpose of grid-scale energy storage. These batteries are either not economical or not feasible to implement into microgrids for electric vehicles (EVs). EV batteries differ from starting, lighting, and ignition batteries as they are designed to give energy over continuous periods of time. Nowadays, most EVs use Li-ion batteries (LIBs). LIBs with nonaqueous electrolytes are dominant in the market, which raises the cost and safety concerns [35]. On the other hand, ZABs designed as a range extending battery and used alongside an LIB could reduce the burden to some degree, with each of the two battery packs designed for specific functions. Vehicles can transition from hybrid EVs to plug-in EVs and eventually to pure EVs, meaning that the vehicles would not consume gasoline and emit no emissions from the exhaust, thereby reducing CO<sub>2</sub> emissions [36].

The cost for battery systems is usually expressed in terms of US\$/kWh. Thus, it depends not only on the total cost but also on the total capacity of the battery; kWh are calculated by multiplying voltage × current × discharge hours/cycle × cycle number. Battery lifetime is greatly affected by the number of discharge/recharge cycles and the depth of discharge in terms of

percentage of total discharge. Major findings for battery values are shown in Table 2.2 for seven battery energy storage technologies.

Table 2.2. Comparison of different battery types [37-42]

	Efficiency (%)	Energy (Wh kg <sup>-1</sup> )	Power (W kg <sup>-1</sup> )	Cycle life	Cost in 2018 (\$/kWh)	Self-discharge rate (%/month)
Pb-acid	~80	30 – 50	75 – 300	500 – 1000	549	4 – 8
Ni-MH	~70	80	200 – 1000	300 – 600	400	15 – 30
Li-ion	>95	75 – 200	150 – 315	1000 – 10,000	175	5 – 10
Zn-ion	>95	50 – 80	1450	3200	140	N/A
Hybrid-Zn	>95	50 – 80	N/A	4000	551	N/A
Na-S	~80	150 – 240	150 – 230	2500 – 4500	907	N/A
Zn-air	~55	300	200	100 – 500	160	3

Pb-acid batteries should not be discharged below 50% of their capacity, as this shortens the battery's life. Even though Pb-acid batteries are inexpensive, their cycle life is limited, leading to a usable life of less than 3 years assuming one cycle per day. Up to now, LIBs offer the best option in terms of cycle life and technological maturity. They can be repeatedly cycled to 50% of capacity, yet are still good for thousands of cycles. Nevertheless, EOS Energy Storage announced that their Aurora product (ZABs using aqueous electrolytes) with 1 MW/4 MWh for grid storage is selling for \$160/kWh and recently they dropped their price to \$95/kWh for orders filled in 2022 [43]. Recent advances in material science and technology innovations offer great promise for ZABs to widen their applications in rechargeable EV batteries and further reduce costs.

### 2.1.3. Challenges for ZABs

The main challenge for an electrically rechargeable ZAB is to improve its cycle life. In addition to the inherent problems of Zn and air electrodes discussed in Section 2.1.1, the operating life of a battery is critically dependent on the environment since ZABs have a half-open structure.

External variables, including temperature and humidity, have immediate effects on electrolytes. In humid conditions, the cell will gain water which can cause flooding and destroy the air electrode. At high temperatures or under dry conditions, the cell will lose water which can promote carbonate formation and increase cell impedance [15]. Electrolytes play a crucial role in the transport of active species and affect nominal cell voltage, energy density, power capability and cycling efficiency [2]. Using the appropriate electrolyte can help minimize or even prevent the problems associated with the two electrodes.

## **2.2. Electrolytes for ZABs**

### **2.2.1. Aqueous electrolytes**

The pH of the electrolyte governs the electrochemistry of Zn-air batteries, as shown in Table 2.3. Under standard conditions, the equilibrium potential range for water electrolysis is 1.23 V (Figure 2.3), which is the main disadvantage of aqueous electrolytes, i.e., they have a narrow electrochemical window. Water electrolysis is kinetically favorable in the sequence of acid > alkaline > neutral conditions due to the ready availability of hydroxide ions ( $\text{OH}^-$ ) for OER in alkaline solutions and hydrogen ions ( $\text{H}^+$ ) for HER in acid solutions [44-46]. It should be noted that OER is desired during the charging process, while HER is an unwanted parasitic reaction. Near-neutral LeClanché-based electrolytes, containing  $\text{NH}_4\text{Cl-ZnCl}_2$ , have been proposed to circumvent carbonate buildup at air electrode pores, but several complex products, instability of solution pH during cycling and the precipitation of unwanted salts still occurs [47, 48]. The Pourbaix diagram also shows that Zn is thermodynamically unstable in aqueous solutions and will spontaneously dissolve to accompany the HER. In solutions with pH ranging from 8 to 11.5, a thin zinc hydroxide/oxide may cover the Zn surface and prevent it from further corrosion [49]. However, the passivating film also reduces discharge capacity and power capability of the Zn

anode. Thus, alkaline solutions such as potassium hydroxide (KOH) or sodium hydroxide (NaOH) solutions have been widely used as the electrolyte for ZABs.

NaOH can be used in primary batteries for longer operational life when high discharge rates are not required. ZABs using NaOH also exhibit less creep and leaking than cells with KOH [15]. On the other hand, KOH is commonly preferred because it has the highest ionic conductivity among alkaline solutions (0.64 S cm<sup>-1</sup> for 30 wt% KOH solution at 25 °C [50]) which allows batteries to discharge better over a larger range of current density. In addition, the carbonate product, K<sub>2</sub>CO<sub>3</sub>, in the air electrode pores has a higher solubility in aqueous electrolyte than that of Na<sub>2</sub>CO<sub>3</sub>. A high concentration of ~6 – 8 M of KOH is typically chosen to take advantage of the highest ionic conductivity; however, other effects of KOH concentration should be considered. For example, the effect of KOH concentration on the solubility of zincate ions is important, as it directly affects the formation of Zn dendrites [51]. Generally speaking, ZABs using acidic, neutral or basic electrolytes still endure the same problems, such as limited electrochemical stability window, flooding, leakage, evaporation, Zn corrosion and dendrite formation to some degree [2].

Table 2.3. Reactions for ZABs in aqueous electrolyte at different pH values [46]

Aqueous electrolyte	Zn electrode	E° (V) vs. SHE	Air electrode	E° (V) vs. SHE
Acid	$Zn \rightarrow Zn^{2+} + 2e^{-}$	-0.762	$O_2 + 4H^{+} + 4e^{-} \rightarrow 2H_2O$	1.23
Neutral	$Zn \rightarrow Zn^{2+} + 2e^{-}$	-0.762	$O_2 + 4H^{+} + 4e^{-} \rightarrow 2H_2O$	0.817
Alkaline	$Zn + 4OH^{-} \rightarrow Zn(OH)_4^{2-} + 2e^{-}$	-1.249	$O_2 + 2H_2O + 4e^{-} \rightarrow 4OH^{-}$	0.401

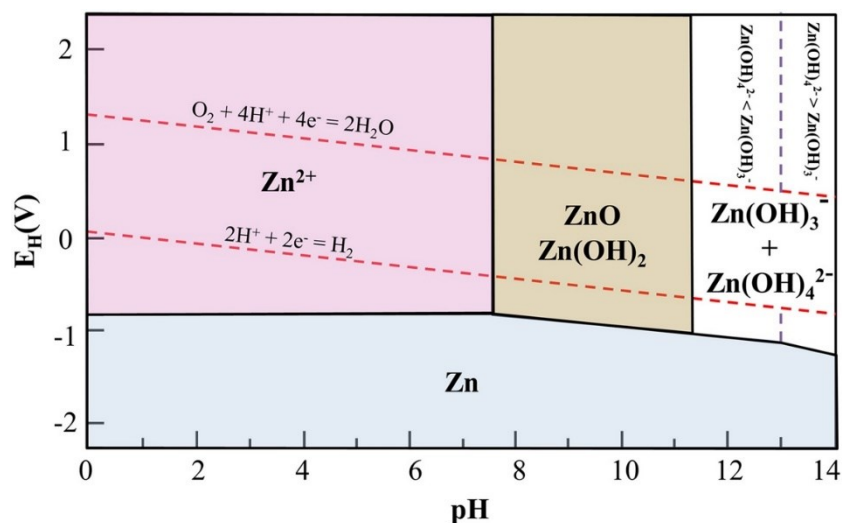


Figure 2.3. Pourbaix diagram of Zn and water at 25 °C.  
(Reproduced with permission from reference [52].)

### 2.2.2. Room temperature ionic liquids

Organic solvents, such as propylene carbonate, ethylene carbonate and dimethylsulfoxide with zinc triflate salt dissolved in them, were reported to exhibit acceptable ionic conductivities of the order of  $10^{-3} \text{ S cm}^{-1}$  for Zn-MnO<sub>2</sub> batteries [53-55]. However, these organic solvents are not suitable for open systems like ZABs due to their volatility, flammability and toxicity [56]. On the other hand, room temperature ionic liquids (RTILs), which are salts that exhibit liquid state under ambient conditions, can potentially overcome a number of limitations faced with aqueous and organic electrolytes due to their unique properties. RTILs can inhibit hydrogen evolution, dendrite formation and carbonation associated with alkaline electrolytes and provide better thermal and electrochemical stability [38]. They are also non-volatile and non-flammable, and a varied combination of organic cations and organic/inorganic anions can be chosen to tune the RTIL characteristics. The anions determine Zn discharge behavior, morphology, growth orientation and water-solubility, while cations stabilize discharge products from the air electrode (e.g., peroxide) [57-59]. ZABs using ILs containing sulfonate anions demonstrated a two-electron ORR pathway,

which is less efficient than the four-electron pathway [60]. Protic additives, such as ethylene glycol, have been shown to promote the four-electron pathway for ORR [61]. Hampered by the high viscosity, the ionic conductivity of RTILs is two orders of magnitude lower than that of a 6 M KOH solution [62]. Thus, Ghazvini et al. added different concentrations of water to reduce the viscosity and improve the conductivity of 1-ethyl-3-methylimidazolium acetate (EMI-Ac). The results showed that ZABs using IL-based electrolytes containing 1 M zinc acetate, EMI-Ac and 20 vol% water can deliver a Coulombic efficiency of 97% for 50 cycles at 300 mA g<sup>-1</sup> [63]. RTILs are more expensive than aqueous electrolytes which limits their applicability to ZABs [12].

### 2.2.3. Polymer electrolytes

Polymer electrolytes offer several advantages over aqueous electrolytes and ionic liquids, such as enhanced resistance to dendrite formation, improved safety features, and excellent flexibility. Thus, they are superior in applications that require portability, flexibility, and varying shape [64]. Solid polymer electrolytes (SPEs), which comprise a polymer matrix and a salt, were introduced to replace the aqueous electrolyte and separator in 1975 [60]. The major problem associated with this type of electrolyte is its low ionic conductivity. At room temperature, the ionic conductivity of poly(ethylene oxide) (PEO) with alkali metal ion salts is from 10<sup>-8</sup> to 10<sup>-7</sup> S cm<sup>-1</sup> [65]. SPEs also have low solubility of zinc salts, so they facilitate the formation of passive layers between the electrolyte and Zn electrode [56, 60]. Additionally, it is difficult to maintain good contact between a fully solid-state electrolyte and the electrodes while the battery volume increases or reduces during charging and discharging, respectively [66]. Therefore, SPEs are rarely used in ZABs.

In contrast, gel polymer electrolytes (GPEs), which contain a certain amount of liquid solvent in a polymer-salt system, possess relatively high ionic conductivities and have been widely

studied in flexible ZABs [25]. GPEs with nonaqueous electrolytes are exclusively studied for batteries such as Li-O<sub>2</sub> and Na-O<sub>2</sub>, where water must be excluded to avoid the reactions between metal and water [67]. For other types of metal-air batteries, such as Zn-air and Al-air, aqueous electrolytes containing KOH and NaOH are primarily used for better kinetics, catalytic activity, higher ionic conductivity and environmental friendliness [67]. The inclusion of an inert polymer into the aqueous KOH electrolyte does not affect the electrochemistry of ZABs [68], while it can enhance the performance of both the anode and cathode due to the following reasons. Firstly, a GPE acts as a separator to reduce dendrite formation and increase Zn utilization. Secondly, it inhibits the aqueous electrolyte from flooding through the air electrode pores, thereby enhancing oxygen access [2]. Vinyl polymers and cellulose derivatives are usually used as the matrices and these are swollen with an alkaline solution. Examples include PEO-based, poly(epichlorohydrin) (PEC)-based, poly(vinyl alcohol) (PVA)-based and poly(acrylic acid) (PAA)-based aqueous electrolytes. However, incorporating a matrix in the electrolyte aggravates the poor buffering property of the discharge products (zincate ions); as such, GPEs were initially used for primary ZABs. Table 2.4 lists some polymer electrolytes used for primary and secondary ZABs.

Table 2.4. Composition and properties of alkaline GPEs for ZABs

Composition		Conductivity (mS/cm)	Performance at room temperature	Ref.
PEC-PEO	KOH (SPE)	1	Discharge voltage of 0.8 V at 14 mA cm <sup>-2</sup> (primary ZAB)	[69]
PVA-PEC	Immersing in 32 wt% KOH	50	Discharge capacity of 1296 mAh at C/20 (primary ZAB)	[70]
PEO-PVA	Aqueous KOH	10	Discharge capacity of 1431 mAh at C/20 (Zn-air primary cell)	[71]
PVA	Immersing in 35 wt% KOH	15	120 cycles at a rate of 50 A kg <sup>-1</sup>	[72]
PEO-PVA	Aqueous KOH	300	30 cycles at a rate of 1 A g <sup>-1</sup>	[73]

It is noted that, in general, ionic conductivity increases with increasing volume fraction of electrolyte relative to the polymer matrix [70]. For instance, the ionic conductivity of an alkaline PVA/PAA GPE can exhibit a range of 142 to 300 mS cm<sup>-1</sup> [74]. Furthermore, GPEs can reach a conductivity value of 460 mS cm<sup>-1</sup>, which is comparable to that of aqueous alkaline solutions, when the hydrogel has a high solvation capability [75]. However, high water content sacrifices the mechanical integrity of the GPEs. Therefore, an appropriate ratio of polymer host and aqueous electrolyte is critical to achieve a good balance between high conductivity and desirable mechanical properties.

### **2.2.3.1. Preparation methods**

Polymer electrolytes can be fabricated by different methods such as solvent-casting, phase-inversion or in situ polymerization [38].

a. Solvent-casting: SPEs were usually prepared by this method. A polymer is dissolved in a low-boiling solvent such as tetrahydrofuran (THF) together with a nonaqueous KOH solution. The resulting solution is cast on a substrate to form films. For example, an alkaline SPE based on a copolymer of epichlorohydrin and ethylene oxide (P(ECH-co-EO)) was prepared by mixing the copolymer and KOH in THF and ethanol, respectively, followed by casting of the film and evaporating the solvent [69].

#### b. Phase-inversion:

Solvent-induced phase-inversion: In this process, a polymer is dissolved in water and the resulting solution is cast on a substrate. Phase separation is induced to obtain GPEs by immersing the binary polymer/solvent mixture into a KOH solution.

Thermally induced phase-inversion: Similar to the previous process, a polymer is also dissolved in water and the resulting solution is cast on a substrate. After that, phase separation is induced by decreasing the temperature below the upper critical solution temperature [76]. Finally, a GPE is obtained by immersing the polymer film into an aqueous electrolyte.

c. In-situ polymerization. In a one-pot synthesis, a precursor consisting of a monomer, crosslinker, initiator and liquid electrolyte is cured under certain conditions (such as UV radiation or thermal radiation) to solidify and form the GPE with the liquid electrolyte evenly distributed in the polymer network [77]. If the monomer is unstable under concentrated KOH conditions, the precursor can be polymerized first in an appropriate solvent (usually water), followed by immersion in a KOH solution to obtain the GPE.

#### **2.2.3.2. Ionic conductivity**

The main difference between SPEs and GPEs is the introduction of a liquid solvent. In GPEs, ion transport is no longer governed by the segmental motion of polymer chains, but occurs in liquid phase or a swollen gelled phase. Specifically, when the polymer host is composed of connected micropores, ionic conductivity depends on the amount of the trapped liquid electrolyte. Otherwise, if the polymer is homogeneously solvated, ionic conductivity depends on the swollen gelled phase [77]. In the most general form, ionic conductivity is defined as *Equation 2.1* [78]:

$$\sigma = Nze\mu \quad \text{Equation 2.1}$$

where  $\sigma$  is the ionic conductivity,  $N$  is number of charge carriers per unit volume,  $z$  is the valence of the ion,  $e$  is the electron charge and  $\mu$  is the mobility of the ions. Here,  $N$  and  $\mu$  are composition and temperature dependent [79]. As such, the ionic conductivity is reported to follow the Arrhenius equation which can be expressed as *Equation 2.2*:

$$\sigma = \frac{\sigma_0}{T} \exp\left(\frac{-E_a}{kT}\right) \quad \text{Equation 2.2}$$

where  $\sigma_0$  is the pre-exponential factor, which is related to the number of charge carriers,  $E_a$  is the activation energy, which can be calculated from plots of  $\log \sigma$  versus  $1/T$ ,  $k$  is the Boltzmann constant and  $T$  is the temperature in Kelvin. For polymer electrolytes, plots of  $\log \sigma$  versus  $1/T$  are typically nonlinear, since ionic conductivity involves the hopping motion of ions coupled with motion of polymeric chains. Thus, the empirical Vogel-Tamman-Fulcher (VTF) equation is generally used to represent the dependence of conductivity with temperature for SPEs above the  $T_g$  (glass transition temperature), for GPEs and even for ionic liquids [77]. The VTF equation can be expressed as *Equation 2.3*:

$$\sigma = \sigma_0 T^{-1/2} \exp\left(\frac{-B}{T - T_0}\right) \quad \text{Equation 2.3}$$

where  $B$  is the pseudo-activation energy and  $T_0$  is referred to as the equilibrium  $T_g$  for polymer electrolytes in Kelvin and is taken as 50 degrees below  $T_g$  ( $T_0 \approx T_g - 50$  K).

#### 2.2.4. Electrolyte additives

In general, each of the previous electrolyte systems has its advantages and disadvantages (Table 2.5). Additives for electrolytes can improve the performance of ZABs, but they inevitably increase the complexity of battery electrochemistry; thus, selection of proper additives is dependent on interactions between the components.

Table 2.5. Comparisons of typical electrolyte systems for ZABs

Electrolyte system	Advantages	Disadvantages
Aqueous (alkaline)	<ul style="list-style-type: none"> <li>– High ionic conductivity (6 M KOH – 640 mS cm<sup>-1</sup>)</li> </ul>	<ul style="list-style-type: none"> <li>– Narrow electrochemical window</li> <li>– High volatility</li> <li>– Zn electrode: dendrite, corrosion</li> <li>– Air electrode: flooding, carbonation</li> </ul>
RTILs	<ul style="list-style-type: none"> <li>– Non-volatile</li> <li>– Wide electrochemical window</li> <li>– Zn electrode: no corrosion, reduced dendrite growth</li> <li>– Air electrode: no carbonation</li> </ul>	<ul style="list-style-type: none"> <li>– Low ionic conductivity (&lt;30 mS cm<sup>-1</sup>)</li> <li>– Promotes two electron pathway</li> <li>– More expensive</li> </ul>
Alkaline GPEs	<ul style="list-style-type: none"> <li>– Good ionic conductivity (100 – 460 mS cm<sup>-1</sup>)</li> <li>– Non-leaking, reduced volatility</li> <li>– Zn electrode: reduced dendrite growth and shape change</li> <li>– Air electrode: reduced flooding</li> </ul>	<ul style="list-style-type: none"> <li>– Narrow electrochemical window</li> <li>– Increased passivation on Zn</li> </ul>

Additives for alkaline solutions have been widely studied to suppress parasitic reactions or to modify the electrochemical response of the anode and cathode. Based on *Reaction 2.4*, researchers have added zinc oxide or zinc acetate into the alkaline electrolyte with the aim of reducing the activity of water and, consequently, the HER (*Reaction 2.9*). Additives can also help in the formation of zincate ions in the vicinity of the Zn electrode surface, thereby promoting cell rechargeability [38]. Inorganic salts, such as KF, K<sub>2</sub>CO<sub>3</sub>, K<sub>3</sub>BO<sub>3</sub>, K<sub>3</sub>PO<sub>4</sub> and K<sub>2</sub>CrO<sub>4</sub>, can be added to enhance electrolyte conductivity, which allows a lower KOH concentration to be used. This reduces the solubility and mass transfer of Zn species in the electrolyte, which helps to suppress dendrite formation [29, 80, 81]. Organic additives, such as sorbitol, thiourea, pyrazole, tartaric/succinic/citric acid, tetra-alkyl ammonium hydroxides and several others, have also been employed in alkaline solutions to suppress dendrite growth and hydrogen evolution. Silicate (SiO<sub>3</sub><sup>2-</sup>), acetate and sodium dodecyl benzene sulfonate surfactants can be used to take advantage

of their physical adsorption on Zn particles to block further precipitation and reduce zinc diffusion into the bulk of the aqueous alkaline electrolyte [82, 83]. Thus, the surfactants effectively help in retaining the Zn porous structure, minimizing passivation and preventing ZnO formation [84]. Water evaporation can be reduced by incorporating hydrophilic species, such as carboxymethyl cellulose (CMC), polyethylene glycol and polysorbate into aqueous electrolytes [85]. Stephen et al. showed that just 50 ppm of branched polyethylenimine improved the durability of Zn electrodes via different mechanisms, including dendrite growth inhibition, increased supersaturation degree of ZnO and increased HER overpotential [26]. In general, these approaches can only work well within certain limits and can be applied to alkaline gel polymer electrolytes, providing they have minimal effects on the stability of the hydrogel network.

## **2.3. Battery configurations**

ZABs can be classified based on several criteria, such as cyclability (primary and secondary batteries) or electrolyte state (non-flow and flow batteries). This literature review first provides a look at cell design, including primary and secondary ZABs with different types of electrolytes, followed by battery stacks with different designs.

### **2.3.1. Cell design**

#### **2.3.1.1. Button/coin cell**

Primary ZAB cells made in button format are widely used for hearing aids [86]. As illustrated in Figure 2.4, ZABs can pack much more Zn in the same volume because the system does not require a thick metal oxide electrode to complete the cell reaction as required for Zn-mercury oxide and Zn-silver oxide batteries. Vent holes at the bottom of the casing allow air access to the cathode during discharge. The air electrode rests flat on the casing and consists of several

hydrophobic, microporous layers (Teflon) that only allow gases to penetrate. The next layer is the active material—a mix of carbon and catalysts which are responsible for the discharging electrochemical reaction. A wire net is also impressed into the mixture to provide an electronic path for the current. A separator/barrier layer is added between the cathode and anode. This layer should be highly absorbent to the electrolyte, yet still act as an insulator to prevent short circuiting. The top of the coin cell contains all the Zn electrode and the majority of the electrolyte. The cell casing and cap also act as the current collectors. The gasket between the cap and casing helps to prevent short circuiting and may be coated with additional sealant material to enhance resistance to leakage [15].

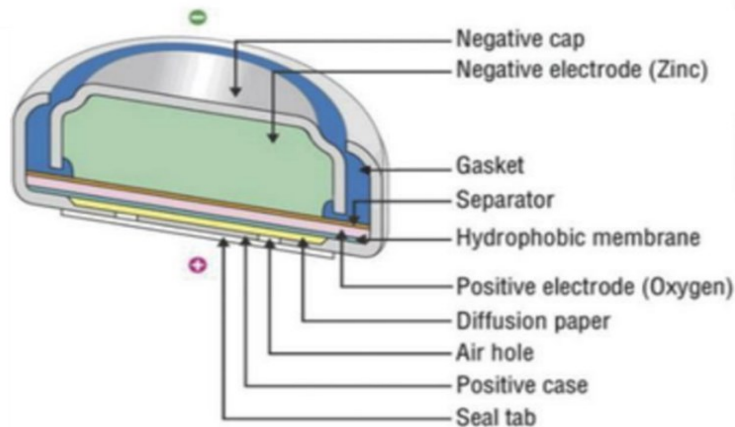


Figure 2.4. Cross section through a ZAB button cell.

(Reproduced from reference [87] - Published by ECS, figure has been modified.)

### 2.3.1.2. Mechanically rechargeable cell

ZABs have the capability to be recharged mechanically or electrically. In the mechanically rechargeable form, fresh Zn paste or pellets are added into a chamber, while zinc oxide is continuously pumped into a waste tank. In this respect, ZABs are essentially Zn-air fuel cells (ZAFCs). There are two main advantages of this system over an electrically charging system. In

principle, ZAFs can be recharged within minutes, rather than hours, and the air electrode will only be operated for ORR during discharge. This latter point is particularly important because of the difficulty in developing bifunctional catalysts which are stable against OER during charge. ZAFs (24 V, 20 Ah) were successfully used in military applications in the 1960s, although they were not pursued due to the limited performance of ZAFs at low temperatures, leaking issues and inconvenience in comparison with lithium batteries [8].

### **2.3.1.3. Prismatic cell**

The prismatic design is the most representative structure of ZABs, where the air and Zn electrodes are assembled in a planar arrangement in an electrolyte. For research purposes, plastic cells/plates can be attached with bolts and nuts and reused to investigate electrodes and electrolytes [88]. ZABs can be positioned horizontally or vertically with some modifications, as shown in Figure 2.5. Both designs have their pros and cons. In the vertical configuration (Figure 2.5a), recharging Zn tends to deposit at the bottom of the Zn electrode due to gravity forces, while electrolyte pressure increases near the vicinity of the air electrode causing more flooding and leakage. In the horizontal configuration (Figure 2.5b), the air electrode facing upward has a better current distribution with the Zn electrode, but there is substantial loss of electrolyte through evaporation and oxygen bubble accumulation can severely increase Ohmic loss or cause complete disconnection between the air electrode and electrolyte. For a quick test, vertical ZABs with proper sealing can provide good performance without oxygen bubble issues, while for long term cycling horizontal ZABs show better performance, if electrolyte is continuously pumped into the cell to maintain good contact.

To study the performance of an individual electrode, a Hg/HgO reference electrode can be added in the electrolyte refilling hole. It is typically connected against the Zn electrode to study

processes such as nucleation and dendritic growth during charging or passivation during discharging [89-91].

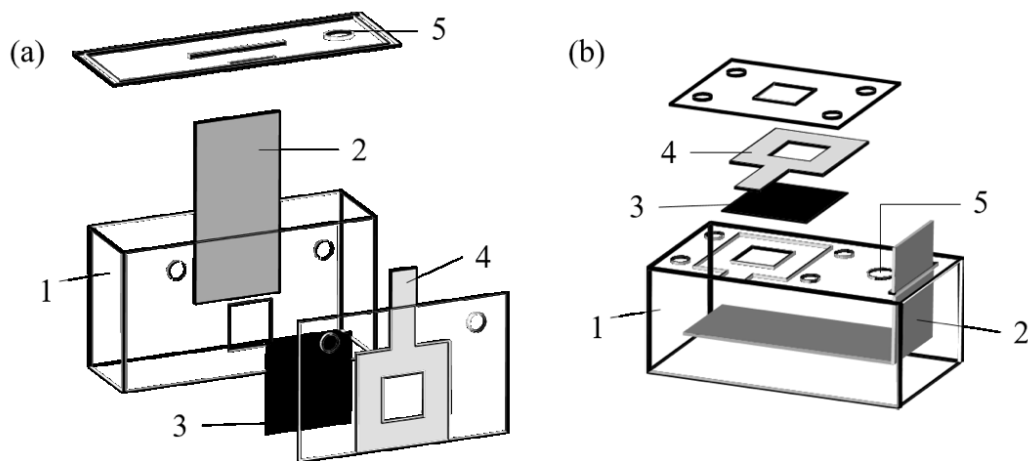


Figure 2.5. Schematic of two cell designs for bi-electrode ZABs in (a) vertical and (b) horizontal placements. 1) Acrylic sheets, 2) Zn, 3) GDL, 4) current collector Ni and 5) refilling hole.

#### 2.3.1.4. Flow cell

This configuration is similar to that of redox flow cells (e.g., vanadium batteries) and hybrid flow cells (e.g., Zn-bromide batteries). The main difference is that ZABs use only one channel where electrolyte is continuously circulated to a settling tank. There are several advantages of using this configuration. At the air electrode, oxygen bubbles that have formed and precipitated carbonates can be rinsed away by circulating electrolyte, while dendrite formation and passivation on the Zn electrode can be avoided since any concentration gradient is reduced. Therefore, flow ZABs provide better performance and longer cycle life than a prismatic cell with a static electrolyte. However, the energy density of the battery is significantly reduced due to extra mass from tubes and pumps, and the complexity of the bulky system strictly limits it to grid storage applications [8, 12].

### 2.3.1.5. Flexible cell

Flexible ZABs are freed from the constraints of rigidity and can be bent, rolled or folded [92]. Since ZABs are exposed to the air, it is not desirable to use liquid electrolytes which can either easily evaporate or leak into delicate electronic components. Therefore, the major focus of current flexible ZABs is on developing a solid-state electrolyte that still maintains adequate ionic conductivity [12]. There are two main configurations for flexible ZABs, as shown in Figure 2.6. In the planar design, thin films of electrodes and polymer electrolyte are assembled layer by layer [72, 93, 94]. In the cable design, the polymer electrolyte wraps around the surface of Zn, while the outside of polymer electrolyte is coated with a flexible air electrode or directly with electrocatalysts [64, 73, 95, 96].

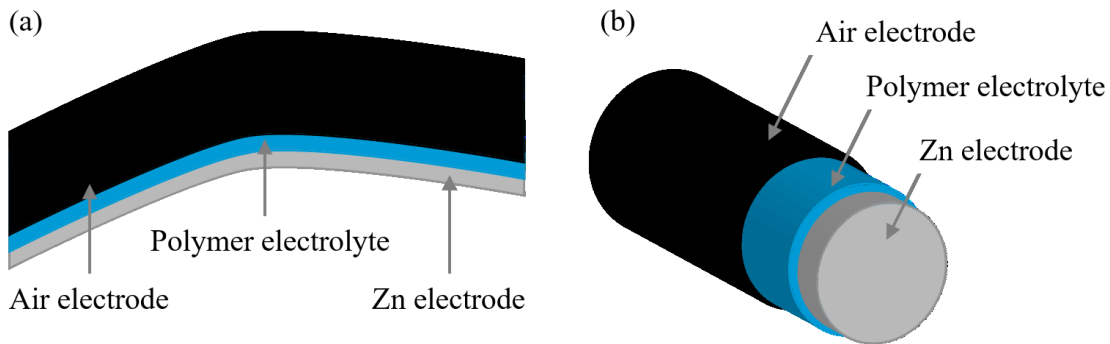


Figure 2.6. Schematic of two typical flexible ZABs: (a) planar-shaped and (b) cable-shaped batteries.

### 2.3.1.6. Tri-electrode cell

The requirements of a stable air electrode in electrically rechargeable ZABs are more stringent than for primary or mechanically rechargeable types, because stable electrocatalysts for reversing the discharge reaction are difficult to obtain and the charging voltage is much higher than the discharge voltage. In fact, Pt has been observed to dissolve during charging and transfer from the air electrode to the Zn electrode during cycling [8]. A tri-electrode configuration in which

the air electrode is decoupled into ORR and OER electrodes can be effective in enhancing voltaic efficiency and battery cycle life [97-103]. As with flow ZABs, adding more electrodes into the system will certainly increase the weight and volume of the cell, thus limiting tri-electrode ZABs to grid stationary storage. However, the improvement in efficiency and stability may be drastic enough that space and weight are not critical criteria. Figure 2.7 shows the electrode configuration in tri-electrode ZABs. The horizontal cell has both air electrodes in the same plane and the Zn electrode below (Figure 2.7a). An alternative to the horizontal cell design is the vertical cell where the Zn electrode and ORR electrode are located on either side of the OER electrode Figure 2.7b.

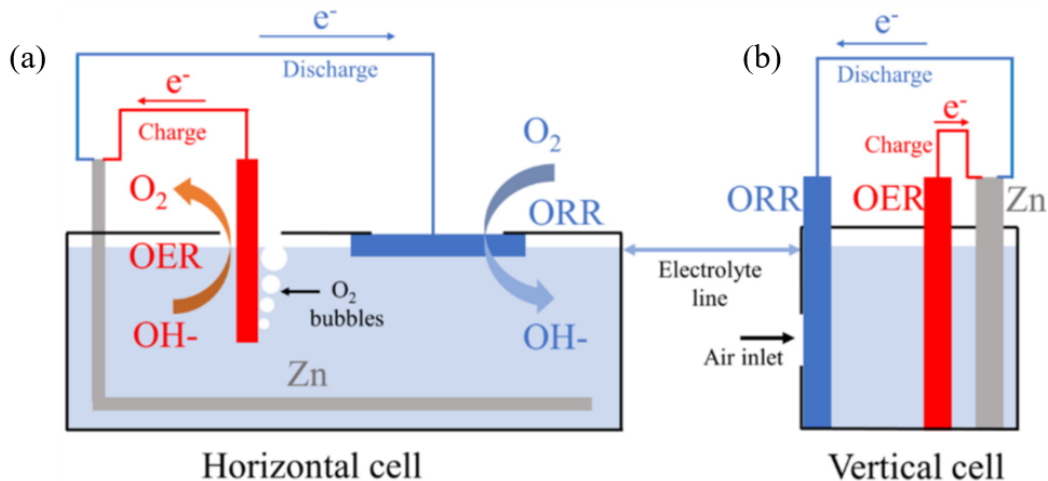


Figure 2.7. Schematic of structures for tri-electrode (a) horizontal cell and (b) vertical cell. (Reproduced with permission from reference [103].)

### 2.3.2. Stack design

The purpose of connecting batteries is to increase battery output to reach expected requirements, such as power, capacity, lifetime, safety, cost and environmental suitability [10].

#### 2.3.2.1. Flexible stretchable stack

Advances in flexible electronic devices with extra functionality have required the development of energy storage systems that can be conformal with deformation while retaining and supplying sufficient energy. Thus, cells are connected in a 2D planar design to maintain the flexible network [104]. Two solid-state ZAB cells connected in series were introduced in 2011 with open circuit potential of 1.52 V [105]. Currently, researchers employ origami (the art of folding) and kirigami (the art of cutting) to make highly stretchable ZAB stacks that can provide various output current (Figure 2.8) [106].

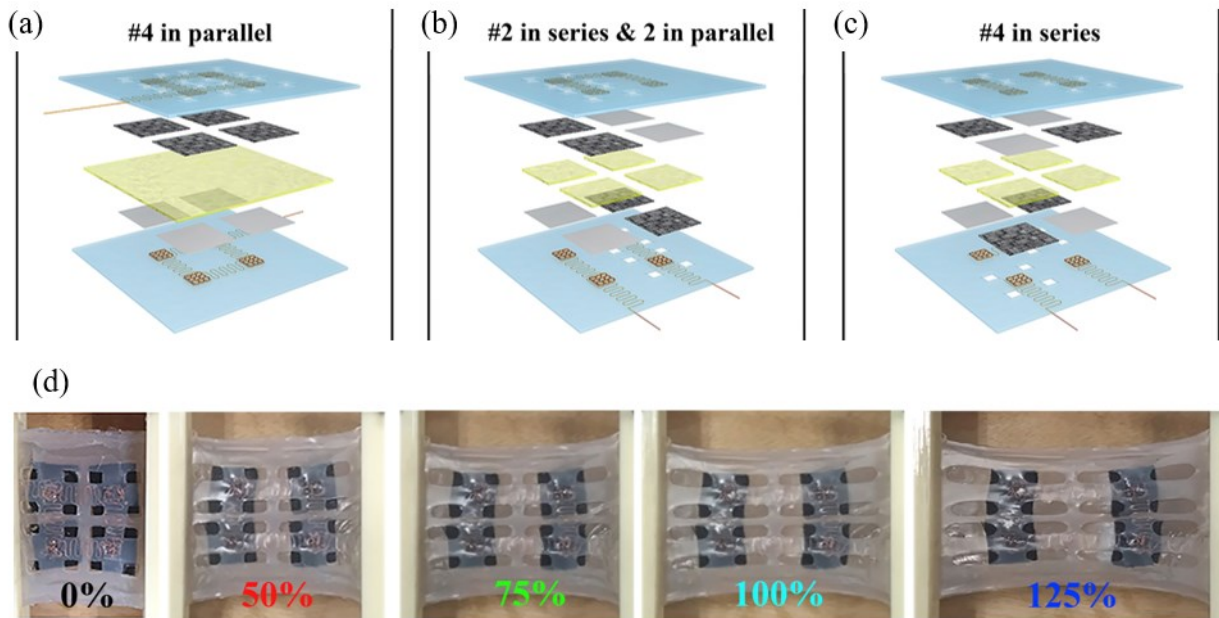


Figure 2.8. Illustration of various configurations in stretchable solid-state ZABs: (a) 4 cells in parallel, (b) 2 modules in series with each module having 2 cells in parallel and (c) 4 cells in series. (d) Photographs of a solid-state ZAB stretched under 0%, 50%, 75%, 100% and 125% strain.

(Reproduced with permission from reference [106], figure has been modified.)

### 2.3.2.1. Non-flow stack

Electrically rechargeable ZABs with a three-cell stack are demonstrated in Figure 2.9. These designs were briefly discussed by Muller et al. in 1995 [107]. The basic unit of the monopolar configuration includes a Zn electrode sandwiched between two bifunctional air electrodes (Figure 2.9a), while the unit in the bipolar configuration only includes one cathode facing an anode (Figure 2.9b). In the monopolar stack, electrodes are connected externally via wires, while in the bipolar stack a bipolar plate with an air-breathing hole connects the Zn electrode of one cell to the air electrode of the adjacent cell internally to raise the battery voltage to the required level. The major advantage of the bipolar arrangement is that cells can be packaged more compactly and the current distribution of the electrodes is slightly more even [12]. The monopolar arrangement offers double the air electrode area, thereby effectively reducing the current density to half on the air electrode [10]. Nevertheless, most research done on aqueous ZAB stacks use a bipolar configuration to reduce evaporation and leakage of electrolyte [108, 109].

Air flow is usually achieved by natural convection, so that the air spacing between cells in is a critical design factor. The distance is a compromise between the need to provide sufficient O<sub>2</sub> for high discharge rates and the requirement of minimal battery volume. Pumping pure O<sub>2</sub> has been used to increase battery power density by minimizing mass transfer effects and preventing carbonation of the alkaline electrolyte. However, this may result in even lower energy densities caused by the extra weight of the fan and by the parasitic currents drawn from the battery [8].

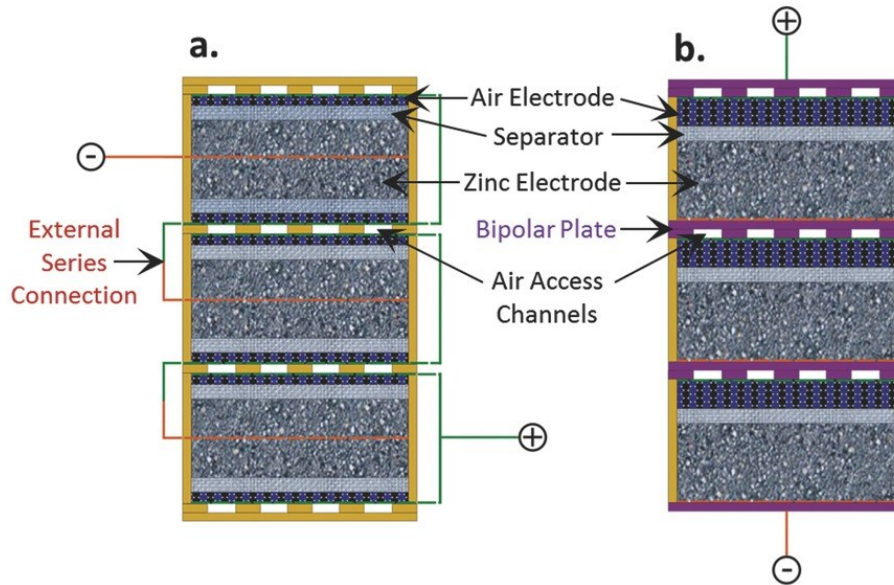


Figure 2.9. Schematic of a multi-cell ZAB pack with (a) monopolar arrangement and (b) bipolar arrangement.

(Reproduced with permission from reference [12].)

### 2.3.2.3. Flow stack

When battery space and weight are minor considerations, flow and tri-electrode designs offer longer cycle life and higher voltaic efficiency than those using a static bi-electrode design. Thus far, Zn-air flow technology has been successfully deployed for stationary energy storage. Solar-powered ZABs from NantEnergy (formerly Fluidic Energy) have covered numerous power outages for more than 200,000 people in over 110 communities in Asia and Africa [110]. Additionally, EOS Energy Storage has installed a 1 MWh system at a New Jersey wastewater treatment plant and previously set the price for a 1 MW/4 MWh grid-scale system (EOS Aurora) at US\$160 per kWh [111]. Some researchers have considered a combination tri-electrode, flow Zn-air system. A Spanish-based plant developed a pilot system with a peak power of 1 kW and a capacity of 4 kWh for stationary energy storage (Figure 2.10a and 2.10b). Atmospheric air is first CO<sub>2</sub>-filtered before circulating in parallel through the system. Three identical stacks are connected

in parallel, where each stack contains 20 cells connected in series. In each cell, the three electrodes are arranged in an ORR / OER / Zn sequence. The pilot battery plant had 40% round-trip efficiency and 2,000 cycles [13]. Additionally, a novel design of a tri-electrode flow Zn-O<sub>2</sub> battery has been proposed (Figure 2.10c and 2.10d). Interestingly, an O<sub>2</sub> recycling system is incorporated with the ZAB stack to reduce the cost of O<sub>2</sub>. Each battery module is made up of 24 individual batteries (6 in series and 4 in parallel). The relative position of the three electrodes is ORR / Zn / OER. Several pipelines are obviously required to supply and collect O<sub>2</sub> for discharge and recharge processes. With the use of O<sub>2</sub> instead of air, the performance of a single cell battery is significantly increased, with a maximum power density of 290 mW cm<sup>-2</sup> and stable cycling for more than 1500 cycles. However, in a 1 kW/1 kWh Zn-O<sub>2</sub> battery system, the power density of the battery stack is reduced to 75 mW cm<sup>-2</sup> [112].

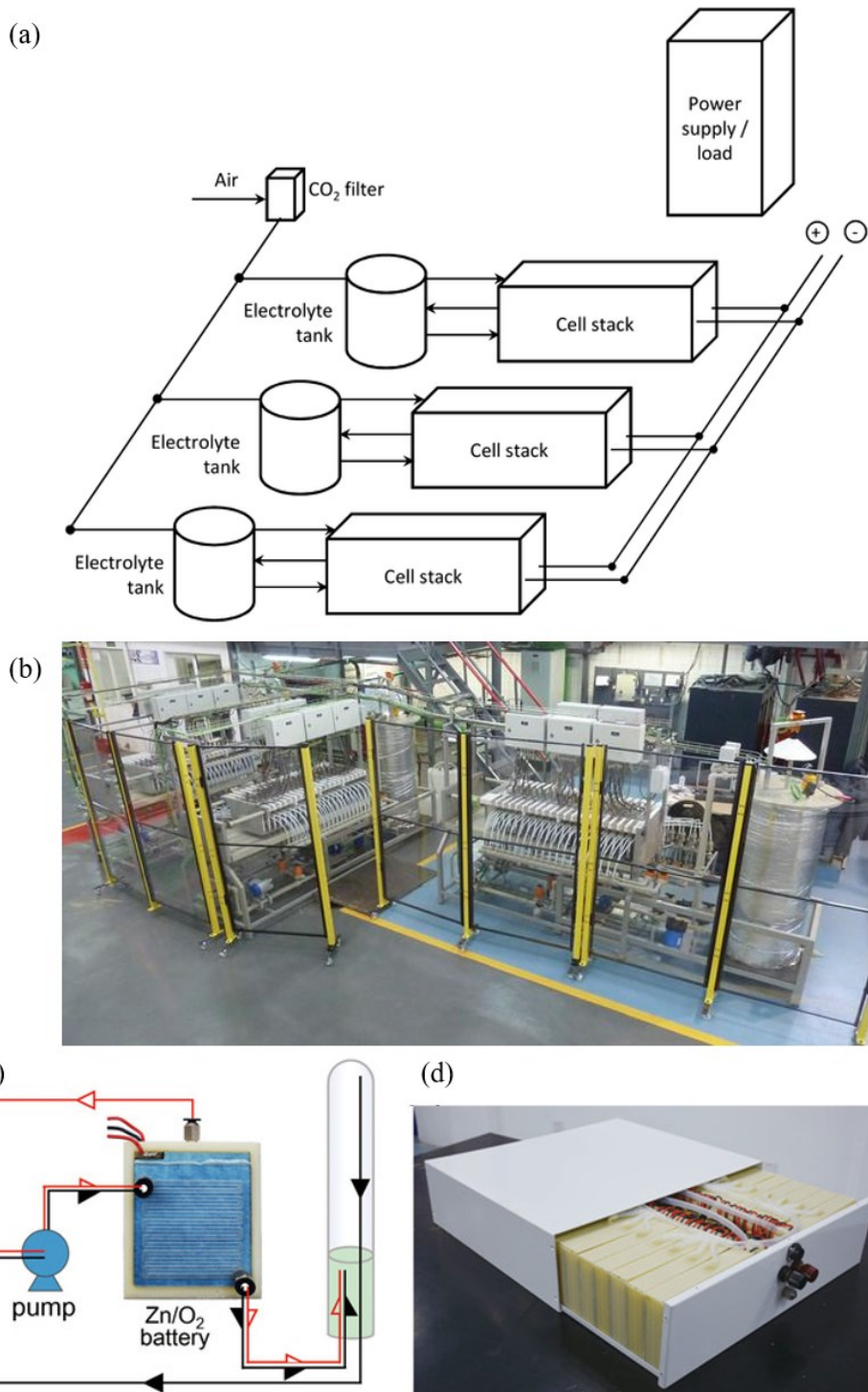


Figure 2.10. (a) Schematic of a tri-electrode flow stack and (b) photograph of a pilot plant (1 kW/4 kWh) [13]. (c) Design of Zn-O<sub>2</sub> stack and (d) photograph of the system (500 W/500 Wh) [112]. (Reproduced with permission from references [13, 112], figure has been modified.)

## 2.4. Key characterization techniques

### 2.4.1. Electrochemical testing

#### 2.4.1.1. Electrochemical Impedance Spectroscopy

Electrochemical impedance spectroscopy (EIS) is a measure of the ability of a circuit to resist electrical current flow. However, different from Ohm's Law ( $V = I \times R$ ) (Equation 2.4), EIS can reveal information about inductance, capacitance, different types of resistance and diffusion behaviour of a cell. EIS is conducted by applying a small AC potential at different frequencies. A typical EIS spectrum is a Nyquist plot which displays the real component of the impedance ( $Z_r$  or  $Z'$ ) vs. the imaginary one ( $Z_i$  or  $-Z''$ ). The plot can be fit to equivalent circuit models as shown in Figure 2.11. In measurements of electrolyte ionic conductivity, the equivalent circuit includes electrolyte resistance (commonly known as bulk resistance  $R_b$  or solution resistance  $R_s$ ), characteristic constant phase elements (Q) and Warburg impedance (W) (Figure 2.11a). Q is used instead of the double layer capacitance to represent an imperfect capacitor caused by surface roughness of the electrodes. W represents the impedance caused by the diffusion process. Among these values,  $R_b$  is particularly important for solid state electrolytes. High resistances may also imply poor wetting characteristics of hydrogel electrolytes compared with conventional alkaline solutions. In full cell testing, the equivalent circuit includes bulk resistance ( $R_b$ ), interfacial resistance ( $R_{int}$ ), charge transfer resistance ( $R_{ct}$ ) and interfacial and double layer characteristic constant phase elements ( $Q_{int}$  and  $Q_{dl}$ ). Since the oxygen reactions are kinetically limited, W is sometimes not observed in a Nyquist plot [12].

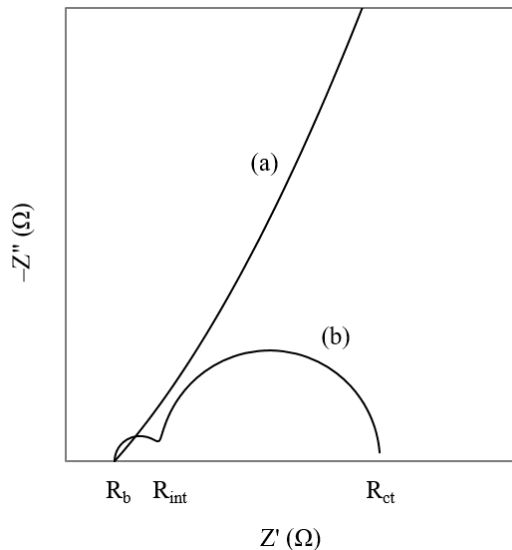


Figure 2.11. Two representative Nyquist plots for EIS data: (a) Ionic conductivity of electrolytes and (b) full cell testing.

#### 2.4.1.2. Cyclic Voltammetry

In cyclic voltammetry (CV), current is recorded as a function of applied voltage as it sweeps back and forth between two potential limits at a given scan rate (Figure 2.12). If a reaction occurs at the electrode during scanning, a peak in the current will appear at a specific potential. Thus, CV is a powerful technique commonly employed to investigate the redox processes of molecular species [113]. In the context of ZABs, CV can be performed in a KOH solution saturated with either O<sub>2</sub> or an inert gas. In Ar or N<sub>2</sub> saturated KOH, the CV data reveals the electrochemical behaviour of the electrode. In O<sub>2</sub> saturated KOH, the CV data is usually dominated by ORR. This can give insight into the stability of the electrode and electrocatalytic activity of catalysts.

Cyclic voltammetry can also be used to find the electrochemical window (EW) of an electrolyte, which is one of the most important characteristics for solvents and electrolytes. A good electrolyte should be neither oxidized nor reduced in the potential range of the electrochemical application. The EW is calculated by subtracting the cathodic potential from the anodic potential

where currents are relatively flat. For aqueous electrolytes, the thermodynamic potential window of water is 1.23 V. Out of this range, water is electrolysed to generate gases [114]. Several studies have increased the EW of aqueous electrolytes to  $\sim 2$  V by using appropriate electrode materials and additives in the electrolytes.

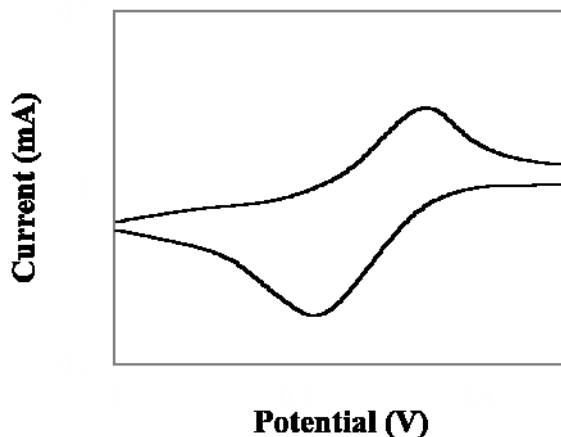


Figure 2.12. An example of CV curve where current is plotted against the voltage applied.

#### 2.4.1.3. Galvanodynamic method

The galvanodynamic method, also known as the polarization technique, measures cell potential as a function of progressively increasing current (Figure 2.13a). The variation between theoretical and operating voltages of the cell represents the losses due to activation, Ohmic resistance and mass transfer polarization. Specifically, at low current density during discharge, a sharp drop in voltage is primarily caused by the slow kinetics of the oxygen reactions. As the magnitude of current increases, linearly increasing voltage loss is dominated by electrolyte resistance and interfacial resistance. Finally, the steep voltage drop at the end is associated with the limited mass transfer of reactants to the electrodes. To determine the maximum power of the cell, a power curve as a function of applied current can be obtained by multiplying the applied current by the output potential [12].

A variation to this technique is to hold the current for a fixed amount of time before increasing it in a step-wise fashion (Figure 2.13b). The result, which is often referred to as a discharge or charge rate test, shows the potential stability at a given current for a period of time.

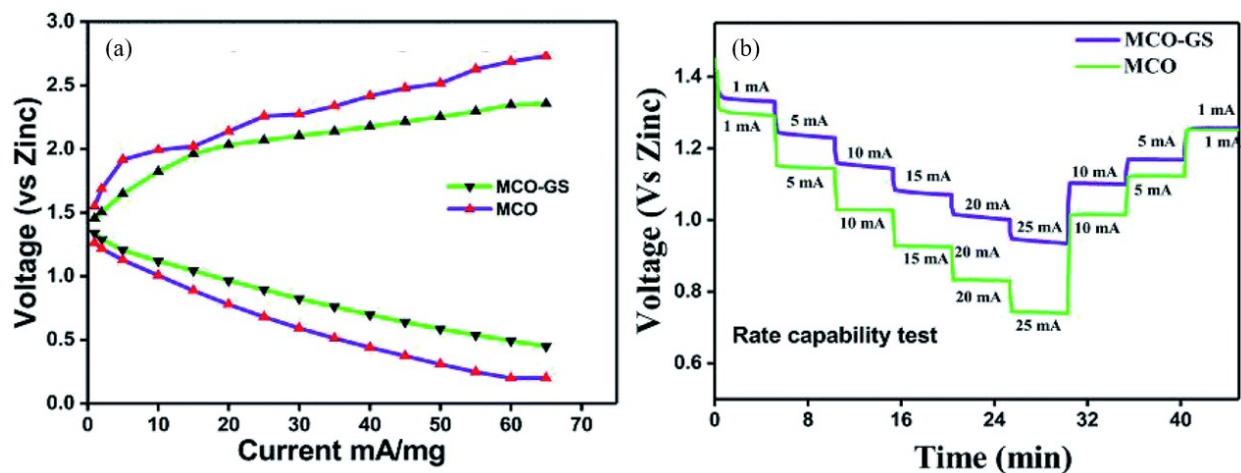


Figure 2.13. Examples of galvanodynamic techniques: (a) discharge-charge polarization profiles and (b) rate test.

(Reproduced from reference [115] - Published by The Royal Society of Chemistry, figure has been modified.)

#### 2.4.1.4. Galvanostatic method

In the galvanostatic method, potential is recorded as a function of a constant current vs. time (Figure 2.14a). The measurement is usually used to yield information on the depth of discharge of the battery. In the context of ZABs, specific capacity ( $\text{mA h g}_{\text{Zn}}^{-1}$ ) is obtained by normalizing capacity by the consumed mass of Zn, since oxygen can be freely withdrawn from the air (Figure 2.14b). This allows a relative comparison to the theoretical specific capacity of  $820 \text{ mA h g}_{\text{Zn}}^{-1}$ . In addition, a specific energy density ( $\text{W h g}_{\text{Zn}}^{-1}$ ) can be obtained by multiplying the specific capacity with an average discharge potential over the discharge period.

To evaluate the durability and cycle life of the battery, galvanostatic cycling is achieved by alternating between positive and negative values of the same current magnitude (Figure 2.14c).

There are a number of parameters to be determined for this test, such as magnitude of current density, number of cycles, length of time per cycle and whether there is rest time between discharge and charge steps. Short cycles are necessary to test cyclability of a cell in a reasonable amount of time. The voltaic efficiency of the battery can be determined by dividing the discharge potential by the charge potential. As such, the stability of the battery can be shown by the changes in efficiency over a number of cycles. The absolute potential difference between charge and discharge values can also be used as a metric for comparison, as long as the cells are tested at similar current densities.

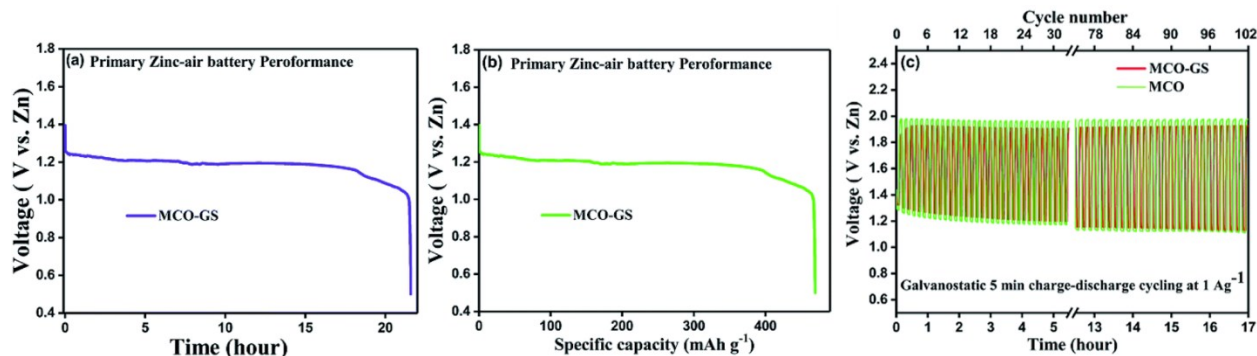


Figure 2.14. Examples of galvanostatic techniques: (a and b) depth of discharge curve and specific capacity of the battery, and (c) cycling test in a short interval (10 min per cycle)

(Reproduced from reference [115] - Published by The Royal Society of Chemistry.)

#### 2.4.2. Scanning electron microscopy and energy dispersive X-ray spectroscopy

Scanning electron microscopy (SEM) coupled with energy dispersive X-ray (EDX) spectroscopy allows observation and characterization of various materials including the microstructure of the catalyst, GDL and ZnO deposits on the Zn electrode after cycling tests. SEM is performed by scanning an electron probe over the specimen surface and provides better resolution (from tens of  $\mu\text{m}$  down to  $\sim 1$  nm) than light microscopy. When a beam of electrons encounters the specimen, key signals such as secondary electrons, backscattered electrons and

characteristic X-rays are emitted and collected by detectors. A schematic of a conventional SEM instrument is shown in Figure 2.15. Secondary electrons (SE) which are loosely bound outer shell or valence electrons give information about the topography of the sample. Backscattered electrons (BSE) have much higher energy and give information about the atomic number of the sample. Characteristic X-ray energies are used to identify the composition of a sample. X-rays can escape from throughout the electron interaction volume, which can be  $\sim 1 \mu\text{m}$  deep into the specimen. Therefore, even for a highly focused electron beam, the spatial resolution of X-ray analysis in SEM will be  $\sim 1 \mu\text{m}^3$  in thick specimens [116]. Depth resolution of the specimen surface can be further improved by lowering the accelerating voltage; however, X-ray yield is significantly reduced.

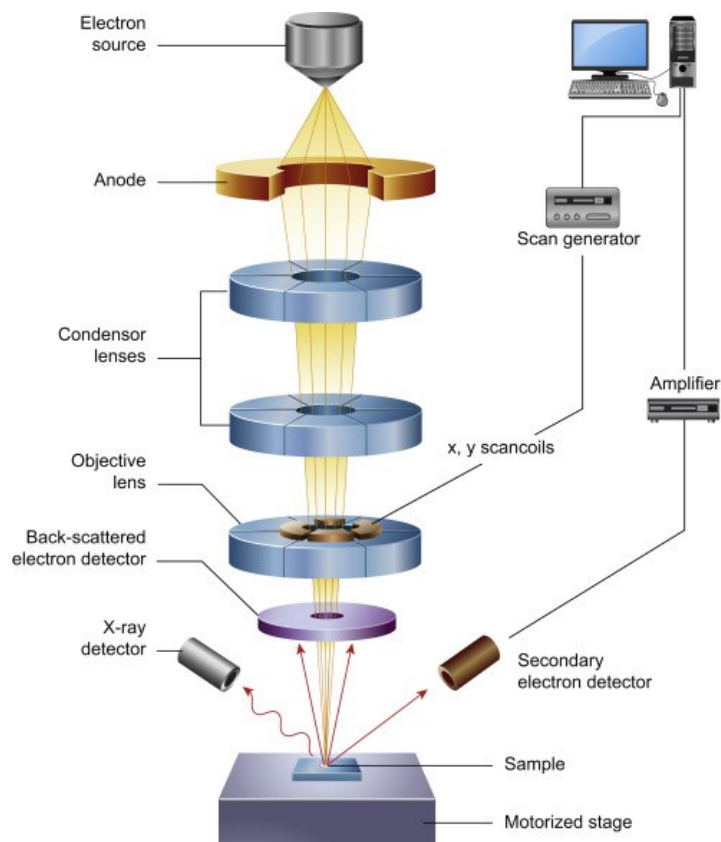


Figure 2.15. Schematic diagram of the core components of an SEM.  
(Reproduced with permission from reference [116].)

### 2.4.3. Fourier transform infrared spectroscopy

Fourier transform infrared spectroscopy (FTIR) is an analytical technique to provide qualitative and quantitative information about a molecular structure. When a molecule is exposed to IR radiation, its vibrating bonds will absorb energy with the same frequency from the IR radiation and increase the amplitude of the oscillation. The energies corresponding to changes in energy state for many functional groups are often found in the mid-IR region with wavenumber (1/wavelength) ranging from 4000 to 400  $\text{cm}^{-1}$ . During measurement, radiation containing all frequencies in this IR region is passed through the sample and the absorbed frequencies appear as a decrease in the resulting signal.

The main part of all FTIR spectrometers is a Michelson interferometer which splits the incident beam into two. When the split beams are recombined, an interference pattern (interferogram) is created. After being treated with a mathematical Fourier transform function, a plot of signal strength vs. wavenumber is produced (Figure 2.16). In general, there are four regions of bonds that can be analyzed from the FTIR spectra, including single bonds, triple bonds, double bonds and fingerprint regions. The absorbed IR frequencies are also dependent upon the symmetry of the structure and neighboring functional groups, which allows for precise identification of the molecule. For example, a double bond carbonyl group ( $\text{C}=\text{O}$ ) can absorb IR radiation at 1680–1630, 1725–1700 and 1800  $\text{cm}^{-1}$  for amide, carboxylic acid and acid chloride, respectively [117].

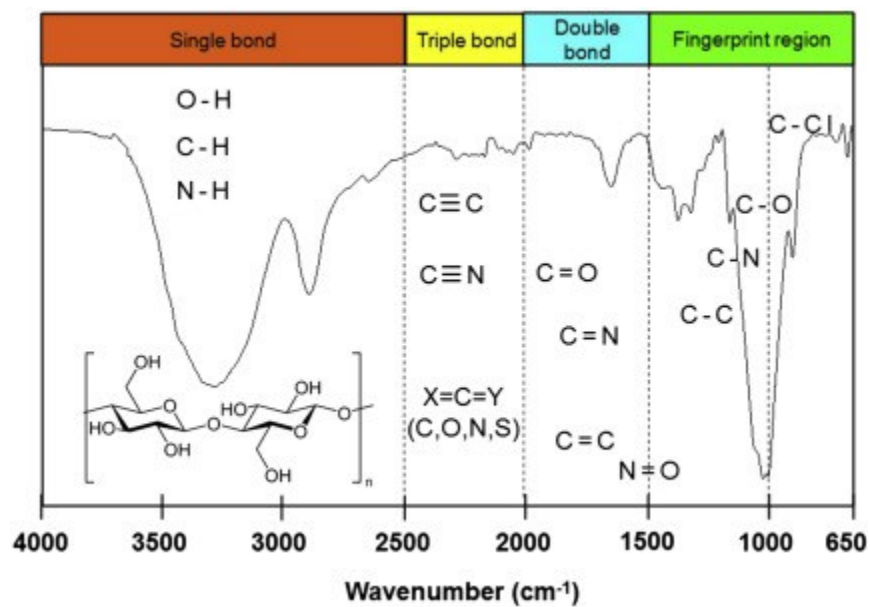


Figure 2.16: Sample FTIR spectrum corresponding to cellulose molecular structure. Common types of bonds absorbed in the approximate regions are also shown.

(Reproduced with permission from reference [117].)

#### 2.4.4. Rheology

Rheology is used to study the viscoelastic properties of materials. The choice of adequate setup depends on the type of materials (Figure 2.17). Typically, a parallel plate geometry works best to determine rheological properties of soft polymers such as hydrogels. In this thesis, two main oscillation tests are used including amplitude sweep and frequency sweep to investigate viscoelastic behavior of the gel polymer electrolytes. In amplitude sweep, frequency is kept constant while strain is controlled to increase in the amplitude in five steps (Figure 2.18a). In frequency sweep, the strain amplitude is kept constant while frequency is increased in five steps (Figure 2.18b) [118].

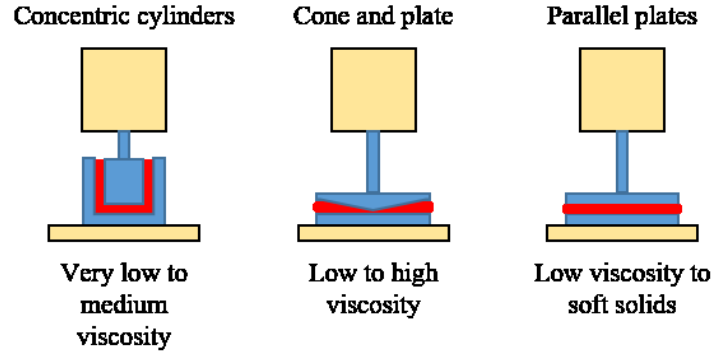


Figure 2.17. Different geometries of rheometers.

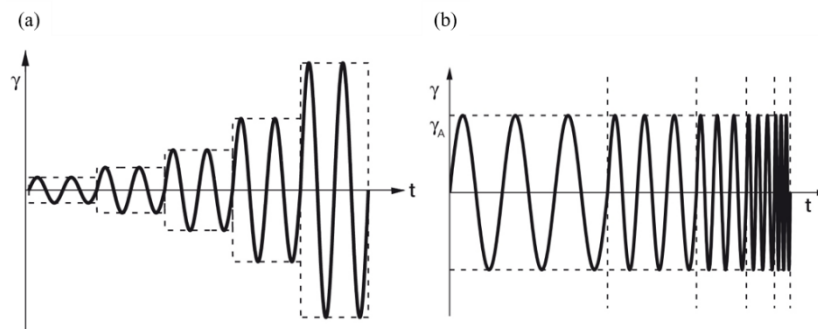


Figure 2.18. Presets for oscillatory tests: (a) amplitude sweep and (b) frequency sweep. (Reproduced with permission from reference [119, 120].)

The ratio of the maximum shear stress amplitude ( $\tau_0$ ) to the maximum shear strain amplitude ( $\gamma_0$ ) is known as the complex modulus ( $G^*$ ) (Equation 2.5). The complex modulus is also expressed as a function of storage modulus ( $G'$ ) (Equation 2.6) and loss modulus ( $G''$ ) (Equation 2.7), which represent elastic (solid) and viscous (liquid) properties, respectively [118].

$$G^* = \frac{\tau_0}{\gamma_0} = \sqrt{(G')^2 + (G'')^2} \quad \text{Equation 2.5}$$

$$G' = G^* \cos \delta \quad \text{Equation 2.6}$$

$$G'' = G^* \sin \delta \quad \text{Equation 2.7}$$

where  $\delta$  is the phase angle ( $0 < \delta < 90^\circ$ ) between the stress and strain (Figure 2.19). For a perfectly elastic solid sample, the stress oscillation is exactly in phase with the imposed strain ( $\delta = 0^\circ$ ), while

for an viscous liquid sample, the stress oscillation is exactly  $\pi/2$  out of phase with the imposed strain ( $\delta = 90^\circ$ ). Most materials have viscoelastic behavior, which is between the two extremes. For the gel state,  $\delta$  is between  $0^\circ$  and  $45^\circ$ . For the fluid-like state,  $\delta$  is between  $45^\circ$  and  $90^\circ$  [121].

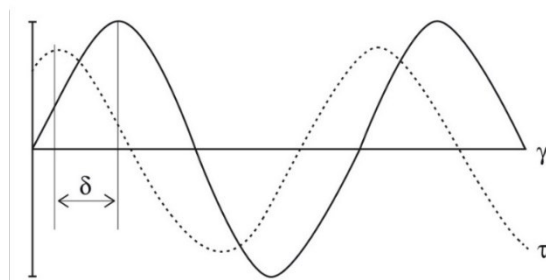


Figure 2.19. Sinusoidal function of shear strain  $\gamma$  and shear stress  $\tau$  versus time for a viscoelastic sample. The two curves are offset by phase shift  $\delta$ .

(Reproduced with permission from reference [119, 120].)

## 2.5. Summary

Given the advantages of Zn's abundance in the Earth's crust, its environmentally benign behaviour and low toxicity, interest in electrically rechargeable Zn-air batteries (ZABs) with high specific energy density has been revived for large-scale energy storage. In spite of the success of primary batteries, the technology and manufacturing readiness levels for secondary ZABs are both low at this stage. Secondary ZABs experience several shortcomings from Zn and air electrodes, which are worsened in aqueous, alkaline electrolytes. The review has highlighted that, in order to achieve a breakthrough in battery performance, selecting a suitable electrolyte system is paramount to cope with the challenges. Furthermore, it is critical to develop a battery design to enhance the durability and activity of innovative electrocatalysts (such as a tri-electrode configuration), as well as to improve cyclability, energy efficiency and power output of ZABs. In this regard, further research into optimizing gel polymer electrolyte as well as battery design is necessary.

## Chapter 3. A Study of Alkaline Gel Polymer Electrolytes for Rechargeable Zinc-air Batteries

A version of this chapter has been published as:

Tran, T.N.T., Chung, H.-J. and Ivey, D.G., *A Study of Alkaline Gel Polymer Electrolytes for Rechargeable Zinc-Air Batteries*. *Electrochimica Acta*, 2019. **327**: p. 135021.

### 3.1. Introduction

Zn-air batteries (ZABs), which employ oxygen from air for the reduction reaction or discharging, have several advantages, such as high specific energy (1218 Wh kg<sup>-1</sup>) and energy density (6136 Wh L<sup>-1</sup>), operational safety, environmental compatibility and large material availability in the Earth's crust, all of which lead to low cost [12]. Since initial commercialization in the 1930s, primary ZABs have been used for a wide range of applications, such as hearing aids, railroad signaling, harbor buoys, underwater navigation and electric fencing [122]. Currently, ZABs are one of the most promising candidates for grid-scale energy storage and electric vehicles (EVs) [12, 18, 123]. One of the major challenges that rechargeable ZABs face is cycle life improvement, which is limited by issues associated with the Zn and air electrodes. The Zn electrode suffers from dendrite formation, shape change, passivation and hydrogen evolution, while the air electrode must contend with slow oxygen reduction reactions and carbonate precipitation. In addition, electrolytes play a crucial role in the transport of active species, as they can affect nominal cell voltage, energy density, power capability and cycling efficiency [2, 12].

Conventionally, alkaline solutions such as potassium hydroxide (KOH) or sodium hydroxide (NaOH) have been used as electrolytes. KOH solutions are preferred because they have

higher ionic conductivity and lower viscosity [124]. However, alkaline solutions suffer from many problems such as electrolyte leakage and water evaporation. A second type of ZAB electrolyte is room temperature ionic liquids (RTILs), which are salts in the liquid state at ambient temperature. They can solve many problems associated with alkaline solutions because of their unique physical and chemical properties. These include non-volatility, low toxicity, good thermal and electrochemical stability and a diverse combination of cations and anions that can be chosen to tune RTIL characteristics [57]. Nevertheless, the ionic conductivity of RTILs is approximately 500 times lower than that of a 6 M KOH solution, which limits their application in ZABs [62]. A third type of electrolyte is gel polymer electrolytes (GPEs). Vinyl polymers and cellulose derivatives are generally used as matrices which swell upon exposure to an alkaline solution [12]. As such, they are able to combine the desirable properties of liquids and solids; e.g., high ionic conductivity and mechanical stability, respectively. Moreover, GPEs also help to enhance the performance of both Zn and air electrodes. For instance, a GPE can act as a separator to reduce Zn dendrite formation and increase Zn utilization (82 – 90%) [12], as well as prevent the electrolyte from penetrating the air electrode pores, thereby enhancing oxygen access [2].

Hydrogels are three dimensional crosslinked network polymers that swell and retain a significant amount of water without dissolving [125] and thus have been utilized as host materials for GPEs in ZABs. Previously most GPEs were fabricated only for primary metal-air batteries [69, 70, 126, 127], due to the poor buffering capability of the solid-state electrolyte which led to low energy efficiency when charging. Nevertheless, Chen et al. reported a flexible and rechargeable ZAB using porous polyvinyl alcohol (PVA) as the GPE. PVA showed outstanding stability over 120 cycles at a rate of 50 A kg<sup>-1</sup> [72]. Peng et al. also reported a rechargeable, flexible and stretchable ZAB with a PVA/poly(ethylene oxide) (PEO)-based alkaline GPE. At the voltage

plateau of 1.0 V, the discharge current density reached  $1 \text{ A g}^{-1}$  and was maintained for 30 discharge/charge cycles [73].

Designing a hydrogel network that has chemical and electrochemical stability, high ionic conductivity and good contact with the electrodes is a major challenge for GPEs. In this study, poly(vinyl alcohol) (PVA), poly(acrylic acid) (PAA) and a charge-symmetric polyampholyte, i.e., poly(4-vinylbenzenesulfonate-*ran*-[3-(methacryloylamino)propyl]trimethylammonium chloride) (denoted hereafter as PAM for simplicity), were selected as model systems. The hydrogels can be classified based on their chemical composition and electrical charge on the functional groups, as shown in Figure 3.1a. Figure 3.1b illustrates their different behavior in a KOH environment. PVA is one of the most widely used polymeric hosts for aqueous KOH, since it has good ionic conductivity and its facile fabrication by a freeze-thaw method is well established. This neutral homopolymer has a semi-crystalline structure; however, KOH can disrupt the crystallinity and convert the polymer into an amorphous phase [128]. A larger fraction of amorphous phase generally offers higher ionic conductivity with weaker mechanical properties [129]. PAA is an anionic homopolymer in a high pH environment (the carboxyl group ( $-\text{COOH}$ ) forming a negatively-charged carboxylate ion ( $-\text{COO}^-$ )); the polymer expands into a fully solvated open coil conformation [130]. The main advantage of PAA is an established one-step synthesis, where the monomers directly polymerize in the KOH solution [75]. PAM is an example of a charge-balanced polyampholytic random copolymer. The advantages of using polyampholytes as GPEs include high water retention ability, due to the electrostatic interactions between the electrostatic groups and water molecules [131, 132], and an antipolyelectrolytic effect where inclusion of salt ions in the dialyzing solution causes swelling of the hydrogel instead of the collapse that occurs in ordinary polyelectrolytes [133].

The purpose of this chapter is to investigate the behavior of three different hydrogel matrices as model GPEs in KOH solutions, which are commonly used for rechargeable ZABs, and compare their performance. Different aspects, including morphology and mechanical strength changes, electrochemical and chemical stability, ionic conductivity, water uptake and battery performance, are tested.

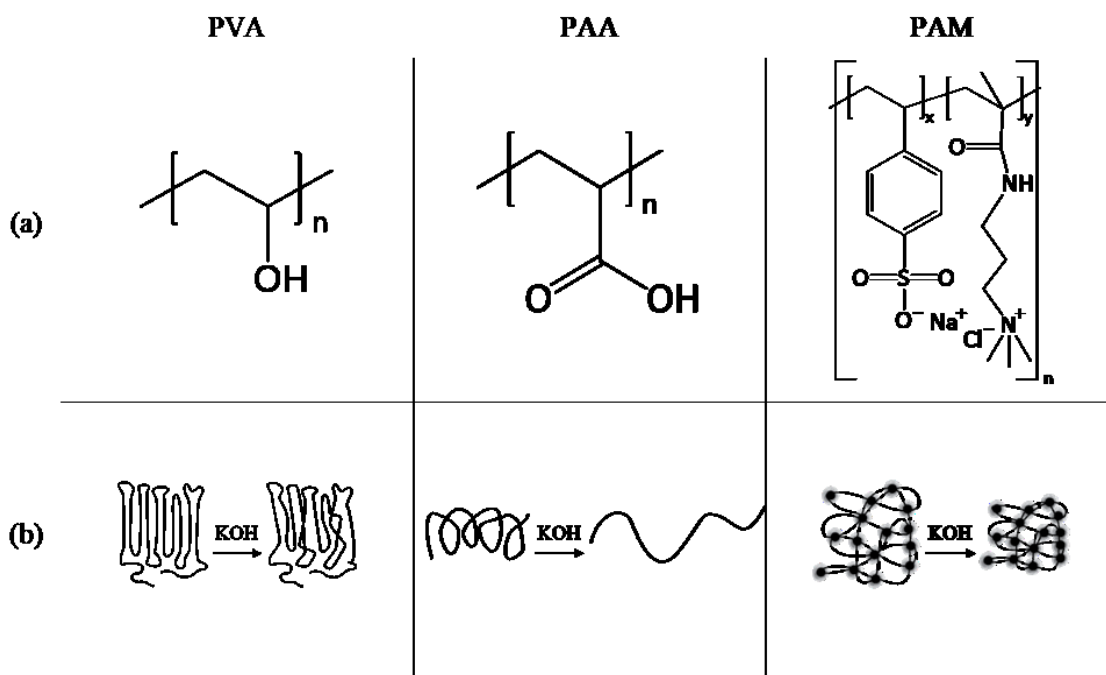


Figure 3.1. (a) Chemical structure of PVA, PAA and PAM. PAM is a random copolymer of two monomers. (b) Schematic illustration of the polymer states in deionized water (DIW) and 6 M KOH solution.

## 3.2. Experimental procedure

### 3.2.1. Synthesis of gel electrolytes

PVA ( $M_w = 146\,000 - 186\,000$ , 99% hydrolyzed), acrylic acid (AA), sodium 4-vinylbenzenesulfonate (NaSS), [3-(methacryloylamino)propyl] trimethylammonium chloride (MPTC), N,N'-methylenebis(acrylamide) (MBAA), potassium persulfate (KPS) and potassium

hydroxide (KOH) were all purchased from Sigma-Aldrich. All chemicals were analytical grade and used as received without further purification.

PVA was dissolved in de-ionized water (DIW) (10% w/v) at 100 °C for 2 h to make a homogeneous solution. This solution was poured into a petri dish and kept frozen at –20 °C overnight and then thawed at 25 °C. This freeze-thaw cycle was repeated three more times with 2 h per step to crosslink the PVA. During this process, intra- and interchain hydrogen bonds were formed [134].

PAA was prepared by mixing AA monomer (1.8 M), MBAA crosslinker (0.3 mol% of total monomers) and KPS thermoinitiator (0.1 mol% of total monomers) in deionized water (DIW). Another sample, designated as PAA6M was prepared by adding AA (1.8 M) to KOH (7.8 M), MBAA (0.3 mol% of total monomers) and KPS (0.1 mol% of total monomers). Solutions were poured into a petri dish and kept in an oven at 70 °C for 8 h to polymerize.

PAM was prepared by random free radical polymerization with a 50/50 monomer molar ratio of NaSS (1 M) and MPTC (1 M). The components were mixed with MBAA (0.3 mol% of total monomers) and KPS (0.1 mol% of total monomers) in DIW. The solution was poured into a petri dish and kept in an oven at 70 °C for 8 h to polymerize.

The thickness of all hydrogels was about 1 mm. PVA and PAM were cut and immersed in 6 M KOH solution for at least a week and are designated as PVA6M and PAM6M, respectively.

### **3.2.2. Materials characterization**

Mechanical strength was measured using a compression tester (Instron 5943) at a rate of 5 mm min<sup>-1</sup> and Young's modulus was calculated within the 3 – 8% strain region. The microstructure of freeze dried hydrogels was observed using field emission scanning electron

microscopy (Zeiss Sigma FESEM operated at 5 kV). Freeze-dried samples were chemically characterized by Fourier transform infrared spectroscopy (Thermo Scientific Nicolet iS50 FTIR). Sixty-four scans with a resolution of  $4\text{ cm}^{-1}$  were averaged to obtain each spectrum.

### 3.2.3. Electrochemical measurements

Electrochemical measurements were carried out with a potentiostat/galvanostat (Autolab PGSTAT302N). Cyclic voltammetry (CV) measurements were done by scanning from 0 V to 2 V vs. stainless steel (SS) at  $10\text{ mV s}^{-1}$  for hydrated GPEs and from 0 V to 5.5 V vs. SS at  $5\text{ mV s}^{-1}$  for freeze-dried samples. The potential values were iR compensated using the bulk resistance values. Conductivities of the GPEs were measured by electrochemical impedance spectroscopy (EIS) at open circuit potential with an applied 10 mV AC potential from 100 kHz to 10 mHz. The gels were sandwiched within SS coin cells (CR2032, MTI Corporation) as shown in Figure 3.2a. For comparison, conductivities of KOH solutions as well as a commercial microporous separator (Celgard 5550) were also measured. EIS spectra were fit to an equivalent circuit using Zsimpwin software (Figure S3.1a) and the extracted resistance values were converted to ionic conductivity using *Equation 3.1*:

$$\sigma = \frac{L}{R \times A} \quad \text{Equation 3.1}$$

where L is the thickness of the sample (cm), A is the contact area of the GPE within the coin cell ( $\text{cm}^2$ ) and R is the bulk resistance ( $\text{m}\Omega$ ). Current densities were normalized to the geometric surface area.

### 3.2.4. Water uptake study

PVA and PAM were kept in 3, 6 or 9 M KOH for at least a week to reach equilibrium, while PAA was directly synthesized with 4.8, 7.8 or 10.8 M KOH. The higher concentration of

KOH in the PAA precursor solution was used to offset the amount of hydroxide ions utilized in neutralizing the AA monomers. Since hydroxide ions are the charge carriers in GPEs [135, 136], the directly-mixed PAA with 4.8, 7.8 and 10.8 M KOH can be compared with PVA and PAM that are immersed in 3, 6, and 9 M KOH solutions, respectively. All polymer samples were refrigerated at  $-20\text{ }^{\circ}\text{C}$  overnight, followed by quenching in liquid nitrogen and then freeze drying ( $-60\text{ }^{\circ}\text{C}$ , 1 torr, Savant SuperModulyo freeze drier) for 2 days. Water uptake was determined from *Equation 3.2*:

$$\text{Water uptake (\%)} = \frac{W_W - W_D}{W_D} \times 100\% \quad \text{Equation 3.2}$$

where  $W_W$  is the weight of the wet sample (g) and  $W_D$  is the weight of the dried sample (g).

### 3.2.5. Cell testing

Zn-air battery testing was done in meshed coin cells (CR2032 case-mesh, MTI Corporation) as shown in Figure 3.2b. Zn foil and the catalyst loaded gas diffusion layer (GDL) were used as the electrodes. Zn-air batteries that used gel electrolytes (PVA6M, PAA6M and PAM6M) were tested and compared with cells that used 6 M KOH and a Cellgard separator.

For discharge testing, 20 nm of Pt was sputtered on the GDL. Battery discharge potentials were measured by a galvanostatic method at a series of current densities of 2, 5, 10 and 20  $\text{mA cm}^{-2}$  for 5 min each with a cut-off voltage of 0.7 V. For cycling tests, Pt/Ru catalyst ink was sprayed onto separate GDL substrates. The ink consisted of 50 mg of Pt/Ru/C powder (40% Pt and 20% Ru, Alfa Aesar) dispersed in 2.0 mL of DIW, 1.0 mL of isopropanol, 0.1 mL of 5 wt% Nafion (D-521) and 0.2 mL of 10 wt% polytetrafluoroethylene (PTFE) (DISP30). The mass loading of Pt/Ru/C ink on the GDL was about  $0.6\text{ mg cm}^{-2}$  after drying in a furnace at  $300\text{ }^{\circ}\text{C}$  for 30 min. The battery discharge and charge potentials were measured galvanostatically at  $0.5\text{ mA cm}^{-2}$  for

10 min cycle<sup>-1</sup>. The discharge-charge efficiency was calculated by dividing the average discharge potential by the average charge potential of the second cycle. EIS was also performed at 1.2 V vs. Zn/Zn<sup>2+</sup> with a 10 mV AC potential from 100 kHz to 10 mHz before and after the cycling test. The EIS spectra were fit to another equivalent circuit as shown in Figure S3.1b.

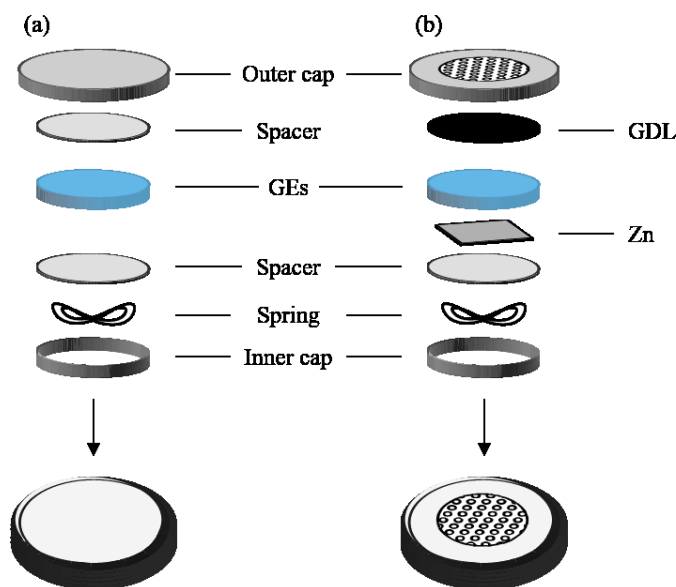


Figure 3.2. Coin cell configurations for (a) CV and EIS measurements and (b) full cell testing using GPEs.

### 3.3. Results and discussion

#### 3.3.1. Mechanical strength, electrochemical window and alkaline stability

PAA was directly polymerized in DIW or in aqueous KOH solutions, while freeze-thawed PVA and as-synthesized PAM were firstly dialyzed in DIW for 8 h, followed by immersion in 3, 6 and 9 M KOH solutions for 3 months. Since the KOH solutions are highly alkaline, a study of polymer degradation over time is required for long-term use in ZABs. The stability of the hydrogels towards alkaline media can be assessed through any changes in color and mechanical strength. Figure 3.3a shows that in 9 M KOH the color of PVA gradually changed from white to brownish yellow after three months of storage, whereas color changes for 3 and 6 M KOH

immersions were negligible. Similar discoloration also occurred when PVA was subjected to high temperatures, forming polyene fractions which indicate degradation [137]. PAM became stiff right after the dialysis process and remained that way after 3 months (Figure 3.3b). During dialysis in DIW, counter ions ( $\text{Na}^+$  and  $\text{Cl}^-$ , see Figure 3.1a) were removed from the PAM network which increased ionic bond formation between polymer backbones to stiffen the samples. Table 3.1 shows that the compression modulus of PAM in 6 M KOH is two orders of magnitude higher than the values for PVA and PAA. Dialyzing PAM in DIW or KOH solution removes salt from the polymer network ( $\text{Na}^+$  and  $\text{Cl}^-$ ) with the concentration gradient acting as the driving force (Figure 3.1). As such, the oppositely charged functional groups collapsed resulting in the increase in mechanical strength [138].

Figure 3.4 shows the morphology changes for all the hydrogels in DIW and 6 M KOH. Cross section images indicate that the hydrogels become more porous under the influence of the KOH solution. For the PAM samples, there are significant differences relative to an earlier report showing FESEM images from DIW and KOH dialyzed samples [139]. Specifically, the morphology of water-dialyzed PAM exhibits a “zipping” mechanism where its polymer networks turn into a microscopic cellular structure with a pore size of  $\sim 20 \mu\text{m}$ . In reference [139], the precursor solution contained an extra 10 wt% of NaCl and an UV-initiator (Irgacure 2959) was used, whereas a thermoinitiator (KPS) was used in this work. The reasons for the morphological differences require further investigation, which is beyond the scope of the current chapter.

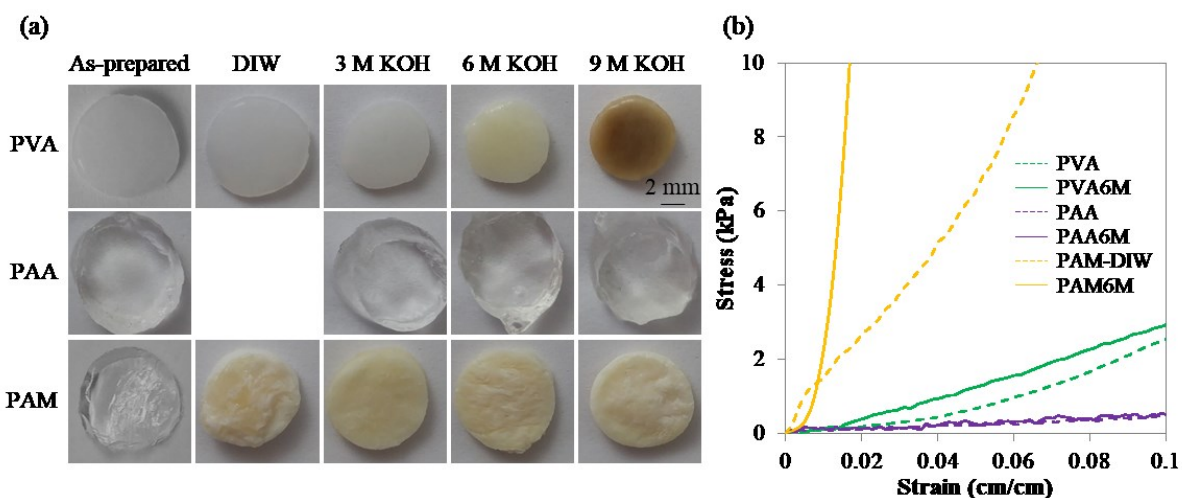


Figure 3.3. (a) Images of PVA, PAA and PAM after storage for 3 months. The PVA and PAM images shown are for the as-prepared condition and after immersion in DIW and 3, 6, and 9 M KOH solutions. (b) Compression test results for PVA, PAA and PAM in DIW and 6 M KOH.

Table 3.1. Compressive modulus (kPa) of hydrogels after immersion in DIW and in 6 M KOH

PVA	PVA6M	PAA	PAA6M	PAM	PAM6M
$24.9 \pm 8.6$	$30.9 \pm 4.0$	$2.8 \pm 0.9$	$5.4 \pm 1.5$	$225.1 \pm 75.5$	$2704.4 \pm 811.9$

\* Hydrogels immersed in KOH are denoted with the suffix 6M, which refers to the concentration.

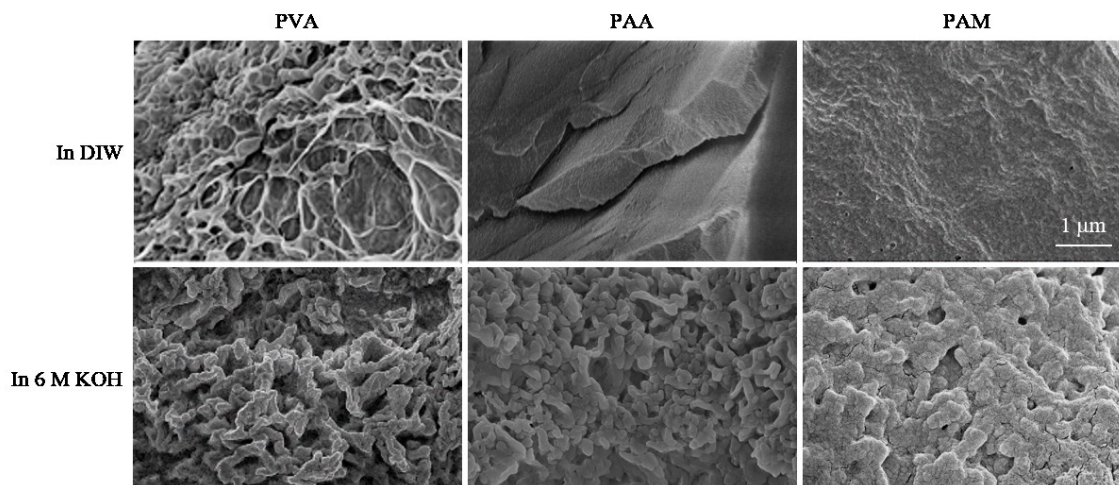


Figure 3.4. FESEM secondary electron (SE) cross section images of PVA, PAA and PAM after immersion in DIW and 6 M KOH.

Degradation of the hydrogels in 6 M KOH after 3-month storage was further investigated by FTIR, which was used to compare the chemical structures of hydrogels after immersion in DIW and 6 M KOH. Figure 3.5a shows the FTIR spectra for PVA. Above  $1400\text{ cm}^{-1}$ , the large band between  $3400$  and  $3200\text{ cm}^{-1}$  is attributed to O–H stretching. The peak at  $2900\text{ cm}^{-1}$  can be assigned to C–H stretching and the peak at  $1435\text{ cm}^{-1}$  is associated with C–H bending. In the  $1400$ – $1000\text{ cm}^{-1}$  range, five peaks are located at  $1380$ ,  $1330$ ,  $1240$ ,  $1135$  and  $1085\text{ cm}^{-1}$ ; these are similar to those previously reported by Elkan et al. [140]. The weak peaks are due to motion of the functional groups in the material, while the sharp peak at  $1085\text{ cm}^{-1}$  represents stretching of the C–O bond. The absorption bands below  $1000\text{ cm}^{-1}$  can be explained as the movement of the carbon skeleton; e.g., the peak at  $840\text{ cm}^{-1}$  is due to out of plane vibration of the C–H bond [140, 141]. Overall, the PVA (as-prepared) and PVA6M spectra are virtually the same.

When polymerizing PAA in alkaline media, neutralization of carboxylic groups occurs which causes loss of hydrogen atoms resulting in the negatively charged form of the functional group ( $-\text{COO}^-$ ) [142]. As a result, the FTIR spectrum is affected (Figure 3.5b). Commonly, the C–H stretching peak near  $2947\text{ cm}^{-1}$  overlaps with the large O–H stretching regions [143]. The spectrum for PAA prepared in DIW shows carbonyl stretching ( $\text{C}=\text{O}$ ) at  $1700\text{ cm}^{-1}$ ,  $\text{CH}_2$  stretching at  $1450\text{ cm}^{-1}$  and C–O stretching coupled with O–H bending vibration at  $1250$ – $1130\text{ cm}^{-1}$  [142–144]. For PAA6M rinsed with DIW, there is antisymmetric and symmetric stretching of carboxylate ions ( $\text{COO}^-$ ) at  $1550$  and  $1395\text{ cm}^{-1}$ , respectively, although  $\text{CH}_2$  stretching is still detected at  $1450\text{ cm}^{-1}$  [144]. The change in absorption bands indicates that at low pH, carboxylate groups of PAA are protonated ( $-\text{COOH}$ ), whereas at high pH the groups are ionized ( $-\text{COO}^-$ ) [144]. To eliminate the influence of the alkaline environment, PAA6M was rinsed with HCl and

then with DIW. The absorption bands are then similar to those of PAA synthesized in DIW (Figure 3.5b).

For PAM (Figure 3.5c), the broad peak at 3600–3200  $\text{cm}^{-1}$  can be assigned to overlapping O–H and N–H stretching, while the C–H stretching peak occurs at 2925  $\text{cm}^{-1}$ . Characteristic bands of the carboxamide group include peaks at 1640 and 1525  $\text{cm}^{-1}$ , which are attributed to C=O stretching [145-147] and N–H bending of amide, respectively. The peak at 1480  $\text{cm}^{-1}$  is assigned to in-plane bending of methyl groups of quaternary ammonium [148], which originate from the monomer MPTC. Characteristic bands of NaSS are found at 1180, 1120, 1035, 1010  $\text{cm}^{-1}$ . The peaks at 1180 and 1035  $\text{cm}^{-1}$  can be attributed to the antisymmetric and symmetric stretching of  $\text{SO}_3^-$  groups, respectively, and the peaks at 1120 and 1010  $\text{cm}^{-1}$  can be assigned to the in-plane skeleton and bending vibration of the benzene ring, respectively [149]. As with PVA, the PAM6M and pristine PAM spectra are essentially the same.

The FTIR analysis shows that the GPEs were prepared successfully and they are quite stable in 6 M KOH solutions.

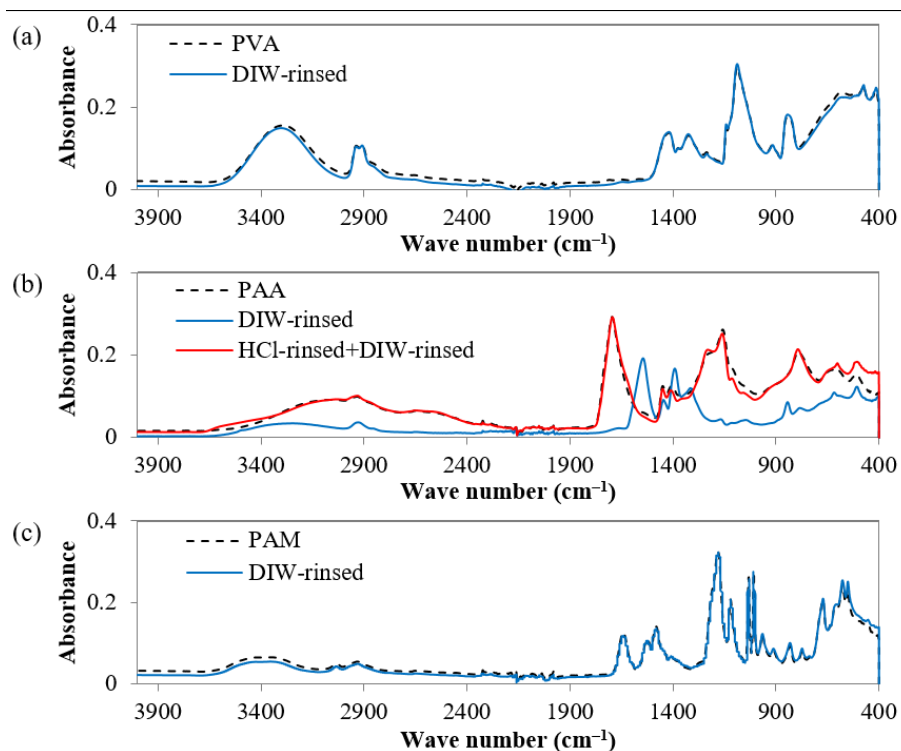


Figure 3.5. FTIR spectra for (a) PVA, (b) PAA and (c) PAM. Dashed lines represent the hydrogels in DIW. Blue solid lines represent the hydrogels in 6 M KOH after rinsing with DIW. The red line in (b) represents PAA6M rinsed with HCl and then with DIW.

The electrochemical stability window of the GPEs was evaluated (Figure 3.6), since a broad potential window is desirable. The parasitic hydrogen evolution reaction (HER) at the Zn electrode in addition to water electrolysis at the air electrode accounts for the pressure increase in ZABs. As shown in Figure 3.6a, the oxidation peak appears at 1.75 V for the 6 M KOH solution and is shifted to a slightly higher potential for the GPEs, which indicates a reduction in the electrochemical activity of water and helps to extend the stability range. From a practical point of view, this means that GPEs still have a narrow electrochemical window as with aqueous solutions.

To eliminate the effect of water splitting, freeze-dried GPEs were used for CV measurement over a broader potential range of 0 to 5.5 V vs. stainless steel (SS). Figure 3.6b shows that the electrolysis peaks at about 1.8 V are significantly reduced; there is no obvious peak for

PAM6M and only PVA6M and PAA6M show peaks at 2 V. This difference may be due to the difference in electrochemical activity of water [150]. The mechanism responsible for the difference requires a separate study, which is beyond the scope of this study. In the literature, a solid state poly(ethylene glycol)-based electrolyte for Al-ion batteries was shown to have an electrochemical stability window of 3 V [151]. Considering that the electrochemical stability windows of PVA, PAA and PAM are at least 2 V, they all are able to sufficiently withstand the operating potentials of ZAB systems, which usually range from 1 – 1.2 V (discharge) to 1.7 – 2 V (charge) vs. Zn/Zn<sup>2+</sup>.

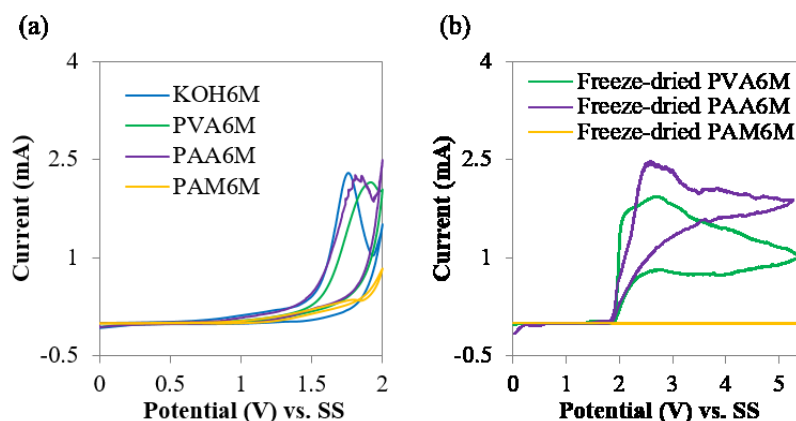


Figure 3.6. CV curves of PVA6M, PAA6M and PAM6M in (a) hydrated states and (b) freeze-dried states.

### 3.3.2. Ionic conductivity in relation to water uptake and temperature

Ionic conductivity is another important parameter of electrolytes. For aqueous electrolytes, relationships between the alkaline concentration, ionic conductivity, ZnO solubility, electrode potential and the limiting current of the Zn electrode have been reported [152]. Electrolytes with higher conductivity can profoundly enhance battery performance, such as rate capability and cycling efficiency [12]. Gilliam et al. collected over 300 data values to develop an empirical relationship between specific conductivity of KOH solutions as a function of concentration and temperature (*Equation 3.3*) [153].

$$\sigma = -2.041(M) - 0.0028(M^2) + 0.005322(M \cdot T) + 207.2 \left(\frac{M}{T}\right) + 0.001043(M^3) - 0.0000003(M^2 \cdot T^2) \quad [153]$$

*Equation 3.3*

where  $\sigma$  represents the specific conductivity in  $\text{S cm}^{-1}$ ,  $M$  is the molarity in  $\text{mol L}^{-1}$  and  $T$  is the temperature in Kelvin. The conductivities of alkaline solutions measured in this work are compared with those calculated from the empirical equation (Figure S3.2). There are differences between the actual values, but the trend is similar. The conductivity reaches a maximum value of  $432 \text{ mS cm}^{-1}$  for the aqueous KOH solution with a concentration of 6 M at  $20^\circ\text{C}$ ; the conductivity for a 9 M KOH concentration is slightly lower (Figure 3.7a). It should be noted that most aqueous ZABs employ a separator which is made of polypropylene. Commercial polypropylene-based separator films, such as Celgard 5550 and Celgard 4560, are common choices in rechargeable ZABs to prevent contact between the two electrodes [12, 152]. In this study, Celgard 5550 was used in the as received condition. Due to its hydrophobicity, polypropylene has a low ionic conductivity ( $\sim 5 \text{ mS cm}^{-1}$ ) which can affect ZAB performance. Sulfonation treatment, which decreases the hydrophobicity, has been reported to improve the ionic conductivity of Celgard 2320 by a factor of 2.3 (from  $15.2$  to  $35.2 \text{ mS cm}^{-1}$ ) compared with the unsulfonated membrane [154]. For the GPEs, PVA6M and PAA6M have the highest conductivities at  $161$  and  $204 \text{ mS cm}^{-1}$ , respectively, for a KOH concentration of 6 M. The conductivities decrease slightly for 9 M KOH. The increase in conductivity with increasing KOH concentration (from 3 M to 6 M) can be attributed to an increase in the number of charge carriers ( $\text{K}^+$  and  $\text{OH}^-$ ). However, at KOH concentrations larger than 6 M, the conductivity decreases because the additional KOH may form ion pairs which increase viscosity and decrease ionic conductivity, instead of creating more charge carriers. It is reasonable to assume that ionic conductivity of GPEs is linked to electrolyte uptake. Indeed, in a fixed system of PAA– $\text{H}_2\text{O}$ –KOH (Figure S3.3), conductivity appears to increase with

increasing water uptake. However, when comparing different hydrogel systems, the amount of electrolyte uptake does not solely determine ionic conductivity. PAM has the lowest conductivity of the GPEs with its conductivity decreasing with increasing KOH concentration. The maximum conductivity for PAM ( $36 \text{ mS cm}^{-1}$ ) occurs at 3 M KOH concentration. It is worth noting that the conductivity for PAM6M is approximately 7 – 10 times lower than that for PVA6M and PAA6M even though its water content is only about 2 – 3 times lower (Figure 3.7b). This behavior indicates that conductivities in PAM depend not only on the amount of electrolyte uptake, but also on the interfacial contact with electrodes, as well as chemical and structural characteristics of the specific hydrogels.

Good contact between GPEs and the electrodes is not only imperative to measure the GPE resistance precisely, it is also required for stable ZAB performance. For this measurement, GPEs were prepared flat and attached in coin cells using a cell holder and a spring clip to apply pressure (Figure S3.4). Since PAM has a higher stiffness in KOH solutions, it was more difficult to make good physical contact with the SS electrodes compared with PVA and PAA. However, according to our model calculation, the interfacial resistance and charge transfer resistance for PAM6M are lower than those for the KOH solutions (further discussed in Section 3.3.3), which suggests that electrochemical contact was established for PAM during the conductivity measurements. Moreover, different aspects of hydrogel structures including molecular weight, hydrophilicity and microstructure also affect ionic conductivity. For example, low molecular weight PVA has a higher conductivity than high molecular weight PVA, with similar compositions (15% w/v) (Figure S3.5). Since the internal structure and chemical homogeneity of the thermoinitiated PAM in this study is unknown at this time, the reasons leading to low conductivity of PAM require further study.

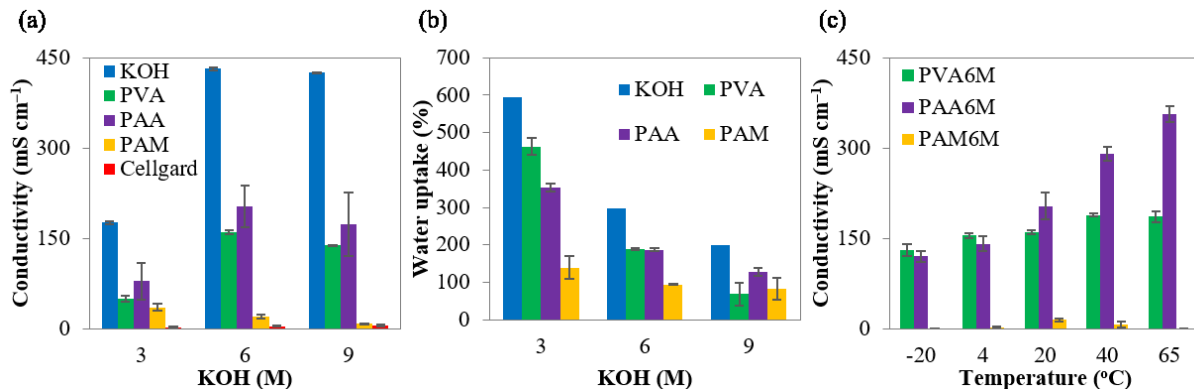


Figure 3.7. (a) Ionic conductivities of aqueous solutions, hydrogels and a commercial separator (Cellgard) at different KOH concentrations. (b) Water content in KOH solutions and GPEs. (c) Conductivities of GPEs in 6 M KOH at different temperatures. Each data point represents an average of 5 measurements and the error bars correspond to one standard deviation.

For long-term use of ZABs, even at room temperature, electrolyte leakage and water evaporation are major problems associated with aqueous electrolytes. Similarly, the conductivity of GPEs gradually decreases over time due to dehydration. Measurements of ionic conductivities when GPEs are exposed to various temperatures may elucidate the water retention capability of GPEs with alkaline solutions in their networks. Each GPE with 6 M KOH was encapsulated in a coin cell and put in a refrigerator/oven for 1 h to allow the sample to reach thermal equilibrium. The conductivity was then immediately measured using EIS. Figure 3.7c shows that at  $-20$  and  $4$  °C, the conductivities of all GPEs are lower relative to the values at room temperature, due to increased viscosity. However, as the temperature is increased from  $20$  °C, the conductivities behave differently. In fact, at temperatures higher than  $20$  °C, two phenomena compete with each other. One phenomenon is a reduction in viscosity, which should favor higher conductivity, and the other is water evaporation, which should hinder conductivity. Among the three GPEs, only PAA6M shows an increase in ionic conductivity over the full temperature range studied. The conductivity for PVA6M increases to  $40$  °C and then levels off. These results are in agreement with the CV tests that show that PAA6M is the most hydrophilic hydrogel among the three

hydrogels, so there should be less loss of water due to evaporation. It has been reported that adding carboxymethyl cellulose can enhance water retention in PVA [155]; however, using additives increases the complexity of the system and additives may induce other side effects. As previously mentioned, PVA also degrades at high temperature; PVA changes color to brownish yellow after EIS testing at 65 °C (Figure S3.6).

### 3.3.3. Performance of Zn-air battery

Discharge profiles for ZABs are shown in Figure 3.8a. At low current densities (2 and 5 mA cm<sup>-2</sup>), ZABs using PVA6M and PAA6M as the electrolyte exhibit similar performance to a ZAB using aqueous alkaline electrolyte. At higher current densities (10 and 20 mA cm<sup>-2</sup>), ZABs with PVA6M and PAA6M have higher discharge potentials compared with the ZAB with 6 M KOH solution. The poorer performance at higher current densities for the liquid electrolyte can be attributed to leaking of the air electrode. With the support provided by the hydrogel, both flooding and detachment of catalysts can be minimized. PAM6M had the worst performance at all current densities. In addition, ZABs using PAM6M were not able to sustain operation at current densities  $\geq 20$  mA cm<sup>-2</sup>. The lower discharge potentials relative to the other two GPEs is due to PAM's low electrolyte content and high internal resistance as previously discussed and shown in Figure 3.7.

Cycling tests were run at a current density of 0.5 mA cm<sup>-2</sup> for the three GPEs and aqueous KOH. In addition, discharge-charge efficiencies were calculated from the second cycle of the discharge-charge profiles (Figure 3.8b), giving values of 72%, 70%, 79% and 66% for ZABs using 6 M KOH, PVA6M, PAA6M and PAM6M, respectively. PAM6M, as expected from the results in Figure 3.8a, had the worst performance and failed after 4 cycles. Water loss contributed to the low efficiency and rapid failure of PAM6M, since water is consumed at the air electrode along with oxygen gas to produce hydroxide ions during discharge ( $O_2 + 2H_2O + 4e^- = 4OH^-$ ). ZABs

using PVA6M and PAA6M as the electrolyte had similar efficiencies for the second cycle to the ZAB using aqueous KOH; in fact, the efficiency for the PAA6M electrolyte was better. ZABs, with 6 M KOH, PVA6M and PAA6M as the electrolytes, cycled longer than the battery with PAM6M and failed, respectively, after 18, 24 and 25 cycles.

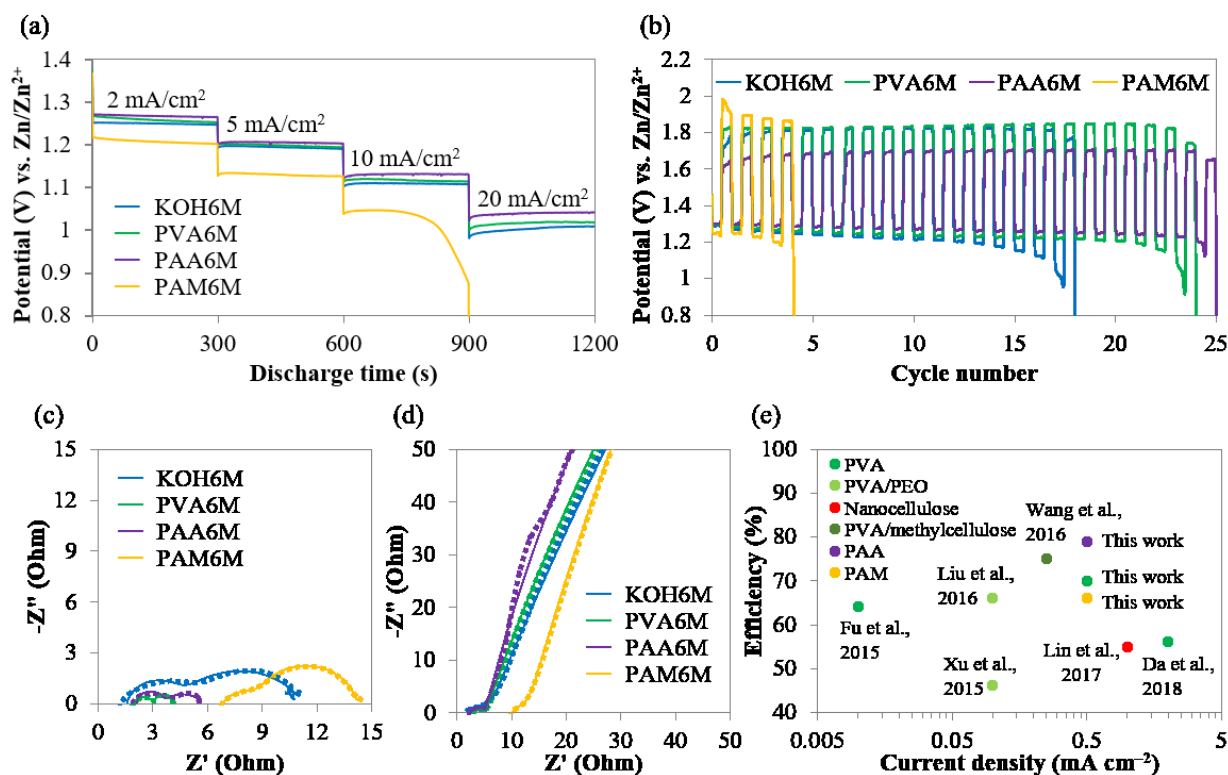


Figure 3.8. (a) Discharge curves for ZABs at various current densities with different electrolytes. (b) Discharge-charge cycling tests at  $0.5 \text{ mA cm}^{-2}$ . EIS plots at  $1.2 \text{ V vs. Zn/Zn}^{2+}$  before (c) and after (d) cycling tests. Symbols represent the measured data and solid lines represent the best fit using the equivalent circuit shown in Figure S3.1b. (e) Discharge-charge efficiency vs. current density ( $1^{\text{st}}$  cycle) for ZABs using GPEs.

EIS measurements were conducted at  $1.2 \text{ V}$  before and after cycling (Figure 3.8 c and d) to help better understand limiting factors during the discharge process. The two semicircles in the Nyquist plots were fit to an equivalent circuit (Figure S3.1b) and the corresponding resistances are listed in Table 3.2.  $R_b$ ,  $R_{\text{int}}$  and  $R_{\text{ct}}$  represent the bulk resistance, the electrode-electrolyte interfacial resistance and the charge transfer resistance, respectively. Among the three resistances, the

interfacial values are particularly important to quantify GPEs, since GPEs generally have poorer wettability than aqueous solutions which can lead to poor electrode contact [12]. Somewhat unexpectedly, the interfacial and charge transfer resistances for all GPEs are lower than those for the KOH solutions (Figure 3.8c and Table 3.2 –  $R_{ct}$  values of 1.07  $\Omega$ , 1.40  $\Omega$  and 5.49  $\Omega$  for PVA6M, PAA6M and PAM6M, respectively, compared with 6.91  $\Omega$  for KOH). A possible explanation is related to electrolyte-air electrode contact. A major problem for aqueous cell system (without a GPE) is flooding, leading to  $K_2CO_3$  precipitation and electrolyte evaporation. As a result, the GDL used in ZABs is often treated with PTFE to reduce electrolyte flooding [156, 157]. As discussed in the Section 3.2.5, the catalyst ink consisted of 0.2 mL of 10 wt% PTFE binder in this study. However, PTFE can also inhibit contact between the aqueous solution and catalysts, thereby increasing the interfacial resistance. During charging, oxygen bubbles that form may increase the amount of electrolyte leaking through the rims of coin cells, resulting in reduced cyclability. One of the merits of using a GPE is that the flooding problem is inherently prevented because liquid components are contained in the hygroscopic polymeric network. In addition, the air electrode catalysts need to be accessed by both electrons and ions to catalyze ORR and OER. Therefore, with the physical support that a GPE provides, both interfacial and charge transfer resistance may be reduced by using GPEs.

Generally, lower total resistance translates into higher discharge voltages. The total resistance values for PVA6M and PAA6M vary from 4 – 6  $\Omega$ , which are lower than the values for KOH solution (~11  $\Omega$ ) and PAM6M (~14  $\Omega$ ). Figure 3.8d also demonstrates that the short cycle life of the battery is due to a significant increase in charge transfer resistance. Even though all resistance values increase,  $R_{ct}$  increased by more than two orders of magnitude from 1 – 7  $\Omega$  to 700 – 1000  $\Omega$ , which caused a drop to the cut-off voltage. Since  $R_{ct}$  is directly related to the air

electrode, the large change in  $R_{ct}$  is likely due to water loss/evaporation and degradation of the Ru and Pt catalysts. In fact, the cycle lifetimes in this study are comparable with some other reports using Pt/C and  $RuO_2$  catalysts for air electrodes and aqueous alkaline solutions as the electrolytes [158, 159]. Both Pt/C and  $RuO_2$  are typically used as benchmark catalysts, when studying other potential candidates. Platinum is an efficient ORR catalyst, while  $RuO_2$  has very good OER activity. Both catalysts are expensive and tend to degrade on cycling; e.g., Pt oxidizes during OER and agglomerates over time leading to reduced performance [156].

Table 3.2. Fitting of EIS results before and after cycling tests

Electrolytes	Before			After		
	$R_b$ ( $\Omega$ )	$R_{int}$ ( $\Omega$ )	$R_{ct}$ ( $\Omega$ )	$R_b$ ( $\Omega$ )	$R_{int}$ ( $\Omega$ )	$R_{ct}$ ( $\Omega$ )
KOH6M	1.53	2.85	6.91	1.79	3.97	1285
PVA6M	1.99	1.04	1.07	3.20	1.97	950.1
PAA6M	2.09	2.30	1.40	2.38	2.65	693.6
PAM6M	6.79	2.00	5.49	10.04	3.05	1010

GPEs have been far less studied compared with electrode materials, even though the matrix materials for electrolytes play a key role in transporting hydroxide ions between the cathode and anode. Results from recent studies for rechargeable ZABs using GPEs, such as PVA [72, 160], PVA/PEO [73, 161], PVA/methylcellulose [162] or nanocellulose [93], are shown in Figure 3.8e as well as results from this study. The GPEs from this work perform well when compared with literature results; however, direct comparisons are difficult to make since tests done in the literature were not done under the same operating conditions nor are different GPEs compared in the same study. This study compares the performance of three GPEs with the same catalyst and electrode materials, so that performance can be directly compared. PAA has the best performance, both during initial cycling and for the limited number of cycles tested.

ZABs have been reported to withstand at least 100 cycles using aqueous electrolytes, but the cyclability of ZABs using GPEs tends to be rather low. For instance, ZABs using PVA/PEO can withstand 20 to 60 cycles at  $0.1 \text{ mA cm}^{-2}$  [73, 161], while Liu et al. reported that ZABs using PVA exhibited stable discharge-charge at  $2 \text{ mA cm}^{-2}$  for 48 cycles [160]. While it is unclear if the reported lower cyclability values are associated with using GPEs, it should be noted that cycling behavior may be improved through the use of alternative catalyst materials and battery designs (e.g., a battery with better sealing or a tri-electrode configuration where the OER and ORR electrodes are separated) [103].

### 3.4. Conclusions

Three different hydrogels were investigated, based on their ionic conductivities, chemical stability, electrochemical windows and mechanical properties, for application as electrolytes in rechargeable ZABs. PVA, PAA and PAM are chemically stable in 6 M concentration alkaline solutions; upon removal of water, the gel polymer electrolytes (GPEs) have a stable electrochemical window of 2 V, which is sufficient for ZAB applications. In addition, PAA with 6 M KOH has the highest conductivity with its conductivity increasing with increasing temperature. This behavior is most likely due to PAA6M's high hydrophilicity. Roughly speaking, there is an inverse proportionality between ionic conductivity and mechanical stiffness. Specifically, at  $20 \text{ }^\circ\text{C}$ , the conductivities of PVA, PAA and PAM with 6 M KOH were 161, 204 and  $21 \text{ mS cm}^{-1}$  while their compressive moduli were 30.9, 5.4 and 2704.4 kPa, respectively.

During full cell testing, it was shown that GPEs can be beneficial to ZAB performance by reducing interfacial and charge transfer resistance. A battery with PAM6M as the electrolyte failed after several cycles, whereas batteries with PVA6M or PAA6M as the electrolyte outperformed batteries with conventional aqueous 6M KOH in terms of cycling number. The battery with

PAA6M electrolyte had the highest initial discharge-charge efficiency of 79% at  $0.5 \text{ mA cm}^{-2}$ . The performance could be enhanced by reducing the GPE thickness, which will decrease bulk resistance.

### 3.5. Supporting information

Figure S3.1a shows a series circuit consisting of GPE resistance ( $R_b$ ), a constant phase element ( $Q$ ) and a Warburg element ( $W$ ).  $Q$  was used instead of the double layer capacitance to represent an imperfect capacitor caused by surface roughness of the Zn electrode and varying pore size distribution within the air electrode.  $W$  represents the impedance caused by the diffusion process. In full cell testing, the equivalent circuit includes GPE resistance ( $R_b$ ), interfacial resistance ( $R_{int}$ ), charge transfer resistance ( $R_{ct}$ ) and interfacial and double layer characteristic constant phase elements ( $Q_{int}$  and  $Q_{dl}$ ) [12] (Figure S3.1b).

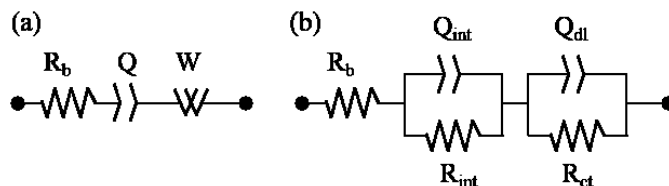


Figure S3.1. Two equivalent circuits for fitting of EIS data: (a) Ionic conductivity measurements and (b) full cell testing.

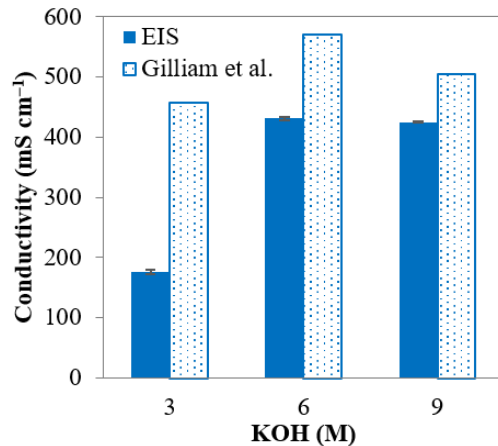


Figure S3.2. Ionic conductivity of KOH solutions measured by EIS compared with calculated data at 20 °C [153].

PAA1 was synthesized from AA monomers with KOH present in the solutions, while PAA2 is PAA that was fully immersed in 3, 6 and 9 M KOH solutions. Both water uptake and conductivity for PAA2 were higher than the corresponding values for PAA1 (Figure S3.3a–b). At 6 M KOH, the conductivity of PAA1 was about 1.3 times lower; however, its compressive modulus was 5 times larger than that for PAA2 (Figure S3.3c). This behavior for the mechanical properties and ionic conductivity is attributed to the amount of aqueous solution retained in the polymer network. More solution retained in the network leads to a higher conductivity, but reduced mechanical strength [163].

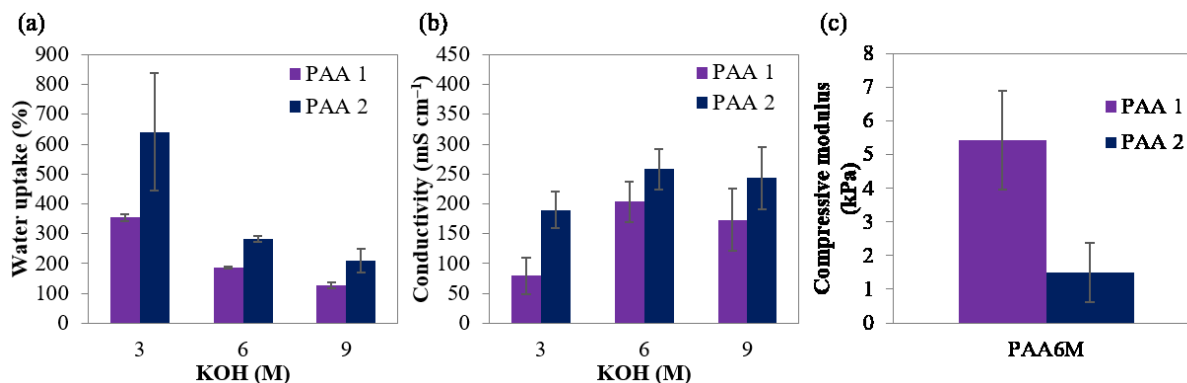


Figure S3.3. (a) Water uptake of PAA at different concentrations of KOH. (b) Conductivity of PAA. (c) Compressive modulus for two PAA6M samples.



Figure S3.4. Coin cell setup for EIS measurement.

PVA samples with high molecular weight (HW) ( $M_w = 146\,000 - 186\,000\text{ g mol}^{-1}$ ) and low molecular weight (LW) ( $M_w = 31\,000 - 50\,000\text{ g mol}^{-1}$ ) were prepared as discussed in the Experimental Procedure. The PVA samples were dialyzed in 6 M KOH solution prior to EIS measurement.

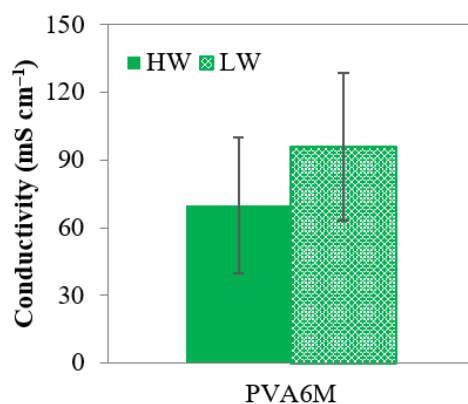


Figure S3.5. Conductivities of PVA6M with different molecular weights.



Figure S3.6. PVA6M after EIS measurements at 65 °C.

## Chapter 4. A Tri-Electrode Configuration for Zinc-air Batteries Using Gel Polymer Electrolytes

A version of this chapter has been submitted as:

Tran, T.N.T., Xiong, M., Clark, M.P., Chung, H.-J. and Ivey, D.G., *A Tri-Electrode Configuration for Zinc-Air Batteries Using Gel Polymer Electrolytes*. 2020.

### 4.1. Introduction

Many start-up companies, such as ZAF Energy Systems, Zinc8 Energy Solutions and NantEnergy, have focused on Zn-air batteries (ZABs), instead of lithium-ion and lead-acid batteries, to create a safer, cheaper and more environmentally friendly alternative for future energy storage. Beginning in 2018, remote villages in Africa and Asia have been receiving electricity from ZABs that can store energy from the sun using solar panels [164]. Primary ZABs are a mature technology with a high energy density ( $6136 \text{ Wh L}^{-1}$ ) and low cost; however, rechargeable ZABs have not enjoyed the same commercial success, mostly because of technical difficulties related to the development of suitable bifunctional oxygen catalysts, a unique Zn electrode design and an advanced electrolyte [12]. Aqueous potassium hydroxide solution (KOH) has become the standard electrolyte for ZABs due to its high ionic conductivity and low viscosity [124], but flooding, water evaporation and carbonate precipitation are the three major hurdles associated with the use of the aqueous electrolyte [2]. As a result, the gas diffusion layer (GDL) at the air electrode is often treated with polytetrafluoroethylene (PTFE) to reduce electrolyte flooding [157, 165]. Unfortunately, PTFE can also hinder contact between the electrolyte and catalysts, thereby increasing the interfacial resistance. In addition, the air electrode catalysts need to be accessed by

both electrons and ions for the oxygen reduction reaction (ORR) and oxygen evolution reaction (OER). We have recently found that gel polymer electrolytes (GPEs) can provide physical support to aid in reducing both interfacial and charge transfer resistance [166]. In addition, the use of GPEs can reduce dendrite formation at the Zn electrode without using a separator [167]. As such, many issues with the air and Zn electrodes can be readily alleviated through the use of GPEs.

To date, low cycle life has hindered the development of a rechargeable ZAB for applications in electronic devices, electric vehicles and grid energy storage. As shown in Table 1, ZABs using aqueous electrolytes have been reported to withstand hundreds of cycles. For example, 270 cycles have been reported for a battery, with an Ag/MnO<sub>2</sub> ORR/OER catalyst, operating at 5 mA cm<sup>-2</sup> with a low initial efficiency of 42% [168]. However, recent studies using improved bifunctional ORR/OER catalysts exhibit very good performance for ZABs (with an aqueous KOH electrolyte) at a higher current density of 20 mA cm<sup>-2</sup> with remarkable initial cycling efficiency of 62% [169]. On the other hand, ZABs employing GPEs have poorer cyclability and current densities compared with liquid electrolyte batteries (Table 4.1). For example, Fu et al. report that ZABs using poly(vinyl alcohol) (PVA) displayed the longest cycle life with 120 cycles at a very low current density of 0.01 mA cm<sup>-2</sup> [72]. There is a tradeoff between current density and cyclability. PVA/poly(ethylene oxide) (PEO) can withstand only 30 – 60 cycles for current densities ranging from 0.05 – 0.1 mA cm<sup>-2</sup> [73, 161], while Liu et al. report that ZABs using PVA showed stable discharge-charge at 2 mA cm<sup>-2</sup> for only 48 cycles [160]. It is also notable that most of the recent reports have only chosen PVA as the gel polymer matrix. The major motivation for using GPEs for ZABs has almost exclusively been for wearable electronics applications in stretchable format. To our knowledge, the use of GPEs for ZABs in grid energy storage has not been discussed and there are no studies dedicated to improving the cycle life of ZABs using GPEs.

In Chapter 3, ZABs with poly(acrylic acid) (PAA) showed potential to outperform batteries with PVA or conventional aqueous 6 M KOH electrolytes in terms of cycling stability [166].

Table 4.1. Comparison of recent rechargeable ZABs

Bifunctional catalyst	Electrolyte	Current density (mA cm <sup>-2</sup> )	Cycle number	Cycling efficiency (%)	Ref.
LaNiO <sub>3</sub> /NCNT	6 M KOH	17.6	75	43	[170]
MnO <sub>2</sub> /Co <sub>3</sub> O <sub>4</sub>	6 M KOH	15	60	55	[171]
Ag/MnO <sub>2</sub>	6 M KOH	5	270	42	[168]
Fe <sub>3</sub> C/Fe <sub>2</sub> O <sub>3</sub> @NGNs	6 M KOH	10	120	56	[172]
Cu <sub>97</sub> P <sub>3-x-y</sub> O <sub>x</sub> N <sub>y</sub> /NPC	6 M KOH	20	200	62	[169]
LaNiO <sub>3</sub> /NCNT	PVA + 6 M KOH	0.01	120	64	[72]
RuO <sub>2</sub> /CNT	PVA/PEO + 6 M KOH	0.05	30	53	[73]
RuO <sub>2</sub> /RGO	PVA/PEO + 6 M KOH	0.1	60	66	[161]
NCNFs	PVA + 6 M KOH	2	48	56	[160]
Co/Co <sub>3</sub> O <sub>4</sub> /3D-NC	PVA/methylcellulose + 6 M KOH	1	N/A	58	[162]

Fe<sub>3</sub>C/Fe<sub>2</sub>O<sub>3</sub>@NGNs: N-doped graphene wrapped Fe<sub>3</sub>C/Fe<sub>2</sub>O

NCNT: N-doped carbon nanotubes

NPC: N, P co-doped carbon

NCNFs: nanoporous carbon nanofiber films

3D-NC: 3D N-doped carbon

To increase the cyclability of ZABs, air electrode materials have been much more studied than either the Zn electrode or electrolytes. Catalysts with high activity towards OER can be adopted from water splitting research [173]; however, catalysts with high activity and stability towards both ORR and OER are difficult to synthesize. Manganese oxide (MnO<sub>x</sub>), which is the frequent choice for ORR catalysts, is not stable under the potentials where the battery is charged (~2 V) because it tends to be oxidized to MnO<sub>4</sub><sup>-</sup> according to the Pourbaix diagram [174].

Choosing a suitable material for the current collector is also challenging. During discharge, oxygen is consumed for the ORR which can only occur if a triple phase boundary is present; i.e.,

oxygen from the air (gas), the electrolyte (liquid) and the catalyst (solid) are in contact. Thus, a Teflon-treated GDL with high surface area is desirable because it allows both air and the liquid electrolyte to penetrate. However, during charging, oxygen is not consumed but evolved from the electrode. Therefore, the OER occurs at a two-phase interface between a liquid (electrolyte) and a solid (catalyst). The GDL structure is not ideal for charging as the escaping oxygen can cause corrosion of carbon and mechanical breakdown of the catalysts [175, 176]. In addition, since the surface concentration of the reactant ( $\text{OH}^-$ ) for the OER is much higher than the oxygen concentration for the ORR, Ni foam which does not require a very high surface area can be a much better current collector than the porous GDL since it has high conductivity and is stable in alkaline solutions.

Developing a tri-electrode configuration in which the air electrode is separated into discharge and charge electrodes can be effective in extending ZAB cycle life, since both air electrodes can be optimized for their specific purpose. In fact, the instability of bifunctional catalysts, which are used to catalyze both ORR and OER, compared with decoupled catalysts has been well documented. For example, in a half cell test at  $100 \text{ mA cm}^{-2}$ , the performance of a commercial  $\text{MnOx}$  electrode showed almost no activity after 10 cycles, while a bi-air-electrode system with  $\text{MnOx}$  (ORR) and stainless steel grid (OER) electrodes displayed little degradation even after 500 cycles [97]. Moreover, deposition of two catalysts on the same substrate to make the electrode bifunctional may cause negative effects on the individual catalytic activity [171]. Adding another metal mesh as the OER electrode does not significantly increase the weight of the battery, while it provides improved performance (Figure S4.1). There have been several reports on ZABs using a tri-electrode configuration [97-103]; however, to the best of our knowledge, there has been no report on tri-electrode systems using GPEs.

In this study, two tri-electrode battery designs, with GPEs (PAA), are proposed to improve ZAB cycle life at an operational current density at  $5 \text{ mA cm}^{-2}$ . Various additives for the GPEs, such as a crosslinking agent and ZnO, are evaluated using the tri-electrode design. Decoupled air electrodes also allow the study of the effects of ZnO on the ORR and OER separately. Mechanisms for the observed phenomena are proposed.

## 4.2. Experimental procedure

### 4.2.1 Synthesis of catalysts

All chemicals were used as received without further purification. Manganese(II) acetate, L-ascorbic acid and sodium dodecyl sulfate (SDS) were purchased from Sigma-Aldrich, while sodium acetate, cobalt(II) sulfate, sodium citrate and boric acid were purchased from Fisher. Iron(II) sulfate was purchased from MP Biomedicals. Deionized water (DIW) was used for all aqueous solution preparation and rinsing.

MnOx on a GDL was utilized as the ORR electrode and bare Ni foam or CoFe on Ni foam was used as the OER electrode. The morphology of the catalysts is shown in Figure S4.2; more details concerning fabrication and characterization of the catalysts can be found in reference [103]. Briefly, electrodeposition of ORR and OER catalysts was performed in a two-electrode cell where GDL and Pt mesh, respectively, were used as the working electrode and the counter electrode. The solution for ORR deposition contained 0.02 M manganese(II) acetate, 0.02 M sodium acetate and  $100 \text{ mg L}^{-1}$  SDS. GDL (Teflon-coated porous carbon paper, SGL 35DC), sectioned into  $5 \text{ cm}^2$  pieces, was used as the substrate for anodic electrodeposition at  $40 \text{ }^\circ\text{C}$ . Pulse electrodeposition at a current density of  $1.2 \text{ mA cm}^{-2}$  was applied for 2400 cycles with 0.25 s on and 0.5 s off per cycle. Samples were rinsed with DIW after deposition and then dried in an oven at  $300 \text{ }^\circ\text{C}$  for 30 min. The solution for OER deposition contained 0.15 M cobalt(II) sulfate, 0.05 M iron(II) sulfate, 0.2

M sodium citrate, 0.2 M boric acid, 0.05 M l-ascorbic acid and 400 mg L<sup>-1</sup> SDS. Ni foam (4 cm<sup>2</sup> pieces) was used as the substrate for cathodic electrodeposition at 40 °C and was cleaned by rinsing with acetone, isopropanol and DIW prior to the deposition. Galvanostatic electrodeposition at a current density of 30 mA cm<sup>-2</sup> was applied for 10 min. Samples were rinsed with DIW afterwards and then dried in air.

#### **4.2.2. Synthesis of gel polymer electrolytes (GPEs)**

Poly(acrylic acid) (PAA) was used as the GPE in this work. Acrylic acid (AA), N,N'-methylenebis(acrylamide) (MBAA) and potassium persulfate (KPS) were purchased from Sigma-Aldrich, while zinc oxide (ZnO) and potassium hydroxide (KOH) were purchased from Fisher. All chemicals were analytical grade and used as received without further purification. GPEs were prepared by mixing AA monomer (1.5 M), MBAA crosslinker (0.1, 0.3, 0.5, 0.7 or 0.9 mol% of total monomers) and KPS thermoinitiator (0.1 mol% of total monomers) in 7.5 M of KOH solution. To make GPEs with ZnO additive, 0.25 M of ZnO was added to the precursor solution. The electrolyte solutions were kept in an oven at 60 °C for 1 h to carry out polymerization.

#### **4.2.3. Cell fabrication**

Two configurations for the tri-electrode ZAB were designed and fabricated and are shown in Figure 4.1. For the planar cell, the ORR electrode and the OER electrode are positioned on the same plane, with the Zn electrode below. The sandwich cell consists of three electrode layers with the ORR electrode on top, the OER electrode on the bottom and a Zn electrode sandwiched between them. The three electrodes were assembled to form a cell through a frame of acrylic sheets. The distance from the Zn electrode to the ORR and OER electrodes was kept at 3 mm. In order to compare the effects of different configurations on battery performance, the total volume for the GPE was fixed at 3 mL, the total mass of Zn used was ~1 g (thickness = 0.2 mm) and

polypropylene film (thickness = 0.3 mm) was used to control the contact area between both air electrodes and the GPE (1 cm<sup>2</sup>). Nickel plate (thickness = 0.5 mm) was used as the current collector for the ORR electrode. The cell components were enclosed with screws and wing nuts and the edges were wrapped with parafilm to prevent drying out of the GPE.

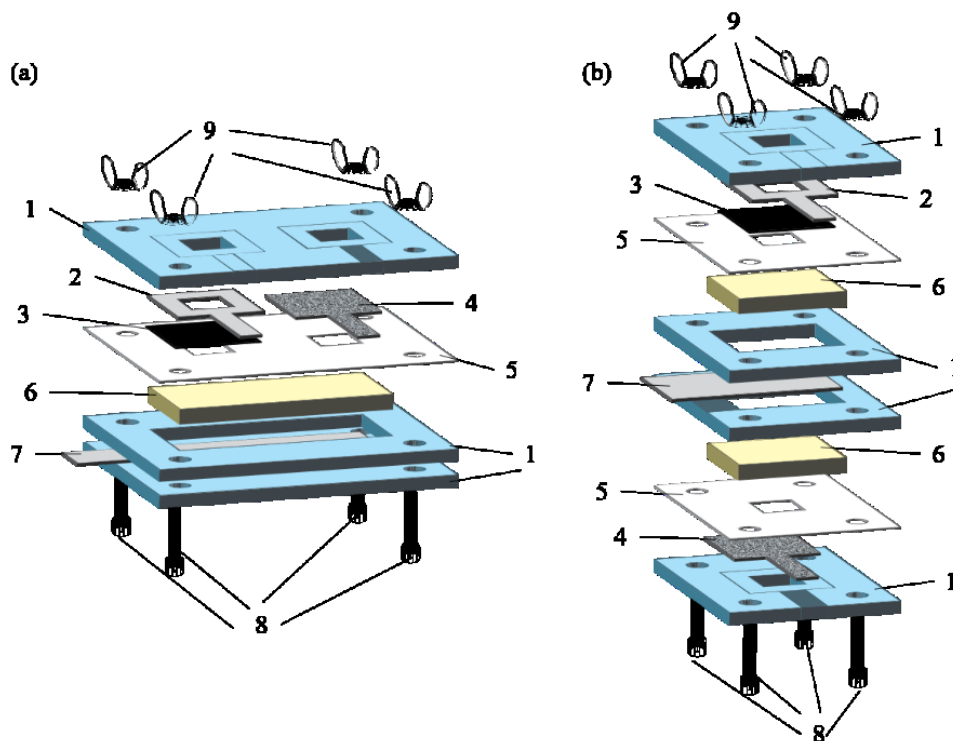


Figure 4.1. Tri-electrode cell assembly: (a) planar and (b) sandwich configurations. 1) Acrylic sheets, 2) current collector, 3) GDL, 4) Ni foam, 5) polypropylene film, 6) GPE, 7) Zn, 8) bolts, 9) nuts.

#### 4.2.4. Material characterization

The microstructure of the catalysts was observed by field emission scanning electron microscopy (Zeiss Sigma FESEM). Electrochemical measurements were carried out with a potentiostat/galvanostat (Autolab PGSTAT302N). The GPEs were enclosed within a stainless steel (SS) coin cell (CR2032 MTI Corporation) and their conductivities were measured by electrochemical impedance spectroscopy (EIS) at open circuit potential with 10 mV AC potential

from 100 kHz to 10 mHz. Mechanical strength was characterized by a rheometer (Kinexus lab+). An amplitude sweep from 0.1 – 100% strain at 1 Hz was measured. GPEs were immersed in 1 M HCl and then rinsed with DIW three times before freeze-drying. Then, freeze-dried samples were chemically characterized by Fourier transform infrared spectroscopy (Thermo Scientific Nicolet iS50 FTIR). Sixty-four scans with a resolution of  $4\text{ cm}^{-1}$  were averaged to obtain each spectrum.

#### **4.2.5. Battery testing**

Full cell testing was mainly done with MnOx catalyst electrodeposited on GDL and Ni foam as the ORR and OER electrodes, respectively, and Zn foil (99% Zn, 0.2-mm thick). However, Ni foam was replaced by CoFe electrodeposited on Ni foam to act as the OER electrode in Section 4.3.4. For rate testing, the ORR electrode and the Zn electrode were connected during discharge, while the OER electrode and the Zn electrode were connected during charge. Battery potential was measured by a galvanostatic method at a series of current densities of 2, 5, 10 and  $20\text{ mA cm}^{-2}$  for 5 min each with a cut-off voltage of 0.8 V. Cycling tests were also done through a galvanostatic method with  $30\text{ min cycle}^{-1}$  with another potentiostat/galvanostat (Biologic VSP-300) which has three connections for the two air electrodes and the Zn electrode. The battery was discharged and charged at  $5\text{ mA cm}^{-2}$  for 10 min and the circuit was kept open for 5 min between steps. The discharge-charge efficiency was calculated by dividing the average discharge potential by the last charge potential during one cycle. Before and after cycling, EIS measurements were also performed with 10 mV AC potential from 100 kHz to 10 mHz at 1.2 and 1.9 V vs.  $\text{Zn/Zn}^{2+}$  to reveal bulk, interfacial and charge transfer resistance during discharge and charge, respectively.

## 4.3. Results and discussion

### 4.3.1. Battery configuration

One of the benefits of using GPEs is that the leaking problem associated with aqueous electrolytes is essentially avoided because the electrolyte is contained within the polymeric host. This helps facilitate cell design and assembly. In this study, the cells are made primarily of acrylic sheets with no gaskets required. Figure 4.2a and b show that the sandwich ZAB configuration outperformed the planar ZAB for both rate testing and cycle testing, exhibiting higher discharge potentials and lower charge potentials. After about 90 cycles, the planar ZAB failed by reaching the cut-off voltage (0.8 V), whereas the sandwich ZAB was still operational with a cycling efficiency of 48%.

The planar cell, with both air electrodes in the same plane and the Zn electrode below, requires fewer layers of acrylic sheets and allows for easy assembly; however, separation of the discharge and charge air electrodes led to preferential depletion and deposition regions for Zn [103]. As such, the Zn electrode had an uneven thickness after cycling. Specifically, the Zn surface close to the ORR side became thinner as Zn dissolution was favored during discharging. Likewise, the Zn surface near the OER electrode increased in thickness. In addition, the parasitic hydrogen evolution reaction (HER) is thermodynamically favored and a Zn electrode at rest will be corroded spontaneously. The Zn plate in the planar cell was removed and the difference in thickness after cycling is clearly visible, as is Zn corrosion on the backside (Figure 4.2c). Unlike sandwich cell, the GPE does not fully cover Zn in the planar cell. This results in higher current density on the Zn electrode and promotes the corrosion of Zn on the back ( $\text{Zn} + 2\text{H}_2\text{O} \rightarrow \text{Zn}(\text{OH})_2 + \text{H}_2\uparrow$ ), which leads to more charge losses and potentially dangerous hydrogen gas buildup [177]. Lee et al. found that HER overpotential is further reduced on a ZnO surface, which means that as more ZnO forms

on the back of the Zn electrode, the self-discharge rate will increase [178]. This could be a major issue for ZABs in flexible/wearable devices [72, 73, 160-162], where the GPE is positioned between the two electrodes with the backside of the Zn electrode exposed.

An alternative to the planar cell design is the sandwich cell. There are two sandwich configurations using aqueous electrolytes: (1) The ORR electrode and OER electrode are located on either side of the Zn electrode or (2) the Zn electrode and ORR electrode are located on either side of the OER electrode. In the second case, the ZAB readily accumulates gas bubbles, resulting in shape change and battery leakage [175]. Thus, a sandwich assembly where the ORR electrode and OER electrode are located on either side of the Zn electrode is considered to be more suitable for ZABs, especially those using GPEs, to prevent both the corrosion of Zn and O<sub>2</sub> gas bubble accumulation (Figure 4.2d). This design is used as the main tri-electrode design in the latter part of the study.

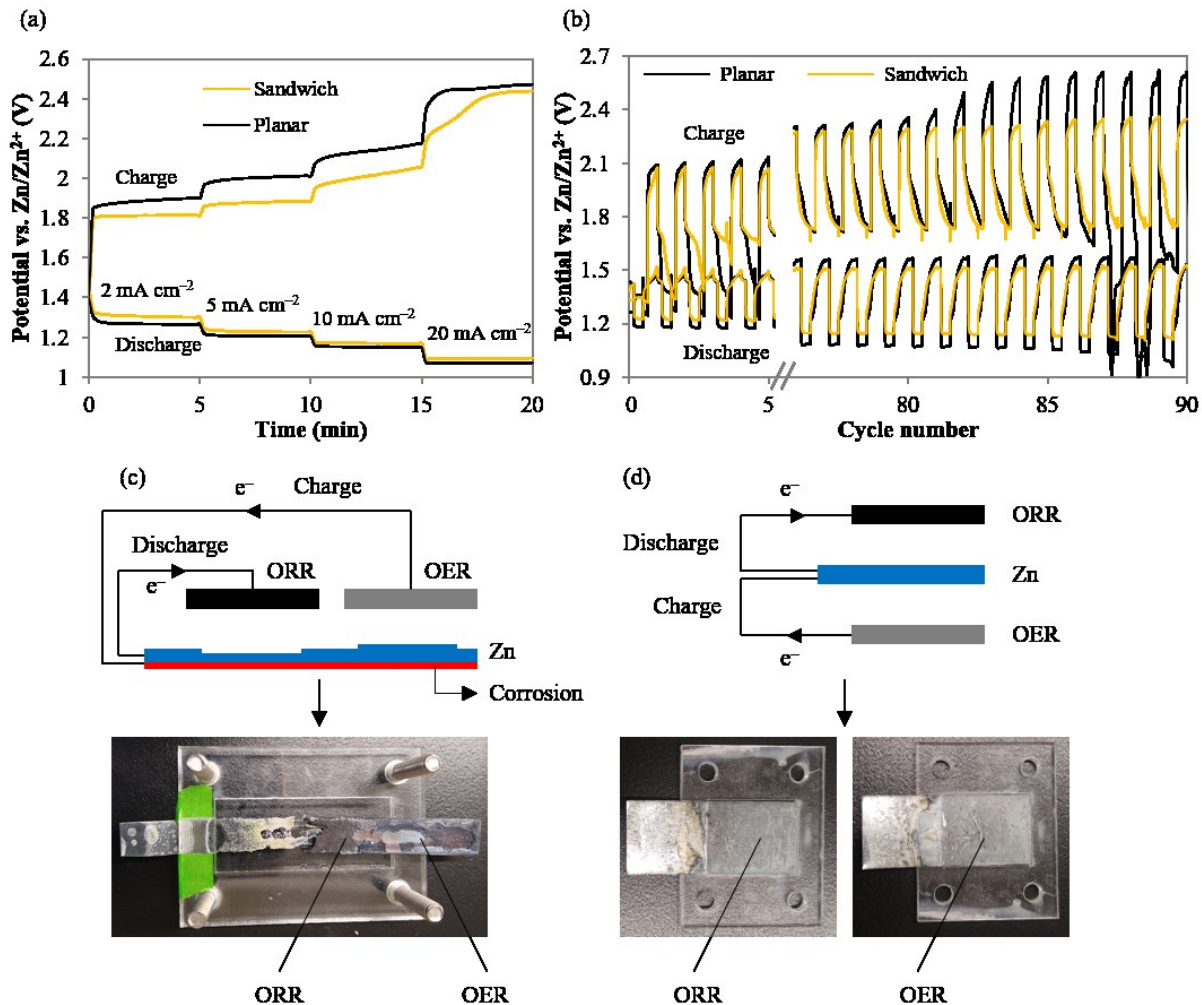


Figure 4.2. Electrochemical evaluation of Zn-air batteries with different configurations, i.e., planar and sandwich. (a) Rate discharge-charge curves and (b) cycling performance at 5 mA cm<sup>-2</sup>. Comparison of the effects of cell configuration on the Zn electrode after cycling tests for the (c) planar cell and (d) sandwich cell.

#### 4.3.2. Effect of crosslinking density

The synthesis condition for the PAA hydrogel GPE was optimized for use in ZABs. Previous studies on synthesizing alkaline PAA as the GPE in Ni/metal hydride cells, Al-air batteries and ZABs did not describe in detail the compositions of monomeric units or additives that make up the polymeric component [75, 179-181]. Specifically, crosslinking density, which is related to the molecular weight between the crosslinks, is an important parameter because it

significantly affects the physical properties of the gels [182]. The ratio of  $G''$  (loss modulus) to  $G'$  (storage modulus), determined in rheology testing, can be used to indicate how solid-like or liquid-like a system is. Conventionally, the ratio is expressed as *Equation 4.1*:

$$\tan(\delta) = \frac{G''}{G'} \quad \text{Equation 4.1}$$

where  $\tan(\delta)$  quantifies the balance between lost and stored energies. When the phase angle  $\delta$  ranges between  $45^\circ$  and  $90^\circ$ , the system is considered to be in the sol state (*i.e.*, liquid-like). Thus, Figure 4.3a shows that the mixture remains in sol form when 0.1 mol% MBAA is added ( $\delta = 58^\circ$ ). When the MBAA content is 0.3 mol% and above, the resulting gel is identified to be in a gel state (*i.e.*, solid-like). As MBAA concentration increases from 0.3 to 0.9 mol%,  $\delta$  decreases from  $34^\circ$  to  $17^\circ$ . The increased storage modulus ratio is consistent with the decreased molecular weight of PAA chains between the crosslinkers, which renders the hydrogel to be stiffer with increasing MBAA concentration.

The discharge-charge rate tests in Figure 4.3b show that MBAA content greatly influences charge potential, but has negligible effect on discharge potential. For current densities from 2 to  $10 \text{ mA cm}^{-2}$ , the charge potential decreases with increasing MBAA content. For lower amounts of MBAA, PAA is easily squeezed through the Ni foam, providing more contact with the OER electrode resulting in charging at lower potentials. However, at  $20 \text{ mA cm}^{-2}$  the charge potentials decrease as the amount of MBAA is increased from 0.1 mol% to 0.5 mol%. There have been several reports showing that oxygen bubbles evolving from the electrolyte can adhere to the charging electrode surface and reduce the conductivity of the electrolyte [183-185]. Figure 4.3c and d show the electrical resistance of the ZAB before and after discharge (at 1.2 V) and charge (at 1.9 V) rate testing, respectively. The data was taken from Figure S4.3 using Zsimpwin software. In general, the total resistance of the battery during discharging ( $13 - 20 \Omega$  after rate testing) was

less affected by the crosslinking density than charging ( $22 - 50 \Omega$  after rate testing). The bulk resistance or the resistance of the PAA ( $R_b$ ) is about 1 to  $1.5 \Omega$  and contributes the least to the overall battery resistance, while the charge transfer resistance ( $R_{ct}$ ) has a much more pronounced effect. Moreover, as shown in Figure 4.3d, after rate testing at 1.9 V there is an obvious increase in interfacial resistance ( $R_{int}$ ) indicating oxygen bubble coalescence. In fact, PAA with 0.3 mol% MBAA has been pushed through the Ni foam by oxygen bubbles during cycling (Figure S4.4). Therefore, efficient removal of oxygen bubbles during OER is important for improving charging performance. For aqueous electrolytes, a pump can be utilized to enhance electrolyte flow [186, 187] or electrode surface wettability can be modified [188, 189] to enhance removal of oxygen bubbles. These methods can eliminate bubble coalescence, but may cause catalyst loss and decrease the activity of the OER electrode. For GPEs, modifying the amount of crosslinking can be effective in controlling removal of bubbles. A schematic illustration of the effect of MBAA crosslinking density on PAA with low to high crosslinking density on Ni foam is shown in Figure 4.3e. The yellow dome in the first schematic represents PAA, with low crosslinking density, which penetrates the Ni foam and traps oxygen bubbles during OER. Increasing the amount of MBAA results in a stronger polymer network that is more difficult to push through the Ni foam (second schematic). For even higher crosslinking density (third schematic), the polymer cannot enter the Ni foam, so the contact area between electrolyte and catalyst is reduced. The optimal concentration of MBAA for PAA in the tri-electrode ZAB is 0.5 mol% monomers and this concentration is used for the latter part of the study. PAA with 0.5 mol% crosslinker has better contact with Ni foam than PAA with 0.7 or 0.9 mol% MBAA, while still allowing oxygen bubbles to escape.

It should be noted that the concentration of crosslinker partly depends on the characteristics of the Ni foam. A less porous structure will likely resist GPE penetration, although a more open

structure will facilitate water evaporation from the GPE. In addition, increasing the crosslinking density reduces GPE conductivity. Further study is needed to optimize the combination of GPE crosslinking density and Ni foam structure.

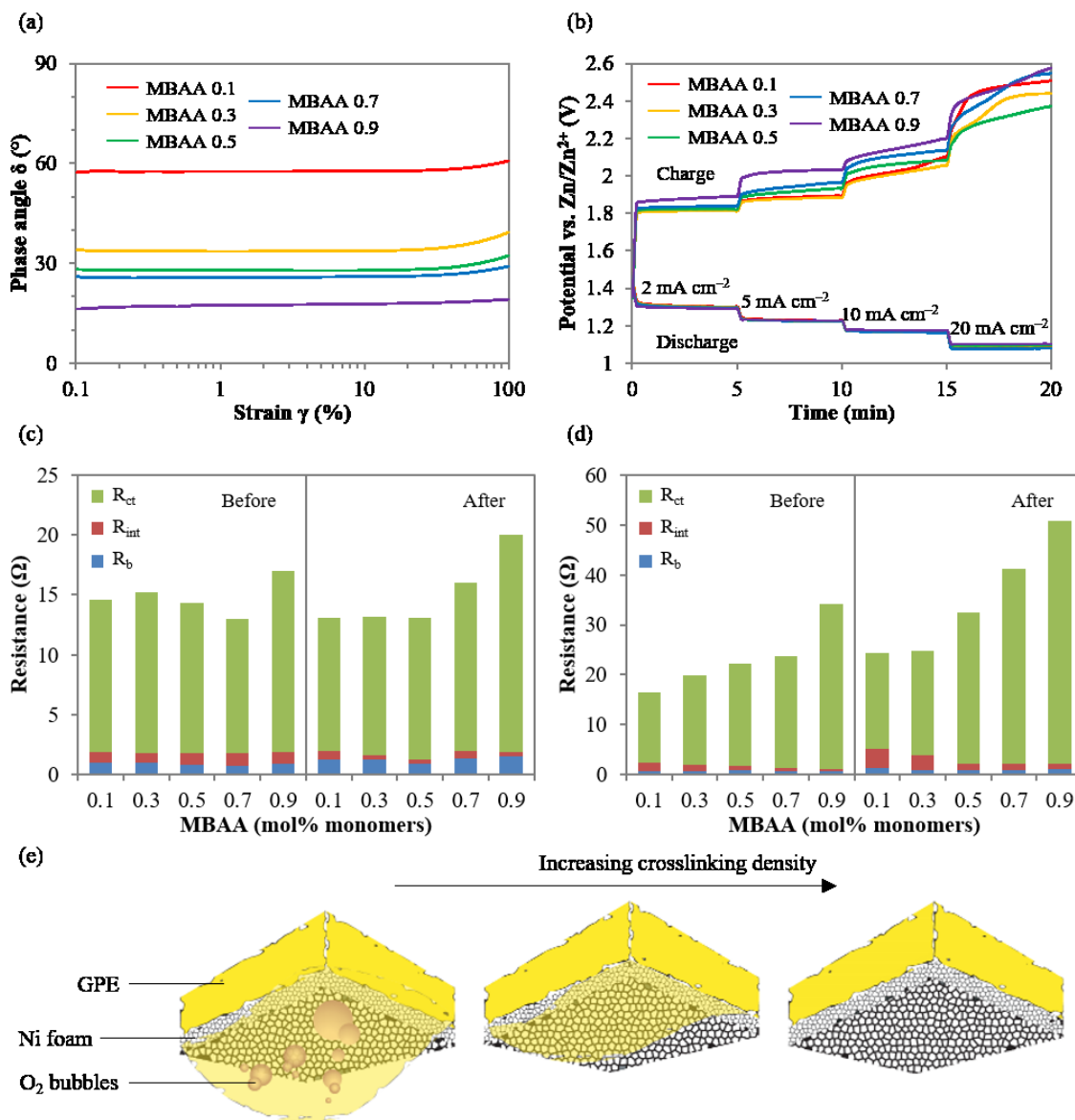
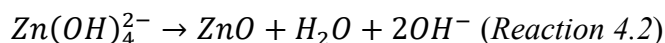
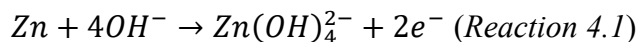


Figure 4.3. (a) Rheology measurements of GPEs with different crosslinking density. (b–d) Electrochemical evaluation of GPEs with different crosslinking density: b) Rate discharge-charge curves; (c,d) electrical resistance of ZABs before and after rate testing for (c) discharge at 1.2 V and (d) charge at 1.9 V. (e) Schematic illustration that describes the degree of penetration of GPEs into Ni foam and its effect on oxygen bubble trapping as a function of crosslinking density of the GPEs.

### 4.3.3. Effect of ZnO additive

During discharge, Zn electrode dissolution occurs in two steps. The first step is oxidation of Zn to zincate ions (*Reaction 4.1*) and then ZnO precipitation takes place when the dissolved zincate ions in solution reach saturation close to the surface (*Reaction 4.2*).



According to these reactions, adding ZnO can help to reduce Zn solubility, which subsequently minimizes any shape change and dendrite formation, and reduces the activity of water which also decreases the amount of hydrogen evolution (HER) [190]. Many investigators use aqueous alkaline electrolytes that are pre-saturated with zincate ions by dissolving ZnO powder [90, 191-194]. However, mitigating one problem can lead to another issue, as increasing zincate ion concentration near the Zn electrode surface can also lead to faster passivation due to increased amounts of precipitated ZnO [12]. In this work ZnO was added during the polymerization process. In order to confirm that there is no significant chemical alteration of polymeric host material, FTIR measurements were carried out. There were no detectable differences in the polymer material (Figure S4.5).

Batteries with alkaline PAA as the electrolyte, with and without ZnO added to both electrolytes (in contact with the OER and ORR electrodes), underwent rate testing (Figure 4.4a). Note that the electrolyte used in all battery tests was PAA with 0.5 mol% MBAA and 7.5 M KOH (denoted as GPE). Comparison of GPE and GPE with ZnO (both electrolytes) shows that GPE has better discharge performance at all current densities tested. The charge potential for GPE is also better at lower current densities, but is worse by 100 mV than GPE with ZnO (labeled as GPE+ZnO

on both sides) at  $20 \text{ mA cm}^{-2}$  (2.37 and 2.27 mV, respectively). In these tests, discharging was performed first, followed by charging.

OER rate testing was then done for electrolytes with and without ZnO added; the batteries were charged either directly (denoted as before discharge in Figure 4.4) or after initial discharge (denoted as after discharge). The GPE with added ZnO exhibits essentially the same behavior, whether the battery is discharged prior to the first charge or not (Figure 4.4b). However, if no ZnO is added to the electrolytes and the battery is discharged first, the OER potential is the lowest for all current densities, except for  $20 \text{ mA cm}^{-2}$ . Because discharge is performed before charging, *Reactions 4.1* and *4.2* readily occur and the discharge product accumulates near the Zn electrode surface. The product is then consumed during charging at current densities of 2 to  $10 \text{ mA cm}^{-2}$ . By the time the highest current density of  $20 \text{ mA cm}^{-2}$  is reached, the zincate ions become depleted, so that a higher OER is needed. When charging is done without prior discharge, the OER potentials are significantly higher, particularly at the highest current densities. Adding ZnO to the electrolyte ensures that the zincate ion concentration remains high enough to facilitate OER, whether or not the battery is discharged prior to charging. Thus, the incorporation of ZnO additives to the alkaline electrolyte system can improve secondary ZAB performance [52].

An attempt was made to evaluate the effects of ZnO added separately to the PAA electrolyte on either side of the Zn electrode, to evaluate ORR and OER performance (denoted as GPE on OER, GPE+ZnO on ORR and GPE on ORR, GPE+ZnO on OER in Figure 4.4a). For the rate test corresponding to the PAA electrolyte containing ZnO on the OER side of the battery (GPE on ORR, GPE+ZnO on OER), the ORR potentials are quite high and essentially the same as those for GPE (black line). The OER potentials correspond to those for PAA containing ZnO on both the ORR and OER sides. In addition, the OER potentials, with the exception of the potential at 20

$\text{mA cm}^{-2}$ , are higher than those for the battery with PAA containing no ZnO. On the other hand, for the rate test corresponding to GPE containing ZnO on the ORR side of the battery (GPE on OER, GPE+ZnO on ORR), the ORR potentials are slightly higher than those for GPE with ZnO on both sides (yellow line). The OER potentials are the lowest, especially at  $20 \text{ mA cm}^{-2}$ . These results may seem surprising, intuitively, as one might expect excess zincate ions in the PAA electrolyte on the OER side to favor charging and lower the potential. However, a recent study has reported a potential problem with using ZnO-saturated electrolyte; i.e., a porous Zn electrode became blocked during cycling, since Zn was plated from both the discharge product and the extra ZnO added in the electrolyte. The resulting densification of the Zn electrode led to a loss of usable capacity, earlier passivation and eventually dendritic growth due to rising deposition overpotentials [195].

Three ZABs were chosen to carry out cycling tests at  $5 \text{ mA cm}^{-2}$  (Figure 4.4c): (1) a battery where both PAA electrolytes did not contain ZnO (labeled as GPE); (2) a battery where only the PAA electrolyte on the OER side contained ZnO (labeled as GPE on ORR, GPE+ZnO on OER); (3) a battery where only the PAA electrolyte on the ORR side contained ZnO (labeled as GPE on OER, GPE+ZnO on ORR). The mechanisms associated with the cycling behavior are illustrated in Figure 4.5 and discussed below. For the first case (no ZnO, Figure 4.5a), a high ORR potential is expected (and is observed;  $\sim 1.22 \text{ V}$ ), since there are no zincate ions to inhibit *Reactions 4.1* and *4.2*. During the first charge, however, the potential is high ( $\sim 2.09 \text{ V}$ ) as there are not many zincate ions on the OER side of Zn. During cycling, zincate ions will accumulate on the ORR side (Figure 4.5a), since OER is electrically favored on the OER side, resulting in the formation of a passive ZnO layer which will lead to an increase in the OER potential and a decrease in the ORR potential.

For the second scenario (ZnO added to the OER side), the discharge potential is essentially the same as that for the first case (no ZnO added) because there are no zincate ions on the ORR side to hinder discharge. Charging occurs at a lower potential ( $\sim 2.0$  V) compared with the first case, because there are zincate ions present on the OER side. As cycling proceeds, the OER potential increases and the ORR potential decreases to a greater extent than for the first case (no ZnO added). This is because zincate ions accumulate on the ORR side changing to ZnO, which lowers the discharge potential, and additional zincate ions are depleted on the OER side (Figure 4.5b), which increases the charge potential. After 40 cycles, this battery (ZnO added to the OER side) has the lowest discharge potential (1.14 V) and the highest charge potential (2.25 V) of the three cases (Figure 4.4c).

For the third scenario (ZnO added to the ORR side), the initial discharge potential is the lowest of the three cases ( $\sim 5$  mV lower), and the initial charge potential is the lowest (1.99 V). This indicates that discharge occurs more readily on the OER side and is hindered by ZnO additives on the ORR side (Figure 4.5c). Charging is more prevalent on the ORR side, because of the excess zincate ions. This battery maintains the lowest charge potential on cycling (2.2 V), along with an intermediate discharge potential ( $\sim 10$  mV higher than the battery with ZnO added to the OER side, Figure 4.4c). These results suggest that adding ZnO to the ORR side provides the best overall long term cycling performance (best efficiency), as the formation of a ZnO passivation layer on the ORR side of Zn is limited.

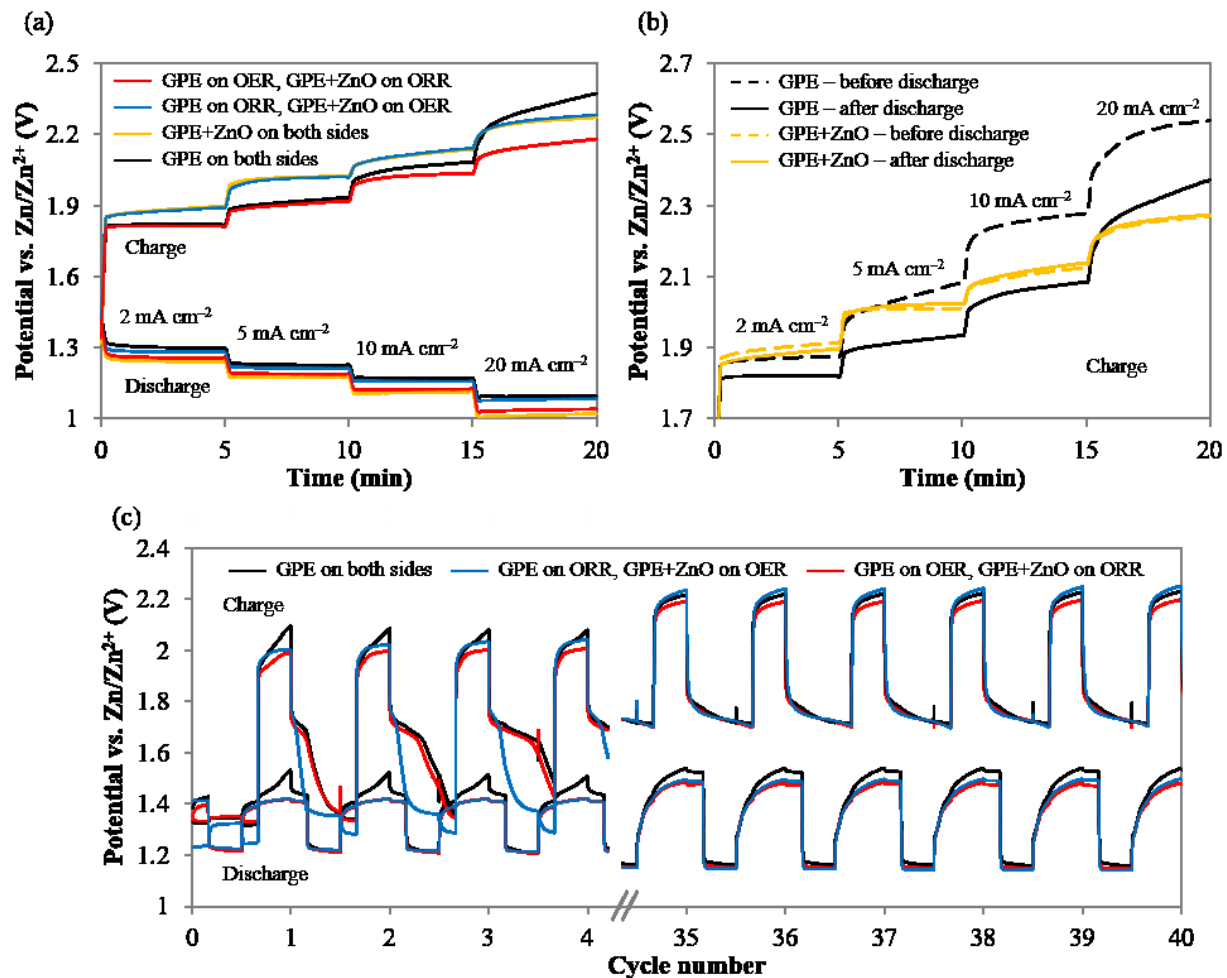


Figure 4.4. Electrochemical evaluation of ZABs using PAA with 0.5 mol% MBAA and 7.5 M KOH, with and without ZnO: (a) Discharge-charge rate curves, (b) charge rate curves and (c) cycling performance at 5 mA cm<sup>-2</sup>.

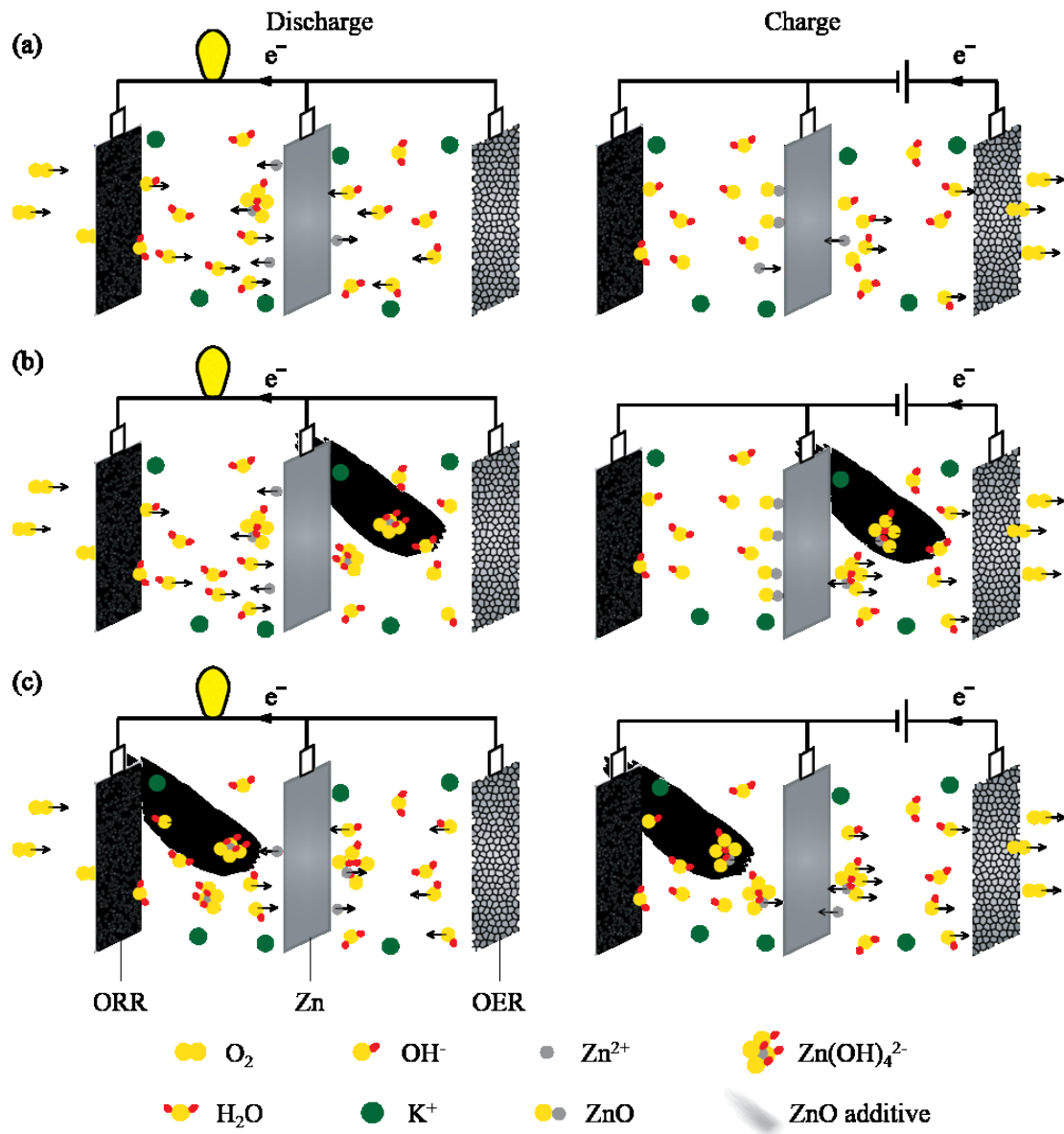


Figure 4.5. Schematic illustration of the effect of ZnO on discharge and charge of a ZAB: (a) Without ZnO, (b) ZnO in OER and (c) ZnO in ORR.

#### 4.3.4. Cycling performance of batteries using GPEs

Apart from studying GPEs, improvements in the OER catalyst are critical to decreasing the charge potential, not only by helping to reduce HER which can cause degradation of the GPE but also to increase cycling efficiency. Ni foam can be used to catalyze OER in alkaline solutions; however, Ni degrades over time [196-198]. A Co-Fe alloy (denoted here as CoFe),

electrodeposited on Ni foam, has been shown to be an active and durable OER electrode [199]. The surface of CoFe is oxidized and is electrochemically active. A comparison of the cycling behavior (at  $5 \text{ mA cm}^{-2}$ ) of Ni foam and Ni foam with electrodeposited CoFe is shown in Figure 4.6a. Ni foam or Ni foam with CoFe is used as the OER electrode, while MnOx is still used as the ORR electrode. The GPE was PAA with 7.5 M KOH and 0.5 mol% MBAA. The initial charge potentials are similar ( $\sim 2.1 \text{ V vs. Zn/Zn}^{2+}$ ), but there is a significant improvement in charge potential with cycling for CoFe on Ni foam. In fact, the OER potential decreases for CoFe on Ni foam, while the OER potential increases for Ni foam; after 90 cycles the difference in OER potential is significant, i.e., 273 mV. The discharge potential for battery using CoFe on Ni foam as OER is slightly worse than that for battery using bare Ni foam as OER probably due to some variation in MnOx activity on GDL; however, the overall cycling efficiency is better for CoFe on Ni foam (Figure 4.6b).

The CoFe on Ni foam OER electrode was coupled with the Mn oxide/GDL ORR electrode in the tri-electrode configuration and cycle tested. Batteries were tested with no ZnO in the PAA electrolytes, with ZnO in the PAA electrolyte in contact with the OER electrode and with ZnO in the PAA electrode in contact with the ORR electrode (Figure 4.6c). Cycling was done at a current density of  $5 \text{ mA cm}^{-2}$ . Initial performance was similar for the batteries with ZnO added to one electrolyte (either on the OER or ORR side), with an initial efficiency of 62% or better. All three batteries were able to withstand at least 80 cycles, but the battery with ZnO in the electrolyte in contact with the ORR electrode had the best long term performance, lasting for at least 100 cycles with a drop in efficiency from 62% to 52% (Figure 4.6d). The battery with no ZnO in the electrolyte failed after 95 cycles, while the battery with ZnO in the electrolyte in contact with the OER electrode failed after 87 cycles (Figure 4.6d). The battery position was also varied from

horizontal (with the OER or ORR positions altered between top and bottom) to vertical during cycling to test the robustness of the batteries. All the batteries were able to operate in the three configurations without loss of performance or leaking (Figure 4.6c).

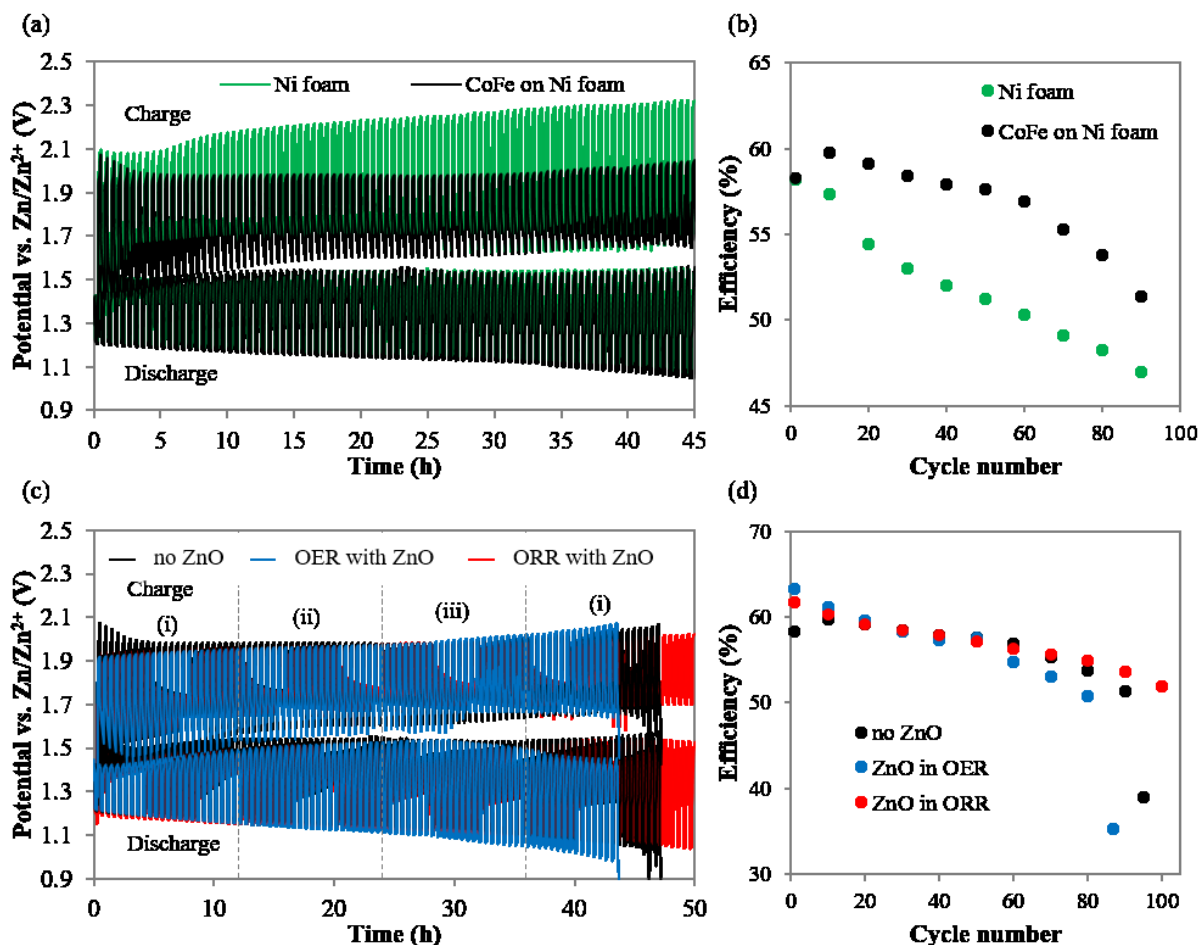


Figure 4.6. (a) Cycling performance of ZABs at 5 mA cm<sup>-2</sup> with different OER catalysts. (b) Discharge-charge efficiency calculated from (a). (c) Cycling performance at 5 mA cm<sup>-2</sup> with different positions: (i) horizontal position (OER at the bottom), (ii) vertical position and (iii) horizontal position (ORR at the bottom). (d) Discharge-charge efficiency calculated from (c).

All reports in the literature on tri-electrode ZABs used alkaline aqueous solutions as the electrolyte. Table 4.2 compares tri-electrode ZABs from the literature with the current work. It is difficult to make direct comparisons as the tests were not done under the same conditions. For example, pure oxygen or processed air was actually fed to the system in some cases instead of

using ambient air. For these cases, the batteries can exhibit long cycle lifetimes (e.g., 200 cycles in 5000 hours [97]), deliver high current densities (e.g., 50 mA cm<sup>-2</sup> [98]) or deliver good cycling efficiency (e.g., 68% at 20 mA cm<sup>-2</sup> [102]). Zhang et al. reported a tri-electrode ZAB using ambient air which can run for 600 cycles (at 2 mA cm<sup>-2</sup> with an efficiency of 57%), but requires refuelling of the Zn anode and electrolyte every 20 hours [99]. Xiong et al. also reported a tri-electrode ZAB using ambient air, where a syringe pump was used to add DIW into the cell at a rate of 0.2 mL h<sup>-1</sup> to compensate for evaporated water [103]. A pump will increase the cost of operation. ZABs from this work only consumed 3 mL of PAA and outperformed one tri-electrode ZAB using an aqueous electrolyte in terms of current density, cycle number and cycling efficiency (reference [101] in Table 4.2). These are highly encouraging results compared with the state of the art for rechargeable ZABs using GPEs. For the current design, the GPE thickness is 3 mm; further reduction in the distance between ORR/OER electrodes and Zn electrode should enhance battery performance.

Table 4.2. Comparison of rechargeable tri-electrode ZABs in chronological order

ORR catalyst	OER catalyst	Electrolyte	Battery design / Position	Current density (mA cm <sup>-2</sup> )	Cycle number	Initial cycling efficiency (%)	Ref.
MnOx*	SS	7 M KOH	Sandwich / Vertical	5 – 15	200	54	[97]
CoO/NCNT**	NiFe LDH	6 M KOH + 0.2 M Zn(Ac) <sub>2</sub>	Sandwich / Vertical	50	10	59	[98]
NPMCs (0.5 mg×cm <sup>2</sup> )	NPMCs (1.5 mg×cm <sup>2</sup> )	6 M KOH	Sandwich / Vertical	2	600	57	[99]
MnOx	Ru/Ti	6 M KOH + 0.4 M ZnO	Sandwich / Horizontal	20	1000	52	[100]
MnOx/CoOx	MnOx/CoOx	6 M KOH + 0.2 ZnCl <sub>2</sub>	OER electrode in the middle / Vertical	1	95	62	[101]
Commercial electrode**	NiFe LDHs	8 M KOH + 0.7 M ZnO	Sandwich / Vertical	20	100	68	[102]
MnOx	CoFe	6 M KOH + 0.25 M ZnO	Planar / Horizontal	20	100	58	[103]
MnOx	CoFe	GPE (7.5 M KOH + 0.25 M ZnO in ORR side)	Sandwich / Vertical + Horizontal	5	100	62	This work

SS: stainless steel. NCNT: N-doped carbon nanotubes. NiFe LDH: NiFe-layered double hydroxide. Zn(Ac)<sub>2</sub>: zinc acetate. NPMCs: N-P co-doped mesoporous nanocarbons.

\* Air was bubbled through KOH solution to remove CO<sub>2</sub> prior to exposure to the ORR electrode.

\*\* O<sub>2</sub> was fed to the ORR electrode.

#### 4.4. Conclusions

A novel tri-electrode ZAB, where the oxygen evolution and oxygen reduction reaction (OER/ORR) electrodes are decoupled and poly(acrylic acid) (PAA) is used as a gel polymer electrolyte (GPE), has been investigated. Two designs were examined. The sandwich cell design is generally more suitable for GPEs than the planar cell design, as it provides more uniform current and prevents Zn corrosion. Polymer crosslinking density affects the charge potential more prominently than the discharge potential. A crosslinking concentration of 0.5 mol% of methylenebisacrylamide (MBAA) gives the best compromise between good contact between PAA and the oxygen evolution reaction (OER) electrode and the ability to remove oxygen bubbles at the OER electrode. Decoupled air electrodes also allow the separate study of ZnO additions to the electrolyte and adding ZnO to ORR side enhances cycling performance of ZABs. The battery can deliver a discharge current of  $5 \text{ mA cm}^{-2}$  for at least 100 cycles and the battery can operate in different orientations, bypassing leaking issues associated with aqueous ZABs.

#### 4.5. Supporting information

To prove the concept that decoupling the ORR and OER is an effective strategy, linear sweep voltammetry (LSV) of bifunctional gas diffusion layer (BGDL) electrodes (sequentially deposited MnOx and CoFe on the GDL) was done to compare MnOx on GDL for ORR and Ni foam or CoFe on Ni foam for OER in 1 M KOH using a standard three-electrode system with Hg/HgO reference and Pt mesh counter electrodes (Figure S4.1). The readers are referred to Xiong et al. for a detailed description of catalyst fabrication and characterization [103, 156]. Figure S4.1a shows that ORR performance of a BGDL was significantly lower compared with the ORR performance of MnOx on GDL. Du et al. also observed that ORR catalytic activity of Co<sub>3</sub>O<sub>4</sub> nanoparticle-modified MnO<sub>2</sub> nanotubes decreased due to partial occupation of MnO<sub>2</sub> by Co<sub>3</sub>O<sub>4</sub>

nanoparticles [171]. After 5 cyclic voltammetry (CV) cycles from  $-0.5$  to  $0.2$  V vs. Hg/HgO, ORR catalytic activity of MnOx increased at high current density due to a phase change. For the BGDL, which was scanned with a wider CV range from  $-0.5$  to  $0.7$  V vs. Hg/HgO, the ORR current density decreased due to the degradation of MnOx to  $\text{MnO}_4^-$  and carbon corrosion as previously discussed. In Figure S4.1b, initial OER performance of CoFe on Ni foam and BGDL is comparable, since the GDL substrate has more surface area, while Ni foam can act as an OER catalyst itself. After 5 CV cycles from  $-0.5$  to  $0.7$  V vs. Hg/HgO, BGDL degraded more than CoFe on Ni foam which was only cycled from  $0.2$  to  $0.7$  V vs. Hg/HgO.

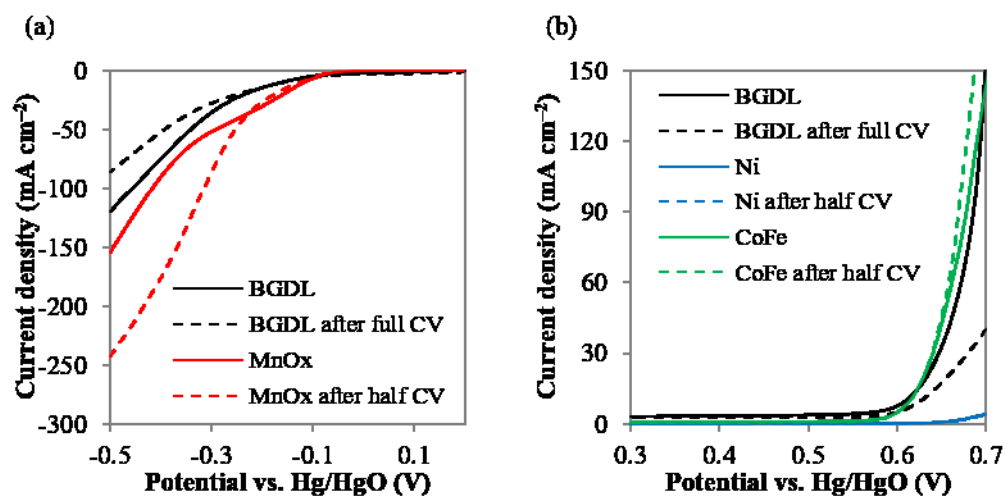


Figure S4.1. LSV curves for different catalysts in oxygen saturated 1 M KOH before and after 5 CV cycles: (a) from  $0.2$  V to  $-0.5$  V vs. Hg/HgO (ORR) and (b) from  $0.3$  V to  $0.7$  V vs. Hg/HgO (OER).

Figure S4.2 shows the morphology changes for GDL and Ni foam before and after deposition of MnOx and CoFe, respectively. For the ORR electrode, annealed MnOx on the GDL still maintains a porous structure with large spaces between MnOx deposits (Figure S4.2b). As such, a large surface area remains for the electrochemical reaction and facilitates the diffusion of oxygen into the ORR reaction zone. For the OER electrode, CoFe is deposited as fine particles on Ni foam (Figure S4.2d).

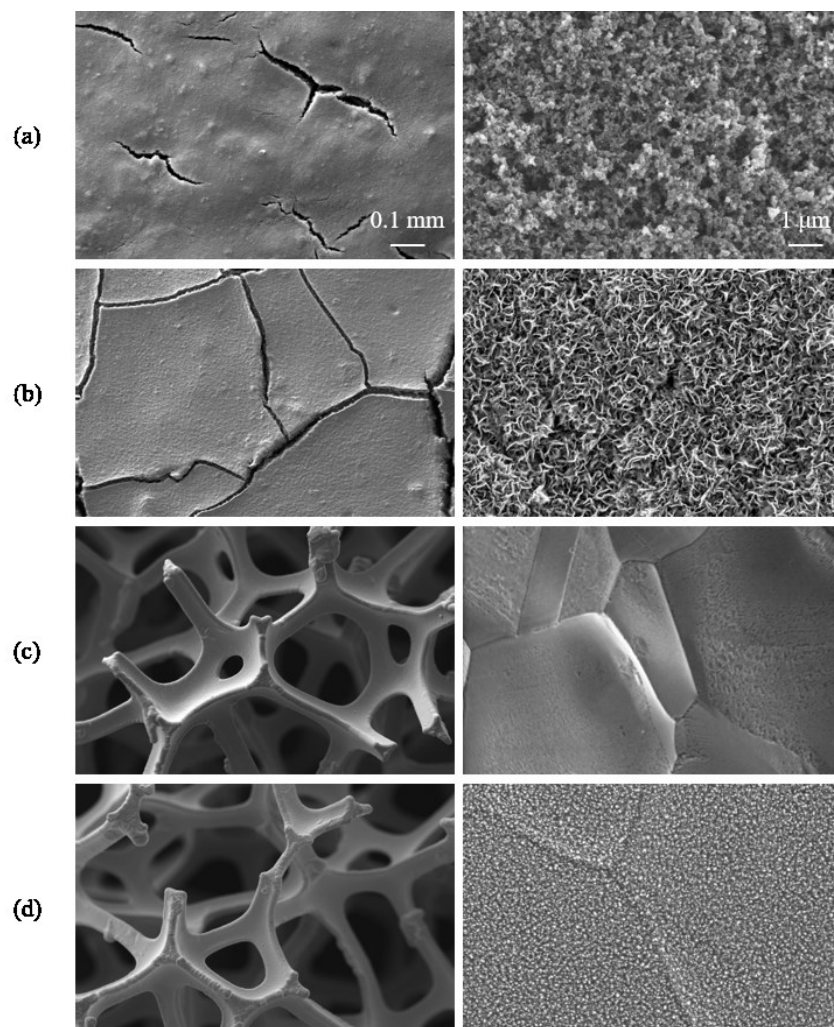


Figure S4.2. SEM secondary electron (SE) images (low and higher magnification) of (a) bare GDL, (b) MnOx on GDL, (c) Ni foam and (d) CoFe on Ni foam.

EIS measurements were conducted at 1.2 V and 1.9 V before and after rate testing. In full cell testing, the equivalent circuit has five elements including GPE resistance or bulk resistance ( $R_b$ ), interfacial resistance ( $R_{int}$ ), charge transfer resistance ( $R_{ct}$ ) and interfacial and double layer characteristic constant phase elements ( $Q_{int}$  and  $Q_{dl}$ ) [12].

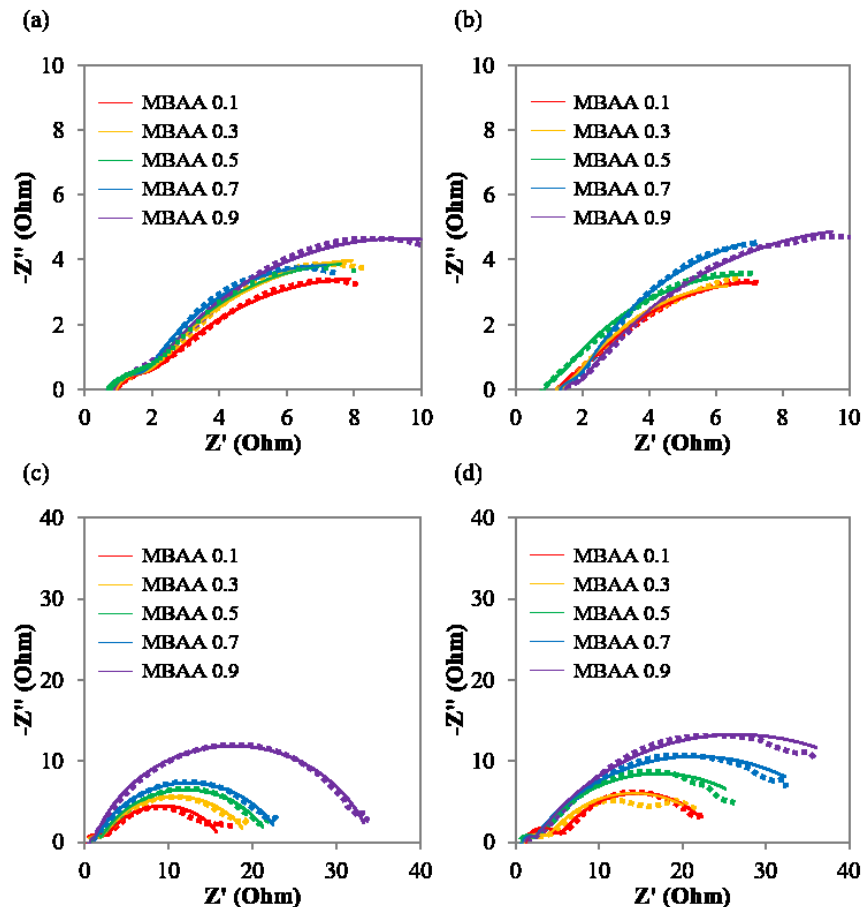


Figure S4.3. EIS of a Zn-air battery before and after rate testing at 1.2 V during discharge (a, c). EIS of a Zn-air battery before and after rate testing at 1.9 V during charge (b, d). Symbols represent the measured data and solid lines represent the best fit using Zsimpwin software.



Figure S4.4. OER electrode using MBAA 0.3 after cycling test showing permeation of GPE through the Ni electrode.

Chemical structures of freeze-dried hydrogels including pristine PAA, PAA in 6 M KOH and PAA in 6 M KOH with 0.25 M ZnO were further investigated by FTIR (Figure S4.5). To remove the effect of the alkaline environment on carboxylate groups ( $-\text{COOH} \rightarrow -\text{COO}^-$ ), GPEs with and without ZnO were rinsed with HCl and then with DIW. The absorption bands are

comparable to those of pristine PAA containing the C–H stretching peak near  $2947\text{ cm}^{-1}$  overlapping with the large O–H stretching regions [143], carbonyl stretching peak (C=O) at  $1700\text{ cm}^{-1}$ , CH<sub>2</sub> stretching peak at  $1450\text{ cm}^{-1}$  and C–O stretching peak coupled with the O–H bending vibration at  $1250\text{--}1130\text{ cm}^{-1}$  [142-144].

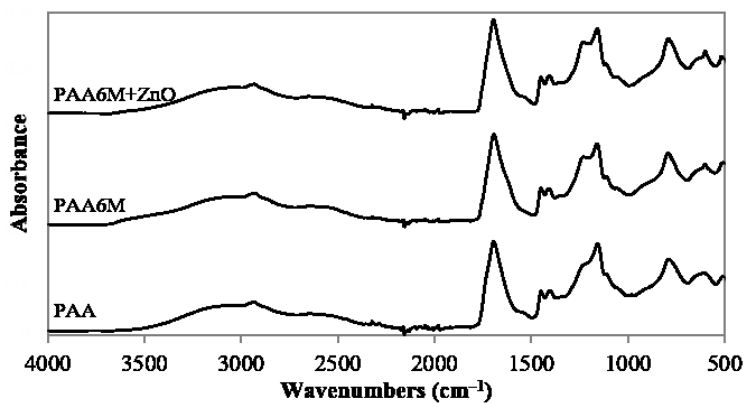


Figure S4.5. FTIR spectra for PAA with 0.3 mol% MBAA: pristine PAA and PAA in 6 M KOH, with and without 0.25 M ZnO, after rinsing with HCl and DIW.

## **Chapter 5. Effects of Crosslinker Concentration in Poly(Acrylic Acid)–KOH Gel Electrolyte on Performance of Zinc-air Batteries**

A version of this chapter has been published as:

Tran, T.N.T., Clark, M.P., Chung, H.-J. and Ivey, D.G., *Effects of Crosslinker Concentration in Poly(Acrylic Acid)–KOH Gel Electrolyte on Performance of Zinc-Air Batteries*. Batteries and Supercaps, 2020. 3(5): p. 409–416.

### **5.1. Introduction**

In the continuing search for sustainable energy storage systems, Zn-air batteries (ZABs) stand out as promising candidates with high energy density, long shelf life when sealed, safe operation and no environmental issues [200]. Zn is also readily available; e.g., Natural Resources Canada reported in 2017 that Canada produced 344,294 tonnes of Zn, ranking it fourth among the world's producers of refined Zn [201]. Going forward, the abundance of Zn offers the potential for lower cost ZABs relative to Li-ion batteries. Until now, the most successful applications for ZABs thus far have been in the primary battery market, including portable medical and telecommunication devices [43]. The development of secondary ZABs is constrained by the performance of the air electrode which limits the round-trip efficiency and cycle life of rechargeable ZABs [202]. Considerable research has been done on bifunctional catalysts for the air electrode to lower the energy barrier for both the oxygen evolution reaction (OER) and oxygen reduction reaction (ORR) in order to improve the energy efficiency of ZABs [203-205]. Other engineering solutions including mechanically rechargeable ZABs and Zn-air flow batteries, in which the electrolyte is circulated in the cell system, have also been proposed [152, 206, 207].

These solutions may be effective for grid energy storage applications, but they add cost and complexity to the system. Furthermore, there have been several reports incorporating tri-electrode designs, where the OER and ORR catalysts are separated to improve ZAB performance [97-103]. A tri-electrode design has its drawbacks, however, since the design is more complex and the specific energy is invariably reduced by the extra mass associated with extra OER electrodes. There are also issues associated with the alkaline, aqueous electrolyte (e.g., KOH) used in ZABs, as it is prone to evaporation, carbonation and flooding [48]. Since electrolytes play a key role in the transport of active species, new electrolyte materials are needed to overcome these challenges.

To alleviate problems associated with carbonation, aqueous, near-neutral pH electrolytes have been proposed. ZABs with LeClanché-based electrolytes containing  $\text{NH}_4\text{Cl}$ – $\text{ZnCl}_2$  have shown good cyclability, but the complex reactions and the precipitation of unwanted salts during gradual evaporation of water still hinder the development of a robust battery [47, 48]. Room temperature ionic liquids (RTILs), which are liquid-state salts under ambient condition, have been employed to address evaporation associated with aqueous electrolytes, since they are non-volatile and more thermally and electrochemically stable [57]. However, the ionic conductivity of RTILs is significantly lower than that of a standard KOH solution, which limits their application in ZABs [62]. Another type of electrolyte is gel polymer electrolytes (GPEs). GPEs employ a class of polymer known as hydrogels, which can absorb a significant amount of water without dissolving and, thus, have been utilized as base materials to hold alkaline solutions in ZABs. The major applications for using GPEs in ZABs has almost exclusively been for wearable electronics device. It is also notable that most of the recent reports have chosen poly(vinyl alcohol) (PVA) as the gel polymer matrix. Pioneered by Fu et al. [72] and Peng et al. [73] in 2015, rechargeable, flexible and stretchable ZABs with a PVA-based alkaline electrolyte had poor cyclability and low current

densities; e.g., ~100 cycles at 0.01 – 0.1 mA cm<sup>-2</sup>. Recently, Zhou et al. reported that ZABs using PVA–KOH could last 60 cycles at 6 mA cm<sup>-2</sup> [208], while Fan et al. developed ZABs (with PVA–KOH) that showed stable charge and discharge at 3 mA cm<sup>-2</sup> for 36 cycles [209]. Lei et al. have reported the longest cycle life (80 cycles) for solid-state ZABs at a low current density of 1 mA cm<sup>-2</sup> [210]. Direct comparisons are difficult to make among the various references, since tests were not done under the same operating conditions. The types of bifunctional catalysts, cycling test parameters, the concentration of the aqueous electrolyte within the polymer and the molecular weight of PVA were different.

In Chapter 3, different hydrogel matrices for KOH solutions were assessed based on mechanical strength, electrochemical and chemical stability, ionic conductivity, water uptake and battery performance [166]. Among them, poly(acrylic acid) impregnated with KOH (PAA–KOH) was the most promising candidate to replace the traditional alkaline solutions. As the polymeric host material, PAA is chemically and electrochemically stable under highly alkaline environments. The conductivity of PAA–KOH remains stable at high temperatures (360 mS cm<sup>-1</sup> at 65 °C) because of its high water retention [166]. In battery testing, ZABs with PAA–KOH electrolytes have the potential to outperform batteries with conventional aqueous electrolytes (e.g., 6 M KOH) by reducing interfacial and charge transfer resistance. In another study by the authors, leakage issues associated with aqueous electrolytes were prevented, allowing the battery to operate in different orientations when using PAA–KOH [211]. The optimal concentration of crosslinker (N,N'-methylenebis(acrylamide) or MBAA) was affected by the characteristics of the Ni current collector; specifically, a less porous Ni foam structure inhibits PAA–KOH penetration, while a more porous structure facilitates penetration and increases water evaporation from the PAA–KOH [211]. For a bi-electrode design, the most frequently used material to support bifunctional catalysts

is a Teflon-coated carbon paper, known as a gas diffusion layer (GDL) [156, 157, 175, 176]. Unlike Ni foam, GDL combines characteristics such as porosity (to allow access to oxygen gas) and hydrophobicity (to prevent flooding of aqueous electrolytes). In spite of the numerous studies done on ZABs that employ PAA–KOH as electrolytes [212-214], there is still a lack of systematic optimization of PAA composition.

The aim of this study is to characterize and optimize the compositions of PAA–KOH electrolytes for bi-electrode ZABs that use a conventional GDL as the support base for bifunctional catalysts. The impact of varying crosslinker concentration on gel properties, including loss and storage moduli, sol-gel fraction, ionic conductivity and water retention ability, are discussed. Attempts are made to explain the effects of crosslinking density on cycling performance of ZABs at a current density of  $5 \text{ mA cm}^{-2}$ . Changes to the Zn electrode morphology in cells using PAA–KOH electrolyte after cycling are also compared with morphology changes in aqueous electrolytes to understand the factors affecting ZAB failure.

## **5.2. Experimental procedure**

### **5.2.1 Synthesis of catalysts**

All chemicals were of analytical grade (>99%) and used as received without further purification. L-ascorbic acid (L-AA) and sodium dodecyl sulfate (SDS) were obtained from Sigma-Aldrich. Manganese(II) sulfate, sodium acetate, cobalt(II) sulfate, sodium citrate and boric acid were obtained from Fisher. Iron(II) sulfate was obtained from MP Biomedicals. Deionized water (DIW) was used to rinse and prepare all aqueous solutions. The gas diffusion layer (GDL) (Teflon-coated porous carbon paper, Sigracet 39 BB) was obtained from the Fuel Cell Store. The GDL was divided into  $5 \text{ cm}^2$  sections and used as the substrate for electrodeposition.

Sequentially electrodeposited MnOx/CoFe on the GDL was utilized as the bifunctional air electrode; MnOx provides ORR activity, while CoFe provides OER activity. Details regarding fabrication and characterization of the catalysts can be found in reference [156]. Briefly, electrodeposition of catalysts was performed at 40 °C in a two-electrode cell where GDL and Pt mesh were used as working and counter electrodes, respectively. First, anodic deposition of MnOx was carried out at a constant current of 40 mA for 10 min in a solution containing MnSO<sub>4</sub> (0.1 M), sodium acetate (0.1 M) and SDS (100 mg L<sup>-1</sup>). Samples were rinsed with de-ionized water (DIW) and then annealed at 300 °C for 30 min. Cathodic deposition of CoFe was then done at a constant current of 200 mA for 2 min in a solution containing CoSO<sub>4</sub> (0.15 M), FeSO<sub>4</sub> (0.05 M), sodium citrate (0.2 M), boric acid (0.2 M), L-AA (0.05 M) and SDS (400 mg L<sup>-1</sup>). Samples were rinsed with DIW afterwards and then dried in air.

### **5.2.2. Synthesis of hydrogel electrolyte**

PAA was used as the host polymer for the PAA–KOH gel electrolyte in this work. Acrylic acid (AA), MBAA and potassium persulfate (KPS) were obtained from Sigma-Aldrich, while potassium hydroxide (KOH) was obtained from Fisher Scientific. PAA–KOH was prepared by mixing 7.5 M KOH, 1.5 M AA, KPS thermoinitiator (0.1 mol% of AA monomers) and MBAA crosslinker (0.1, 0.3, 0.5, 0.7 or 0.9 mol% of AA monomers). The polymer electrolytes, with different crosslinking concentrations are hereafter denoted as MBAA 0.1, MBAA 0.3, MBAA 0.5, MBAA 0.7 and MBAA 0.9, respectively. The electrolyte solutions were kept in an oven at 60 °C for 1 h to carry out polymerization and then allowed to cool overnight to room temperature.

### **5.2.3. Cell fabrication**

Two designs for bi-electrode ZABs were fabricated and are shown in Figure 5.1. The different designs were necessary because aqueous KOH electrolyte and PAA–KOH gel electrolyte,

respectively, require different device configurations. Both cells were made from a frame of acrylic sheets and the air electrode was positioned on top with a Zn electrode below. The ZAB using PAA–KOH as the electrolyte was stacked in layers (Figure 5.1a), while the cell built using a conventional aqueous KOH electrolyte (6 M concentration) needed the walls to be sealed to prevent leaking (Figure 5.1b). In addition, a hole was cut on top of the cell for electrolyte refilling purposes. The contact area between the air electrode and electrolyte, for both cells, was controlled ( $1 \text{ cm}^2$ ) and the total mass of Zn used was  $\sim 1 \text{ g}$  (0.2 mm thick).

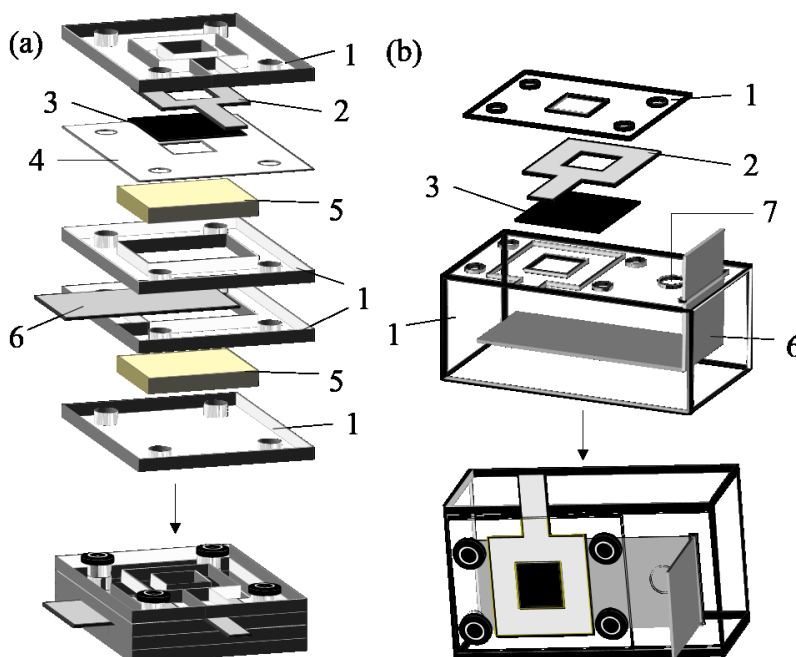


Figure 5.1. Homemade cell assembly for bi-electrode ZABs using (a) a PAA–KOH electrolyte and (b) an aqueous electrolyte. 1) Acrylic sheets, 2) current collector Ni, 3) GDL, 4) polypropylene film, 5) GPE, 6) Zn, 7) refilling hole.

#### 5.2.4. Material characterization

The morphologies of the air and Zn electrodes, before and after battery cycling, were characterized using scanning electron microscopy (Zeiss EVO M10 SEM and Zeiss Sigma FESEM (field emission)), coupled with energy dispersive X-ray (EDX) spectroscopy. The amount of ZnO coverage on the Zn electrode surface was of particular interest. EDX spectra were taken from

several areas of the Zn electrode. For batteries using aqueous electrolyte, the Zn electrode was cleaned with DIW to remove any residual KOH before SEM imaging, so the amount of ZnO coverage on the Zn surface was directly correlated with the amount of oxygen (*Equation 5.1*).

$$\%ZnO = \text{at}\%O \div \text{at}\%Zn \times 100\% \quad \text{Equation 5.1}$$

For batteries using PAA–KOH as the electrolyte, the Zn electrode was not cleaned with DIW prior to SEM examination to prevent swelling of any PAA–KOH that may be covering portions of the Zn electrode. Thus, the amount of ZnO on the Zn electrode surface was determined after subtracting the oxygen amount from PAA–KOH and KOH, which are related to the amount of C in the polymer (C<sub>3</sub>H<sub>4</sub>O<sub>2</sub>) and K in the KOH, respectively. The amount of ZnO was then calculated from the following *Equation 5.2*:

$$\%ZnO = \left( \text{at}\%O - \frac{2}{3} \text{at}\%C(\text{in } C_3H_4O_2) - \text{at}\%K(\text{in } KOH) \right) \div \text{at}\%Zn \times 100\% \quad \text{Equation 5.2}$$

where at% signifies the amounts of the elements in atomic percent.

Conductivities for PAA were measured by electrochemical impedance spectroscopy (EIS) at open circuit potential with an applied 10 mV AC potential from 100 kHz to 10 mHz using a potentiostat/galvanostat (Autolab PGSTAT302N). Rheological properties were characterized with a rheometer (Kinexus Lab+). First, the linear viscoelastic region (LVER) was determined by an amplitude sweep from 0.1 – 100% strain at 1 Hz and then a frequency sweep at 1% strain was done from 0.01 – 10 Hz.

The masses of as-prepared PAA–KOH electrolytes ( $W_{\text{gel}}$ ) with different crosslinker amounts were determined from the sum of the masses of the components. Then the samples were neutralized with 1 M HCl and rinsed with DIW. The gels were freeze-dried overnight and dried again in a vacuum oven at 45 °C to achieve a completely dried state ( $W_i$ ). For sol-gel fraction

analysis, the dried PAA samples were subjected to Soxhlet extraction using DIW as the solvent at 100 °C for 12 h. Extracted gels were dried again. The gel fraction was calculated from the masses of the initial dry gel ( $W_i$ ) and the extracted dry gel ( $W_f$ ) [215, 216]:

$$\text{Sol fraction (\%)} = \left[ \frac{W_i - W_f}{W_i} \right] \times 100 \quad \text{Equation 5.3}$$

$$\text{Gel fraction (\%)} = 100 - \text{Sol fraction} \quad \text{Equation 5.4}$$

For evaporation tests, 3 mL of aqueous KOH 6 M and PAA–KOH with different crosslinker amounts (0.1, 0.3, 0.5, 0.7 and 0.9 mol%) were contained in separate tubes, each with an open area of 0.8 cm<sup>2</sup> (d = 1 cm). The tubes were kept under vacuum at 45 °C. The tube masses were measured at 1 h intervals over an 8 h period. The mass loss at each interval was equal to the tube mass at a particular interval minus the mass from the previous interval.

### 5.2.5. Battery testing

For rate testing, battery potential was measured using a galvanostatic method for a range of current densities, i.e., 2, 5, 10 and 20 mA cm<sup>-2</sup>, for 10 min each with a cut-off voltage of 0.8 V (discharge) and 2.5 V (charge). Cycling tests were also done through a galvanostatic method with 30 min per cycle using another potentiostat/galvanostat (Biologic VSP-300). The battery was discharged and charged at 5 mA cm<sup>-2</sup> for 10 min and the circuit was kept open for 5 min between steps. The purpose of the battery rest period between discharging and charging was to allow the battery to stabilize and cool. Blurton et al. found that heat generation during discharge and charge is a major consideration for battery management, as it can facilitate self-discharge and water evaporation [8]. The discharge-charge efficiency was calculated by dividing the lowest discharge potential by the highest charge potential during one cycle.

### 5.3. Results and discussion

#### 5.3.1. Properties of PAA–KOH gel electrolytes

The states of PAA–KOH can be visibly assessed, as shown in Figure 5.2a. Tubes containing the various electrolytes were inverted and the flow behavior was observed. After 2 min, the MBAA 0.1 sample was the only electrolyte to flow. In order to assess the mechanical behavior of the solid hydrogels, rheological measurements were made to determine the ratio between the elastic modulus  $G'$  (reversibly stored energy; mechanical strength as a continuum) and the loss modulus  $G''$  (irreversibly lost energy; dissipated by viscous flow) for each PAA–KOH gel electrolyte with varying MBAA (crosslinker) concentration.  $\tan(\delta)$  was used to quantify the balance between lost and stored energies, where  $\delta$  is the phase angle. Conventionally, gels (solid-like state) are considered to have formed when  $\tan(\delta) = G'' / G'$  is less than 1, whereas  $\tan(\delta)$  larger than 1 corresponds to a sol (liquid-like state). Firstly, an amplitude sweep at a frequency of 1 Hz was carried out on PAA–KOH to determine its linear viscoelastic region (LVER), where the elastic modulus remains constant over a small change in the strain (Figure 5.2b). PAA–KOH with 0.1 mol% MBAA has a  $\tan(\delta)$  value of 1.56 in the LVER. In accordance with the physical appearance of a viscous fluid (leftmost vial in Figure 5.2a), the crosslinker content is not sufficient to form a gel. As the MBAA concentration is increased from 0.3 to 0.9 mol%,  $G'$  values increase from 149 to 250 Pa, while  $G''$  values decrease from 101 to 74 Pa in the LVER. All PAA–KOH samples with MBAA concentration in the range of 0.3 to 0.9 mol% can be considered as GPEs, since the  $\tan(\delta)$  values are below 1. Hydrogels formed using higher crosslinking agent concentrations have shorter strand lengths between crosslinks and are more physically stable [217, 218].

Secondly, a frequency sweep between 0.01 and 10 Hz was performed at 1% maximum strain, which is within the LVER of the polymers. In an ideal gel system, the  $\tan(\delta)$  value is nearly

constant over wide frequency ranges [219-221]. As with the amplitude sweep,  $G'$  is higher than  $G''$  for PAA–KOH containing 0.3 to 0.9 mol% MBAA over the entire frequency range, whereas  $G''$  is higher than  $G'$  when 0.1 mol% MBAA is added (Figure 5.2c). A plot of complex viscosity as a function of frequency,  $|\eta^*| = \sqrt{(G'/\omega)^2 + (G''/\omega)^2}$ , is shown in Figure 5.2d, based on the data in Figure 5.2c. The complex viscosity is almost independent of frequency for 0.1 mol% MBAA, which means that the sample is a fluid with a non-associated structure [221, 222].

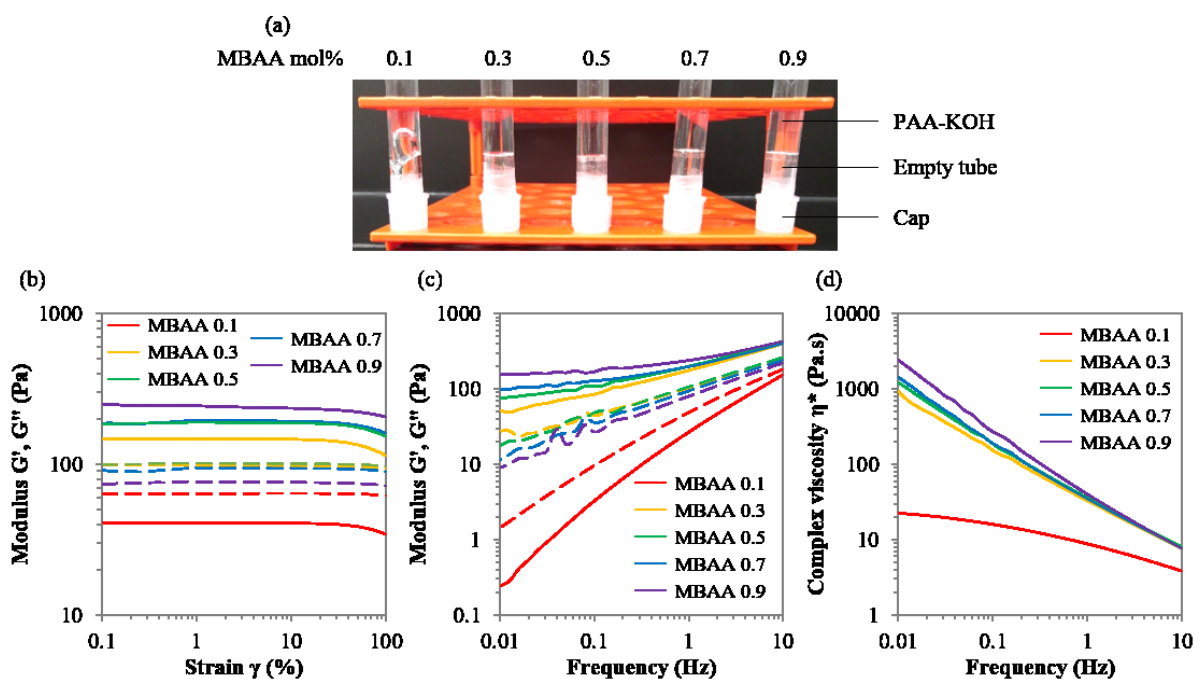


Figure 5.2. Rheological properties of PAA–KOH with varying crosslinking concentrations. (a) Photograph showing flow behavior of various GPEs 2 min after the containers have been inverted. (b) LVER region for the GPEs determined by amplitude sweeps from 0.1 to 100% strain at 1 Hz. (c)  $G'$  and  $G''$  moduli as a function of frequency. (d) Complex viscosity determined by a frequency sweep. In (b) and (c), the solid lines represent the  $G'$  modulus and the dashed lines represent the  $G''$  modulus.

In low-molecular-weight polymer electrolytes ( $\sim 2000$  g/mol for poly(ethylene oxide)), ionic conduction takes place by two means [223, 224]. In the first mechanism, which is known as fluctuation-driven diffusion, ion motion is mediated by segmental motion of the surrounding polymer chains. As such, conduction is determined by interactions between ions and polymers and

the glass transition temperature ( $T_g$ ) of the polymer. The second mechanism, vehicular diffusion, occurs by the diffusion of the whole polymer chain interconnected with ions [225]. As shown in Figure 5.3a, crosslinker amount does not change the total mass or volume of PAA–KOH significantly; thus the ratio between the weight of as-prepared PAA–KOH and dry PAA remains approximately constant (11.7 to 11.8). Sol-gel fraction analysis was carried out to determine the uncrosslinked fraction of AA monomers and whether or not this fraction contributes to ionic conductivity. The gel fraction of the hydrogels (i.e., fraction of AA monomer that participated in gelation) increases with increasing crosslinker content (Figure 5.3b). PAA–KOH with 0.3 mol% MBAA and 0.5 mol% MBAA have the same conductivities, i.e.,  $270 \text{ mS cm}^{-1}$ , even though the 0.3 mol% MBAA sample had 15% more sol fraction. With the addition of ZnO, however, the ionic conductivities showed a nearly monotonic decrease with increasing MBAA content ( $224, 211, 188$  and  $173 \text{ mS cm}^{-1}$  for 0.3, 0.5, 0.7 and 0.9 mol% MBAA, respectively, Figure 5.3c). This result indicates that the actual ionic conductivity may be dependent on the interplay between the effective mesh size and the hydrodynamic radius of charge conducting ions. When ZnO particles are dispersed into an alkaline solution, zincate complexes ( $\text{Zn(OH)}_4^{2-}$ ) are formed with a thin electric dipole layer of the solvent attached to the complex surface which influences the Brownian motion of the particles in the medium [226]. Pessine et al. reported that the “solvodynamic radii” of  $\text{Zn(OH)}_4^{2-}$  calculated from the Stokes-Einstein equation had a range of values from 0.35 to 0.41 nm [226]. For hydroxide ions, Roobottom et al. reported that the “thermochemical radius” is 0.152 nm [227]. This size is comparable to the radius of  $\text{H}_9\text{O}_5^-$  ( $\text{OH}^-$  ion forming hydrogen bonds with four adjacent water molecules) which was reported to vary from 0.138 to 0.16 nm [228]. Based on these references, it is hypothesized that zincate ions are large enough that their transport may be

physically hindered by the PAA mesh at high MBAA content, leading to a lower conductivity for PAA–KOH.

Hydrogels, especially PAA, have a wide range of applications within agriculture, cosmetic and hygienic products, the pharmaceutical industry and wastewater treatment, all because of PAA's high absorbance and water retention ability [229, 230]. These attributes can have a substantial impact on ZABs as well. ZABs use oxygen from the air for the ORR reaction, so water evaporation is inevitable. PAA electrolytes can reduce water loss, which was demonstrated by exposing PAA–KOH with different MBAA concentrations, as well as an aqueous KOH solution (6 M KOH), to a vacuum for 8 h at 45 °C. As shown in Figure 5.3d, PAA electrolytes can reduce water loss by 50% compared with aqueous KOH solutions. This is achievable due to the water states in hydrogels, which can be classified into three types: normal water/water interaction (free water), weakened water/water interaction (weakly bound water to the polymer) and extremely weakened water/water bonding (strongly bound water to the polymer). The structure of free water is similar to that of bulk water and its interaction with polymer chains is negligible. On the other hand, functional groups in the hydrogels can capture nearby water molecules through hydrogen bonding or other strong interactions, leading to the formation of strongly bound water. Weakly bound water is due to second-order interaction between the nearly-free water molecules and the strongly bound water molecules [231, 232]. It was previously reported that even when free water is expelled from a hydrogel network, bound water still remains [233]. Water retention is similar for PAA–KOH with 0.3, 0.5 and 0.7 mol% MBAA (112.7, 111.6 and 113.3 mg of water loss, respectively). However, there is a more marked decrease for 0.9 mol% MBAA (130.2 mg of water loss). A higher crosslinking density may create a denser network which affects the interaction between carboxyl functional groups of PAA with surrounding water molecules. The polymer

structure shrinks, so that the network voids available for retaining water are reduced and water retention is decreased [234].

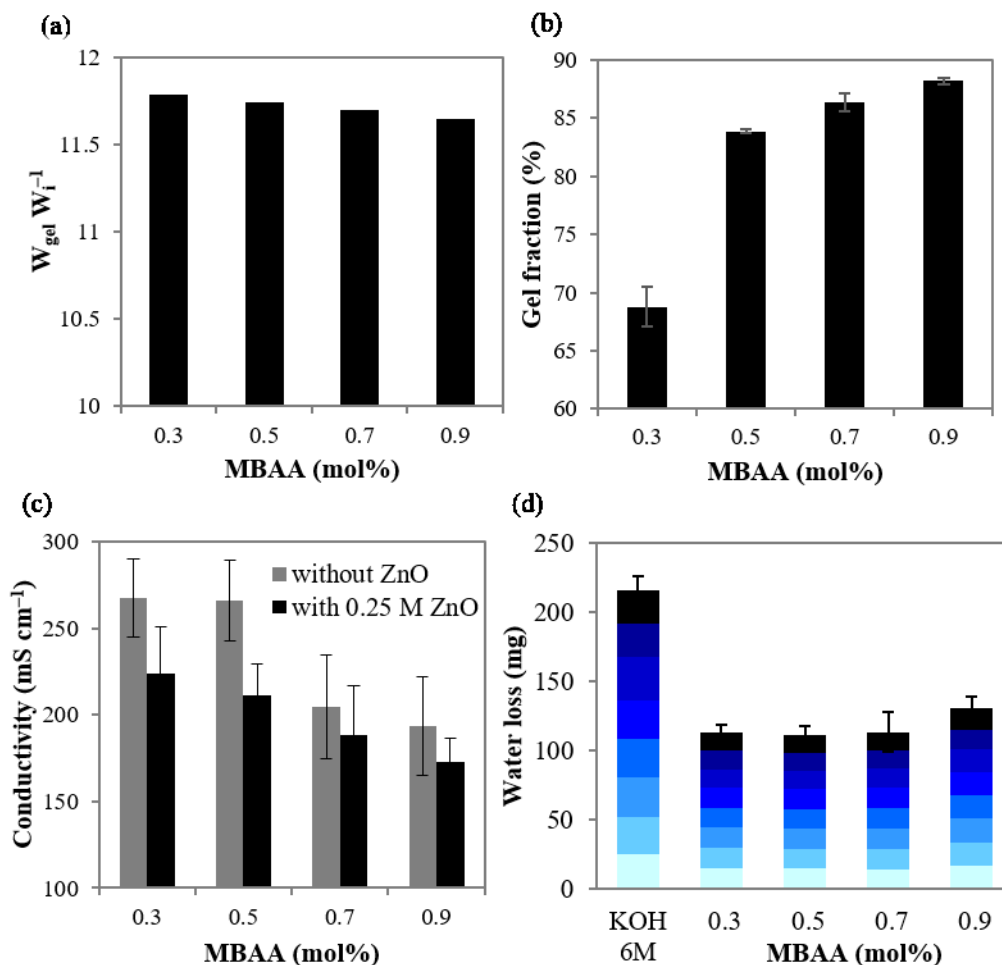


Figure 5.3. (a) Ratio between the weight of as-prepared PAA-KOH and dry PAA. (b) Gel fraction, (c) ionic conductivity and (d) water loss for PAA-KOH as a function of crosslinker concentration. In (d), each colour bar represents an hourly measurement.

### 5.3.2. Performance of Zn-air batteries

ZABs were fabricated by sandwiching the electrolyte between a Zn metal sheet and a GDL coated with the ORR/OER catalyst (MnOx/CoFe). The deposition of MnOx/CoFe on the GDL generated several cracks on the surface (Figure 5.4a). As such, pathways for diffusion of oxygen into the ORR reaction zone still existed. The thickness of the MnOx/CoFe layer on the GDL was

~7 – 9  $\mu\text{m}$ , which was confirmed through cross-sectional SEM imaging of the catalysts on the GDL (Figure S5.1a). According to the EDX line scans (Figure S5.1b), the catalyst layer is Fe/Co-rich on the surface with larger amounts of Mn in the subsurface region. Rate tests at several current densities for batteries using PAA–KOH as the electrolyte, with different MBAA concentrations, are shown in Figure 5.4b. The MBAA amount has minimal influence on the discharge potential, but significantly affects the charge potential. Specifically, the charge potential reached a limiting value of 2.5 V at 20  $\text{mA cm}^{-2}$  for PAA–KOH with 0.9 mol% MBAA. These results are similar to the work done in Chapter 4 using PAA–KOH electrolyte in a tri-electrode battery design [211].

Battery cycling tests were done at a current density of 5  $\text{mA cm}^{-2}$  for the four types of PAA–KOH electrolytes and for aqueous KOH. Initially, ZABs using PAA–KOH as the electrolyte exhibit better performance than the battery with aqueous KOH 6 M as the electrolyte. Discharge potentials for the ZAB cell using 6 M KOH are about the same as those for the cells using PAA–KOH; however, the charge potential for the cell with the aqueous electrolyte is significantly larger (about 150 mV). The discharge-charge efficiencies, which were calculated from the second cycle of the discharge-charge profiles (Figure 5.4c), are ~60% for ZABs using PAA–KOH and only ~55% for the ZAB using 6 M KOH aqueous electrolyte. With GPEs, zincate ions do not travel very far from the Zn surface, so Zn can be redeposited more easily resulting in a lower charge voltage. For aqueous alkaline electrolytes, to facilitate OER and reduce the likelihood of the hydrogen evolution reaction (HER), many investigators pre-saturate the electrolyte with zincate ions by dissolving ZnO powder [90, 191-194]. The hydrogel electrolytes, as expected from Chapter 3, also had better performance because of improved physical contact with the air electrode which reduced both interfacial and charge transfer resistance. The hydrophobic nature of the air electrode, on the other hand, hindered contact with the aqueous electrolyte [166].

The efficiency of the ZAB using the aqueous electrolyte gradually improved during cycling to approach the performance of the batteries with PAA–KOH (containing 0.3 to 0.5 mol% MBAA). After 80 cycles, the ZAB with the aqueous electrolyte had better efficiency; the efficiency reached 57% at the 100<sup>th</sup> cycle. The improvement in efficiency can be attributed to partial GDL degradation during the OER which increased the wettability of the GDL. After 100 cycles, ZABs using 0.3 or 0.5 mol% MBAA (as the electrolyte) had similar efficiencies of 53%, while the efficiency for 0.7 mol% MBAA was reduced to 48%. The ZAB with 0.3 mol% MBAA managed ~120 cycles (Figure S5.2), while that with 0.9 mol% MBAA only managed 80 cycles before failure. SEM images of the Zn electrode after cycling in ZAB with 0.3 mol% MBAA are shown in Figure S5.2 and no dendrites were found on the Zn surface.

The general mechanisms associated with the cycling behavior of ZAB using PAA–KOH with varying MBAA content as the electrolyte are illustrated in Figure 5.4d. During the discharge process, zincate ions diffuse into PAA–KOH. The depth of diffusion is larger for PAA–KOH with low crosslinker concentration (Figure 5.4d, top left) compared with PAA–KOH with high crosslinker concentration (Figure 5.4d, top right). For the latter case, a ZnO layer forms at the Zn/PAA–KOH interface. During cycling, the ZAB cell increases in volume, which is caused by (1) the density difference between metallic Zn and the discharge product ZnO on the Zn electrode [90] and (2) oxygen bubble accumulation during the OER [189]. PAA–KOH with a low crosslinking density is soft so that the polymer network can accommodate the change in volume, i.e., the polymer can squeeze between cracks in the catalyst layer (Figure 5.4d, bottom left). PAA–KOH with a higher crosslinking density is stiffer and, as such, PAA–KOH may lose contact with the air electrode due to oxygen bubble accumulation (Figure 5.4d, bottom right). With repeated charging cycles, a layer of oxygen gas accumulates in the vicinity of the air electrode, which

increases interfacial resistance, reduces the charging efficiency and even damages the battery [189, 235]. Therefore, removal of the bubbles must be effectively controlled. As shown in Figure S5.3, adhesion between the GDL and PAA–KOH is drastically reduced when the MBAA content in PAA is increased from 0.3 mol% to 0.9 mol%. Values of adhesion strength are also shown in Table S5.1. A less sticky electrolyte will likely provide spaces for bubble coalescence and escape from the electrode surface; however, highly crosslinked structures will resist ion transport, which explains the similar performance for PAA–KOH with 0.3 mol% MBAA and 0.5 mol% MBAA. Even in the aqueous electrolyte, oxygen bubbles produced during the OER process can easily adhere to the charging electrode and may be stable for many hours or even days creating a significant energy barrier [183, 236]. The cell potential, surface tension of the electrolyte, properties of electrode material and bubble interaction with the electrode can all influence bubble behavior [236, 237].

Cycling tests were carried out in 6 M KOH electrolytes (aqueous) with horizontal and tilted positions (Figure S5.4). Photographs of the cell in the tilted configuration ( $\sim 15^\circ$  to the horizontal) are shown in Figure S5.5. Overall the efficiencies are similar; however, the discharge voltage for the horizontal cell is unstable and depends on oxygen bubble escape. Bubble accumulation results in a decrease in discharge potential, which recovers when the bubbles escape (Figure S5.4b). A brown deposit has collected at the bottom of the cell, due to loss of catalyst from the GDL (Figure S5.5b). In addition, the top view of the battery showed signs of electrolyte flooding (Figure S5.5c). Even though the battery efficiency increased during cycling for the ZAB with the aqueous electrolyte, battery integrity was compromised. Thus, ZABs using PAA–KOH are a more promising candidate for portable applications, since the hydrogel electrolyte has the benefits of

being solid-state while still possessing high ionic conductivity which ensures battery integrity. Further study is needed to optimize PAA–KOH composition and battery design.

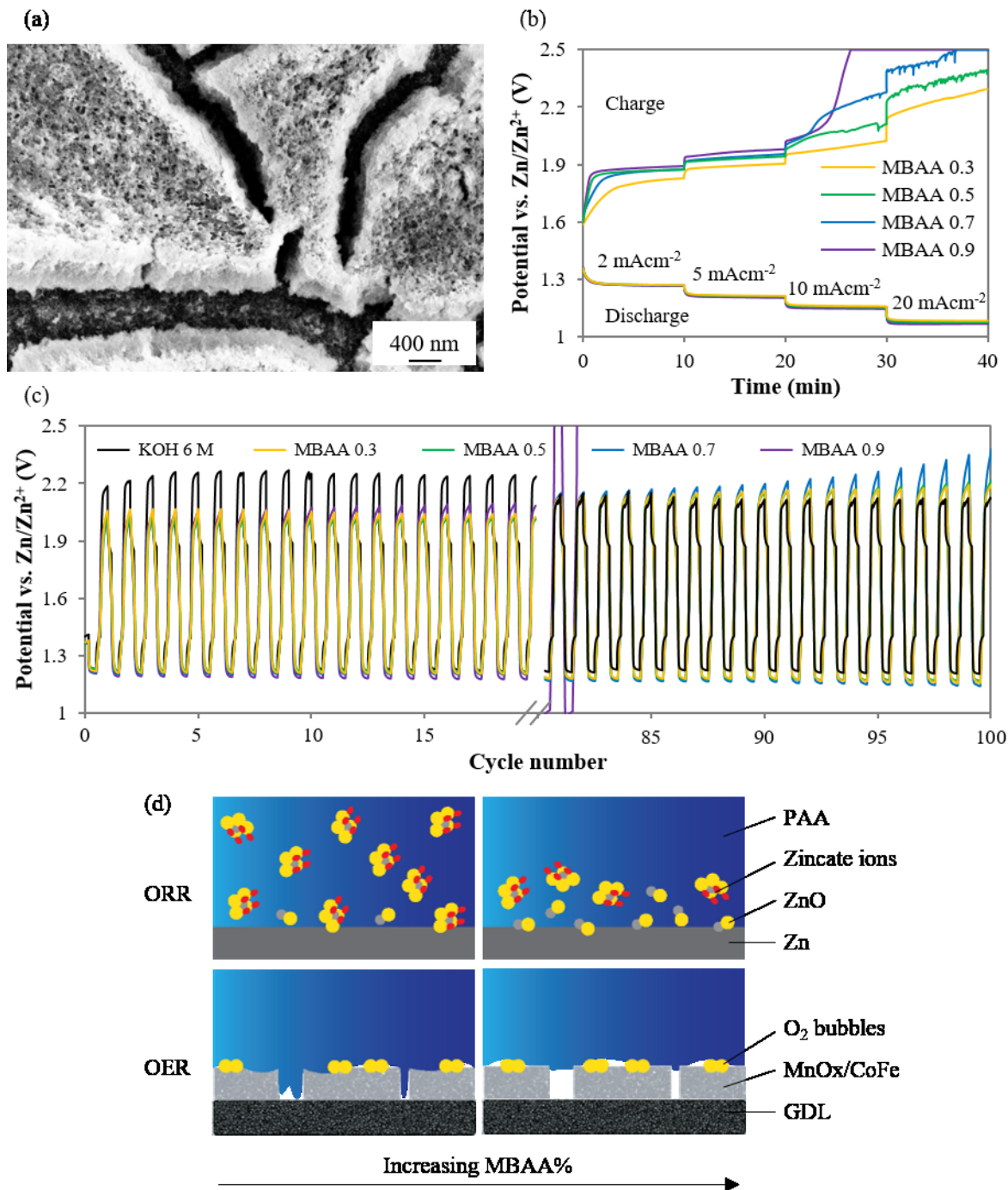


Figure 5.4. (a) FESEM SE image of MnOx/CoFe on GDL. Evaluation of ZABs using PAA–KOH with various MBAA concentrations: (b) rate discharge-charge curves and (c) cycling performance at 5 mA cm<sup>-2</sup>. (d) Schematic illustration of the effects of crosslinking density on discharge and

charge of a ZAB. White regions in the schematic represent cracks in the catalyst layer or gaps at the catalyst/electrolyte interface.

### 5.3.3. Post testing analysis of Zn electrode

With advancements in catalysts and battery designs to assist with air electrode issues, the cycle life of rechargeable ZABs can be limited by changes in the Zn electrode related to dendrite formation, undesired relocation and passivation [238]. During recharging, Zn is redeposited onto the Zn surface from zincate ions in the electrolyte. The redeposited Zn can take the form of mossy, layer-like, boulder-like and dendritic shapes. Among these, dendrites are needle-like in nature and grow axially, which can either cause internal short circuits or detachment of Zn from the electrode, resulting in reduction of the battery capacity [239]. Moshtev et al. report that overpotential is a critical variable in dendrite formation and developed an equation to predict the time for the appearance of dendrites [51]. However, Ito et al. showed that current density ratio (effective current density over limiting current density) determines Zn morphology [240]. There are many other factors affecting dendrite formation, including the substrate material, methods of surface preparation, electrode porosity, temperature, electrolyte composition and flow rate [240, 241]. As such, a universal model governing morphology of the Zn deposit does not exist. Generally, Zn deposits tend to be mossy or spongy at low current densities, layer-like at intermediate current densities and boulder-like or dendritic at high current densities [175]. In this study, the Zn electrode was initially a flat sheet, but its morphology after cycling in the aqueous electrolyte (6 M KOH) became uneven with crystalline, hexagonal structures of Zn deposited on top of one another (Figure 5.5a). This morphology occurs because Zn is dissolved in the electrolyte during discharge and then re-deposited at different locations during charge. For highly porous Zn electrodes with large surface areas, the modification in morphology during cycling can result in shape change of

the Zn electrode, leading to the loss of utilization rate, discharge capacity and energy density of ZABs [12].

When PAA–KOH is used as the electrolyte, Zn surface features are reduced, in part because different deposits form (Figure 5.5b–e). Huang et al. reported that electrostatic interaction between the negatively charged acrylate groups along the PAA–KOH chains and positively charged Zn ions formed during the discharge process produces a quasi-solid electrolyte interface between the electrolyte and Zn electrode [242]. This interaction can help retain  $\text{Zn}^{2+}$ , which is beneficial in preventing dendrite formation; however, it can also result in premature supersaturation of zincate ions and formation of ZnO. Shape change on the Zn surface is also reduced with increasing MBAA content in the electrolyte, since the presence of a stiffer solid-state electrolyte generates a larger compressive stress field around any dendritic protrusions thereby restricting their growth [243].

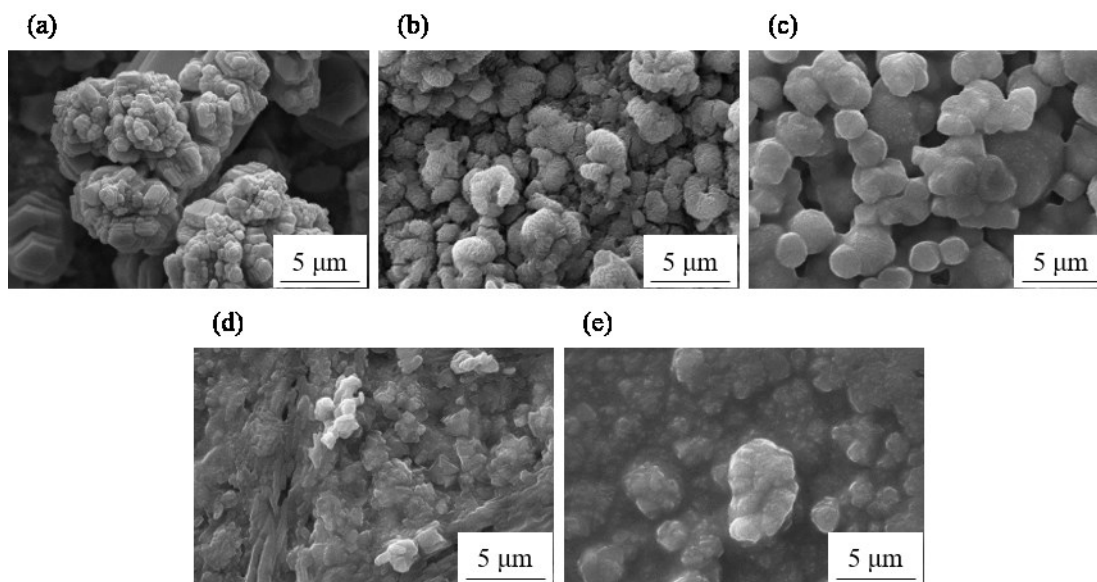


Figure 5.5. Morphology of Zn electrode from ZABs after cycling tests at  $5 \text{ mA cm}^{-2}$  using (a) aqueous electrolyte (6 M KOH), (b – e) PAA–KOH with 0.3, 0.5, 0.7, and 0.9 mol% MBAA, respectively.

Although the PAA–KOH electrolyte can restrict dendrite formation and shape change of the Zn electrode, ZAB cyclability is reduced with increasing crosslinker concentration. As mentioned in Section 5.3.1, diffusion of zincate ions dominates when the polymer mesh size is reduced. Zincate ions can accumulate at the Zn surface leading to formation of a ZnO insulating layer which terminates the discharge process and inhibits the reverse conversion to metallic Zn, limiting battery capacity and rechargeability [239, 244]. EDX analysis of the Zn electrode surface was done after cycling batteries operating with aqueous and polymer electrolytes (Figure S5.6). Semi-quantitative data was obtained and the results are summarized in Table 5.1. The Zn electrode was not passivated in the aqueous solution, but the amount of ZnO coverage on the surface of the Zn electrode increased from about 67% to 100% for ZABs using PAA–KOH with 0.3 mol% and 0.9 mol% MBAA, respectively, indicating that passivation is a major cause for failure of ZABs with polymer electrolytes during cycling.

Table 5.1. EDX analysis of Zn surface after cycling test at  $5 \text{ mA cm}^{-2}$

	<i>at%C</i>	<i>at%K</i>	<i>at%O</i>	<i>at%Zn</i>	<i>%ZnO</i>
6 M KOH	33.9	0	0	66.1	<b>0</b>
MBAA 0.3	39.2	7	41.4	12.4	<b>67</b>
MBAA 0.9	37.8	10.6	43.7	7.9	<b>100</b>

#### 5.4. Conclusions

Poly(acrylic acid) impregnated with potassium hydroxide (PAA–KOH) using various crosslinker (N,N'-methylenebis(acrylamide) or MBAA) concentrations was synthesized for use as a gel polymer electrolyte for Zn-air batteries (ZABs). The effects of crosslinking density on rheological properties, sol-gel fraction, conductivities and water retention abilities of PAA–KOH

were evaluated. A low concentration of MBAA (0.3 – 0.5 mol%) was sufficient to fabricate an effective hydrogel electrolyte; higher crosslinking densities result in lower ionic conductivity and higher water evaporation rates. ZABs using a bifunctional air electrode, consisting of a gas diffusion layer (GDL) support with a MnO<sub>x</sub>/CoFe catalyst layer and PAA–KOH with 0.3 mol% or 0.5 mol% MBAA as the electrolyte, had better initial efficiencies than batteries with aqueous electrolytes (60% vs. 55%) and were relatively stable for at least 100 cycles (53% efficiency). Failure analysis of the Zn electrode after cycling shows that a higher crosslinker content in PAA–KOH can help reduce dendrite formation and shape change of Zn electrode, but facilitates passivation of the Zn surface.

## 5.5. Supporting information

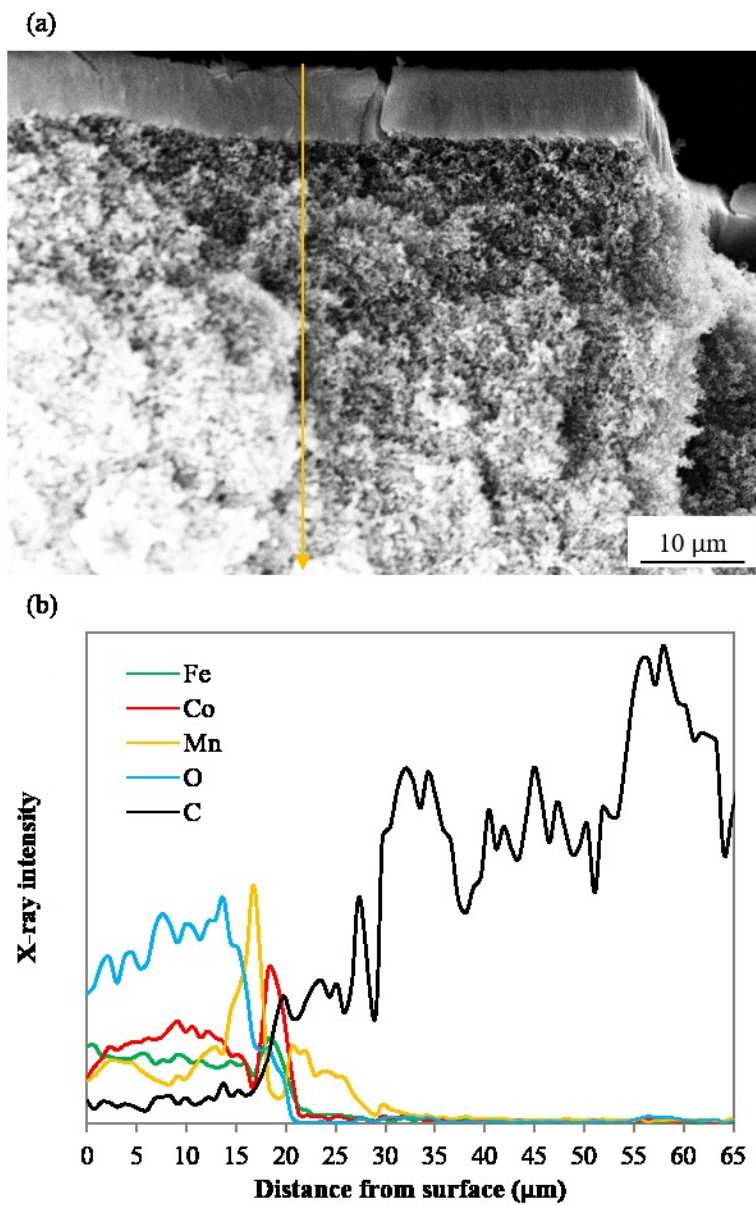


Figure S5.1. (a) Cross section SEM SE image of catalysts on GDL. (b) EDX line scans through the depth of the catalyst layer and GDL.

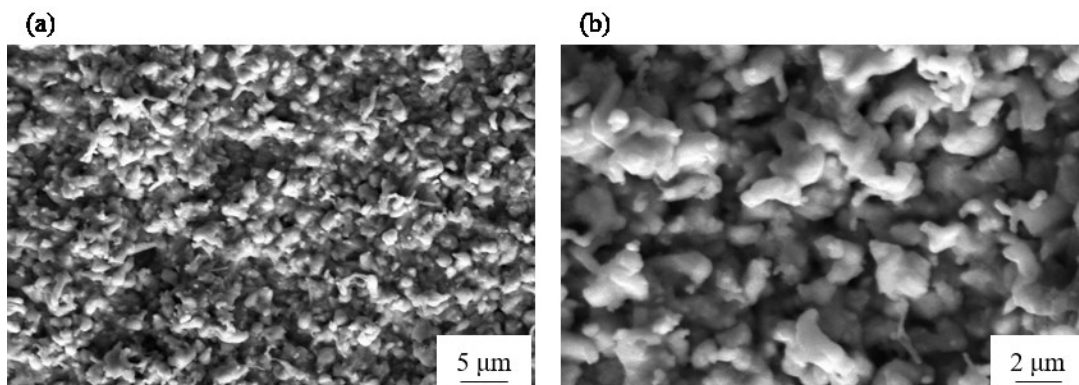


Figure S5.2. SEM SE images showing the morphology of Zn electrode from ZAB with 0.3 mol% MBAA after 120 cycles at  $5 \text{ mA cm}^{-2}$ : (a) low magnification and (b) high magnification.

A 90° peeling test was conducted to determine the peeling strength of the fabricated PAA on the GDL using an Instron 5943. PAA on a GDL was secured to a platform and then a poly(ethylene terephthalate) (PET) film was placed on top by applying pressure with the index finger. The PET pad was attached to a set of upper clamps and was peeled mechanically from the GDL at a speed of  $10 \text{ mm min}^{-1}$ . The peeling strength ( $\text{N mm}^{-1}$ ) was calculated by dividing the highest load (N) from the peeling test by the width (mm) of the bonded pad. PAA adheres more strongly to PET than to the GDL (Figure S5.3b), allowing for measurement of the adhesion strength of PAA on the GDL. PAA becomes less tacky with increasing MBAA content (Figure S5.3c) and peels away from the PET first but remains on the GDL.

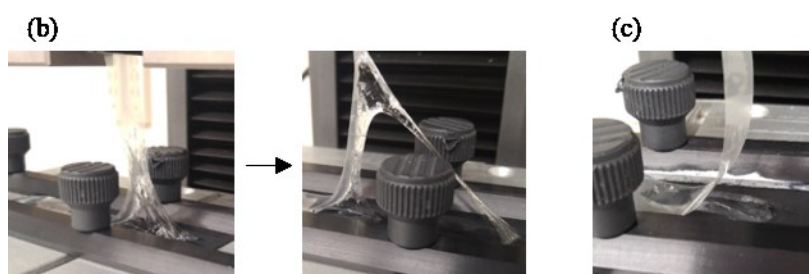
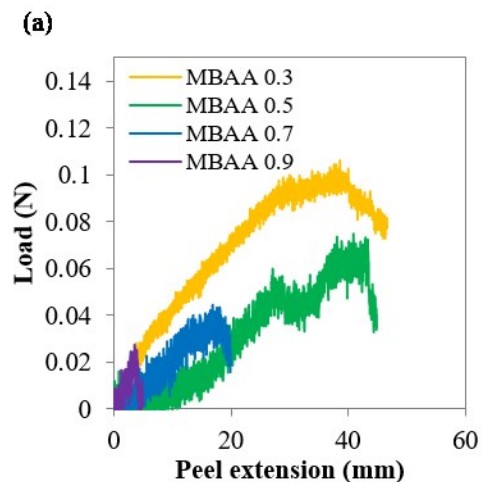


Figure S5.3. (a) Peeling test between PAA–KOH, with different MBAA content, and the GDL. Photographs demonstrating the different adhesive behavior between GDL and (b) 0.3 mol% MBAA and (c) 0.9 mol% MBAA. In (b), the 0.3 mol% MBAA sample adheres to both surfaces (PET and the GDL) and peels away from the GDL during testing. In (c), the 0.9 mol% MBAA sample is easily removed from both surfaces.

Table S5.1. Calculated peeling strength values between PAA and GDL

MBAA (mol%)	0.3	0.5	0.7	0.9
Peeling strength (N mm <sup>-1</sup> )	0.01	0.007	0.004	0.002*

\* Represents the peeling strength between PAA and PET.

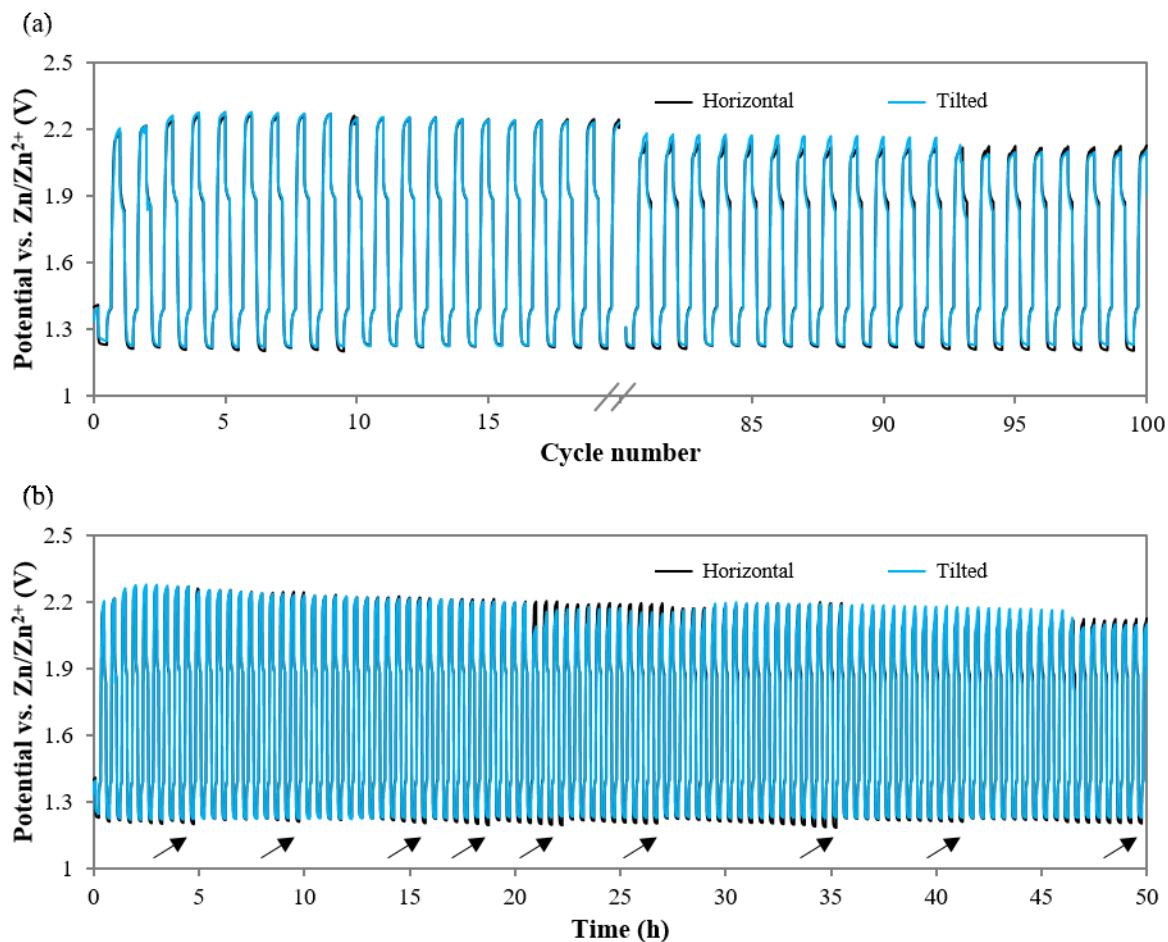


Figure S5.4. Cycling performance of ZAB using 6 M KOH (aqueous) in horizontal and tilted placements. (a) Cell potential as a function of cycle number with the first 20 and last 20 cycles shown. (b) Full cycling performance as a function of time. The arrows indicate when the discharge voltage recovers after oxygen bubbles escape.

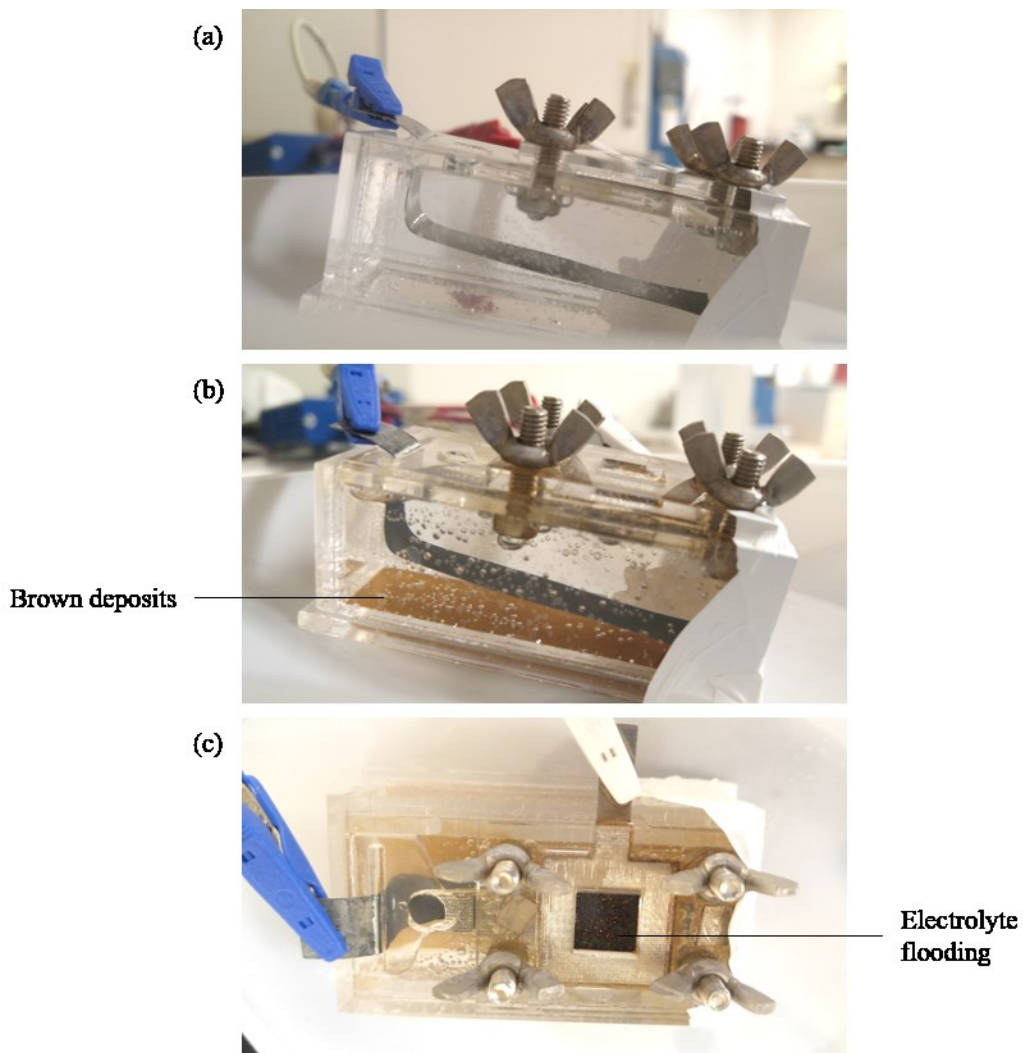


Figure S5.5. Photographs of a ZAB with an aqueous electrolyte (6 M KOH), (a) before cycling and (b–c) after cycling. The side view of the ZAB (b) shows evidence of catalyst degradation in the form of a brown deposit at the bottom of the cell. The top view of the ZAB (c) shows that electrolyte has seeped through the GDL.

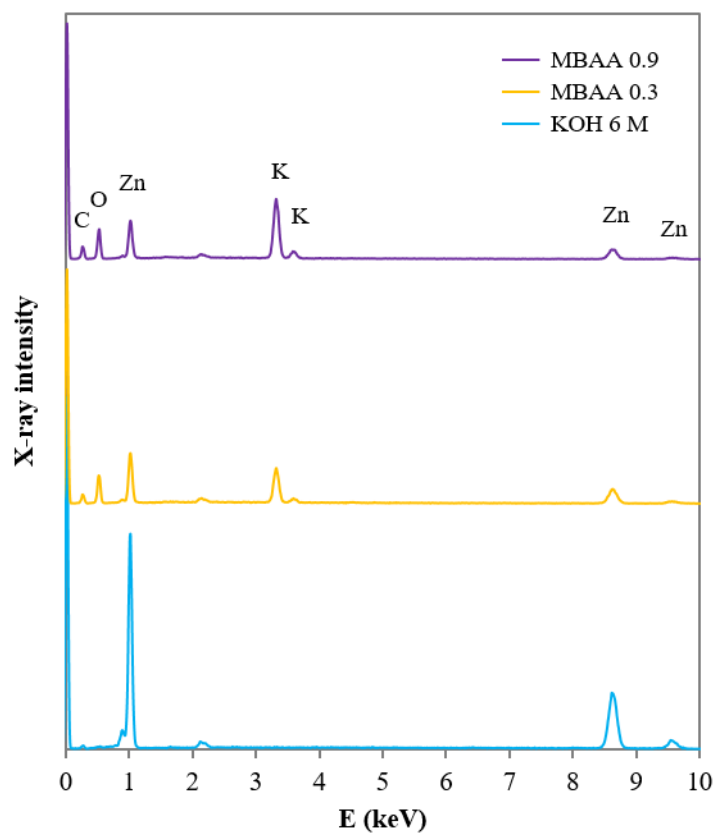


Figure S5.6. EDX spectra of Zn electrodes after cycling with an aqueous electrolyte (6 M KOH) and with PAA-KOH containing 0.3 mol% and 0.9 mol% MBAA.

## Chapter 6. Compositional Effects of Gel Polymer Electrolyte and Battery Design for Zinc-air Batteries

A version of this chapter has been accepted as:

Tran, T.N.T., Aasen, D., Zhalmuratova, D., Labbe, M., Chung, H.-J. and Ivey, D.G., *Compositional Effects of Gel Polymer Electrolyte and Battery Design for Zinc-Air Batteries*. Batteries and Supercaps, 2020. doi:10.1002/batt.202000054.

### 6.1. Introduction

Compared to other batteries and capacitors, Zn-air batteries (ZABs) offer several advantages, e.g., safety, low cost and high specific energy density ( $1218 \text{ Wh kg}^{-1}$ ) [12]. To avoid complexities in the construction of flexible batteries, gel polymer electrolytes (GPEs) are used to contain alkaline, aqueous solutions in a polymer host. As alternatives to aqueous electrolytes, GPEs prevent flooding of the air electrode and leakage concerns associated with liquid electrolytes, inhibit dendrite formation on the Zn electrode and reduce carbonation at the air electrode. In fact, GPEs are widely employed in energy storage devices because they are safe and flexible, making them adaptable to various designs; some can be engineered to be thermally responsive or self-healing [245, 246].

The popular choices for the polymer host include poly(ethylene oxide) (PEO), poly(vinyl alcohol) (PVA), polyacrylamide, cellulose, gelatin and poly(acrylic acid) (PAA), as well as dual-network gels that are based on these polymers [67, 74, 209, 247-251]. Since 2002, PVA–KOH has become the alkaline GPE of choice with an ionic conductivity in the range of  $1 - 100 \text{ mS cm}^{-1}$ ; conductivity depends on electrolyte content and concentration in the GPE [70-73, 127]. On the

other hand, PAA–KOH has a much higher conductivity ( $200 - 460 \text{ mS cm}^{-1}$ ) due to its hydrophilicity and can be fabricated via one-pot synthesis since acrylic acid monomers are miscible with highly concentrated KOH, which eliminates the need for solvent-casting or dialyzing processes [166]. Most research work up to now has focused on utilizing PAA-based GPEs' mechanical durability for flexible [212-214] and stretchable ZAB applications [250]. To the best of our knowledge, PAA–KOH composition has previously been optimized solely based on ionic conductivity for primary Al-air batteries [75]. The optimized product contained  $\sim 8.2 \text{ M}$  of KOH,  $1 \text{ M}$  of PAA and  $74 \text{ mM}$  of crosslinker before percolation. For rechargeable applications, the effects of gel composition, including additives, and gel mechanical properties on battery performance require further investigation.

KOH provides the electrolytic ion species to GPEs and additives can be incorporated in GPEs to improve the cycle life of ZABs. Zinc compounds, such as zinc chloride ( $\text{ZnCl}_2$ ), zinc oxide ( $\text{ZnO}$ ) or zinc acetate ( $\text{Zn}(\text{Ac})_2$ ), are reported to generate zincate ions and act as a corrosion inhibitor [252-254]. These materials can be incorporated in the Zn electrode or mixed in the electrolyte. Park et al. reported that ZnO is the most soluble substance of the three compounds in alkaline solutions. Thus, after the first charging process, the highest discharge capacities were obtained from a Zn anode with ZnO. Additionally, since more zincate ions were generated, better reversibility of the zincate ions during charging was achieved for ZnO compared with the other zinc compounds [254]. On the other hand, several reports use aqueous alkaline electrolytes that are pre-saturated with ZnO powder ( $\sim 0.6 \text{ M}$ ) [90, 191-194]. The optimal amount of ZnO appears not to have been identified; e.g., Gaikwad et al. prepared PAA in saturated ZnO [105], while some others do not use any additives [251]. Although ZnO is considered to be helpful for the oxygen evolution reaction (OER), excessive amounts of ZnO may reduce the conductivity of GPEs and

trigger early passivation. Therefore, identifying an optimized amount of ZnO in PAA–KOH gel is needed.

Even though Li-ion batteries (LIBs) are commercially available for electric vehicles (EVs) with a full charge range from 200 to 400 km, their energy density is not entirely adequate for EVs. Compared with ZABs, LIBs have a lower theoretical specific energy ( $260 \text{ Wh kg}^{-1}$ ) [255]. The capacity of LIBs for current EVs, such as the Renault Twizy, Hyundai Ioniq, Nissan Leaf and VW E–Golf, often range from 6 to 30 kWh [256]. Targets set by the United States Advanced Battery Consortium LLC for EVs require power supply voltages of 220 V – 420 V with usable energy of 45 kWh [257]. From a practical point of view, however, it is very challenging to obtain an efficient electrically rechargeable ZAB. This involves a stack consisting of hundreds of ZAB cells in series to raise the voltage to the required level. However, ZABs can act as a range extender in conjunction with a LIB pack. Solid-state ZABs, which are cheaper than LIBs and more resilient against shock, vibration and high temperature than aqueous ZABs, can provide a compact, lower power, continuous discharging source for EVs and home grid energy storage [43, 177]. A conventional ZAB which is constructed in a planar arrangement where one Zn electrode is paired with one air electrode has a theoretical open circuit voltage of  $\sim 1.6 \text{ V}$ . In Chapter 4, tri-electrode ZABs with PAA showed promising performance in terms of cycling stability [211]. However, in a commercial battery pack, a tri-electrode design would be complex. On the other hand, an alternative to a tri-electrode cell design is a configuration with two bifunctional air electrodes located on either side of the Zn electrode. This design increases the air electrode area without significantly increasing the cell volume, which helps to enhance the specific power of a ZAB considerably. This single cell design is made more feasible when employing GPEs, since the solid

nature and hydrophilicity of the polymer network can prevent leakage issues associated with liquid electrolytes.

In this study, two inevitable issues are addressed that secondary ZABs experience during operation: (1) There is an increase in volume and pressure during the oxygen reduction reaction (ORR) and (2) oxygen bubbles are released during the OER. Herein, we hypothesize that stiffness and stickiness of a GPE are particularly important to a rechargeable ZAB; e.g., a weaker GPE can undergo deformation to accommodate the volume change of the battery and a less adhesive GPE on the air electrode allows space for oxygen bubbles to coalesce and escape. Therefore, the first objective of this study is to address the effects of the physical properties of GPEs on battery performance by varying the concentrations of monomers and crosslinkers. The second objective is to find an optimized amount of Zn compound (either ZnO or Zn(Ac)<sub>2</sub>) as an additive in GPEs. Finally, a complete comparison of cell configurations is demonstrated. A PAA-based GPE is chosen because of its availability, safety and facile fabrication, which involves one-step polymerization of monomers in an alkaline KOH precursor solution. In this sense, this study stands as a starting point for the research of GPEs in solid-state rechargeable ZABs in grid energy storage devices and EV applications.

## **6.2. Experimental procedure**

### **6.2.1 Synthesis of catalysts**

All chemicals were of analytical grade and used as received without further purification. Iron(II) sulfate (FeSO<sub>4</sub>·7H<sub>2</sub>O), cobalt(II) acetate (Co(CH<sub>3</sub>COO)<sub>2</sub>·4H<sub>2</sub>O), sodium hydroxide (NaOH) and ethanol were obtained from Fisher. Nafion (5% w/w in water and 1-propanol) was obtained from Alfa Aesar. Nitrogen-doped multiwalled carbon nanotubes (N-CNTs) (30 – 50 nm diameter, 1 – 2 μm length) were obtained from MKnano. The gas diffusion layer (GDL) (Teflon-

coated porous carbon paper, Sigracet 39 BB) was obtained from the Fuel Cell Store. Deionized water (DIW) was used to rinse and prepare all aqueous solutions.

GDL impregnated with (Co,Fe)<sub>3</sub>O<sub>4</sub> decorated N-CNTs was utilized as the bifunctional air electrode; details regarding fabrication and characterization of the catalysts can be found in reference [258]. Briefly, N-CNTs (50 mg), FeSO<sub>4</sub>·7H<sub>2</sub>O (175 mg), Co(CH<sub>3</sub>COO)<sub>2</sub>·4H<sub>2</sub>O (35 mg) and NaOH (80 mg) were stirred in 10 mL of ethanol at 800 RPM for 10 min. The suspension was sonicated for 5 h and then Nafion (1 mL) and ethanol (15 mL) were added to the catalyst suspension. To prepare air electrodes, the GDL was sectioned into 4.5 cm diameter circles and soaked in the catalyst suspension for 20 min under sonication. Afterwards, 5 mL of the catalyst suspension was vacuum filtered through each substrate. The GDL pieces were annealed at 300 °C for 30 min. The mass loading of catalysts on the GDL was ~2.5 mg cm<sup>-2</sup> [258].

### 6.2.2. Synthesis of hydrogel electrolyte

PAA-KOH was used as the hydrogel electrolyte in this work. Acrylic acid (AA) (containing 200 ppm mequinol as inhibitor), N,N'-methylenebis(acrylamide) (MBAA) and potassium persulfate (KPS) were obtained from Sigma-Aldrich, while solid potassium hydroxide (KOH), zinc oxide (ZnO) and zinc acetate (Zn(Ac)<sub>2</sub>) were obtained from Fisher. PAA-KOH was prepared by mixing the AA monomer, MBAA crosslinker and KPS thermoinitiator in a KOH solution with varying concentrations, as shown in Table 6.1. The solutions were mixed using a vortexer. The electrolyte solutions were kept in an oven at 60 °C for 1 h to carry out polymerization and then allowed to cool overnight to room temperature. The concentration of KPS was fixed at 1.5 mM, which is consistent with our previous studies [211, 259]. Different concentrations of PAA were utilized, i.e., 0.25, 0.5, 1, 1.5 and 2 M, and the KOH concentration was increased accordingly to ensure there was at least 6 M KOH in the PAA-KOH network. The samples are denoted as P-

K1, P-K2, P-K3, P-K4 and P-K5, respectively. The crosslinker amount was adjusted to the minimum value for the PAA-KOH samples to exhibit gel-like structural consistency. For P-K1, the minimum crosslinker amount to prepare a gel-like sample could not be identified, since a gel-like consistency was not observed even when the MBAA concentration reached the solubility limit (Table S6.1, Figure S6.1).

Table 6.1. Compositions of PAA-KOH samples

Sample	KOH (M)	PAA (M)	MBAA (mM)	KPS (mM)	Final state
<b>P-K1</b>	6.25	0.25	130*	1.5	Liquid-like
<b>P-K2</b>	6.5	0.5	30	1.5	Gel-like
<b>P-K3</b>	7	1	7	1.5	Gel-like
<b>P-K4</b>	7.5	1.5	5	1.5	Gel-like
<b>P-K5</b>	8	2	3	1.5	Gel-like

\*Solubility limit

The concentration of ZnO or Zn(Ac)<sub>2</sub> in the PAA-KOH electrolyte was also varied; i.e., 0, 0.1, 0.25, 0.4 and 0.5 M, in order to evaluate their effect on ZAB performance. The different concentrations of the additives were added separately until the gel color turned opaque, indicating the supersaturation of ZnO or Zn(Ac)<sub>2</sub> (Figure S6.2).

### 6.2.3. Cell fabrication

Two designs for bi-electrode ZABs were fabricated and are shown in Figure 6.1. In general, a ZAB using PAA-KOH as the electrolyte can be fabricated as stacked layers using acrylic sheets as the battery casing. A conventional design is shown in Figure 6.1a in which one air electrode is positioned on top with one Zn electrode below. Most experiments in this work were conducted using this cell. To exploit the benefits of the solid hydrogel electrolyte, a double air electrode design was used and compared with the single air electrode design (Figure 6.1b). In the double air

electrode design, the Zn electrode is sandwiched between two bifunctional air electrodes. The contact area between the air electrode and the electrolyte was controlled (1 cm<sup>2</sup> each side) and the thickness of the Zn sheet was 0.2 mm. The GPE thickness was 3 mm.

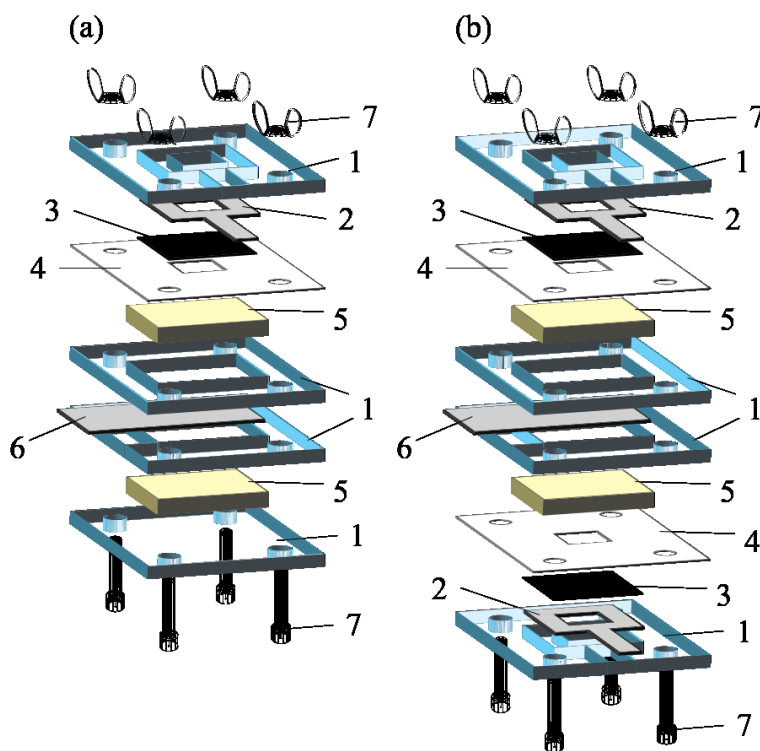


Figure 6.1. Homemade cell assembly for bi-electrode ZABs. (a) Single air electrode (SAE) and (b) double air electrode (DAE) designs. 1) Acrylic sheets, 2) Ni current collector, 3) GDL impregnated with (Co,Fe)<sub>3</sub>O<sub>4</sub> decorated N-CNTs, 4) polypropylene film, 5) PAA-KOH, 6) Zn, 7) bolts and nuts.

#### 6.2.4. Materials characterization

Conductivities of aqueous electrolyte solutions were measured with a conductivity probe (Mettler Toledo InLab 731-ISM). Conductivities of PAA-KOH were evaluated by electrochemical impedance spectroscopy (EIS) at open circuit potential with an applied 10 mV AC potential from 100 kHz to 10 mHz using a potentiostat/galvanostat (Autolab PGSTAT302N).

Mechanical properties of the gels were measured using a tensile tester (Instron 5943) at a rate of 10 mm min<sup>-1</sup> until failure (Figure S6.3). The force and initial cross-sectional area of the samples were used to calculate engineering stress, and the displacement and initial length were used to obtain engineering strain. Ultimate tensile strength was calculated from *Equation 6.1* while elongation at break was calculated by *Equation 6.2*, where  $F_{\max}$ ,  $A_o$ ,  $\Delta L$ , and  $L_o$  are the maximum force, initial area, the change in length and original length of the samples, respectively. Young's modulus was calculated from the slope within the linear strain region.

$$\sigma_{\text{UTS}} = \frac{F_{\max}}{A_o} \quad \text{Equation 6.1}$$

$$\text{EL}\% = \frac{\Delta L}{L_o} \quad \text{Equation 6.2}$$

A 90° peeling test was conducted to determine the peeling strength between the fabricated PAA–KOH and the GDL substrate using an Instron 5943. PAA–KOH on the GDL was secured to a platform and then a Canon Type E transparency film was placed on top by pressing with the index finger. The transparency film was attached to a set of upper clamps and was peeled mechanically from the GDL at a speed of 50 mm min<sup>-1</sup> (Figure S6.4). The peeling strength (mN mm<sup>-1</sup>) was calculated by dividing the average load (mN) of the peeling test by the width of the bonded pad (10 mm). Comparing the GDL and transparency film, PAA was stickier on the transparency film, allowing for the measurement of the adhesion strength of PAA on GDL.

The weight fraction of KOH was determined by the ratio of 6 M KOH mass equivalent in the medium that contributed to the ionic conductivity over the total mass of the PAA–KOH gel. The volume fraction of AA was determined by the ratio of volume of AA added over the total volume of PAA–KOH gel.

### 6.2.5. Battery testing

Before and after cycling, EIS measurements were performed with 10 mV AC potential from 100 kHz to 10 mHz at 1.2 V vs. Zn/Zn<sup>2+</sup> to reveal bulk, interfacial and charge transfer resistance. For rate testing, battery potential was measured by a galvanostatic method at a series of current densities of 2, 5, 10 and 20 mA cm<sup>-2</sup> for 5 min each with cut-off voltages of 0.6 V (discharge) and 2.5 V (charge), unless specified otherwise.

The time for charging a fresh ZAB with 0.25 M of ZnO in the PAA–KOH gels at 20 mA cm<sup>-2</sup> was determined to be ~2 h from *Equation 6.3*, where I is applied current (A), z is the number of electrons transferred, N is amount of ZnO (mol), F is the Faraday constant and t is charging time (s).

$$I = \frac{zFN}{t} \quad \text{Equation 6.3}$$

Cycling tests were also done through a galvanostatic method, with 30 min per cycle, using another potentiostat/galvanostat (Biologic VSP-300). The battery was discharged and charged at 10 or 20 mA cm<sup>-2</sup> for 10 min and the circuit was kept open for 5 min between steps. The discharge-charge efficiency was calculated by dividing the lowest discharge potential by the highest charge potential during the second cycle and the last cycle.

Specific capacity was calculated from the galvanostatic discharge and normalized to the mass of consumed Zn from *Equation 6.4*, where C is specific capacity (mAh g<sub>Zn</sub><sup>-1</sup>), I is discharge current (A), t is discharge time (s) and m is the mass of consumed Zn (g).

$$C = \frac{It \times 1000}{m \times 3600} \quad \text{Equation 6.4}$$

## 6.3. Results and discussion

### 6.3.1. Evaluation of PAA–KOH gel electrolytes

The conductivity of an alkaline solution with a concentration of 6 to 6.5 M KOH reaches a maximum value of  $\sim 650 \text{ mS cm}^{-1}$  at room temperature (Figure 6.2a). At higher concentrations, the conductivity decreases because excess charge carriers ( $\text{K}^+$  and  $\text{OH}^-$ ) increase solution viscosity and resistivity. These values are also in agreement with literature data [50, 260, 261]. The conductivities of alkaline solutions containing AA monomers are reduced; e.g., the highest values are 608, 571, 501, 438 and  $383 \text{ mS cm}^{-1}$  for solutions containing 0.25, 0.5, 1, 1.5 and 2 M AA, respectively. The peak conductivities are also shifted towards higher concentrations of KOH; e.g., the highest conductivity of an electrolyte with 2 M AA is obtained at 8 M KOH, which can be ascribed to compensation of charge carriers between the hydroxide ions and carboxyl groups of AA monomers. Understanding this offset effect is important to achieve a GPE with a high conductivity, which is vital in obtaining high battery performance.

As shown in Figure 6.2b, the conductivities of all PAA–KOH gels are significantly reduced to  $\sim 280 \text{ mS cm}^{-1}$ . This can be readily understood by the conductivity equation,  $\sigma = Nze\mu$ , where  $\sigma$  is the ionic conductivity,  $N$  is the number of ions (anions or cations) present per unit volume,  $z$  is the valence of the ion,  $e$  is the electron charge and  $\mu$  is the mobility of the ions [78]. Upon polymerization, the presence of a polymeric network decreases both the  $N$  and  $\mu$  values, leading to a decrease in  $\sigma$ . Here, the decrease in  $N$  is due to the volume fraction occupied by the immobile polymer network and the decrease in  $\mu$  can be explained by the reduced apparent mobility of  $\text{K}^+$  and  $\text{OH}^-$  ions by the presence of the polymer network.

Thermodynamic behavior of the ternary KOH–ZnO–H<sub>2</sub>O system was experimentally investigated by Dirkse in 1959. In aqueous electrolyte, ZnO was found to be saturated at 0.5 M in 6 M KOH [262]. Several studies reported that ionic conductivities decreased with increasing amount of ZnO [262, 263]. In agreement with the literature, the addition of 0.25 M ZnO reduces ionic conductivity of PAA–KOH gels; e.g., the conductivities of P–K2 and P–K5 gels decrease to 237 and 186 mS cm<sup>-1</sup>, corresponding to a reduction of 15 to 30% of the initial conductivity, respectively. As shown in Figure 6.2c, P–K2 has a slightly higher weight fraction of KOH (28.1 vs 27 w/w%, respectively) and 4 times lower volume fraction of PAA than P–K5, while both have similar ionic conductivities of ~280 mS cm<sup>-1</sup>. After adding 0.25 M ZnO, the volume of PAA in the gel remains unchanged; e.g., 3.4 vs 13.7 v/v% for P–K2 and P–K5, respectively. However, the weight fraction of KOH for all GPEs is further reduced at 5 w/w%. According to real-solution studies (without polymeric host), all the 0.25 M ZnO appears to be Zn(OH)<sub>4</sub><sup>2-</sup> in a highly alkaline solution (~6.5 M KOH) [264]. Although zincate ions are not the dominant charge carriers, they form tetrahedral structures with OH<sup>-</sup> ions, which results in a decrease in the net charge carrier ion concentration (N value of [OH<sup>-</sup>]). The presence of the large ionic complex may also affect the overall mobility of the charge carrier ions. In addition, it can also be postulated that a larger amount of PAA will lead to a smaller mesh size between polymeric networks that can effectively block large ions such as zincate ions. In Chapter 5, the authors found similar effects for PAA-based gels with varying concentrations of crosslinker [259].

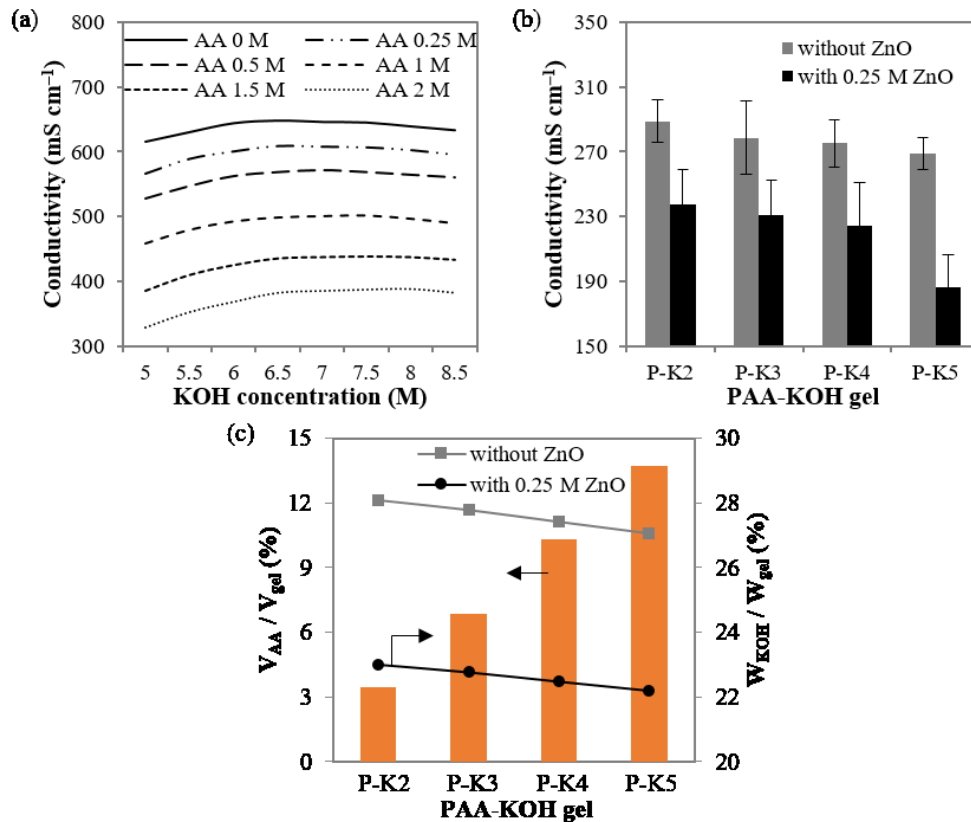


Figure 6.2. Evaluation of PAA-KOH. (a) Conductivity of aqueous electrolytes, with different amounts of AA monomer, as a function of KOH concentration. (b) Conductivity of PAA-KOH, with and without ZnO, as a function of PAA concentration. (c) Mass ratio of 6 M KOH and volume ratio of AA contained within the PAA-KOH gels.

Although ZnO decreases the conductivity of PAA-KOH gels, it can help to reduce water activity and Zn corrosion which helps to minimize shape change and dendrite formation [52, 190, 265]. Having zincate ions readily available in the electrolyte can also benefit the charging process [211]. OER rate testing was done for PAA-KOH gels with and without ZnO added (P-K2-ZnO and P-K2, respectively); the batteries were first discharged and then charged twice afterwards (Figure 6.3a). The charging curves for P-K2-ZnO exhibit essentially the same behavior. However, if no ZnO is added to the electrolyte (P-K2), the OER potential is only low at current densities of 2 and 5 mA cm<sup>-2</sup> for the first charging step and then becomes significantly larger at higher current densities, particularly for the second charging process. Since discharge is performed at all current

densities before charging, the zincate ion formation reaction ( $\text{Zn} + 4\text{OH}^- \rightarrow \text{Zn}(\text{OH})_4^{2-} + 2\text{e}^-$ ) has already occurred and the zincate ion discharge product accumulates near the Zn electrode surface. The product is readily consumed during charging at current densities of 2 to 5  $\text{mA cm}^{-2}$ . By the time a higher current density of 10  $\text{mA cm}^{-2}$  is reached, the zincate ions become depleted, so that a higher potential is required. Adding ZnO or  $\text{Zn}(\text{Ac})_2$  to the electrolyte ensures that the zincate ion concentration remains high enough to facilitate OER.

An attempt was made to compare the effects of the additives. Newly made batteries with different concentrations of ZnO or  $\text{Zn}(\text{Ac})_2$  were subjected to charging at 20  $\text{mA cm}^{-2}$  (Figure S6.5). Without any additives the ZAB reached the cut-off voltage virtually instantaneously. As the additive concentration is increased, the battery can maintain the charging potential for a longer period of time indicating that more zincate ions are available with a higher concentration of additives. In general, ZnO performs better as an additive than  $\text{Zn}(\text{Ac})_2$  in the gel electrolytes; as such, subsequent testing used only ZnO as an additive. An additive concentration of 0.5 M was the highest to be investigated since the gel became opaque (Figure S6.2). Increasing the zincate ion concentration in the vicinity of the Zn electrode surface can also result in faster passivation of the Zn electrode through the following reaction:  $\text{Zn}(\text{OH})_4^{2-} \rightarrow \text{ZnO} + \text{H}_2\text{O} + 2\text{OH}^-$  [266, 267]. Figure 6.3b shows the combined effects of discharging and different concentrations of ZnO added to GPEs on charging profiles at 20  $\text{mA cm}^{-2}$ . For this experiment, cut-off voltages for discharge and charge were adjusted to 0.9 V and 2.2 V, respectively, because the thickening passive film could hamper the charging reaction. In other words, as the passive layer grows, there is less Zn active area for the charging reaction so that a high current density will require a higher voltage [24, 239]. It can be seen that the discharging time is prolonged by 1.4 h with the addition of 0.25 M ZnO (discharging times of 6.9 h and 8.3 h for P-K2 and P-K2-0.25 M ZnO, respectively). Even

with a supersaturated amount of ZnO, the battery can still last for 7.3 h (P-K2-0.5 M ZnO). For the charging process, batteries without ZnO can maintain charging for 5.7 h. The charging time increases to 7.2 h for 0.1 M ZnO and stabilizes at ~9.5 h for 0.25 to 0.5 M of ZnO. This result clearly shows that ZnO has positive effects on both discharging and charging for rechargeable ZABs, while an excessive amount of ZnO is not beneficial for discharging. The optimum amount of ZnO was determined to be 0.25 M and was used for all subsequent tests. All PAA-KOH gels are denoted as P-K-ZnO hereafter for simplicity.

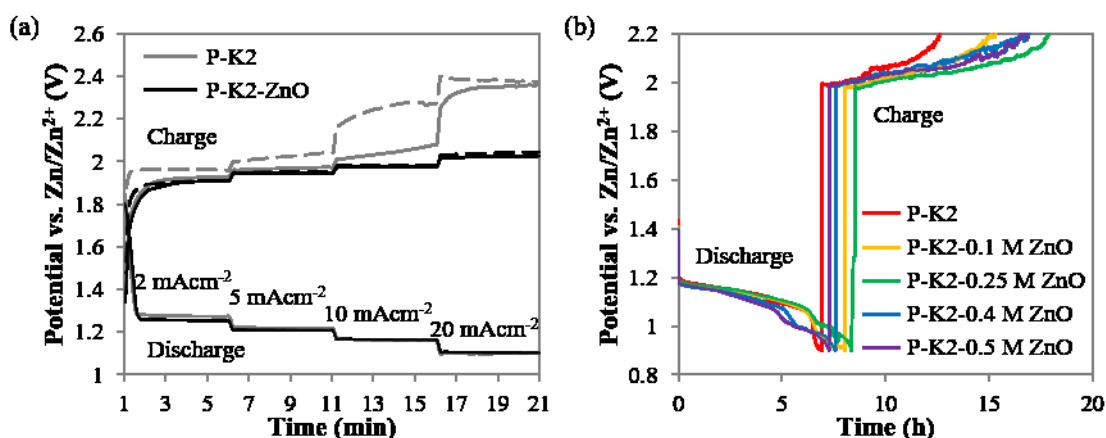


Figure 6.3. Electrochemical evaluation of PAA–KOH gels with various concentrations of ZnO. (a) Rate test with the sequence discharge-charge-charge for ZABs using P–K2, with and without 0.25 M ZnO, at different current densities. Dashed lines represent the second charging cycle. (b) Discharge-charge curves for ZABs using different concentrations of ZnO in P–K2 gels at a current density of 20 mA cm<sup>-2</sup>.

Mechanical properties of hydrogels depend on the types and concentrations of crosslinking agents and polymeric monomers, as well as synthetic processes. Stress-strain and load-strain curves for as-prepared PAA–KOH gels are shown in Figure 6.4, while Young’s moduli and peeling strengths calculated from Figure 6.4a–b, respectively, are listed in Table 6.2. With increasing AA content, tensile strength first increases and then decreases because it depends on both the concentration of AA monomers and the concentration of MBAA crosslinkers. Since these amounts vary simultaneously, no particular trend is observed for tensile strength. The elongation at failure increases with increasing amount of crosslinker (Figure 6.4a). Tensile strength is lowest at ~0.1 kPa for P–K2–ZnO and highest at 4.6 kPa for P–K4–ZnO. The elongation at failure increases from 0.7 to 9.7 mm/mm for P–K2–ZnO and P–K5–ZnO, respectively.

The tackiness of hydrogel electrolytes on the GDL can be assessed by both the adhesive force and the corresponding displacement (Figure 6.4b). All samples showed mostly adhesive failure which means delamination at the interface, while cohesive failure is associated with tearing

of the PAA–KOH gels [268, 269]. In this study, the average force after the maximum detachment force is considered as a measure of adhesive force [270]. P–K2–ZnO has the lowest adhesive force of 0.004 N. Adhesive force increases drastically with higher concentration of AA; e.g., P–K3–ZnO, P–K4–ZnO and P–K5–ZnO have forces of 0.045, 0.085 and 0.18 N, respectively. Different peeling behaviors for these gels are also shown in Figure S6.4. The aim of the mechanical tests is to evaluate various characteristics related to the synthesis parameters and network formation of the weak hydrogel electrolytes and to propose how their properties may affect battery performance, which is further discussed in Section 6.3.2. More specifically, the hydrogel stiffness can affect the ability of ZABs to accommodate volume changes in the battery during discharge and charge processes, while the stickiness of gel electrolytes on GDL may be correlated to the efficiency in removing oxygen bubbles during the charging process.

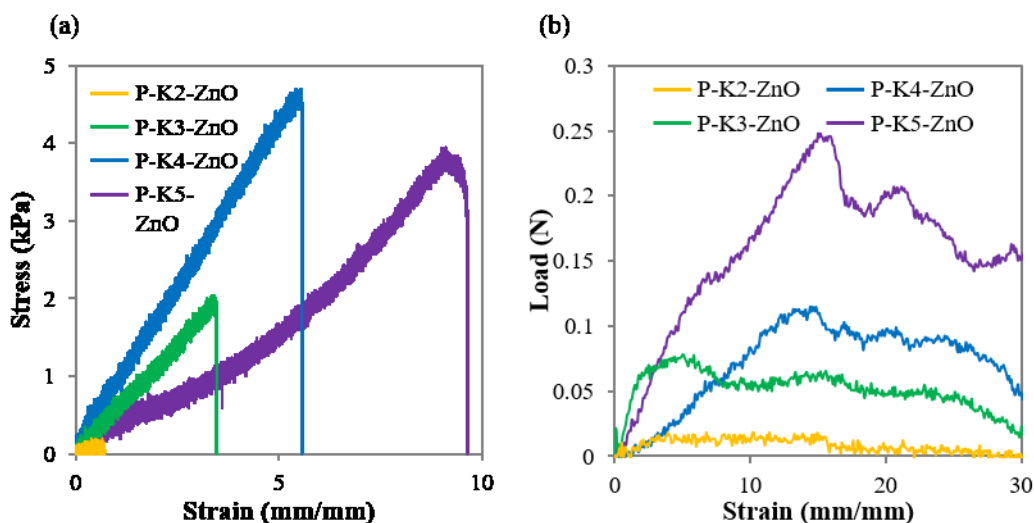


Figure 6.4. Mechanical properties of PAA–KOH gels. (a) Tensile stress–strain curves at a rate of  $10 \text{ mm min}^{-1}$  and (b) peeling strengths of PAA–KOH on GDL at a rate of  $50 \text{ mm min}^{-1}$ .

Table 6.2. Mechanical property parameters for PAA–KOH

Samples	P–K2–ZnO	P–K3–ZnO	P–K4–ZnO	P–K5–ZnO
Tensile strength (kPa)	0.2	2.0	4.7	3.9
Elongation (mm/mm)	0.7	3.5	5.7	9.6
Young’s modulus (Pa)	159.6	557.3	829.9	378.5
Peeling strength (mN mm <sup>-1</sup> )	0.4	4.5	8.5	18
Failure mode	Adhesive	Adhesive	Adhesive	Adhesive

### 6.3.2. Effects of PAA matrix on cycling performance of ZABs

Benefiting from their solid-like nature, PAA–KOH electrolytes in ZABs can prevent the leaking and flooding issues that are associated with aqueous solutions. In Figure 6.5a, the discharge-charge rate tests show that PAA content in the network has a negligible effect on short-term battery performance. The efficiencies for each step were calculated by dividing the discharge potential by the charge potential. At current densities of 2, 5, 10 and 20 mA cm<sup>-2</sup>, the discharge-charge efficiencies are respectively ~67, 62.4, 59.1 and 54.7%. However, a high concentration of PAA does have a negative effect on depth of discharge (Figure 6.5b). At 20 mA cm<sup>-2</sup>, the battery capacity is reduced from 163 to 127 mAh for P–K2–ZnO and P–K5–ZnO, respectively. This result is expected based on ionic conductivity measurements, as zincate ions cannot diffuse as easily in a denser polymer network.

To meet stringent criteria for the development of secondary ZABs, gel electrolytes also need to be able to accommodate volume changes and provide bubble management during cycling. It is well-known that during discharge the Zn electrode undergoes a volume expansion due to ZnO formation. Since the mass densities of Zn, Zn(OH)<sub>4</sub><sup>2-</sup> and ZnO are 7.14, 3.05 and 5.61 g cm<sup>-3</sup>, respectively, a completely discharged Zn electrode may increase its active volume by approximately 27% [271]. Such a pronounced change in volume leads to flooding of liquid

electrolyte (for aqueous ZABs) through the large pores of the GDL [272]. In addition, interfacial interaction between the gel electrolyte and GDL plays a key role in bubble management. During charging, oxygen bubbles are produced ( $2\text{OH}^- \rightarrow \frac{1}{2}\text{O}_2 + \text{H}_2\text{O} + 2\text{e}^-$ ) and these bubbles can accumulate between the catalyst layer on the GDL and the electrolyte. In short, a volume increase can occur during discharging when Zn converts to ZnO, or from charging when O<sub>2</sub> bubbles cannot diffuse through the GDL. Elastic/plastic deformation of GPEs allows some room for volume changes of the battery [273]. In order to decouple the volume change caused by discharging, fresh batteries were used for charging tests. Over-charging curves are similar for all PAA compositions (Figure 6.5b). Interestingly, physical breakout through the GDL in batteries using P–K3–ZnO, P–K4–ZnO and P–K5–ZnO electrolytes was observed after 80, 52 and 78 min, respectively, as indicated by the arrows in Figure 6.5b, although the batteries still managed to function until the test ended. After the tests, the ZAB using P–K2–ZnO retains its original appearance, while the batteries with the other PAA–KOH gels exhibit breakthrough of the GDL (Figure 6.5c). Therefore, using GPEs that are sticky may backfire by allowing O<sub>2</sub> to quickly build up inside the battery. It should be noted that the ZAB with P–K4–ZnO had the earliest breakout although it is half as sticky as P–K5–ZnO, and has the highest Young’s modulus. It is speculated that stiffer GPEs do not accommodate deformation, thus the elevated pressure will push the GDL outward sooner.

The electrical resistance of the ZABs was further investigated at 1.2 V before and after cycling at 20 mA cm<sup>-2</sup> (Figure 6.5d). The results are shown in Figure S6.6 and Table S6.2. In general, the total resistance of the as prepared or fresh batteries (9 – 11 Ω) increases after 20 cycles (13 – 22 Ω) due to a variety of reasons including water evaporation, bifunctional catalyst degradation, Zn electrode passivation and oxygen bubble coalescence in the polymer network. The bulk resistance (R<sub>b</sub>) is 0.9 – 1.3 Ω for as prepared batteries and increases to 2 – 3.5 Ω after 20

cycles. The resistance increase of the PAA-based electrolytes may be due to the formation of a froth layer that adheres to the air electrode surface during charging [184]. There is an obvious decrease in the interfacial resistance ( $R_{\text{int}}$ ), which is considered to be the adsorption resistance of the gas species (oxygen in this case) on the air electrode [274]. After cycling, the hydrophobic pores of the air electrode enhance wettability and provide more area for gas adsorption and diffusion.  $R_{\text{int}}$  also contributes the least to the overall battery resistance ( $< 0.3 \Omega$  after 20 cycles). The charge transfer resistance ( $R_{\text{ct}}$ ) is considered to be affected by both the electrocatalytic activity of the catalysts under a fixed applied voltage and the accessible area of active sites [275]. At 1.2 V, oxygen from the air and water from the electrolyte are consumed to produce hydroxide ions ( $\text{O}_2 + 2\text{H}_2\text{O} + 4\text{e}^- \rightarrow 4\text{OH}^-$ ).  $R_{\text{ct}}$  for P-K5-ZnO is significantly higher than that of other gel electrolytes in the as prepared batteries, because of the reduction in mobility and activity of water in the denser hydrophilic polymer network. After cycling, batteries using P-K2-ZnO retained the lowest  $R_{\text{ct}}$  values. This could be due to the influence of the bubble layer that forms between the air electrode and GPEs, which can obstruct the path for  $\text{H}_2\text{O}$  transport to the electrode surface. In order to protect the integrity of ZABs and allow the reverse diffusion of oxygen, P-K2-ZnO was chosen for subsequent cycling tests.

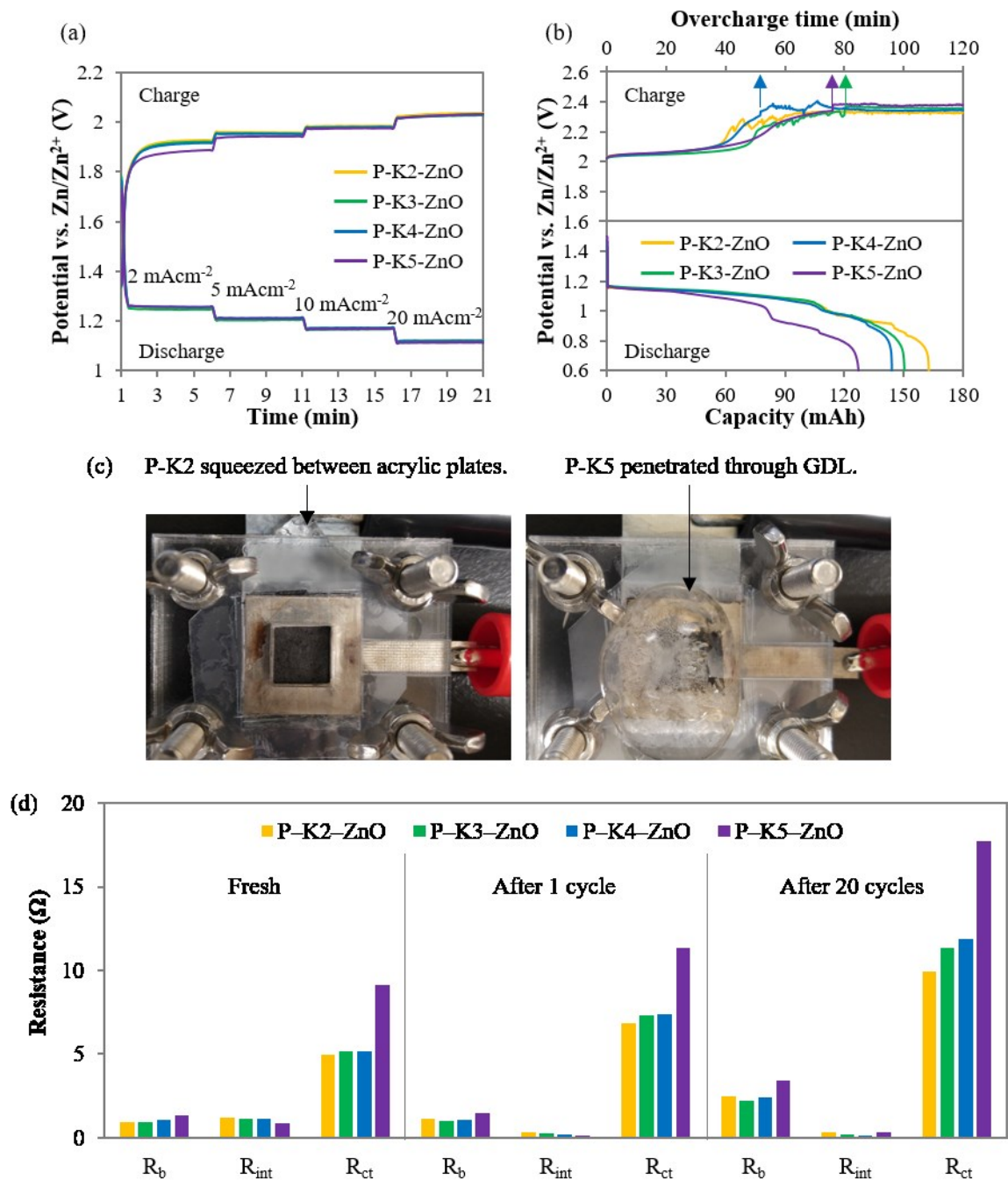


Figure 6.5. Evaluation of ZABs using PAA-KOH with various PAA concentrations. (a) Discharge-charge rate curves. (b) Full discharge and overcharge performance at 20  $\text{mA cm}^{-2}$ . Arrows indicate the moment PAA-KOH protruded through and fractured the GDL. (c) Photographs showing the appearance of ZAB cells after charging. P-K2 squeezed between the acrylic plates and P-K5 penetrated through the GDL. (d) Electrical resistance for ZABs at 1.2 V before and after cycling at 20  $\text{mA cm}^{-2}$ .

### 6.3.3. Effect of battery design on ZAB performance

For aqueous electrolytes, a horizontal battery configuration is favored over a vertical configuration since it allows for more evenly distributed Zn deposition by reducing dendrite growth and electrode deformation [100]. For gel electrolytes, a vertical framework can be used to take advantage of gravity effects to facilitate the removal of oxygen bubbles. Both horizontal and vertical ZABs were cycled at  $20 \text{ mA cm}^{-2}$ . As shown in Figure 6.6a, the charge/discharge performance of horizontal and vertical cells is essentially the same at the beginning; however, after 23 h (~45 cycles) the vertical cell starts to show better efficiency. At the 160<sup>th</sup> cycle (80 h), the efficiencies are 38.8% and 47.5% for the horizontal and vertical configurations, respectively.

Tri-electrode battery designs, where the ORR and OER occur on separate electrodes, have been proposed and tested as a means of improving air electrode efficiency. Tri-electrode designs, however, add more complexity to the battery and reduce its specific energy as a result of the extra mass from the additional electrode. The necessity for tri-electrode batteries has been mitigated somewhat by recent improvements in the energy efficiency of bifunctional catalysts [250, 276-283]. A variation on the tri-electrode concept can be implemented by combining the benefits of a bifunctional catalyst and the solid state nature of gel electrolytes to double the area of the air electrode, thereby reducing its effective current density. In fact, this is a basic unit cell of the monopolar stack battery which was discussed by Muller et al. in 1995 [107]. As a proof-of-concept, two cell designs in a vertical configuration were utilized, one with a single air electrode (SAE) and one with a double air electrode (DAE); details are provided in Section 6.2.3. At a current of  $2 \times 2.5 \text{ mA cm}^{-2}$  (Figure 6.6b), the DAE can deliver a capacity of  $730 \text{ mAh g}_{\text{Zn}}^{-1}$  which exceeds the capacity of the SAE design ( $623 \text{ mAh g}_{\text{Zn}}^{-1}$ , at  $5 \text{ mA cm}^{-2}$ ), contributing to a high specific energy of  $913 \text{ Wh kg}_{\text{Zn}}^{-1}$ . It should be noted that the specific capacity depends on discharge rate. As the

current increases to 20 mA, the capacity of the DAE design decreases to 55%, while that of the SAE design drops to 46%. Figure 6.6c shows the power–current curves for ZABs. Since the maximum power is similar for the SAE and DAE designs (146 and 135 mW cm<sup>-2</sup>, respectively), the final power obtained from the DAE is almost twice as high as that of SAE. The power output is superior to previously reported rechargeable ZABs (Table 6.3), including those using alkaline solutions as electrolytes.

The DAE design also exhibits excellent cycling performance at 20 mA; its initial efficiency is the same as that for the SAE operating at 10 mA cm<sup>-2</sup> (Figure 6.6d). The final efficiency for ZABs using the SAE design is 53.9% at 10 mA cm<sup>-2</sup>, while that using the DAE design is 52.6% at 2×10 mA cm<sup>-2</sup>. The small amount of degradation at the end of cycling is believed to be caused by evaporation of water in the gels; however, the efficiency is still higher than a battery with a SAE design operating at the same current output (47.5% at 20 mA cm<sup>-2</sup>). Table 6.3 shows a comparison of the battery performance between this work and the recent literature, for both aqueous and polymer electrolytes. A direct comparison can be made with reference [258], as the same bifunctional catalysts were used in both studies. The efficiencies of ZABs using gel electrolytes are comparable with aqueous electrolytes at current densities of 20 mA cm<sup>-2</sup>. With proper cell design, gel electrolytes are a potential alternative to aqueous electrolytes, offering stable cyclability (190 cycles, equivalent to 95 h at 2×10 mA cm<sup>-2</sup>, Figure S6.7) and higher specific power with no leaking issues.

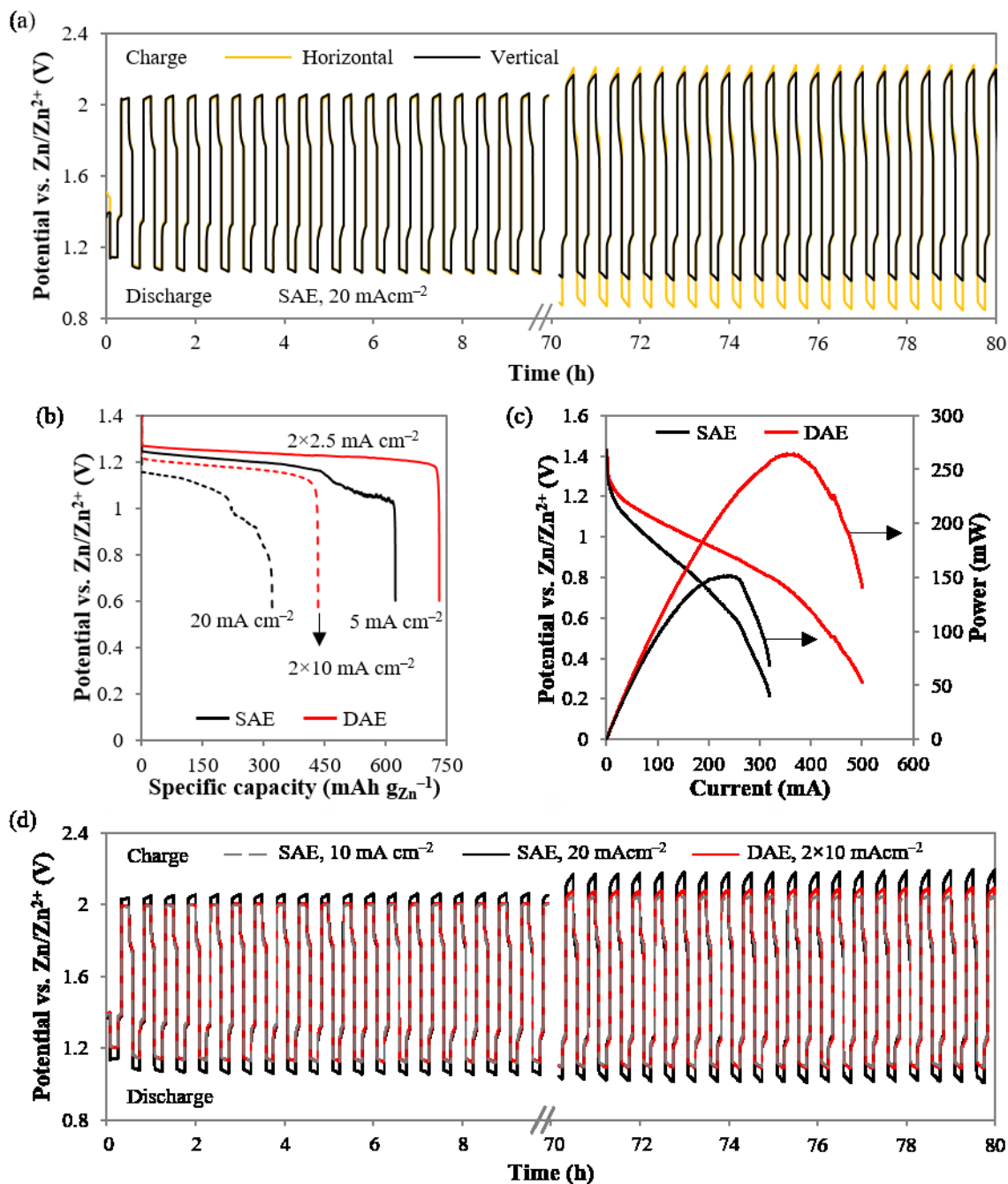


Figure 6.6. (a) Cycling performance at 20 mA cm<sup>-2</sup> for ZAB with vertical and horizontal orientations. (b–d) Comparison of ZABs using P–K2–ZnO electrolyte with two battery designs: (b) full discharge curves at 5 and 20 mA; (c) polarization and power curves, and (d) cycling performance of ZABs at 10 and 20 mA cm<sup>-2</sup> using the SAE design and at 2×10 mA cm<sup>-2</sup> using the DAE design.

Table 6.3. Comparison of ZAB cycling performance and maximum power density for this work and the recent literature

Bifunctional catalysts	Electrolyte	Current density (mA cm <sup>-2</sup> )	Cycle number	Initial – final efficiency (%)	Specific energy (Wh kg <sub>zn</sub> <sup>-1</sup> )	Power density (mW cm <sup>-2</sup> )	Ref
(Co,Fe) <sub>3</sub> O <sub>4</sub> /N-CNT	0.5 M PAA, 6.5 M KOH, 0.25 M ZnO, SAE design	20	160 (30 min / cycle)	54.7 – 47.5	748 @ 5 mA cm <sup>-2</sup>	146	This work
(Co,Fe) <sub>3</sub> O <sub>4</sub> /N-CNT	0.5 M PAA, 6.5 M KOH, 0.25 M ZnO, DAE design	2×10	160 (30 min / cycle)	60.8 – 52.6	913 @ 5 mA cm <sup>-2</sup>	2×135	This work
(Co,Fe) <sub>3</sub> O <sub>4</sub> /N-CNT	6 M KOH, 0.25 M ZnO	20	200 (30 min / cycle)	59.7 – 53.5	N/A	158	[258]
[Fe(CN) <sub>6</sub> ] <sup>3-</sup> @(ZIF-8)	6 M KOH, 0.2 M Zn(Ac) <sub>2</sub>	5	120 (5 min / cycle)	57.9 – 57.9	927.9 @ 5 mA cm <sup>-2</sup>	22.2	[276]
NPSC-Co <sub>2</sub> Fe <sub>1</sub>	6 M KOH, 0.2 M Zn(Ac) <sub>2</sub>	10	150 (20 min / cycle)	58.7 – 55	N/A	174.6	[277]
NP-Co <sub>3</sub> O <sub>4</sub> /CC	6 M KOH	5	1200 (20 min / cycle)	63.5 – 54.5	N/A	200	[278]
Co <sub>3</sub> O <sub>4</sub> @N-CNMA/CC	10 w/v% PVA, 9 M KOH	1	24 (20 min / cycle)	67 – 60	1010 @ 1 mA cm <sup>-2</sup>	65	[279]
SilkNC/KB	2.5 w/v% PVA, 7 M KOH, 0.1 M Zn(Ac) <sub>2</sub>	1	30 (20 min / cycle)	47.8 – 47.8	N/A	32.3	[280]
MnO <sub>2</sub> /NRGO-Urea	3 g polyacrylamide, 20 wt% KOH	5	140 (10 min / cycle)	64.9 – 56	850 @ 10 mA cm <sup>-2</sup>	105	[281]
LaMnO <sub>3</sub>	1.1 M PAA, 8.6 M KOH	5	100 (10 min / cycle)	64 – 57.5	730 @ 10 mA cm <sup>-2</sup>	52.9	[282]
CoPS	7 wt% PAA-K, 6 M KOH, 0.2 M Zn(Ac) <sub>2</sub>	5	150 (10 min / cycle)	60 – 52.5	891 @ 10 mA cm <sup>-2</sup>	N/A	[283]
Fe-N-C / 2D porous carbon	PANa-cellulose, 6 M KOH, 0.2 M Zn(Ac) <sub>2</sub>	5	660 (10 min / cycle)	59 – 58	930 @ 5 mA cm <sup>-2</sup>	108.6	[250]

ZIF-8: zeolitic imidazolate framework-8; NPSC-Co<sub>2</sub>Fe<sub>1</sub>: multi-doped nanoporous carbon; NP-Co<sub>3</sub>O<sub>4</sub>/CC: nitrogen-doped cobalt oxide on carbon cloth; Co<sub>3</sub>O<sub>4</sub>@N-CNMA/CC: nitrogen-doped carbon nano-micro arrays on flexible carbon cloth, SilkNC/KB: silk-derived defect-rich and nitrogen-doped nanocarbon electrocatalyst/Ketjenblack,

MnO<sub>2</sub>/NRGO-Urea manganese dioxide nanowires supported on nitrogen-doped reduced graphene oxide; CoPS: cobalt phosphosulphide on carbon cloth, PAA-K: potassium salt-based poly(acrylic acid), PANa-cellulose: dual-network hydrogel electrolyte-based sodium polyacrylate (PANa) and cellulose.

## 6.4. Conclusions

Various compositions of poly(acrylic acid) (PAA) were evaluated as the host material for an alkaline electrolyte in Zn-air batteries (ZABs). The effects of different gel electrolyte additives on the performance of a ZAB system were also evaluated. The addition of ZnO aided the charging process and reduced corrosion of the Zn electrode. The optimum concentration of ZnO was 0.25 M in PAA-KOH gels, which is lower than the saturation concentration that has been reported for aqueous, alkaline electrolytes. PAA stiffness and adhesion of the PAA matrix to the air electrode also affected battery performance. The lowest amount of monomer studied (0.5 M of AA) along with the highest amount of crosslinker (30 mM of MBAA) were the most suitable precursors for the fabricated PAA network, since this material was able to adapt to volume changes in the battery and facilitate the release of oxygen bubbles during charging.

A double air electrode (DAE) battery design was developed and compared with a conventional single air electrode (SAE) battery. The DAE, incorporated in a ZAB with a PAA-KOH electrolyte, had a high specific energy (913 Wh kg<sub>Zn</sub><sup>-1</sup>), excellent cycling stability (at least 190 cycles at 2×10 mA cm<sup>-2</sup>) and high power density output (2×135 mW cm<sup>-2</sup>). This study opens up new horizons for battery design to take advantage of solid state electrolytes and optimize the performance of ZABs.

## 6.5. Supporting information

Table S6.1. Physical forms of PAA–KOH gels with different concentrations of MBAA

MBAA (mM)	1	3	5	7	25	30	130
PAA 0.25 M KOH 6.25 M	–	–	–	–	–	–	Liquid (P–K1)
PAA 0.5 M KOH 6.5 M	–	–	–	–	Liquid	Gel (P–K2)	–
PAA 1 M KOH 7 M	–	–	Liquid	Gel (P–K3)	–	–	–
PAA 1.5 M KOH 1.5 M	–	Liquid	Gel (P–K4)	–	–	–	–
PAA 2 M KOH 8 M	Liquid	Gel (P–K5)	–	–	–	–	–

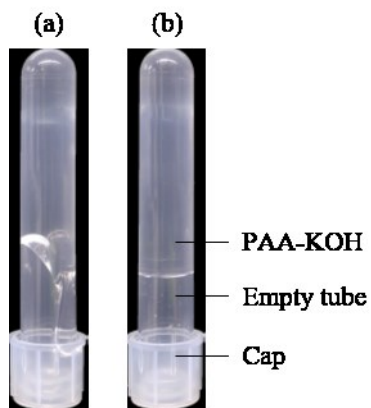


Figure S6.1. Photograph demonstrating the different forms of PAA–KOH. (a) P–K1 is liquid and flows after the tube is inverted. (b) P–K2 is a gel and does not flow.

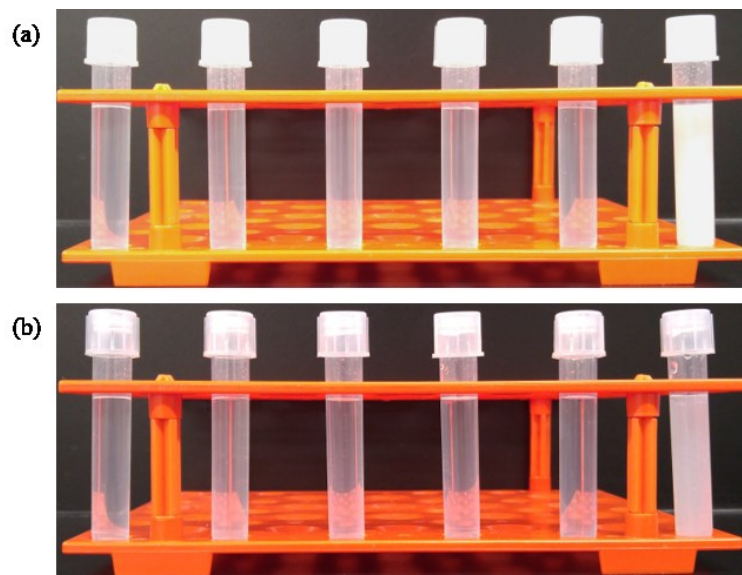


Figure S6.2. Photographs showing PAA-KOH with different concentrations of additives. (a) P-K2 containing 0, 0.1, 0.2, 0.3, 0.4 and 0.5 M ZnO (from left to right). (b) P-K2 containing 0, 0.1, 0.2, 0.3, 0.4 and 0.5 M of Zn(Ac)<sub>2</sub> (from left to right).

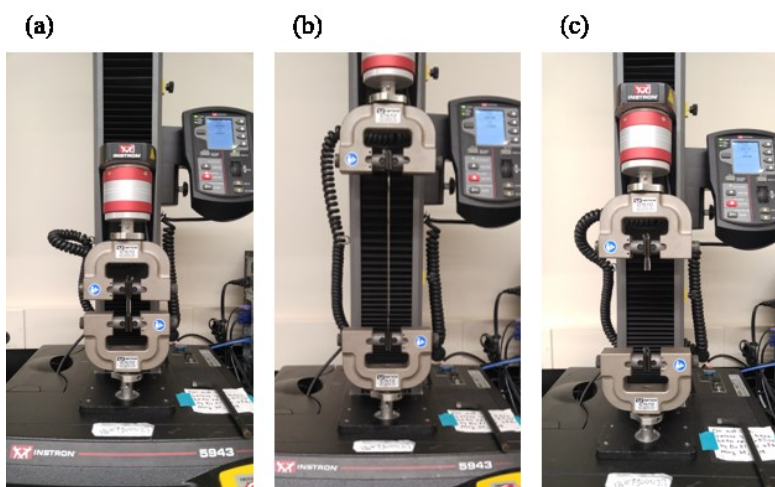


Figure S6.3. Photographs showing tensile test of P-K5 at (a) initial, (b) stretching and (c) failure stages.

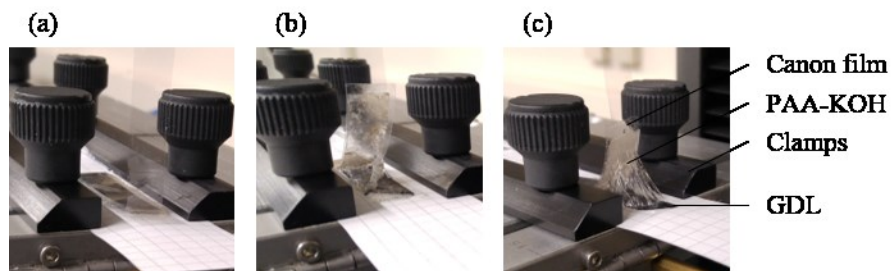


Figure S6.4. Photographs showing peeling test of all PAA-KOH samples: (a) During the initial stage. (b) P-K2 is easily removed from both surfaces. (c) P-K5 is sticky to both surfaces (Canon film and GDL) and it is peeled from the GDL afterwards.

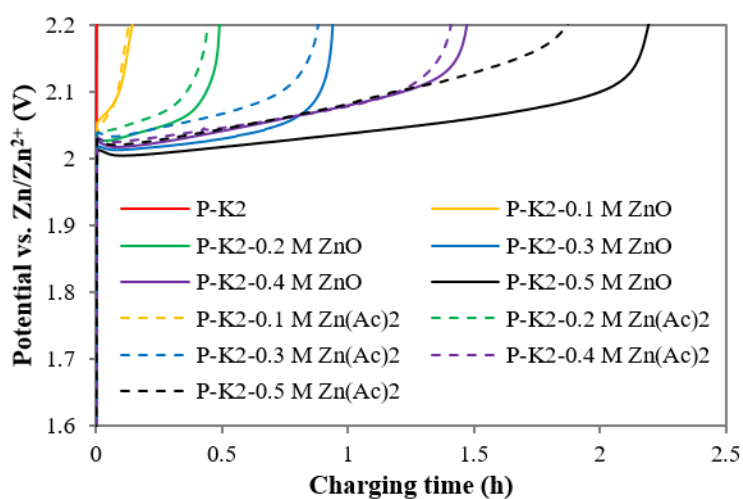


Figure S6.5. Overcharge performance of ZABs at  $20 \text{ mA cm}^{-2}$ . Solid lines represent P-K2 with ZnO, while dashed lines represent P-K2 with Zn(Ac)<sub>2</sub>.

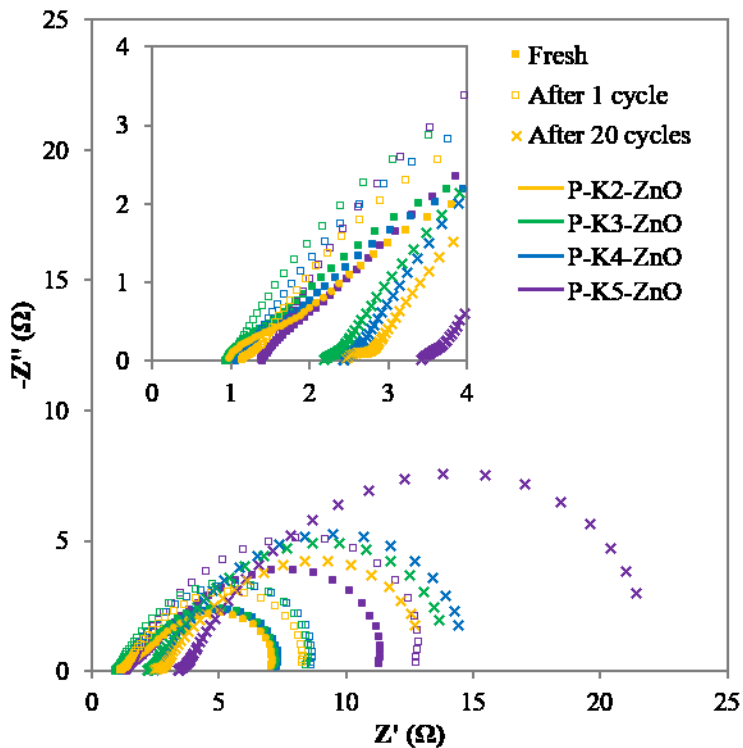


Figure S6.6. Nyquist plots of ZAB impedance before and after cycling. The inset plot shows lower resistance range.

Table S6.2. Resistance information for ZABs. Data was obtained using Zsimpwin software

	Fresh			After 1 cycle			After 20 cycle		
	$R_b$ ( $\Omega$ )	$R_{in}$ ( $\Omega$ )	$R_{ct}$ ( $\Omega$ )	$R_b$ ( $\Omega$ )	$R_{in}$ ( $\Omega$ )	$R_{ct}$ ( $\Omega$ )	$R_b$ ( $\Omega$ )	$R_{in}$ ( $\Omega$ )	$R_{ct}$ ( $\Omega$ )
P-K2-ZnO	0.92	1.22	4.97	1.13	0.32	6.86	2.47	0.30	9.95
P-K3-ZnO	0.91	1.15	5.17	1.01	0.24	7.29	2.19	0.17	11.32
P-K4-ZnO	1.04	1.10	5.18	1.09	0.18	7.41	2.38	0.14	11.89
P-K5-ZnO	1.34	0.85	9.15	1.44	0.14	11.31	3.41	0.30	17.71

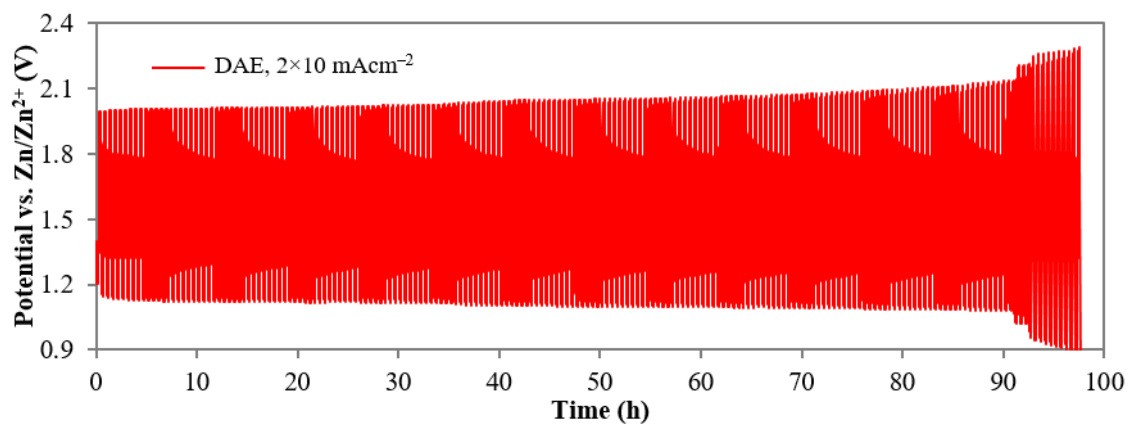


Figure S6.7. Cycling performance at  $2 \times 10 \text{ mA cm}^{-2}$  for ZAB using P-K2-ZnO until failure

## **Chapter 7. Conclusions and Future Work**

### **7.1 Conclusions**

The thesis presented different approaches to develop gel polymer electrolytes (GPEs) (Chapters 3, 5, 6) and battery designs (Chapters 4, 6) for Zn-air batteries (ZABs). The main achievements of this work are discussed in the following subsections.

#### **7.1.1. Influence of different hydrogel networks on characteristics of GPEs**

In Chapter 3, hydrogels with different network electrical charge were investigated as host materials for alkaline electrolyte. Several ways to evaluate the performance of GPEs were demonstrated. PVA, PAA and PAM were relatively stable in 6 M KOH solutions; upon removal of water, all GPEs had a stable electrochemical window of 2 V. Among the GPEs, PAA with 6 M KOH had the highest conductivity with its conductivity increasing with increasing temperature. PAA-KOH showed a continuous increase in ionic conductivity from 121 to 360 mS cm<sup>-1</sup> over the the temperature range studied (-20 to 65 °C). This indicated the good water retention capability of PAA with alkaline solutions in its network. During full cell testing, it was shown that GPEs can be beneficial to ZAB performance by reducing interfacial and charge transfer resistance. Batteries with PVA-KOH or PAA-KOH as the electrolyte outperformed batteries with 6 M KOH (aqueous) in terms of cycling number. Specifically, the battery with PAA-KOH had the highest initial discharge-charge efficiency of 79% at 0.5 mA cm<sup>-2</sup>.

#### **7.1.2. Optimization of poly(acrylic acid) (PAA)-based GPEs**

In Chapter 5, the cycle life of ZABs using PAA-based electrolyte was shown to change by varying its crosslinker concentration (MBAA). Gels with lower crosslinker content were weaker, but had higher conductivity and better water retention. On the other hand, higher crosslinker

content in the gel network can help reduce dendrite formation and shape change of the Zn electrode, but facilitated passivation of the Zn surface. ZABs using a bifunctional air electrode, consisting of a gas diffusion layer (GDL) support with a MnO<sub>x</sub>/CoFe catalyst layer and low crosslinked PAA–KOH, had better initial efficiencies than ZABs with aqueous electrolytes (60% vs. 55% at 5 mA cm<sup>-2</sup>) and were relatively stable for at least 100 cycles (53% efficiency).

Various compositions of PAA-based electrolytes were further evaluated in Chapter 6. Stiffness and adhesion of the PAA to the air electrode were found to affect battery performance. In 6 M KOH, the lowest amount of monomer (0.5 M of AA) along with the highest amount of crosslinker (30 mM of N,N'-methylenebis(acrylamide) (MBAA)) were the most suitable precursors for the fabricated PAA–KOH network, since this material was able to adapt to volume changes in the battery and facilitate the release of oxygen bubbles during charging. Additionally, the effects of different additives on the performance of a ZAB system were evaluated. The optimum concentration of ZnO was 0.25 M in PAA-based GPEs, which is lower than the saturation concentration that has been reported for aqueous, alkaline electrolytes.

### **7.1.3. Battery configurations**

In Chapter 4, a novel solid-state tri-electrode ZAB, where the oxygen evolution and oxygen reduction reaction (OER/ORR) electrodes were decoupled was investigated. The sandwich cell design (ORR/Zn/OER) is generally more suitable for GPEs than the planar cell design, as it provides more uniform current distribution on the Zn electrode. Decoupled air electrodes also allowed the separate study of ZnO additions to the electrolyte. It was found that adding ZnO to the ORR side enhanced cycling performance of ZABs. The battery delivered a discharge current of 5 mA cm<sup>-2</sup> for at least 100 cycles and the battery was able to operate in different orientations, bypassing leakage issues associated with aqueous ZABs.

A variation on the tri-electrode concept was implemented in Chapter 6 by combining the benefits of a bifunctional catalyst and the solid state nature of gel electrolytes to double the area of the air electrode, without increasing the battery mass. The double air electrode (DAE) design was compared with a conventional battery. The DAE, incorporated in a ZAB with a PAA-based electrolyte, had a high specific energy ( $913 \text{ Wh kg}_{\text{Zn}}^{-1}$ ), excellent cycling stability (190 cycles at  $2 \times 10 \text{ mA cm}^{-2}$ ) and high power density output ( $2 \times 135 \text{ mW cm}^{-2}$ ).

## **7.2. Future Work**

Based on the results from the studies conducted in this thesis research, the following recommendations are proposed for future work.

### **7.2.1. Further investigation on polymer matrix**

PAA is a very attractive host material due to its chemical stability in highly concentrated alkaline environments and the large number of carboxyl groups which help to retain water. It was shown that the optimum PAA concentration should be as low as possible, since PAA adheres to the air electrode which can increase charge transfer resistance. However, mechanical strength is reduced with low concentrations of PAA. In addition, the PAA network does not provide selectivity for ions. Thus, zincate ions can diffuse from the Zn electrode to the air electrode, which is driven by concentration gradient. The introduction of cellulose into the PAA network crosslinked by MBAA can vastly enhance its mechanical strength. The reported dual network GPE can be stretched up to 1200%, even when containing 300% of 6 M KOH aqueous solution (versus the weight of hydrogel) [250]. The cellulose can be modified through surface-quaternization to enhance its conductivity and mobility towards  $\text{OH}^-$  [284]. The modification can help to reduce zincate crossover to the air electrode and to retain battery capacity during discharge and charge cycling.

### 7.2.2. Further investigation on electrolyte additives

Although 6 M KOH provides the highest ionic conductivity, it has been reported that dendrite growth and corrosion of Zn can be reduced by using a lower concentration of KOH [12, 285]. Alternatively, 4 M KOH has been chosen with additives, including saturated ZnO, 2 M KF and 2 M K<sub>2</sub>CO<sub>3</sub>, to increase ionic conductivity and enhance cycle life of ZABs [29, 286]. Three additives were chosen for different benefits. It is well known that ZnO not only hinders the HER but also ensures that the zincate ion concentration remains high enough to facilitate the OER during charging. The fluorine ions from KF were found to reduce the overpotential toward both the ORR and OER [287], while adding K<sub>2</sub>CO<sub>3</sub> may lessen the negative impact of carbonation in the pores of the air electrode [288]. As mentioned in Section 2.2.4, a combination of mitigation strategies can be utilized with different additives in the base alkaline electrolyte; however, a balance among alkaline electrolyte, additives and polymer matrix must be found.

### 7.2.3. Device optimization

Cell configurations can be further adjusted to improve battery electrochemical performance and safety. For example, to increase areal contact between the GPE and electrodes, electrolyte precursors can be polymerized within the battery. In secondary ZABs, Zn corrosion can produce hydrogen which is potentially explosive; venting holes in the battery casing can prevent pressure build-up within the cell. Modeling can be used to assist with practical research and may help in developing the best architecture to enhance reaction kinetics and mass transport within the cell based on parameters such as temperature, humidity and air/oxygen flow rate.

## References

- [1] F. Liu, H.-J. Chung, and J.A.W. Elliott. *ACS Appl. Energy Mater.*, **2018**. 1(4), 1489-1495.
- [2] M. Xu, D.G. Ivey, Z. Xie, and W. Qu. *J. Power Sources*, **2015**. 283, 358-371.
- [3] *Statistical Review of World Energy*. 2020; Available from: <https://www.bp.com/>.
- [4] M.C. Argyrou, P. Christodoulides, and S.A. Kalogirou. *Renewable Sustainable Energy Rev.*, **2018**. 94, 804-821.
- [5] M. Aneke and M. Wang. *Appl. Energy*, **2016**. 179, 350-377.
- [6] Z. Chang and X.b. Zhang, in *Metal-Air Batteries*. **2018**, 1-9.
- [7] S. Li, L. Ma, Y. Xia, H. Luo, L. Qiu, and C. Cheng, in *Advanced Nanomaterials for Electrochemical-Based Energy Conversion and Storage*, F. Ran and S. Chen, Editors. **2020**, Elsevier, 191-222.
- [8] K.F. Blurton and A.F. Sammells. *J. Power Sources*, **1979**. 4(4), 263-279.
- [9] T. Zhang, Z. Tao, and J. Chen. *Mater. Horiz.*, **2014**. 1(2), 196-206.
- [10] Q. Liu, Z. Pan, E. Wang, L. An, and G. Sun. *Energy Storage Mater.*, **2019**.
- [11] J.-S. Lee, S. Tai Kim, R. Cao, N.-S. Choi, M. Liu, K.T. Lee, and J. Cho. *Adv. Energy Mater.*, **2011**. 1(1), 34-50.
- [12] J. Fu, Z.P. Cano, M.G. Park, A. Yu, M. Fowler, and Z. Chen. *Adv. Mater.*, **2017**. 29(7), 1604685.
- [13] B. Amunátegui, A. Ibáñez, M. Sierra, and M. Pérez. *J. Appl. Electrochem.*, **2018**. 48(6), 627-637.
- [14] M. Wang, H. Ji, S. Liu, H. Sun, J. Liu, C. Yan, and T. Qian. *Chem. Eng. J.*, **2020**. 393, 124702.
- [15] B.R. Thomas, in *Linden's Handbook of Batteries, Fourth Edition*. **2011**, McGraw-Hill Education: New York.
- [16] J. Stamm, A. Varzi, A. Latz, and B. Horstmann. *J. Power Sources*, **2017**. 360, 136-149.
- [17] W. Lao-atiman, K. Bumroongsil, A. Arpornwichanop, P. Bumroongsakulsawat, S. Oлару, and S. Kheawhom. *Front. Energy Res.*, **2019**. 7(15).
- [18] Y. Li and H. Dai. *Chem. Soc. Rev.*, **2014**. 43(15), 5257-5275.
- [19] C.R. Raj, A. Samanta, S.H. Noh, S. Mondal, T. Okajima, and T. Ohsaka. *J. Mater. Chem. A*, **2016**. 4(29), 11156-11178.

- [20] G. Wu, K.L. More, C.M. Johnston, and P. Zelenay. *Science*, **2011**. 332(6028), 443-447.
- [21] T.H. Wu, Y. Zhang, Z.D. Althouse, and N. Liu. *Mater. Today Nano*, **2019**. 6, 100032.
- [22] W. Niu and Y. Yang, in *Advanced Nanomaterials for Electrochemical-Based Energy Conversion and Storage*, F. Ran and S. Chen, Editors. **2020**, Elsevier, 161-190.
- [23] J. Zhang, Q. Zhou, Y. Tang, L. Zhang, and Y. Li. *Chem. Sci.*, **2019**. 10(39), 8924-8929.
- [24] J. Yi, P. Liang, X. Liu, K. Wu, Y. Liu, Y. Wang, Y. Xia, and J. Zhang. *Energy Environ. Sci.*, **2018**. 11(11), 3075-3095.
- [25] Y. Sun, X. Liu, Y. Jiang, J. Li, J. Ding, W. Hu, and C. Zhong. *J. Mater. Chem. A*, **2019**. 7(31), 18183-18208.
- [26] X. Chen, Z. Zhou, H.E. Karahan, Q. Shao, L. Wei, and Y. Chen. *Small*, **2018**. 14(44), 1801929.
- [27] D. Ozgit, P. Hiralal, and G.A.J. Amaratunga. *ACS Appl. Mater. Interfaces*, **2014**. 6(23), 20752-20757.
- [28] J. Vatsalarani, S. Geetha, D.C. Trivedi, and P.C. Warriar. *J. Power Sources*, **2006**. 158(2), 1484-1489.
- [29] A.R. Mainar, L.C. Colmenares, H.-J. Grande, and J.A. Blázquez. *Batteries*, **2018**. 4(3), 46.
- [30] K. Zhao, C. Wang, Y. Yu, M. Yan, Q. Wei, P. He, Y. Dong, Z. Zhang, X. Wang, and L. Mai. *Adv. Mater. Interfaces*, **2018**. 5(16), 1800848.
- [31] Z. Zhou, Y. Zhang, P. Chen, Y. Wu, H. Yang, H. Ding, Y. Zhang, Z. Wang, X. Du, and N. Liu. *Chem. Eng. Sci.*, **2019**. 194, 142-147.
- [32] J. Yu, G. Li, H. Liu, L. Zeng, L. Zhao, J. Jia, M. Zhang, W. Zhou, H. Liu, and Y. Hu. *Adv. Sci.*, **2019**. 6(18), 1901458.
- [33] J.K. Nørskov, J. Rossmeisl, A. Logadottir, L. Lindqvist, J.R. Kitchin, T. Bligaard, and H. Jónsson. *J. Phys. Chem. B*, **2004**. 108(46), 17886-17892.
- [34] L. Han, Y. Sun, S. Li, C. Cheng, C.E. Halbig, P. Feicht, J.L. Hübner, P. Strasser, and S. Eigler. *ACS Catal.*, **2019**. 9(2), 1283-1288.
- [35] Y. Liu, Q. Sun, W. Li, K.R. Adair, J. Li, and X. Sun. *Green Energy & Environment*, **2017**. 2(3), 246-277.
- [36] J.H. Williams, A. DeBenedictis, R. Ghanadan, A. Mahone, J. Moore, W.R. Morrow, S. Price, and M.S. Torn. *Science*, **2012**. 335(6064), 53-59.
- [37] K. Mongird, V. Viswanathan, P. Balducci, J. Alam, V. Fotedar, V. Koritarov, and B. Hadjerioua. 2019.

- [38] A.R. Mainar, E. Iruin, L.C. Colmenares, A. Kvasha, I. de Meatza, M. Bengoechea, O. Leonet, I. Boyano, Z. Zhang, and J.A. Blazquez. *J. Energy Storage*, **2018**. 15, 304-328.
- [39] H. Chen, T.N. Cong, W. Yang, C. Tan, Y. Li, and Y. Ding. *Prog. Nat. Sci.*, **2009**. 19(3), 291-312.
- [40] N.D. Ingale, J.W. Gallaway, M. Nyce, A. Couzis, and S. Banerjee. *J. Power Sources*, **2015**. 276, 7-18.
- [41] M.J. Riezenman. *IEEE Spectrum*, **1995**. 32(5), 51-56.
- [42] A. Rathi. *How we get to the next big battery breakthrough*. 2019; Available from: <https://qz.com/1588236/how-we-get-to-the-next-big-battery-breakthrough/>.
- [43] S.B. Sherman, Z.P. Cano, M. Fowler, and Z. Chen. *AIMS Energy*, **2018**. 6(1), 121-145.
- [44] S.M.L. Agostinho, R.F.V.V. Jaimes, L. Vairolette, and I.V.d. Souza Santos. *Quim. Nova*, **2019**. 42, 453-457.
- [45] B. Hwang, E.-S. Oh, and K. Kim. *Electrochim. Acta*, **2016**. 216, 484-489.
- [46] Y. Cheng and S.P. Jiang. *Prog. Nat. Sci.: Mater. Int.*, **2015**. 25(6), 545-553.
- [47] S. Clark, A. Latz, and B. Horstmann. *ChemSusChem*, **2017**. 10(23), 4735-4747.
- [48] S. Clark, A.R. Mainar, E. Iruin, L.C. Colmenares, J.A. Blázquez, J.R. Tolchard, A. Latz, and B. Horstmann. *J. Mater. Chem. A*, **2019**. 7(18), 11387-11399.
- [49] X.G. Zhang, in *Corrosion and Electrochemistry of Zinc*. **1996**, Springer US.
- [50] D.M. See and R.E. White. *J. Chem. Eng. Data*, **1997**. 42(6), 1266-1268.
- [51] R.V. Moshtev and P. Zlatilova. *J. Appl. Electrochem.*, **1978**. 8(3), 213-222.
- [52] A. R. Mainar, O. Leonet, M. Bengoechea, I. Boyano, I. de Meatza, A. Kvasha, A. Guerfi, and J. Alberto Blázquez. *Int. J. Energy Res.*, **2016**. 40(8), 1032-1049.
- [53] H. Ye and J.J. Xu. *J. Power Sources*, **2007**. 165(2), 500-508.
- [54] G.G. Kumar and S. Sampath. *J. Electrochem. Soc.*, **2003**. 150(5), A608-A615.
- [55] G.G. Kumar and S. Sampath. *Solid State Ionics*, **2003**. 160(3), 289-300.
- [56] J.J. Xu, H. Ye, and J. Huang. *Electrochem. Commun.*, **2005**. 7(12), 1309-1317.
- [57] M.-J. Deng, J.-M. Chen, K.-T. Lu, C.-C. Wang, J.-F. Lee, and J.-K. Chang. *RSC Adv.*, **2012**. 2(25), 9383-9386.

- [58] M. Xu, D.G. Ivey, Z. Xie, and W. Qu. *Electrochimica Acta*, **2013**. 89(Supplement C), 756-762.
- [59] M. Xu, D.G. Ivey, W. Qu, Z. Xie, and Y.H. Bing. Vol. 50. **2013**: ECS Transactions. 13-22.
- [60] T. Yu, R. Cai, and Z. Chen, in *Metal-Air Batteries*, X.b. Zhang, Editor. **2018**, 265-291.
- [61] C. Pozo-Gonzalo, C. Virgilio, Y. Yan, P.C. Howlett, N. Byrne, D.R. MacFarlane, and M. Forsyth. *Electrochem. Commun.*, **2014**. 38, 24-27.
- [62] D. Schröder, in *Analysis of Reaction and Transport Processes in Zinc Air Batteries*. **2016**, Springer Fachmedien Wiesbaden, 1-16.
- [63] M.S. Ghazvini, G. Pulletikurthi, T. Cui, C. Kuhl, and F. Endres. *J. Electrochem. Soc.*, **2018**. 165(9), D354-D363.
- [64] J. Park, M. Park, G. Nam, J.-s. Lee, and J. Cho. *Adv. Mater.*, **2015**. 27(8), 1396-1401.
- [65] D.K. Cha and S.-M. Park. *J. Electroanal. Chem.*, **1998**. 459(1), 135-144.
- [66] G.M. Stone, S.A. Mullin, A.A. Teran, D.T. Hallinan, A.M. Minor, A. Hexemer, and N.P. Balsara. *J. Electrochem. Soc.*, **2012**. 159(3), A222-A227.
- [67] H. Peng, Y. Xu, J. Pan, Y. Zhao, L. Wang, and X. Shi, in *Metal-Air Batteries*, X.b. Zhang, Editor. **2018**, 367-396.
- [68] R. Othman, W.J. Basirun, A.H. Yahaya, and A.K. Arof. *J. Power Sources*, **2001**. 103(1), 34-41.
- [69] N. Vassal, E. Salmon, and J.F. Fauvarque. *Electrochim. Acta*, **2000**. 45(8), 1527-1532.
- [70] C.-C. Yang, S.-J. Lin, and S.-T. Hsu. *J. Power Sources*, **2003**. 122(2), 210-218.
- [71] C.-C. Yang and S.-J. Lin. *J. Power Sources*, **2002**. 112(2), 497-503.
- [72] J. Fu, D.U. Lee, F.M. Hassan, L. Yang, Z. Bai, M.G. Park, and Z. Chen. *Adv. Mater.*, **2015**. 27(37), 5617-22.
- [73] Y. Xu, Y. Zhang, Z. Guo, J. Ren, Y. Wang, and H. Peng. *Angew. Chem., Int. Ed. Engl.*, **2015**. 54(51), 15390-4.
- [74] G.M. Wu, S.J. Lin, and C.C. Yang. *J. Membr. Sci.*, **2006**. 280(1), 802-808.
- [75] Z. Zhang, C. Zuo, Z. Liu, Y. Yu, Y. Zuo, and Y. Song. *J. Power Sources*, **2014**. 251, 470-475.
- [76] O. M'barki, A. Hanafia, D. Bouyer, C. Faur, R. Sescousse, U. Delabre, C. Blot, P. Guenoun, A. Deratani, D. Quemener, and C. Pochat-Bohatier. *J. Membr. Sci.*, **2014**. 458, 225-235.

- [77] L. Long, S. Wang, M. Xiao, and Y. Meng. *J. Mater. Chem. A*, **2016**. 4(26), 10038-10069.
- [78] P. Atkins, J. De Paula, and J. Keeler. **2018**: Oxford University Press. 908.
- [79] R. Christensen, G. Olson, and S.W. Martin. *J. Phys. Chem. B*, **2013**. 117(51), 16577-16586.
- [80] R.F. Thornton and E.J. Carlson. *Journal of The Electrochemical Society*, **1980**. 127(7), 1448-1452
- [81] T.C. Adler, F.R. McLarnon, and E.J. Cairns. *Industrial & Engineering Chemistry Research*, **1998**. 37(8), 3237-3241.
- [82] H. Yang, Y. Cao, X. Ai, and L. Xiao. *J. Power Sources*, **2004**. 128(1), 97-101.
- [83] J.Y. Huot. *J. Appl. Electrochem.*, **1992**. 22(5), 443-447.
- [84] A.R. Mainar, L.C. Colmenares, J.A. Blázquez, and I. Urdampilleta. *Int. J. Energy Res.*, **2018**. 42(3), 903-918.
- [85] C. Sequeira and D. Santos. **2010**: Woodhead Publishing. 632.
- [86] *Starting Your Digital Hearing Aid Batteries*. 2012; Available from: <https://www.hear-better.com/blog/starting-your-digital-gearing-aid-batteries/>.
- [87] M. Lefler, J. Stuart, J. Parkey, and S. Licht. *J. Electrochem. Soc.*, **2016**. 163(5), A781-A784.
- [88] P.-C. Li, Y.-J. Chien, and C.-C. Hu. *J. Power Sources*, **2016**. 313, 37-45.
- [89] C. Biegler. *J. Electrochem. Soc.*, **1983**. 130(12), 2303.
- [90] S. Müller, F. Holzer, and O. Haas. *J. Appl. Electrochem.*, **1998**. 28(9), 895-898.
- [91] J.T. Nichols, F.R. McLarnon, and E.J. Cairns. *Chem. Eng. Commun.*, **1985**. 37(1-6), 355-379.
- [92] Y. Li, J. Fu, C. Zhong, T. Wu, Z. Chen, W. Hu, K. Amine, and J. Lu. *Adv. Energy Mater.*, **2019**. 9(1), 1802605.
- [93] J. Zhang, J. Fu, X. Song, G. Jiang, H. Zarrin, P. Xu, K. Li, A. Yu, and Z. Chen. *Adv. Energy Mater.*, **2016**. 6(14), 1600476.
- [94] C.-Y. Su, H. Cheng, W. Li, Z.-Q. Liu, N. Li, Z. Hou, F.-Q. Bai, H.-X. Zhang, and T.-Y. Ma. *Adv. Energy Mater.*, **2017**. 7(13), 1602420.
- [95] H. Cheng, M.-L. Li, C.-Y. Su, N. Li, and Z.-Q. Liu. *Adv. Funct. Mater.*, **2017**. 27(30), 1701833.
- [96] F. Meng, H. Zhong, D. Bao, J. Yan, and X. Zhang. *J. Am. Chem. Soc.*, **2016**. 138(32), 10226-10231.

- [97] G. Toussaint, P. Stevens, L. Akrou, R. Rouget, and F. Fourgeot. *ECS Trans.*, **2010**. 28(32), 25-34.
- [98] Y. Li, M. Gong, Y. Liang, J. Feng, J.-E. Kim, H. Wang, G. Hong, B. Zhang, and H. Dai. *Nat. Commun.*, **2013**. 4, 1805.
- [99] J. Zhang, Z. Zhao, Z. Xia, and L. Dai. *Nat. Nanotechnol.*, **2015**. 10, 444.
- [100] W. Hong, H. Li, and B. Wang. *Int. J. Electrochem. Sci.*, **2016**. 11, 3843-3851.
- [101] G.-P. Kim, H.-H. Sun, and A. Manthiram. *Nano Energy*, **2016**. 30, 130-137.
- [102] Z. Yan, E. Wang, J. Gao, J. Yang, C. Wu, L. Jiang, M. Zhu, and G. Sun. *ChemElectroChem*, **2017**. 4(9), 2190-2195.
- [103] M. Xiong, M.P. Clark, M. Labbe, and D.G. Ivey. *J. Power Sources*, **2018**. 393, 108-118.
- [104] W. Liu, M.-S. Song, B. Kong, and Y. Cui. *Adv. Mater.*, **2017**. 29(1), 1603436.
- [105] A.M. Gaikwad, G.L. Whiting, D.A. Steingart, and A.C. Arias. *Adv. Mater.*, **2011**. 23(29), 3251-3255.
- [106] S. Qu, Z. Song, J. Liu, Y. Li, Y. Kou, C. Ma, X. Han, Y. Deng, N. Zhao, W. Hu, and C. Zhong. *Nano Energy*, **2017**. 39, 101-110.
- [107] S. Mueller, F. Holzer, O. Haas, C. Schlatter, and C. Comninellis. *Chimia*, **1995**. 49, 27-32.
- [108] H. Ma, B. Wang, Y. Fan, and W. Hong. *Energies*, **2014**. 7(10), 6549-6557.
- [109] S. Müller, O. Haas, C. Schlatter, and C. Comninellis. *J. Appl. Electrochem.*, **1998**. 28(3), 305-310.
- [110] *NantEnergy Announces Largest Global Deployment of Novel Air Breathing Zinc Rechargeable Battery System and Breakthrough in Cost Barrier*. 2018; Available from: <https://www.businesswire.com/news/home/20180926005265/en/NantEnergy-Announces-Largest-Global-Deployment-Novel%20Air-Breathing>.
- [111] A. Colthorpe. *Baby steps for EOS' zinc batteries in US ahead of 40MWh project, company targets UK for 2020*. 2019; Available from: <https://www.energy-storage.news/news/baby-steps-for-eos-zinc-batteries-in-us-ahead-of-40mwh-project-company-targ>.
- [112] Z. Yan, J. Gao, M. Liu, E. Wang, and G. Sun. *Energy Technol.*, **2018**. 6(2), 246-250.
- [113] N. Elgrishi, K.J. Rountree, B.D. McCarthy, E.S. Rountree, T.T. Eisenhart, and J.L. Dempsey. *J. Chem. Educ.*, **2018**. 95(2), 197-206.
- [114] H. Tomiyasu, H. Shikata, K. Takao, N. Asanuma, S. Taruta, and Y.-Y. Park. *Sci. Rep.*, **2017**. 7(1), 45048.

- [115] S.G. Chandrappa, P. Moni, G. Karkera, and A.S. Prakash. *Nanoscale Adv.*, **2019**. 1(6), 2392-2399.
- [116] B.J. Inkson, in *Materials Characterization Using Nondestructive Evaluation (NDE) Methods*, G. Hübschen, I. Altpeter, R. Tschuncky, and H.-G. Herrmann, Editors. **2016**, Woodhead Publishing, 17-43.
- [117] M.A. Mohamed, J. Jaafar, A.F. Ismail, M.H.D. Othman, and M.A. Rahman, in *Membrane Characterization*, N. Hilal, A.F. Ismail, T. Matsuura, and D. Oatley-Radcliffe, Editors. **2017**, Elsevier, 3-29.
- [118] C.W. Liew, R. Durairaj, and S. Ramesh. *PLoS One*, **2014**. 9(7), e102815.
- [119] T.G. Mezger. **2018**, Austria: Anton Paar GmbH.
- [120] *Basics of rheology*. [cited 2020 April]; Available from: <https://wiki.anton-paar.com/en/basics-of-rheology/>.
- [121] *A Basic Introduction to Rheology*. 2016; Available from: <https://cdn.technologynetworks.com/TN/Resources/PDF/WP160620BasicIntroRheology.pdf>.
- [122] T.B. Reddy. **2010**: McGraw-Hill Education. 1200.
- [123] X. Zhang, X.-G. Wang, Z. Xie, and Z. Zhou. *Green Energy Environ.*, **2016**. 1(1), 4-17.
- [124] L.S. Darken and H.F. Meier. *J. Am. Chem. Soc.*, **1942**. 64(3), 621-623.
- [125] E.M. Ahmed. *J. Adv. Res.*, **2015**. 6(2), 105-121.
- [126] C.-C. Yang and S.-J. Lin. *J. Power Sources*, **2006**. 112(2), 497-503.
- [127] G.-M. Wu, S.-J. Lin, and C.-C. Yang. *J. Membr. Sci.*, **2006**. 275(1), 127-133.
- [128] A.A. Mohamad, N.S. Mohamed, M.Z.A. Yahya, R. Othman, S. Ramesh, Y. Alias, and A.K. Arof. *Solid State Ionics*, **2003**. 156(1), 171-177.
- [129] D.T. Hallinan and N.P. Balsara. *Annu. Rev. Mater. Res.*, **2013**. 43(1), 503-525.
- [130] T. Swift, L. Swanson, M. Geoghegan, and S. Rimmer. *Soft Matter*, **2016**. 12(9), 2542-2549.
- [131] N.A. Choudhury, S. Sampath, and A.K. Shukla. *Energy Environ. Sci.*, **2009**. 2(1), 55-67.
- [132] X. Peng, H. Liu, Q. Yin, J. Wu, P. Chen, G. Zhang, G. Liu, C. Wu, and Y. Xie. *Nat. Commun.*, **2016**. 7, 11782.
- [133] A.V. Dobrynin, R.H. Colby, and M.J. Rubinstein. *Polym. Sci., Part B: Polym. Phys.*, **2004**. 42, 3513-3538.

- [134] J. Tavakoli, J. Gascooke, N. Xie, B.Z. Tang, and Y. Tang. *ACS Applied Polymer Materials*, **2019**. 1(6), 1390-1398.
- [135] L. Ye and Z. Feng, in *Polymer Electrolytes*, C. Sequeira and D. Santos, Editors. **2010**, Woodhead Publishing, 550-582.
- [136] A.R.M. Zahid, M.N. Masri, M.H. Hussin, and M.B.A. Bakar. *AIP Conf. Proc.*, **2018**. 2030(1), 020278.
- [137] L.V. Smirnov, N.V. Platonova, and K.R. Popov. *Zh. Prikl. Spektrosk.*, **1967**. 7(1), 94-98.
- [138] T.L. Sun, T. Kurokawa, S. Kuroda, A.B. Ihsan, T. Akasaki, K. Sato, M.A. Haque, T. Nakajima, and J.P. Gong. *Nat. Mater.*, **2013**. 12, 932.
- [139] X. Li, H. Charaya, T.N.T. Tran, B. Lee, J.-Y. Cho, and H.-J. Chung. *MRS Commun.*, **2018**. 8(3), 1079-1084.
- [140] E.R. Blout and R. Karplus. *J. Am. Chem. Soc.*, **1948**. 70(2), 862-864.
- [141] H.S. Mansur, C.M. Sadahira, A.N. Souza, and A.A.P. Mansur. *Mater. Sci. Eng.: C*, **2008**. 28(4), 539-548.
- [142] M. Todicaa, R. Stefanb, C.V. Popa, and L. Olar. *Acta Phys. Pol., A*, **2015**. 128(1), 128-135.
- [143] J. Dong, Y. Ozaki, and K. Nakashima. *J. Polym. Sci., Part B: Polym. Phys.*, **1997**. 35(3), 507-515.
- [144] L.J. Kirwan, P.D. Fawell, and W. van Bronswijk. *Langmuir*, **2003**. 19(14), 5802-5807.
- [145] R.K. Mishra, K. Ramasamy, N.N. Ban, and A.B.A. Majeed. *J. Appl. Polym. Sci.*, **2013**. 128(5), 3365-3374.
- [146] L. Jiang, X. Kong, Z. Lu, and S. Hou. *J. Appl. Polym. Sci.*, **2015**. 132(4).
- [147] W. Wei, X. Qi, J. Li, Y. Zhong, G. Zuo, X. Pan, T. Su, J. Zhang, and W. Dong. *Int. J. Biol. Macromol.*, **2017**. 101, 474-480.
- [148] A. Pourjavadi, S.M. Fakoorpoor, and S.H. Hosseini. *Carbohydr. Polym.*, **2013**. 93(2), 506-511.
- [149] J.C. Yang, M.J. Jablonsky, and J.W. Mays. *Polymer*, **2002**. 43(19), 5125-5132.
- [150] J. Wei, J. Zhou, S. Su, J. Jiang, J. Feng, and Q. Wang. *ChemSusChem*, **2018**. 11(19), 3410-3415.
- [151] S. Song, M. Kotobuki, F. Zheng, Q. Li, C. Xu, Y. Wang, W.D.Z. Li, N. Hu, and L. Lu. *Solid State Ionics*, **2017**. 300, 165-168.

- [152] A.L. Zhu, D.P. Wilkinson, X. Zhang, Y. Xing, A.G. Rozhin, and S.A. Kulinich. *J. Energy Storage*, **2016**. 8, 35-50.
- [153] R.J. Gilliam, J.W. Graydon, D.W. Kirk, and S.J. Thorpe. *Int. J. Hydrogen Energy*, **2007**. 32(3), 359-364.
- [154] G.M. Wu, S.J. Lin, J.H. You, and C.C. Yang. *Mater. Chem. Phys.*, **2008**. 112(3), 798-804.
- [155] A. Pawlicka and J.P. Donoso, in *Polymer Electrolytes*, C. Sequeira and D. Santos, Editors. **2010**, Woodhead Publishing, 95-128.
- [156] M. Xiong and D.G. Ivey. *J. Electrochem. Soc.*, **2017**. 164(6), A1012-A1021.
- [157] M. Xiong and D.G. Ivey. *Electrochim. Acta*, **2018**. 260, 872-881.
- [158] J. Yin, Y. Li, F. Lv, Q. Fan, Y.-Q. Zhao, Q. Zhang, W. Wang, F. Cheng, P. Xi, and S. Guo. *ACS Nano*, **2017**. 11(2), 2275-2283.
- [159] P. Da, M. Wu, K. Qiu, D. Yan, Y. Li, J. Mao, C. Dong, T. Ling, and S. Qiao. *Chem. Eng. Sci.*, **2018**.
- [160] Q. Liu, Y. Wang, L. Dai, and J. Yao. *Adv. Mater.*, **2016**. 28(15), 3000-3006.
- [161] X. Wang, J. Gao, Z. Cheng, N. Chen, and L. Qu. *Angew. Chem., Int. Ed.*, **2016**. 55(47), 14643-14647.
- [162] C. Lin, S.S. Shinde, Y. Wang, Y. Sun, S. Chen, H. Zhang, X. Li, and J.-H. Lee. *Sustainable Energy Fuels*, **2017**. 1(9), 1909-1914.
- [163] H. Charaya, X. Li, N. Jen, and H.-J. Chung. *Langmuir*, **2019**. 35(5), 1526-1533.
- [164] *NantEnergy announces rechargeable zinc-air battery system*. 2018; Available from: <https://www.latimes.com/business/la-fi-zinc-air-battery-20180926-story.html>.
- [165] Y. Liang, Y. Li, H. Wang, J. Zhou, J. Wang, T. Regier, and H. Dai. *Nat. Mater.*, **2011**. 10, 780.
- [166] T.N.T. Tran, H.-J. Chung, and D.G. Ivey. *Electrochim. Acta*, **2019**. 327, 135021.
- [167] T.K.A. Hoang, T.N.L. Doan, C. Lu, M. Ghaznavi, H. Zhao, and P. Chen. *ACS Sustainable Chem. Eng.*, **2017**. 5(2), 1804-1811.
- [168] F.W.T. Goh, Z. Liu, X. Ge, Y. Zong, G. Du, and T.S.A. Hor. *Electrochim. Acta*, **2013**. 114, 598-604.
- [169] B. Yuan, G. Nam, P. Li, S. Wang, H. Jang, T. Wei, Q. Qin, X. Liu, and J. Cho. *J. Power Sources*, **2019**. 421, 109-115.

- [170] Z. Chen, A. Yu, D. Higgins, H. Li, H. Wang, and Z. Chen. *Nano Lett.*, **2012**. 12(4), 1946-1952.
- [171] G. Du, X. Liu, Y. Zong, T.S.A. Hor, A. Yu, and Z. Liu. *Nanoscale*, **2013**. 5(11), 4657-4661.
- [172] Y. Tian, L. Xu, J. Qian, J. Bao, C. Yan, H. Li, H. Li, and S. Zhang. *Carbon*, **2019**. 146, 763-771.
- [173] S. Park, Y. Shao, J. Liu, and Y. Wang. *Energy Environ. Sci.*, **2012**. 5(11), 9331-9344.
- [174] P.Y. Chan and R.M. Siti, in *Semiconductors*, R. Inguanta and C. Sunseri, Editors. **2018**, IntechOpen: London, United Kingdom.
- [175] P. Pei, K. Wang, and Z. Ma. *Appl. Energy*, **2014**. 128, 315-324.
- [176] L. Li, S. Liu, and A. Manthiram. *Nano Energy*, **2015**. 12, 852-860.
- [177] V. Caramia and B. Bozzini. *J. Renew. Sustain. Ener.*, **2014**. 3(2), 28.
- [178] C.W. Lee, S.W. Eom, K. Sathiyarayanan, and M.S. Yun. *Electrochim. Acta*, **2006**. 52(4), 1588-1591.
- [179] G.Q. Zhang and X.G. Zhang. *Electrochim. Acta*, **2004**. 49(6), 873-877.
- [180] Z. Wang and S. Mitra. *J. Power Sources*, **2014**. 266, 296-303.
- [181] C. Iwakura, S. Nohara, N. Furukawa, and H. Inoue. *Solid State Ionics*, **2002**. 148(3), 487-492.
- [182] A.A. Askadskii. *Polym. Sci. U.S.S.R.*, **1990**. 32(10), 2061-2069.
- [183] J.H. Weijs and D. Lohse. *Phys. Rev. Lett.*, **2013**. 110(5), 054501.
- [184] D. Kiuchi, H. Matsushima, Y. Fukunaka, and K. Kuribayashi. *J. Electrochem. Soc.*, **2006**. 153(8), E138-E143.
- [185] H. Matsushima, T. Iida, and Y. Fukunaka. *J. Solid State Electrochem.*, **2012**. 16(2), 617-623.
- [186] J. Eigeldinger and H. Vogt. *Electrochim. Acta*, **2000**. 45(27), 4449-4456.
- [187] R.J. Balzer and H. Vogt. *J. Electrochem. Soc.*, **2003**. 150(1), E11-E16.
- [188] G. Sakuma, Y. Fukunaka, and H. Matsushima. *Int. J. Hydrogen Energy*, **2014**. 39(15), 7638-7645.
- [189] K. Wang, P. Pei, Z. Ma, H. Chen, H. Xu, D. Chen, and H. Xing. *J. Power Sources*, **2015**. 296, 40-45.

- [190] R. Shivkumar, G. Paruthimal Kalaignan, and T. Vasudevan. *J. Power Sources*, **1995**. 55(1), 53-62.
- [191] P. Bonnicksen and J.R. Dahn. *J. Electrochem. Soc.*, **2012**. 159(7), A981-A989.
- [192] S. Wang, Z. Yang, and L. Zeng. *J. Electrochem. Soc.*, **2009**. 156(1), A18-A21.
- [193] J. Huang, Z. Yang, R. Wang, Z. Zhang, Z. Feng, and X. Xie. *J. Mater. Chem. A*, **2015**. 3(14), 7429-7436.
- [194] J. Yu, H. Yang, X. Ai, and X. Zhu. *J. Power Sources*, **2001**. 103(1), 93-97.
- [195] J.F. Parker, I.R. Pala, C.N. Chervin, J.W. Long, and D.R. Rolison. *J. Electrochem. Soc.*, **2016**. 163(3), A351-A355.
- [196] C.A.C. Sequeira, D.M.F. Santos, E. Cameron, and P.S.D. Brito. *Mater. Technol.*, **2008**. 23(3), 142-144.
- [197] J.C.B. Nadesan and A.C.C. Tseung. *J. Electrochem. Soc.*, **1985**. 132(12), 2957-2959.
- [198] P.W.T. Lu and S. Srinivasan. *J. Electrochem. Soc.*, **1978**. 125(9), 1416-1422.
- [199] M. Xiong and D.G. Ivey. *Electrochem. Commun.*, **2017**. 75, 73-77.
- [200] S.F. Bender, J.W. Cretzmeyer, and T.F. Reise, in *Handbook of Batteries, 3rd Edition*, D. Linden and T.B. Reddy, Editors. **2002**, McGraw-Hill: New York.
- [201] *Zinc facts*. 2019; Available from: <https://www.nrcan.gc.ca/our-natural-resources/minerals-mining/minerals-metals-facts/zinc-facts/20534>.
- [202] Z. Wang, J. Ang, J. Liu, X.Y.D. Ma, J. Kong, Y. Zhang, T. Yan, and X. Lu. *Appl. Catal., B*, **2019**, 118344.
- [203] Z. Huang, X. Qin, G. Li, W. Yao, J. Liu, N. Wang, K. Ithisuphalap, G. Wu, M. Shao, and Z. Shi. *ACS Appl. Energy Mater.*, **2019**. 2(6), 4428-4438.
- [204] J. Sun, H. Yin, P. Liu, Y. Wang, X. Yao, Z. Tang, and H. Zhao. *Chem. Sci.*, **2016**. 7(9), 5640-5646.
- [205] K. Sakaushi, T.-P. Fellingner, and M. Antonietti. *ChemSusChem*, **2015**. 8(7), 1156-1160.
- [206] B. Pichler, B.S. Berner, N. Rauch, C. Zelger, H.-J. Pauling, B. Gollas, and V. Hacker. *J. Appl. Electrochem.*, **2018**. 48(9), 1043-1056.
- [207] P. Pei, Z. Ma, K. Wang, X. Wang, M. Song, and H. Xu. *J. Power Sources*, **2014**. 249, 13-20.
- [208] T. Zhou, W. Xu, N. Zhang, Z. Du, C. Zhong, W. Yan, H. Ju, W. Chu, H. Jiang, C. Wu, and Y. Xie. *Adv. Mater.*, **2019**. 31(15), 1807468.

- [209] X. Fan, J. Liu, J. Ding, Y. Deng, X. Han, W. Hu, and C. Zhong. *Front. Chem.*, **2019**. 7(678).
- [210] H. Lei, Z. Wang, F. Yang, X. Huang, J. Liu, Y. Liang, J. Xie, M.S. Javed, X. Lu, S. Tan, and W. Mai. *Nano Energy*, **2019**, 104293.
- [211] T.N.T. Tran, M. Xiong, M.P. Clark, H.J. Chung, and D.G. Ivey. *Electrochim. Acta*, **2020** (submitted).
- [212] C. Guan, A. Sumboja, H. Wu, W. Ren, X. Liu, H. Zhang, Z. Liu, C. Cheng, S.J. Pennycook, and J. Wang. *Adv. Mater.*, **2017**. 29(44), 1704117.
- [213] W. Zang, A. Sumboja, Y. Ma, H. Zhang, Y. Wu, S. Wu, H. Wu, Z. Liu, C. Guan, J. Wang, and S.J. Pennycook. *ACS Catal.*, **2018**. 8(10), 8961-8969.
- [214] C. Guan, A. Sumboja, W. Zang, Y. Qian, H. Zhang, X. Liu, Z. Liu, D. Zhao, S.J. Pennycook, and J. Wang. *Energy Storage Mater.*, **2019**. 16, 243-250.
- [215] S. Shah, N.M. Ranjha, and Z. Javaid. *Iran. Polym. J.*, **2013**. 22(11), 811-820.
- [216] S.M.H. Bukhari, S. Khan, M. Rehanullah, and N.M. Ranjha. *Int. J. Polym. Sci.*, **2015**. 2015, 15.
- [217] S. Ganguly, S. Mondal, P. Das, P. Bhawal, P.P. Maity, S. Ghosh, S. Dhara, and N.C. Das. *Int. J. Biol. Macromol.*, **2018**. 111, 983-998.
- [218] S. Bashir, Y.Y. Teo, S. Ramesh, and K. Ramesh. *Polymer*, **2018**. 147, 108-120.
- [219] M.J. Moura, M.M. Figueiredo, and M.H. Gil. *Biomacromolecules*, **2007**. 8(12), 3823-3829.
- [220] X. Liu, M. Chang, B. He, L. Meng, X. Wang, R. Sun, J. Ren, and F. Kong. *J. Colloid Interface Sci.*, **2019**. 538, 507-518.
- [221] L.-Y. Xia, X. Zhang, M. Cao, Z. Chen, and F.-G. Wu. *Biomacromolecules*, **2017**. 18(10), 3073-3081.
- [222] O. Arnolds, H. Buggisch, D. Sachsenheimer, and N. Willenbacher. *Rheol. Acta*, **2010**. 49(11), 1207-1217.
- [223] S.D. Druger, A. Nitzan, and M.A. Ratner. *J. Chem. Phys.*, **1983**. 79(6), 3133-3142.
- [224] A. Nitzan and M.A. Ratner. *J. Phys. Chem.*, **1994**. 98(7), 1765-1775.
- [225] A.A. Teran, M.H. Tang, S.A. Mullin, and N.P. Balsara. *Solid State Ionics*, **2011**. 203(1), 18-21.
- [226] E. Pessine, S. Agostinho, and H. Chagas. *Can. J. Chem.*, **2011**. 64, 523-527.
- [227] H.K. Roobottom, H.D.B. Jenkins, J. Passmore, and L. Glasser. *J. Chem. Educ.*, **1999**. 76(11), 1570.

- [228] A. Botti, F. Bruni, S. Imberti, M.A. Ricci, and A.K. Soper. *J. Mol. Liq.*, **2005**. 117(1), 81-84.
- [229] J. Xie, X. Liu, and J. Liang. *J. Appl. Polym. Sci.*, **2007**. 106(3), 1606-1613.
- [230] Q. Lv, M. Wu, and Y. Shen. *Colloids Surf., A*, **2019**. 583, 123972.
- [231] K. Kudo, J. Ishida, G. Syuu, Y. Sekine, and T. Ikeda-Fukazawa. *J. Chem. Phys.*, **2014**. 140(4), 044909.
- [232] X. Zhou, F. Zhao, Y. Guo, B. Rosenberger, and G. Yu. *Sci. Adv.*, **2019**. 5(6), eaaw5484.
- [233] N. Wang, G. Ru, L. Wang, and J. Feng. *Langmuir*, **2009**. 25(10), 5898-5902.
- [234] W.B. Wang and A.Q. Wang. *Adv. Mater. Res.*, **2010**. 96, 177-182.
- [235] C.A.C. Sequeira, D.M.F. Santos, B. Šljukić, and L. Amaral. *Braz. J. Phys.*, **2013**. 43(3), 199-208.
- [236] D. Zhang and K. Zeng. *Ind. Eng. Chem. Res.*, **2012**. 51(42), 13825-13832.
- [237] C. Meng, B. Wang, Z. Gao, Z. Liu, Q. Zhang, and J. Zhai. *Sci. Rep.*, **2017**. 7(1), 41825.
- [238] J. Fu, R. Liang, G. Liu, A. Yu, Z. Bai, L. Yang, and Z. Chen. *Adv. Mater.*, **2019**. 31(31), 1805230.
- [239] Z. Zhao, X. Fan, J. Ding, W. Hu, C. Zhong, and J. Lu. *ACS Energy Lett.*, **2019**. 4(9), 2259-2270.
- [240] Y. Ito, X. Wei, D. Desai, D. Steingart, and S. Banerjee. *J. Power Sources*, **2012**. 211, 119-128.
- [241] R.Y. Wang, D.W. Kirk, and G.X. Zhang. *J. Electrochem. Soc.*, **2006**. 153(5), C357-C364.
- [242] Y. Huang, Z. Li, Z. Pei, Z. Liu, H. Li, M. Zhu, J. Fan, Q. Dai, M. Zhang, L. Dai, and C. Zhi. *Adv. Energy Mater.*, **2018**. 8(31), 1802288.
- [243] P. Barai, K. Higa, and V. Srinivasan. *Phys. Chem. Chem. Phys.*, **2017**. 19(31), 20493-20505.
- [244] Y. Wu, Y. Zhang, Y. Ma, J.D. Howe, H. Yang, P. Chen, S. Aluri, and N. Liu. *Adv. Energy Mater.*, **2018**. 8(36), 1802470.
- [245] X. Cheng, J. Pan, Y. Zhao, M. Liao, and H. Peng. *Adv. Energy Mater.*, **2018**. 8(7), 1702184.
- [246] M. Liao, J. Wang, L. Ye, H. Sun, Y. Wen, C. Wang, X. Sun, B. Wang, and H. Peng. *Angew. Chem., Int. Ed.*, **2020**. 59(6), 2273-2278.
- [247] Z. Wang, X. Meng, Z. Wu, and S. Mitra. *J. Energy Chem.*, **2017**. 26(1), 129-138.

- [248] S. Yang and K. Kim. *J. Electrochem. Sci. Technol.*, **2018**. 9(4), 339-344.
- [249] O. Kwon, H.J. Hwang, Y. Ji, O.S. Jeon, J.P. Kim, C. Lee, and Y.G. Shul. *Sci. Rep.*, **2019**. 9(1), 3175.
- [250] L. Ma, S. Chen, D. Wang, Q. Yang, F. Mo, G. Liang, N. Li, H. Zhang, J.A. Zapien, and C. Zhi. *Adv. Energy Mater.*, **2019**. 9(12), 1803046.
- [251] A. Poosapati, E. Jang, D. Madan, N. Jang, L. Hu, and Y. Lan. *MRS Commun.*, **2019**. 9(1), 122-128.
- [252] L. Bockstie, D. Trevethan, and S. Zaromb. *J. Electrochem. Soc.*, **1963**. 110(4), 267.
- [253] R.S.M. Patnaik, S. Ganesh, G. Ashok, M. Ganesan, and V. Kapali. *J. Power Sources*, **1994**. 50(3), 331-342.
- [254] D.-J. Park, W.-G. Yang, H.-W. Jeong, and K.-S. Ryu. *Bull. Korean Chem. Soc.*, **2017**. 38(7), 706-710.
- [255] B. Zhu, X. Wang, P. Yao, J. Li, and J. Zhu. *Chem. Sci.*, **2019**. 10(30), 7132-7148.
- [256] C. Iclodean, B. Varga, N. Burnete, D. Cimerdean, and B. Jurchiş. *IOP Conf. Ser.: Mater. Sci. Eng.*, **2017**. 252, 012058.
- [257] *Goals for Advanced High-Performance Batteries for Electric Vehicle (EV) Applications*. [cited 2020 05]; Available from: [https://www.uscar.org/guest/article\\_view.php?articles\\_id=85](https://www.uscar.org/guest/article_view.php?articles_id=85).
- [258] D. Aasen, M.P. Clark, and D.G. Ivey. *Batteries Supercaps*, **2020**. 3(2), 174-184.
- [259] T.N.T. Tran, M.P. Clark, H.J. Chung, and D.G. Ivey. *Batteries Supercaps*, **2020**. 3(5), 409-416.
- [260] R.J. Guanti and P.J. Moran. *J. Appl. Electrochem.*, **1986**. 16(5), 678-682.
- [261] X. Zhu, H. Yang, Y. Cao, and X. Ai. *Electrochim. Acta*, **2004**. 49(16), 2533-2539.
- [262] T.P. Dirkse. *J. Electrochem. Soc.*, **1959**. 106(2), 154-155.
- [263] W.H. Dyson, L.A. Schreier, W.P. Sholette, and A.J. Salkind. *J. Electrochem. Soc.*, **1968**. 115(6), 566.
- [264] A. Anderko, J.W. Berthold, M. Rafal, and S.J. Sanders, in *Proceedings of the Symposium on Rechargeable Zinc Batteries: Commemorating the 100th Birthday of A. N. Frumkin*, A.J. Salkind, F. McLarnon, and V.S. Bagotskii, Editors. **1996**, The Electrochemical Society: Pennington, NJ, 262.
- [265] X.Y. Wang, J.M. Wang, Q.L. Wang, H.B. Shao, and J.Q. Zhang. *Mater. Corros.*, **2011**. 62(12), 1149-1152.

- [266] M. Bockelmann, L. Reining, U. Kunz, and T. Turek. *Electrochim. Acta*, **2017**. 237, 276-298.
- [267] M. Bockelmann, M. Becker, L. Reining, U. Kunz, and T. Turek. *J. Electrochem. Soc.*, **2018**. 165(13), A3048-A3055.
- [268] M.V. Hoang, H.-J. Chung, and A.L. Elias. *J. Micromech. Microeng.*, **2016**. 26(10), 105019.
- [269] C.f. Chen and K. Wharton. *RSC Adv.*, **2017**. 7(3), 1286-1289.
- [270] M. Horstmann, W. Müller, and B.D. Asmussen, in *Bioadhesive Drug Delivery Systems: Fundamentals, Novel Approaches, and Development*, E. Mathiowitz, D.E. Chickering-III, and C.-M. Lehr, Editors. **1999**, CRC Press: New York, 175-195.
- [271] T. Arlt, D. Schröder, U. Krewer, and I. Manke. *Phys. Chem. Chem. Phys.*, **2014**. 16(40), 22273-22280.
- [272] D. Schröder, T. Arlt, U. Krewer, and I. Manke. *Electrochem. Commun.*, **2014**. 40, 88-91.
- [273] J. Fu, in *Chemical Engineering*. 2018, University of Waterloo: Waterloo, Ontario, Canada, 147.
- [274] M. Wang, Z. Wang, and Z. Guo. *Int. J. Hydrogen Energy*, **2009**. 34(13), 5311-5317.
- [275] C.N. Ho and B.J. Hwang. *J. Electroanal. Chem.*, **1994**. 377(1), 177-190.
- [276] D. Chen, J. Ji, Z. Jiang, M. Ling, Z. Jiang, and X. Peng. *J. Power Sources*, **2020**. 450, 227660.
- [277] K. He, J. Zai, X. Liu, Y. Zhu, A. Iqbal, T. Tadesse Tsega, Y. Zhang, N. Ali, and X. Qian. *Appl. Catal., B*, **2020**. 265, 118594.
- [278] X. Wang, Z. Liao, Y. Fu, C. Neumann, A. Turchanin, G. Nam, E. Zschech, J. Cho, J. Zhang, and X. Feng. *Energy Storage Mater.*, **2020**. 26, 157-164.
- [279] Y. Zhong, Z. Pan, X. Wang, J. Yang, Y. Qiu, S. Xu, Y. Lu, Q. Huang, and W. Li. *Adv Sci (Weinh)*, **2019**. 6(11), 1802243.
- [280] C. Wang, N.-H. Xie, Y. Zhang, Z. Huang, K. Xia, H. Wang, S. Guo, B.-Q. Xu, and Y. Zhang. *Chem. Mater.*, **2019**. 31(3), 1023-1029.
- [281] H. Miao, B. Chen, S. Li, X. Wu, Q. Wang, C. Zhang, Z. Sun, and H. Li. *J. Power Sources*, **2020**. 450, 227653.
- [282] H. Miao, X. Wu, B. Chen, Q. Wang, F. Wang, J. Wang, C. Zhang, H. Zhang, J. Yuan, and Q. Zhang. *Electrochim. Acta*, **2020**. 333, 135566.
- [283] B. Roy, K.J. Shebin, and S. Sampath. *J. Power Sources*, **2020**. 450, 227661.
- [284] X. Cheng, J. Wang, Y. Liao, C. Li, and Z. Wei. *ACS Appl. Mater. Interfaces*, **2018**. 10(28), 23774-23782.

- [285] T.P. Dirkse and R. Timmer. *J. Electrochem. Soc.*, **1969**. 116(2), 162-165.
- [286] A.R. Mainar, E. Iruin, L.C. Colmenares, J.A. Blázquez, and H.-J. Grande. *Energy Sci. Eng.*, **2018**. 6(3), 174-186.
- [287] I. Hwang, E. Ahn, and Y. Tak. *Int. J. Electrochem. Sci.*, **2014**. 9(10), 5454-5466.
- [288] D. Schröder, N.N. Sinai Borker, M. König, and U. Krewer. *J. Appl. Electrochem.*, **2015**. 45(5), 427-437.
- [289] X. Wang, Z. Liu, and T. Zhang. *Small*, **2017**.
- [290] B.F. Palmer. *Clin J Am Soc Nephrol*, **2015**. 10(6), 1050-60.
- [291] S. Komaba, J. Arakawa, M. Seyama, T. Osaka, I. Satoh, and S. Nakamura. *Talanta*, **1998**. 46(6), 1293-1297.
- [292] T. Zhang, X. Chang, W. Liu, X. Li, F. Wang, L. Huang, S. Liao, X. Liu, Y. Zhang, and Y. Zhao. *Journal of Trace Elements in Medicine and Biology*, **2017**. 44(Supplement C), 104-108.
- [293] M. Odijk, E.J. van der Wouden, W. Olthuis, M.D. Ferrari, E.A. Tolner, A.M.J.M. van den Maagdenberg, and A. van den Berg. *Sensors and Actuators B: Chemical*, **2015**. 207(Part B), 945-953.
- [294] A.S. Lima, N. Bocchi, H.M. Gomes, and M.F. Teixeira. *Sensors (Basel)*, **2009**. 9(9), 6613-25.
- [295] A. Thube and S. Kulkarni.
- [296] I.S. El Otmani, A. Jarmoumi, M. Bouatia, B. Mojemmi, M.O. Idrissi, M. Draoui, and N. Kamal. *Journal of Chemical and Pharmaceutical Research*, **2015**. 7(8), 862-867.
- [297] V. Albert, A. Subramanian, K. Rangarajan, and R.M. Pandey. *Journal of laboratory physicians*, **2011**. 3(2), 104.
- [298] B.-S. Yu, L.-H. Nie, and S.-Z. Yao. *Journal of Chromatography B: Biomedical Sciences and Applications*, **1997**. 693(1), 43-49.
- [299] H. Chen, Y.-S. Gal, S.-H. Kim, H.-J. Choi, M.-C. Oh, J. Lee, and K. Koh. *Sensors and Actuators B: Chemical*, **2008**. 133(2), 577-581.
- [300] X. Li, L. Liu, X. Wang, Y.S. Ok, J.A.W. Elliott, S.X. Chang, and H.-J. Chung. *Sci. Rep.*, **2017**. 7, 1685.
- [301] J. Bobacka, A. Ivaska, and A. Lewenstam. *Chemical reviews*, **2008**. 108(2), 329-351.
- [302] L. van de Velde, E. d'Angremont, and W. Olthuis. *Talanta*, **2016**. 160, 56-65.

- [303] H. Beyer and W. Walter, in *Organic Chemistry - A Comprehensive Degree Text and Source Book*. Woodhead Publishing.
- [304] C. Jones and J. Thornback, in *Medicinal Applications of Coordination Chemistry*. Royal Society of Chemistry.
- [305] W. Steglich, B. Fugmann, and S. Lang-Fugmann, in *RÖMPP Encyclopedia Natural Products*. Thieme Medical Publishers Inc.
- [306] A.R. Berens. *J. Vinyl Technol.*, **1989**. 11(4), 171-175.
- [307] G. Harsanyi. **1995**: CRC Press. 464.
- [308] J. Bobacka and A. Ivaska. *Compr. Anal. Chem.*, **2007**. 49, 73-86.
- [309] M. Fibbioli, W.E. Morf, M. Badertscher, N.F. de Rooij, and E. Pretsch. *Electroanalysis*, **2000**. 12(16), 1286-1292.
- [310] J. Bobacka. *Electroanalysis*, **2006**. 18(1), 7-18.
- [311] A. Michalska. *Analytical and bioanalytical chemistry*, **2006**. 384(2), 391-406.
- [312] R. Mamińska and W. Wróblewski. *Electroanalysis*, **2006**. 18(13-14), 1347-1353.
- [313] J.-P. Veder, R. De Marco, K. Patel, P. Si, E. Grygolowicz-Pawlak, M. James, M.T. Alam, M. Sohail, J. Lee, and E. Pretsch. *Analytical chemistry*, **2013**. 85(21), 10495-10502.
- [314] J. Bobacka. *Analytical chemistry*, **1999**. 71(21), 4932-4937.
- [315] W.-S. Han, Y.-H. Lee, K.-J. Jung, S.-Y. Ly, T.-K. Hong, and M.-H. Kim. *Journal of Analytical Chemistry*, **2008**. 63(10), 987-993.
- [316] S.C. Hobaica. *Journal of Polymer Science Part B: Polymer Physics*, **2003**. 41(8), 807-822.
- [317] J. Luo, H. Zhang, X. Wang, J. Li, and F. Wang. *Macromolecules*, **2007**. 40(23), 8132-8135.
- [318] J. Bobacka, A. Ivaska, and A. Lewenstam. *Electroanalysis*, **2003**. 15(5-6), 366-374.
- [319] J. Hu, A. Stein, and P. Bühlmann. *TrAC, Trends Anal. Chem.*, **2016**. 76, 102-114.
- [320] J. Bobacka, A. Ivaska, and A. Lewenstam. *Anal. Chim. Acta*, **1999**. 385(1), 195-202.
- [321] N. Zine, J. Bausells, F. Vocanson, R. Lamartine, Z. Asfari, F. Teixidor, E. Crespo, I.A.M. de Oliveira, J. Samitier, and A. Errachid. *Electrochim. Acta*, **2006**. 51(24), 5075-5079.
- [322] W.-S. Han, Y.-H. Lee, K.-J. Jung, S.-Y. Ly, T.-K. Hong, and M.-H. Kim. *J. Anal. Chem.*, **2008**. 63(10), 987-993.

- [323] Z. Mousavi, J. Bobacka, A. Lewenstam, and A. Ivaska. *J. Electroanal. Chem.*, **2009**. 633, 246-252.
- [324] J. Ping, Y. Wang, J. Wu, and Y. Ying. *Electrochem. Commun.*, **2011**. 13(12), 1529-1532.
- [325] N.M. Ivanova, I.V. Podeshvo, M.Y. Goikhman, A.V. Yakimanskii, and K.N. Mikhelson. *Sens. Actuators, B*, **2013**. 186, 589-596.
- [326] G. Vardar, M. Altikatoglu, D. Ortac, M. Cemek, and I. Isildak. *Biotechnol. Appl. Biochem.*, **2015**. 62(5), 663-8.
- [327] D. Siswanta, Y.D. Wulandari, and J. Jumina. *Eurasian Journal of Analytical Chemistry*, **2016**. 11(2), 115-125.
- [328] X. Zeng and W. Qin. *Anal. Chim. Acta*, **2017**. 982, 72-77.
- [329] Z.A. Boeva and V.G. Sergeyev. *Polym. Sci., Ser. C*, **2014**. 56(1), 144-153.
- [330] C. Silva, J. Pavez, J. Francisco Silva, M. Sancy, J. Guerrero, M. A. Pa' Ez, and J. Zagal. Vol. 522. **2010**. 112-124.
- [331] K.M. Molapo, P.M. Ndangili, R.F. Ajayi, G. Mbambisa, S.M. Mailu, N. Njomo, M. Masikini, P. Baker, and E.I. Iwuoha. *Int. J. Electrochem. Sci.*, **2012**. 7(12), 11859 - 11875.
- [332] N. Su. *Polymers*, **2015**. 7(9), 1473.
- [333] I. Sapurina and J. Stejskal. *Polym. Int.*, **2008**. 57(12), 1295-1325.
- [334] R. De Levie. *Electrochimica Acta*, **1965**. 10(2), 113-130.
- [335] H.K. Song, H.Y. Hwang, K.H. Lee, and L.H. Dao. *Electrochimica Acta*, **2000**. 45(14), 2241-2257.
- [336] E. Bakker, E. Pretsch, and P. Buhlmann. *Anal. Chem.*, **2000**. 72(6), 1127-33.
- [337] in *Clinical Methods: The History, Physical, and Laboratory Examinations*, H.K. Walker, W.D. Hall, and J.W. Hurst, Editors. **1990**, Butterworth Publishers, a division of Reed Publishing.: Boston.
- [338] D. Kim, J. McCoy, and C. Nimigeon, in *Handbook of Ion Channels*. **2015**, CRC Press, 13-23.
- [339] R. Chang and J.W. Thoman, Jr., in *Physical Chemistry for the Chemical Sciences*. University Science Books.
- [340] A. Depauw, E. Dossi, N. Kumar, C. Fiorini-Debuisschert, G. Huberfeld, M.H. Ha-Thi, N. Rouach, and I. Leray. *Chemistry*, **2016**. 22(42), 14902-14911.

## **Appendix. Potassium Ion-selective Electrode Using Polyaniline and Matrix-Supported Ion-Selective PVC Membrane**

A version of this appendix has been published as:

Tran, T.N.T., Qiu, S. and Chung, H.-J., *Potassium Ion-selective Electrode Using Polyaniline and Matrix-Supported Ion-Selective PVC Membrane*. IEEE Sensors Journal, 2018. **18**(22): p. 9081–9087.

### **A.1. Introduction**

Wearable devices for health monitoring have created new opportunities for personalized remote healthcare in recent years [289]. Chemical homeostasis is one of the most important subjects for sensors. Among chemicals, potassium ions have critical importance for all levels of vital activities [290]. In fact, potassium monitoring in food and serum [291], urine [292] and potentially in the brain [293] has been a routine analysis in the clinical and medical fields to reveal physical conditions of the patients having renal diseases, hypopotassemia, alkalosis, cirrhosis of liver or using diuretic drugs [294]. Thus, a miniaturized  $K^+$  sensor is in high demand for wearable health monitoring system.

Conventional  $K^+$  sensing methods include flame photometry [295-297], ion chromatography [298], surface plasmon resonance [299] and electrochemical detection [300]. Among these technologies, an electrochemical ion-selective electrode (ISE) has many advantages including fabrication simplicity, high selectivity towards a specific ion, fast response time, wide linear range, reproducibility and potential for miniaturization [301]. Using solid-state ISEs without

an internal filling solution provides a durable, flexible and portable ion sensor that can easily be miniaturized.

Ionophores, complex molecules that allow permeation of  $K^+$  ions while blocking others, is the key material for solid-state ion-selective electrodes. The discovery of ionophores for  $K^+$  detection was based on biological research which revealed that valinomycin, a dodecadepsipeptide antibiotic which can be isolated from *Streptomyces*, possesses an internal cavity whose size matches closely with the diameter of  $K^+$  [302]. This means that valinomycin can easily form ionic bonds with  $K^+$ . Other ions, for example  $Na^+$ , whose diameter is significantly smaller than the pore, cannot form a complex together; the selectivity for  $K^+$  over  $Na^+$  exceeds 1000 times [303-305]. The mobility of ionophore and lipophilic counterions in the ion-selective membrane significantly affect the frequency of interaction of  $K^+$  and the ionophore at the polymer/solution interface, which is important for the functionality of an ISE. Due to the concentration gradient,  $K^+$  that forms ionic bonds with ionophores are mobile inside the liquid phase (plasticizer) of the ion-selective membrane, while other species are blocked outside. In rigid polyvinyl chloride (PVC), the diffusion coefficient is in the range of  $10^{-6}$   $cm^2/s$  for small gas molecules such as  $H_2$  and  $He$ , and up to  $10^{-17}$   $cm^2/s$  for  $CCl_4$ , let alone bulky organic molecules such as valinomycin [306]. Hence, adding plasticizer to the PVC membrane is necessary to promote diffusion of ionophores and to equilibrate the chemical potential more quickly. This way, response time is shortened. The diffusion coefficient of valinomycin through a membrane consisting of about 33% PVC – bis(2-ethylhexyl) sebacate (DOS) is of the order of  $10^{-8}$   $cm^2/s$  [307].

Figure A.1a illustrates the mechanism that causes the issue of potential instability when the ion-selective membrane is in direct contact with the electron-conducting substrate. According to the Nernst equation, the membrane potential changes logarithmically with  $K^+$  ion activity; this can

only be true when  $[K^+]$  transduces to the electric potential without any delay or loss [308]. Here, the water layer at the interface between the ion-selective membrane and the electrically conducting substrate damps out the capacitive junction and, as a result, there is no transition from ions to electrons [302]. In 2000, it was shown that a thin water layer between Au and an ion-selective membrane is responsible for the potential drift and such problems can be reduced by depositing a lipophilic monolayer, such as thiol compounds, on top of the metal contact [309]. Alternatively, a conducting polymer between the electronic conductor and the ion-selective membrane can give high potential stability, but does not influence the analytical performance of the ISE including selectivity, sensitivity and limit of detection [308]. Over the past few years, conducting polymers have been applied as promising ion-to-electron transducers for solid contact ISEs because they exhibit both electrical and ionic conductivity, which means they can help the ion-to-electron transition by oxidation/reduction of conducting polymers (Figure A.1b) [310, 311]. Many electronically conducting polymers, including polypyrroles [312], poly(3-octylthiophene) (POT) [313], and poly(3,4-ethylene-dioxythiophene) (PEDOT) [314] and polyaniline (PANI) [315], were tested as ion-to-electron transducers. It should be noted that PANI does not prevent water layer formation; rather, its conductivity is stable over a wide range of water content [316, 317]. Therefore, in this study, PANI was chosen due to its high conductivity in the presence of water ( $10^{-3} - 10^{-2}$  S/cm) and facile synthesis.

With the emergence of flexible and wearable bioelectronics, there has been a revival of ion-selective electrodes in the last few years owing to their potential for miniaturization. This novel application requires a complete integrated system of ISE and reference electrode (RE). Most of the recent studies solely focus on the modifications of the working electrode (WE) while the effect of RE modification is less frequently studied (see Table A.1 and references therein). In fact, the

stability of miniaturized REs has been a longstanding issue for potentiometric measurements using solid-state electrodes [309, 318]. The purpose of an RE is to provide a stable potential that is independent of the surrounding sample. A major issue of a solid-state Ag/AgCl RE is the leakage of inorganic salt [319]. In this study, we employed a NaCl-saturated PVB membrane to prevent leakage of AgCl; the aim of our work was to come up with a simple method to fabricate a  $K^+$  ISE with high selectivity and stable sensitivity. We applied a commercial screen-printed electrode (SPE) with an extra intermediate layer (polyaniline) to solve the potential drift problem. Additionally, the miniaturized RE (Ag/AgCl) was placed on the same plane as the WE and was modified by polyvinyl butyral (PVB) and a sodium chloride layer to maintain constant concentration of chloride ions and prevent leaking of silver chloride. Finally, our  $K^+$  ISE exhibits good selectivity ( $-\log K_{K^+, Na^+} = 4.36$ ), high sensitivity (60.5 mV/decade), low concentration for the limit of detection ( $10^{-5.8}$  M), large range of linear detection ( $10^{-5} - 1$  M) and potential stability (up to 12 h). The high concentration of NaCl mimics the salt bridge; thus the output stability was further enhanced.

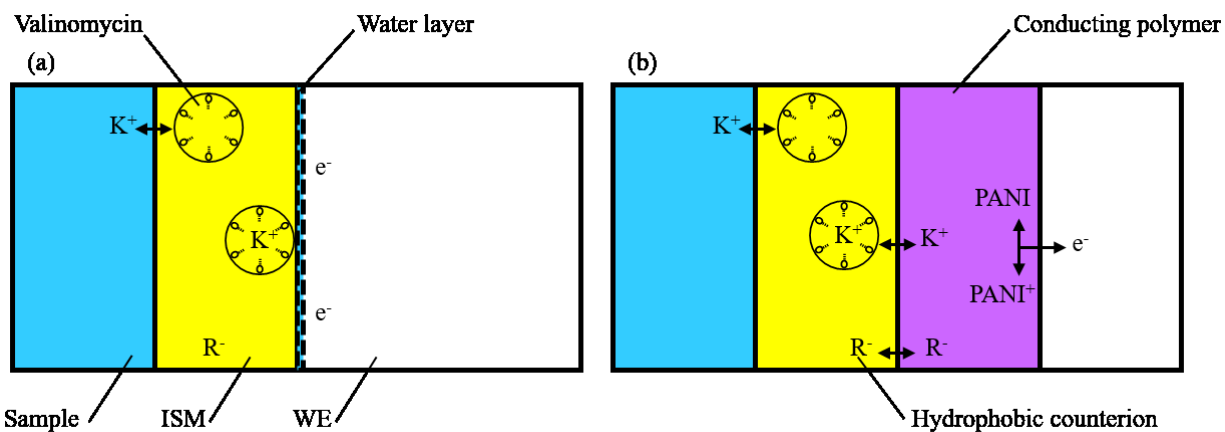


Figure A.1. Schematics that describe: (a) the water layer that forms between the ion-selective membrane and electronically conducting substrate and (b) how an electrochemically transducing intermediate layer, such as polyaniline (PANI), mitigates the adverse effect by the water layer.

Table A.1. Summary of recent studies of solid-state potassium ion-selective electrodes

Electrode	Intermediate layer/ Ionophore	Reference	Selectivity ( $-\log K_{K^+, Na^+}$ )	Sensitivity (mV/decade)	LOD ( $10^{-n}$ M)	Linear range (M)	Ref.
GC	N/A / valinomycin	SCE	N/A	49	5	$10^{-5} - 10^{-1}$	[320]
Pt	Ppy / calixarene	N/A	N/A	51	5.7	$10^{-5.2} - 10^{-1}$	[321]
Pt	PANI / dbdb-18-6	SCE	2.5	58	5.8	$10^{-5} - 10^{-1}$	[322]
Au	PEDOT-PSS / valinomycin	Ag/AgCl/3 M KCl	3	61.3	3	$10^{-3} - 10^{-1.5}$	[323]
GC	Graphene / valinomycin	N/A	N/A	58.4	6.2	$10^{-5.8} - 10^{-1}$	[324]
Graphite	Mixture of CB, poly(amidoacid) Cu(I) complex, resin / valinomycin	Ag/AgCl/3.5 M KCl	N/A	59	7	$10^{-6} - 10^{-1}$	[325]
Cu	Graphite-epoxy-hardener / valinomycin	Solid Ag/AgCl	4.11	44	4.4	$10^{-4.3} - 10^{-1}$	[326]
Ag	N/A / PBE	Ag/AgCl/3 M KCl	1.3	56.3	4.7	$10^{-4} - 10^{-1}$	[327]
GC	Hexanethiolate monolayer protected gold cluster / valinomycin	Ag/AgCl/3 M KCl	N/A	57.4	6.1	$10^{-5} - 10^{-1}$	[130]
Pt	Ppy and zeolite / valinomycin	Ag/AgCl/3 M KCl	N/A	54.2	5.1	$10^{-5} - 10^{-2}$	[300]
GC	MoO <sub>2</sub> / valinomycin	Ag/AgCl/3 M KCl	N/A	55	5.5	$10^{-5} - 10^{-3}$	[328]
Carbon SPE	PANI / valinomycin	Modified solid Ag/AgCl	4.36	60.5	5.8	$10^{-5} - 1$	This work

LOD: limit of detection; GC: glassy carbon; N/A: not available; SCE: saturated calomel electrode; Pt: platinum; Ppy: polypyrrole; PANI: polyaniline; dbdb-8-6: 4',4''(5'')-di-tert-butylidibenzo-18-crown-6-ether; PEDOT-PSS: poly(3,4-ethylenedioxythiophene) polystyrene sulfonate; CB: carbon black; PBE: poly(benzyl eugenol); SPE: screen-printed electrode.

## A.2. Materials and methods

### A.2.1. Materials and instruments

Aniline, potassium ionophore I (Valinomycin), potassium tetrakis(4-chlorophenyl)borate (KTCBP), bis(2-ethylhexyl) sebacate (DOS), high molecular weight poly(vinyl chloride) (PVC), tetrahydrofuran (THF), potassium chloride (KCl), sodium chloride (NaCl), polyvinyl butyral (PVB, Butvar® B-98), methanol (CH<sub>3</sub>OH), ammonium chloride (NH<sub>4</sub>Cl) and iron(III) chloride (FeCl<sub>3</sub>) were purchased from Sigma-Aldrich. Hydrochloric acid was purchased from Caledon Laboratories Ltd. Magnesium chloride (MgCl<sub>2</sub>) and calcium chloride (CaCl<sub>2</sub>) were purchased from Fisher Scientific. All chemicals were of analytical grade and used as received without further

purification. Artificial blood serum (pH 7.4) was prepared by adding 0.05 mM  $\text{NH}_4\text{Cl}$ , 130 mM  $\text{NaCl}$ , 0.8  $\text{MgCl}_2$  and 1.4 mM  $\text{CaCl}_2$  in de-ionized water (DIW).

The morphology of polyaniline was observed by field-emission scanning electron microscopy (Zeiss EVO MA10, Jena, Germany). Electrochemical measurements were carried out with an AUTOLAB potentiostat/galvanostat (PGSTAT302N, Metrohm Autolab B.V., Utrecht, The Netherlands). Commercial screen-printed electrodes (DRP 150, DropSense, S.L., Llanera, Spain) containing a carbon WE (diameter: 4 mm), a solid  $\text{Ag}/\text{AgCl}$  RE and a platinum counter electrode were used to prepare  $\text{K}^+$  ISEs. All the experiments were conducted at room temperature (20 °C).

### **A.2.2. PANI polymerization**

The carbon WE on SPE was coated with PANI by using cyclic voltammetry from 0 to 1 V vs.  $\text{Ag}/\text{AgCl}$  with a scan rate of 100 mV/s in 0.03 M aniline and 0.5 M  $\text{HCl}$ . The process was repeated for 30 cycles and stopped at 1 V. Here, we denote the PANI coated SPE as SPE/PANI. After that, SPE/PANI was dried in an oven for 30 min at 110 °C. Then SPE/PANI was inserted into 0.1 M  $\text{KCl}$  and cyclic voltammetry from -0.5 to 1 V vs.  $\text{Ag}/\text{AgCl}$  with scan rate of 100 mV/s was performed to characterize the PANI layer.

### **A.2.3. Preparation of $\text{K}^+$ ion-selective electrode**

The ion-selective membrane (ISM) cocktail used in this work consisted of 2% valinomycin, 0.6% KTCPB, 64.7% DOS and 32.7% PVC (w/w%). Then, 100 mg of the mixture was dissolved in 1 mL THF. As shown in Figure A.2, 10  $\mu\text{L}$  of the valinomycin-containing solution was deposited on SPE/PANI and allowed to dry at room temperature overnight. Here, we denote the trilayer WE as SPE/PANI/V. A control sample to study the efficacy of the PANI intermediate layer

was also prepared by drop casting the ISM cocktail on bare SPE without the PANI layer; we denote this sample as SPE/V. In addition, solution for the RE was made of 79.1 mg PVB and 50 mg NaCl in 1 mL methanol. 3  $\mu$ L of this solution was drop cast onto the Ag/AgCl RE.

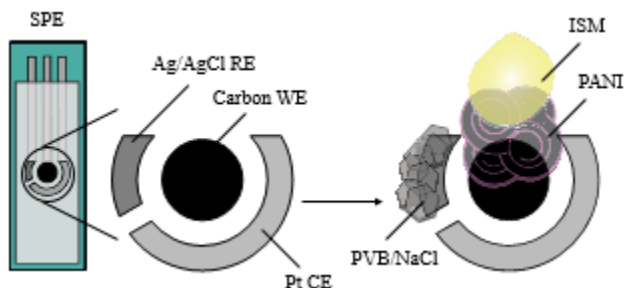


Figure A.2. Modified electrode configuration of solid contact K<sup>+</sup> ISE (ion-selective electrode).

#### A.2.4. Electromotive force (EMF) measurements

Prepared electrodes (SPE/V and SPE/PANI/V) were conditioned in 0.01 M KCl solution for 2 h prior to use. The selectivity factors were determined by separate solution methods to measure the EMF of different solutions of K<sup>+</sup>, NH<sub>4</sub><sup>+</sup>, Na<sup>+</sup>, Mg<sup>2+</sup>, Ca<sup>2+</sup> and Fe<sup>3+</sup> at the same activity (0.1 M).

Sensitivity of the K<sup>+</sup> ISE was determined by measuring in diluted KCl solution through 8 concentration steps (1, 10<sup>-1</sup>, 10<sup>-2</sup>, 10<sup>-3</sup>, 10<sup>-4</sup>, 10<sup>-5</sup>, 10<sup>-6</sup> and 10<sup>-7</sup> M KCl). After measuring the electrode in a solution for 120 s, the electrode was quickly cleaned with DIW and immersed in the next solution. Similarly, response of the K<sup>+</sup> ISE was measured in artificial serum spiked with KCl concentrations between 10<sup>-5</sup> and 1 M.

#### A.2.5. Electrochemical impedance spectroscopy (EIS)

EIS was done with SPE/V, SPE/PANI/V and SPE/PANI/V without the modified RE. Impedance spectra were recorded in the frequency range 100 kHz to 10 mHz at the open circuit potential in 0.1 M KCl. The modulation amplitude used was 10 mV. Data was fit based on the

equivalent circuit models in ZSimpWin software to elucidate the electrochemical process between the interface of the solution and electrode.

### A.2.6. Potential stability measurements

Potential measurements were performed for SPE/PANI/V with and without the PVB/NaCl layer on the RE in 0.1 M KCl for 12 h.

## A.3. Results and discussion

### A.3.1. Characterization of polyaniline

In general, electrochemical polymerisation of aniline can be carried out using one of three techniques: (i) potentiostatic method (applying a constant voltage), (ii) cyclic voltammetry (CV) and (iii) galvanostatic method (applying a constant current) to an aqueous solution of aniline. PANI was deposited on the WE as described in the experimental section using CV. Here, we adopted the CV method for PANI deposition because it allows a more homogeneous deposition [329]. We found that 30 cycles allowed the best result for PANI layer quality, in terms of the balance between thickness and adhesion. Figure A.3 shows the morphological contrast between SPE and SPE/PANI. Here, we confirmed that 30 CV cycles allowed well-distributed granular PANI to be homogeneously deposited on the carbon electrode.

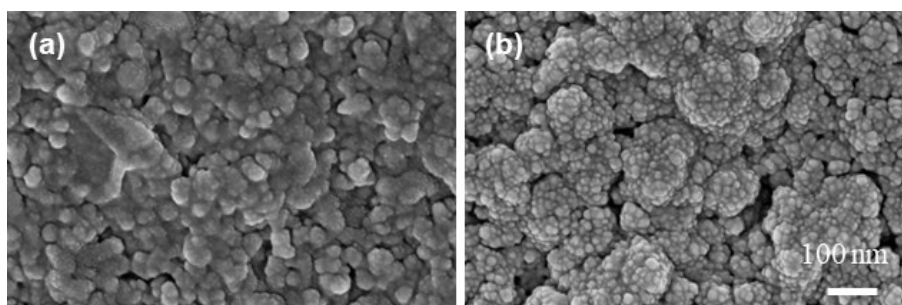


Figure A.3. SEM SE images showing morphology of (a) SPE (bare carbon WE) and (b) SPE/PANI (PANI deposited on carbon WE by 30 CV cycles).

Figure A.4a shows the polymerization of aniline in 0.5 M HCl. The wide oxidation peak in the first cycle at 0.8 V vs. Ag/AgCl reflects the nucleation of aniline onto the site of carbon. After the first scan, this oxidation peak decreases and well-defined new peaks at 0.2 and 0.35 V indicate the growth of the PANI film [330]. After the polymerization step, the electrode was inserted into a solution of 0.1 M KCl to evaluate the quality of the formed polymer layer. In Figure A.4b, the redox peaks at 0.130 V and 0.370 V are assigned to the reduction of partly oxidized emeraldine (electrically conducting) to the reduced form leucoemeraldine (electrically insulating) and vice versa. The produced PANI varies with oxidation states ranging from leucoemeraldine (fully reduced) to emeraldine (half oxidized) to pernigraniline (fully oxidized) [331]. The CV results in Figure A.4a indicate that some portion of the produced PANI is leucoemeraldine, which has the worst electrical conductivity among PANI ( $10^{-10} - 10^{-8}$  S/cm) states. Fortunately, leucoemeraldine is very unstable and can easily be converted to emeraldine salt, which is electrically conducting ( $10^{-2} - 10^{-1}$  S/cm), when dipped in an acidic medium [332, 333].

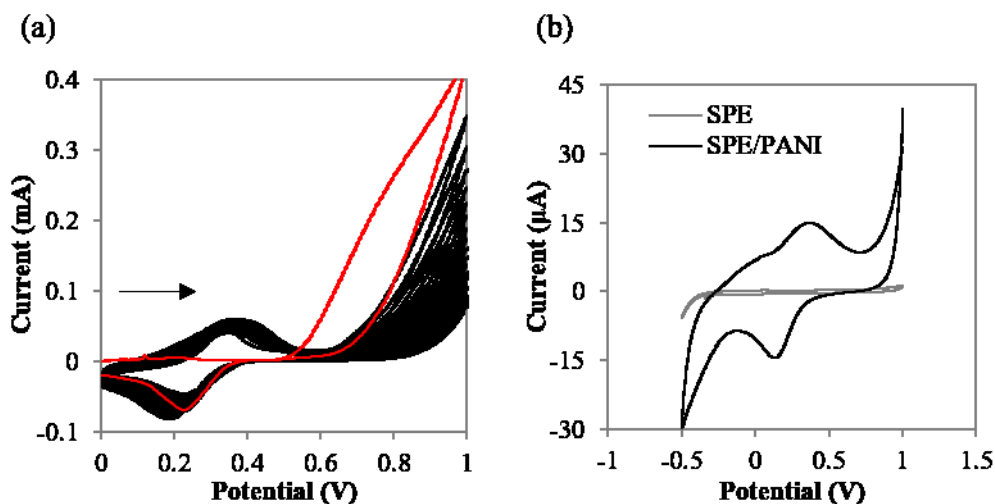


Figure A.4. Cyclic voltammetry (CV) spectra obtained (a) during deposition of PANI in 0.5 M HCl (30 cycles overlapped; red line shows the first scan) and (b) after the 30-cycle deposition of PANI in 0.1 M KCl for quality evaluation (third scan). The spectrum from pure SPE is overlain for comparison.

Figure A.5a shows a Nyquist plot from EIS measurements of bare SPE and SPE/PANI in 0.1 M KCl solution, with a modulation amplitude of 10 mV, and the corresponding simulation results. Here, the imaginary axis for bare SPE is nearly perpendicular with the real axis. Thus, the spectrum of bare SPE can be fit to a series circuit of solution resistance ( $R_s$ ) and double layer capacitance ( $C_{dl}$ ). On the other hand, the spectrum of SPE/PANI inclines outward. In this case, a series of solution resistance ( $R_s$ ), a constant phase element (CPE) and Warburg impedance ( $Z_w$ ) is fit. A CPE is a fitting parameter in electrochemical impedance measurements to represent an imperfect capacitor. There are many factors that cause a CPE, such as surface roughness, varying thickness or pore size distribution across electrode surface, resulting in inhomogeneous reaction rate [334, 335]. The adoption of a CPE in the equivalent circuit for SPE/PANI is reasonable because PANI deposited on the electrode surface increases electrode surface roughness and homogeneity.

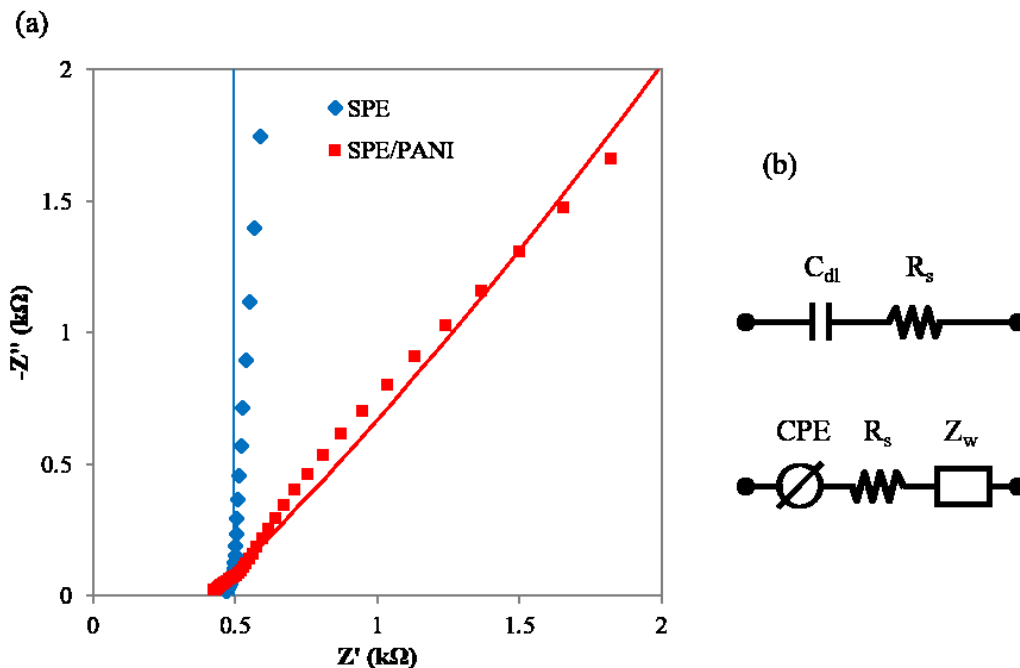


Figure A.5. (a) EIS results at high frequency for the WE before and after aniline polymerization in 0.1 M KCl. The dot results were obtained from experiments, while the lines represent fitting of data using ZSimpWin. (b) Two equivalent circuits to fit SPE (top) and SPE/PANI (bottom).

### A.3.2. Selectivity test

The selectivity coefficient  $K_{ij}^{\text{pot}}$  is one of the most important parameters to determine the quality of an ISE. The selectivity is determined by a combination of ionophore and other electrode membrane components. Here, the Nernst equation for real solutions consisting of ion of interest  $i$  and interfering species  $j$  is *Equation A.1*:

$$E = E^0 + \frac{RT}{z_i F} \ln \left( a_i + \sum_{j=1}^n K_{ij}^{\text{pot}} (a_j)^{z_i/z_j} \right) \quad \text{Equation A.1}$$

with  $E$ : electrode potential,  $E^0$ : standard electrode potential,  $R$ : gas constant,  $T$ : absolute temperature,  $z$ : valence of the ion,  $F$ : Faraday constant and  $a$ : activity of the ion.

In our study, we employed a separate solution method to measure selectivity coefficient  $K_{ij}^{\text{pot}}$  [336]. The potential of SPE/PANI/V is measured with separate solutions of cations at the same activity (0.1 M). If the measured values are  $E_i$  and  $E_j$  for  $K^+$  and other interferents, respectively, the value of  $K_{ij}^{\text{pot}}$  may be calculated from Equation A.2:

$$\log K_{ij}^{\text{pot}} = \frac{(E_j - E_i)z_i F}{RT \ln 10} + \left( 1 - \frac{z_i}{z_j} \right) \log a_i \quad \text{Equation A.2}$$

As shown in Figure A.6,  $K_{ij}^{\text{pot}}$  was obtained for mono-, di- and trivalent cations.  $\text{NH}_4^+$  can interfere the most with  $K^+$  detection because  $\text{NH}_4^+$  has a similar value of hydrated ionic radius as the  $K^+$  ion. For biomedical applications, such as analyzing human interstitial fluid,  $\text{Na}^+$  and  $K^+$  are of the most concern. Here,  $[\text{Na}^+]$  typically varies between 145 – 155 mM while the  $K^+$  level fluctuates between 3.5 – 5.5 mM [337]. Our sensing electrode displayed a  $K_{ij}^{\text{pot}}$  ratio of  $\text{Na}^+$  over  $K^+$  to be about  $4.32 \times 10^{-5}$ , meaning it takes more than 23,000  $\text{Na}^+$  ions to modulate the electrode

potential in the same manner as one  $K^+$  ion does. Therefore, the selectivity of our electrode is adequate to apply in analyzing human interstitial fluid.

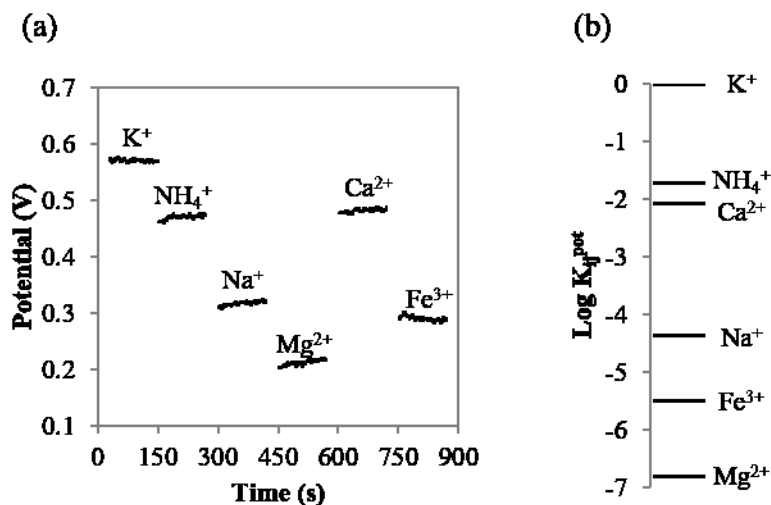


Figure A.6. Response of  $K^+$  ISE for different cations at the same activity (0.1 M). (a) Potential values from potentiometry measurement and (b) selectivity coefficient  $K_{ij}^{pot}$  calculated from (a).

### A.3.3. Sensitivity test

Figure A.7a shows the potential output between the working electrode and the REs when SPE/V and SPE/PANI/V were employed as WEs, respectively, with respect to time immersed in the KCl solution with varying ionic concentration. The figure also shows that inclusion of the PANI interlayer remarkably reduces the potential drift. Constructing a calibration curve (i.e., replotting the average potential values against  $[K^+]$ ) in Figure A.7b shows that SPE/V and SPE/PANI/V have a linear range from  $10^{-4}$  to 1 M and  $10^{-5}$  to 1 M KCl, respectively. As a result, the detection limit was improved from  $10^{-4.3}$  M (SPE/V) to  $10^{-5.8}$  M (SPE/PANI/V) of KCl, and sensitivity increased from  $52.3 \pm 3.1$  mV/decade (SPE/V) to  $60.5 \pm 5.3$  mV/decade (SPE/PANI/V).

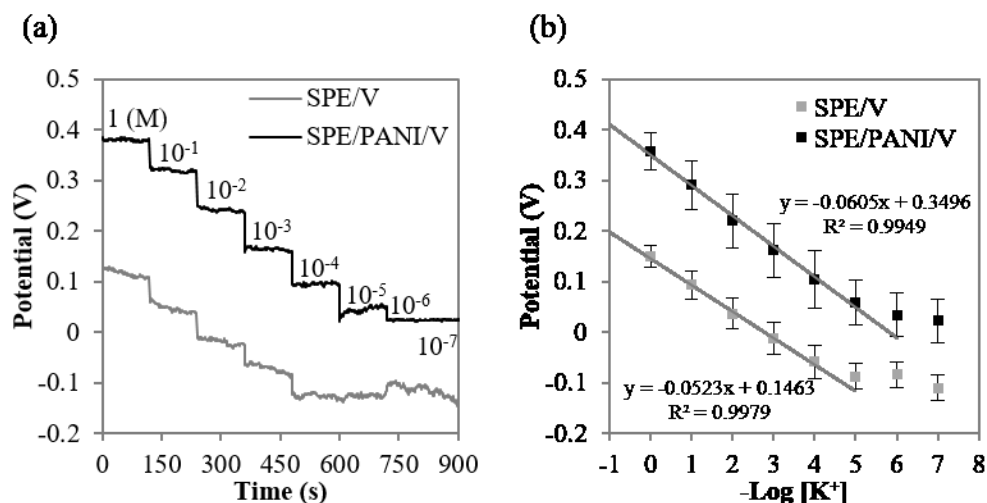


Figure A.7. (a) Electromotive force (EMF) measurements recorded for decreasing concentration of K<sup>+</sup> in DIW. (b) Average calibration curve (N = 3).

#### A.3.4. EIS

In this part, EIS measurements (Figure A.8a) were fit to the equivalent circuit (Figure A.8b) representing solution resistance ( $R_s$ ), charge transfer resistance ( $R_{ct}$ ) at the membrane/solution interface, CPE and the finite-length Warburg impedance ( $Z_w$ ). As mentioned before, a CPE was used instead of a capacitor for better agreement with the measurement. We intended to determine whether there is a qualitative difference between the three differently modified electrodes, i.e., SPE/V, SPE/PANI/V, and SPE/PANI/V, with PVB modified REs. As can be seen in Figure A.8a, a smaller semicircle indicates a reduction in charge transfer resistance of SPE/PANI/V compared to SPE/V. In addition, the PVB modification on RE did not impact the characteristics of K<sup>+</sup> ISE.

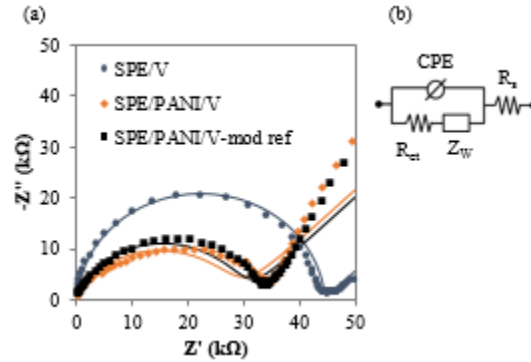


Figure A.8. (a) Impedance measurements for SPE/V, SPE/PANI/V (with as-received RE) and SPE/PANI/V with PVB modified RE. (b) Equivalent circuit used for simulations to fit the measured EIS spectra.

### A.3.5. Artificial serum test

Ion fluxes are highly regulated across human cell membranes by specific ion channels. Especially crucial for signaling in nerve and muscle cells are  $K^+$  ions, for which intracellular and extracellular concentration exhibits the utmost level of selective control between 130 – 150 and 3.5 – 5.5 mM, respectively [338-340]. Any disequilibrium implies neuronal diseases (e.g., epilepsy) or nephrosis (e.g., renal failure), where the  $K^+$  concentration in the extracellular space reaching up to 10 mM may cause a stroke [322, 340]. Extracellular fluids (blood plasma and interstitial fluid) contain various analytes from cations, anions, organic acids and proteins. Figure A.9 shows that, in artificial blood serum,  $K^+$  ISE still gives a good linear result covering from  $10^{-3}$  to 1 M with  $54.8 \pm 1.2$  mV/decade and a detection limit of  $10^{-3.5}$  M of KCl, which is well below the normal level in human extracellular fluids.

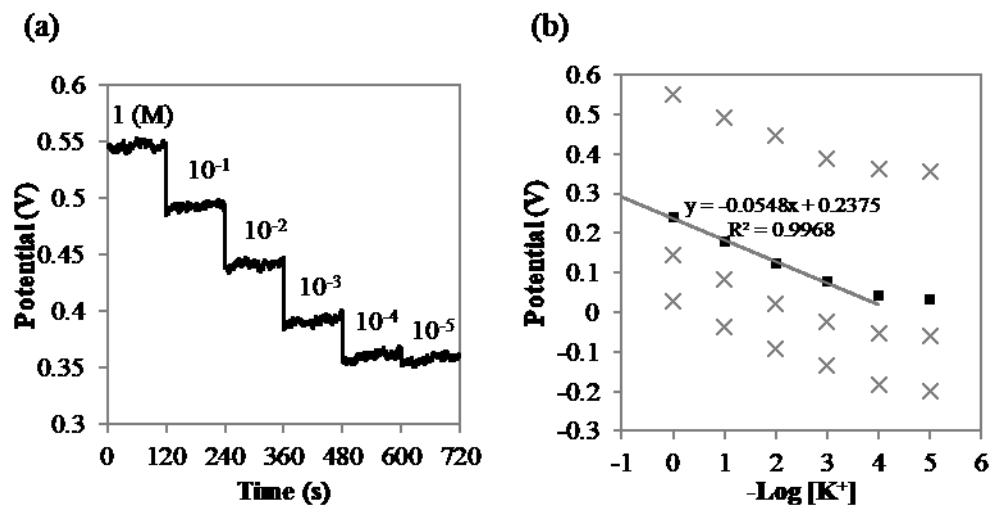


Figure A.9. (a) EMF measurements recorded for decreasing concentration of K<sup>+</sup> in artificial serum. (b) Average calibration curve (■) showing linear range from 10<sup>-3</sup> to 1 M with  $54.8 \pm 1.2$  mV/decade. Grey marks (×) represent data for three sensors with similar sensitivity.

### A.3.6. Potential stability

This test was carried out to evaluate the stability of K<sup>+</sup> ISE when the RE is covered with the PVB/NaCl layer. The solid Ag/AgCl RE is unstable due to delamination of AgCl salt in aqueous solution. As shown in Figure A.10, the potential drift of the K<sup>+</sup> electrode vs. Ag/AgCl was calculated by measuring the slope of potential in the first 3 h to be  $1.17 \mu\text{V/s}$ , followed by severe instability. On the other hand, the potential drift of the K<sup>+</sup> electrode vs. modified Ag/AgCl was  $0.78 \mu\text{V/s}$  in 12 h, while the signal stayed stable and consistent over the entire duration of the measurement. Therefore, the PVB/NaCl membrane has been shown to prevent leaking of AgCl.

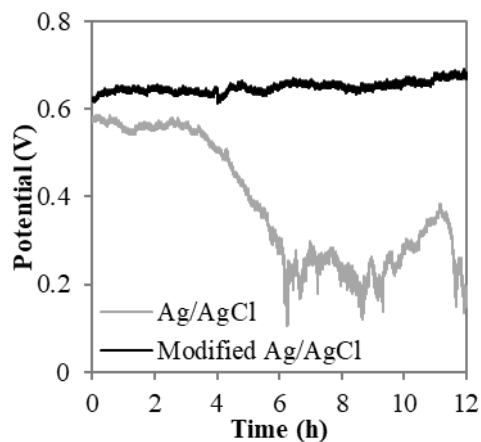


Figure A.10. EMF measurements in 0.1 M KCl of  $K^+$  ISE with and without PVB/NaCl layer on the RE.

#### A.4. Conclusions

In this study, PANI has been shown to enhance the performance of a potassium sensor whose sensitivity was 60.5 mV/decade. The limit of detection for potassium ions was  $10^{-5.8}$  M. In addition, the modified solid Ag/AgCl RE prolongs the stability of the output potential. PANI based potassium ion-selective electrodes and PVB/NaCl coated REs have been tested in artificial serum. The demonstrated high sensitivity, short-term stability and all-in-one solid-state setup may add another stepping stone towards biomedical applications for monitoring the concentration of  $K^+$  in important healthcare applications, such as blood, plasma, serum and sweat in future studies.